Ministry of Education and Science of the Russian Federation
Saint Petersburg National Research University of Information
Technologies, Mechanics, and Optics

NANOSYSTEMS:

PHYSICS, CHEMISTRY, MATHEMATICS

2016, volume 7(4)

Наносистемы: физика, химия, математика
2016, том 7, № 4

NANOSYSTEMS:

PHYSICS, CHEMISTRY, MATHEMATICS

Address: University ITMO, Kronverkskiy pr., 49, St. Petersburg 197101, Russia.
Phone: +7(812)232-67-65, **Journal site:** http://nanojournal.ifmo.ru/,
E-mail: popov1955@gmail.com

AIM AND SCOPE

The scope of the journal includes all areas of nano-sciences. Papers devoted to basic problems of physics, chemistry, material science and mathematics inspired by nanosystems investigations are welcomed. Both theoretical and experimental works concerning the properties and behavior of nanosystems, problems of its creation and application, mathematical methods of nanosystem studies are considered.

The journal publishes scientific reviews (up to 30 journal pages), research papers (up to 15 pages) and letters (up to 5 pages). All manuscripts are peer-reviewed. Authors are informed about the referee opinion and the Editorial decision.

CONTENT

Papers, presented at NANO-2015 In this issue we continue to publish works presented at International Conference on Nanomaterials and Nanotechnology (NANO 2015), 7-10 December 2015, Tamil Nadu, India.

NANOSYSTEMS: PHYSICS, CHEMISTRY, MATHEMATICS, 2016, 7 (4), P. 583–591

Optical properties of sodium niobate thin films

V. Lingwal[1], A. S. Kandari[2], N. S. Panwar[2]

[1]Pt. L.M.S. Govt. PG College Rishikesh, Uttarakhand, 249 201, India
[2]USIC, HNB Garhwal University, Srinagar (Garhwal), Uttarakhand, 246 174, India
lingwalv@yahoo.co.in, kandarialok@gmail.com, nspusic@gmail.com

PACS 77.55.fj, 78.20.Ci **DOI 10.17586/2220-8054-2016-7-4-583-591**

$NaNbO_3$ thin films were deposited under different conditions by rf magnetron sputtering of ceramic target. Spectral transmission of the deposited films was measured in the UV-Visible-near IR range. Films deposited at 300 °C showed more absorption, and films annealed at 300 °C showed less absorption than those deposited at room temperature (RT), which was found to be consistent with their X-ray diffraction (XRD) patterns. From the observed transmission spectra, refractive index, optical band gap, absorption coefficient, extinction coefficient and film thickness were calculated for the deposited films. Refractive index at 550 nm wavelength was found to be 2.11, 2.01 and 2.34 for the films deposited at RT, 300 °C and annealed at 300 °C, respectively. The refractive index was found to be almost constant with respect to frequency for the films annealed at 300 °C. Optical band gap was found 3.82, 3.7 and 3.81 eV for the films deposited at RT, 300 °C, and annealed at 300 °C, respectively. Film thickness was shown to decrease with annealing. Absorption and extinction coefficients decreased with increasing wavelength, in all the samples. Band gaps associated with different interactions have been calculated for the deposited films. Phonon assisted indirect forbidden transition was most favorable in the deposited films.

Keywords: Ferroelectrics, antiferroelectrics, thin films, sputtering, transmission.

Received: 27 January 2016

Revised: 21 June 2016

1. Introduction

The physical properties of thin film material depend on its thickness, surface to volume ratio, microstructure and microchemistry; which strongly depend on its growth process. The most conspicuous phenomena associated with thin films are optical ones. The studies on electric properties as well as the emission of electrons from thin films have made extraordinarily rapid advances in recent years, due to their wide tailor-made applications.

Dielectric materials employed in optical coatings include fluorides (e.g., MgF_2, CeF_3), oxides (e.g., Al_2O_3, TiO_2, SiO_2, Ta_2O_5), sulfides (e.g., ZnS, CdS), assorted compounds (e.g., ZnSe, ZnTe), etc. An essential common feature of dielectric optical materials is their low absorption coefficients ($\alpha < 10^3$/cm) in some relevant portion of the spectrum, where they are essentially transparent. Ferroelectric materials, such as $LiNbO_3$, $KNbO_3$, K(Ta, Nb)O_3, $PbTiO_3$ based materials, etc., are useful in optical applications, e,g., in infrared detectors, optical waveguide devices, optical memories and displays, spatial light modulators, frequency doublers for diode lasers, etc. [1–11]. Application of ferroelectric films in these devices hinges on successful integration of ferroelectric films into semiconductors or other useful substrates.

Nonmetallic materials may be opaque or transparent to visible light, and if transparent, they often appear colored. In principle, light radiation is absorbed in this group of materials by three basic mechanisms; viz., electronic polarization, electronic transitions across the band gap and electronic excitations to impurity or defect levels, which also influence their transmission characteristics. Absorption by electronic polarization is important only at light frequencies in the vicinity of the relaxation frequency of the constituent atoms. The other two mechanisms involve electron transitions, which depend on the electronic energy band structure of the materials; one of these absorption mechanisms involves the absorption as a consequence of electron excitations across the band-gap; the other is related to electron excitations to impurity or defect levels that lie within the band gap. Absorption of a photon may promote or excite an electron, across the band gap, from the nearly filled valence band to an empty state within the conduction band, thus creating a free electron in the conduction band and a hole in the valence band. The excitation energy E is related to the absorbed photon frequency (ν); i.e., $E = h\nu$. These excitations with the accompanying absorption can take place only if the photon's energy is greater than that of the band gap E_g, i.e., if $h\nu > E_g$. At the minimum wavelength for visible light, $E = 3.1$ eV, means no visible light is absorbed by nonmetallic materials having band gap energy (Eg) greater than about 3.1 eV; these materials, if of high purity, will appear transparent and colorless. Optical measurements constitute the most important means of determining the inter-band structure of the materials. Photon induced inter-band electronic transitions can occur between different bands. Also optical measurements can be used to study lattice vibrations.

In the present study, $NaNbO_3$ films were deposited on the quartz substrate using the rf magnetron sputtering method. Films were deposited at room temperature and at varying substrate temperatures. The room temperature deposited films were annealed at different temperatures. Optical parameters were measured for $NaNbO_3$ films deposited at room temperature, at 300 °C, and post deposition annealed at 300 °C. Deposited films were characterized using XRD method.

2. Preparation

Thin films of $NaNbO_3$ were deposited by the rf magnetron sputtering of bulk $NaNbO_3$ pellet targets. Films were deposited on to clean Quartz (Qz) and monocrystalline silicon surfaces. Ceramic pellets of $NaNbO_3$ of 36 mm diameter and 2.5 mm thickness were used as sputtering targets. The targets were prepared by the conventional solid-state reaction method. The pumping system used was a combination of 300 l/sec diffusion pump and a 200 l/min rotary pump. The system gives an ultimate vacuum of 3×10^{-5} mbar. The pressure was monitored using a Pirani and a Penning gauge combination. The vacuum chamber was a 300 mm diameter stainless steel cylinder. The target disk was mechanically clamped to a water-cooled assembly with magnetic arrangement. The system was arranged in sputter down configuration with a substrate-target distance of 30 mm. Separate feed-troughs were fitted for heater connections, and for the thermocouple that is used in contact with the substrate to estimate its temperature. Argon (99.999 %) was used as sputtering gas. An rf system from CVC Scientific Products Ltd, Wakingham, England, was used for sputtering. Films were deposited at a working pressure of 1×10^{-3} mbar, for 30 minutes, at different substrate temperatures. All the films were deposited at a forward power of 30 W, whereas reverse power was zero. The cleanliness of the substrate's surface exerts a decisive influence on film growth and adhesion. A thoroughly cleaned substrate is a prerequisite for the preparation of films with reproducible properties. Quartz substrates were rinsed with a laboratory detergent and then rinsed with distilled water and lastly wiped with soft dry cloth with little trace of acetone. The temperature of the substrate was monitored using a cromel-alumel thermocouple. The deposited films were left in the chamber for 2 hrs and then removed for experimental investigations. The films deposited at room temperature were annealed post-deposition, in a furnace at different temperatures, in the presence of ambient oxygen.

3. Characterization

3.1. X-ray diffraction patterns

The structures of the deposited $NaNbO_3$ films, at room temperature (RT) and at substrate temperature 225, 270, 300 and 375 °C, were studied by x-ray diffraction with the help of Philips Analytical X-ray Diffractometer (PW 3710), using CuKα_1 radiation of wavelength 1.54056 Å. Peak indexing was done by using the Joint Committee on Powder Diffraction Standards (JCPDS) data cards. The XRD patterns obtained are shown in Fig. 1. The RT deposited films exhibited crystalline structure with different orientations. However, it has been reported earlier that oxide films deposited at RT, generally, show amorphous nature and crystalline structure is set at higher temperatures [12–15].

The experimental investigations have shown that the properties of oxides depend on its growth process and post annealing process [15]. To study the effect of annealing, films deposited at RT were annealed at 400, 500 and 600 °C. The XRD patterns of annealed films are depicted in Fig. 2.

From the XRD patterns of $NaNbO_3$ films deposited at different substrate temperatures (at 225, 270, 300 and 375 °C) (Fig. 1), it has been observed that films deposited at 225 and 270 °C show crystalline structure with single face orientation while films deposited at substrate temperatures of 300 and 375 °C showed amorphous nature.

From the XRD patterns of the annealed films (Fig. 2), it has been observed that annealing up to 500 °C changes the orientation of the deposited films, and annealing at higher temperature (600 °C) shows amorphous films. The observed amorphous nature of the films annealed at higher temperatures ($\geq$ 600 °C) may be due to a deficiency of volatile sodium ions. The films deposited at RT were oriented in (101) and (221) directions. Films deposited at substrate temperatures of 225 and 270 °C and the films annealed at 400 and 500 °C showed orientation towards the (002) plane. This orientation is due to the coalescing islands, which proceed until the film reaches continuity.

3.2. Transmission spectra

The spectral transmissions (at 6 ° angle of incidence) of the $NaNbO_3$ films were measured using a UV-visible-near infrared double beam spectrophotometer (Hitachi, model 330). The observed transmission spectra of the $NaNbO_3$ films deposited at different conditions are shown in Figs. 3 – 5. It has been observed that the films deposited at 300 °C substrate temperature show more absorption while those films annealed at 300 °C shows less

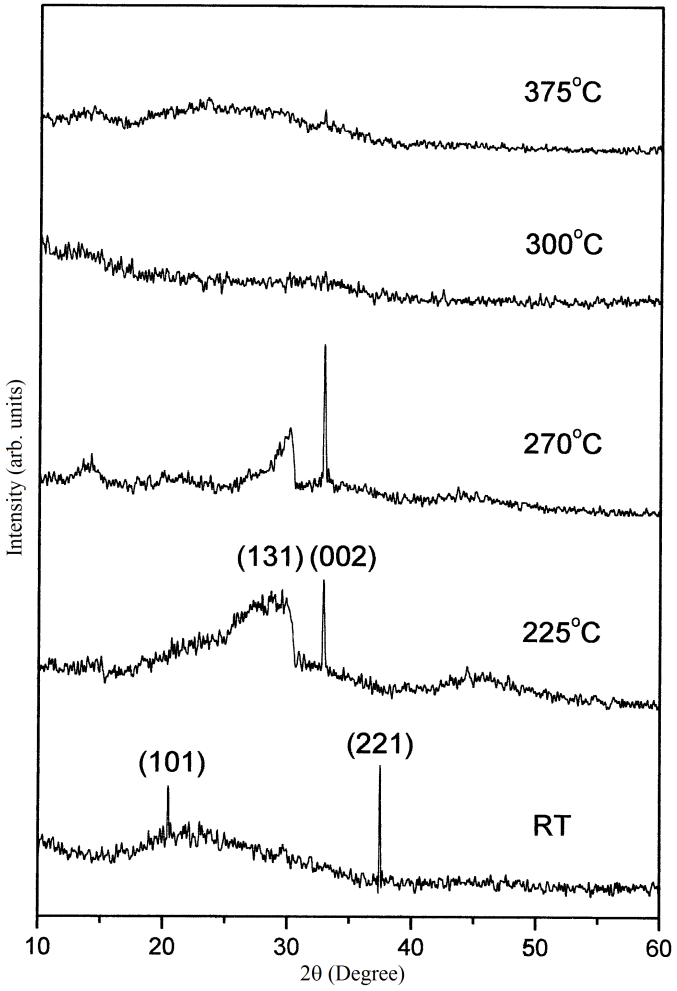

FIG. 1. X-ray diffraction patterns of $NaNbO_3$ films, deposited at different substrate temperatures

absorption than the films deposited at RT. The observed high absorption of the films also suggests an amorphous nature for the deposited films at higher substrate temperature, as has been observed in the XRD study. The lower absorption of the annealed films, at 300 °C, suggests a reorientation of the film crystallites in single face and also to the decrease in oxygen vacancies in the deposited films when annealed in the presence of ambient oxygen, as has been observed from the XRD patterns. The increase in absorption in the films, deposited at 300 °C, may be due to the higher oxygen deficiency and some amount of sodium deficiency, so the deposited films may not be in stoichiometric composition [16]. These deficiencies, in the films, may also be caused by the preferential sputtering, which removes atoms from the film leaving the deposited film sub-stoichiometric [17].

The preferential sputtering in oxide thin films can be explained on the basis of Winter and Sigmund model [16], according to which, the energy transfer coefficient in a head on collision process between an ion of mass m and a target of mass M is given by $E_T = 4mM/(m+M)^2$. Applying this equation to the collision of oxygen with oxygen and niobium atoms of the growing film, with oxygen, yields value of E_T as 1.0 for oxygen-oxygen and 0.5 for oxygen-niobium collision. This means that only 50 % of the energy is transferred in the case of oxygen-niobium collisions. Hence, more energy is delivered to the oxygen atoms than to the niobium atoms, leading to higher re-sputtering of oxygen atoms from the film. Compounds made up of elements with smaller difference in masses have fewer tendencies to be sputtered out from the film. The sub-stoichiometry causes degradation in the refractive index of the film.

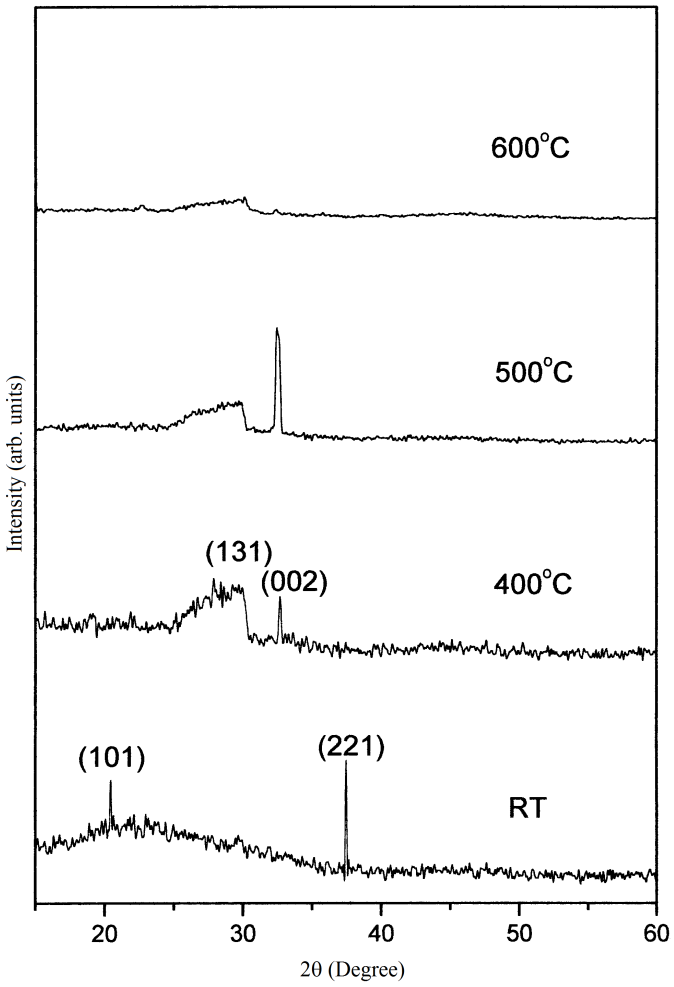

FIG. 2. X-ray diffraction patterns of $NaNbO_3$ films, deposited at room temperature (RT) and annealed at different temperatures

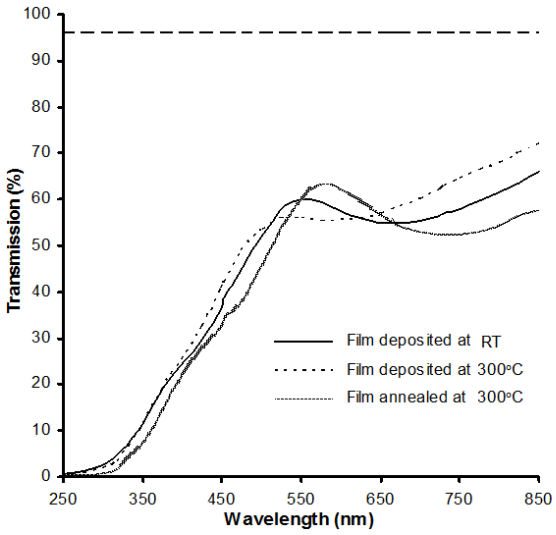

FIG. 3. Transmission spectra of $NaNbO_3$ films prepared at different conditions

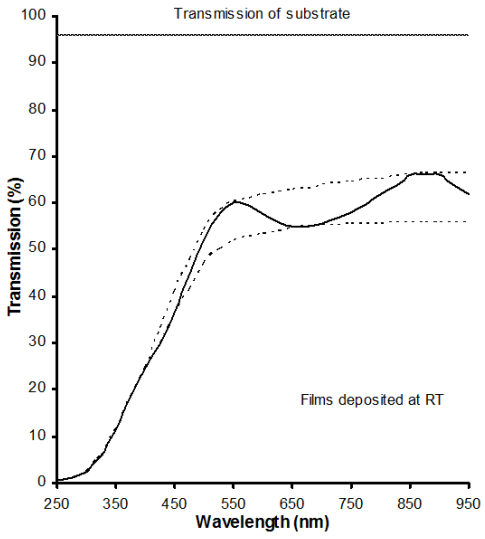

FIG. 4. Envelope of the transmission spectra of the $NaNbO_3$ films, deposited at RT

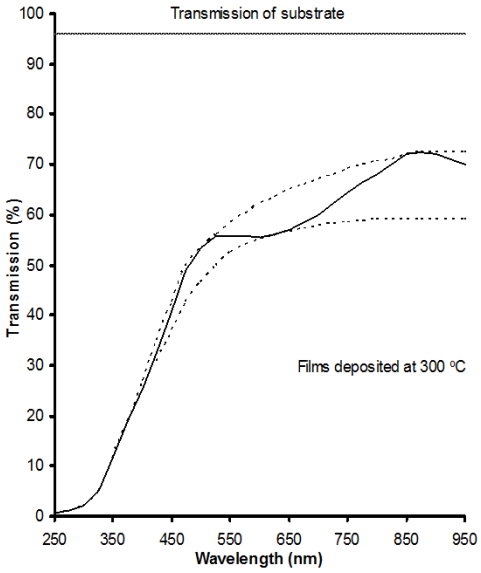

FIG. 5. Envelope of the transmission spectra of the $NaNbO_3$ films, deposited at 300 °C

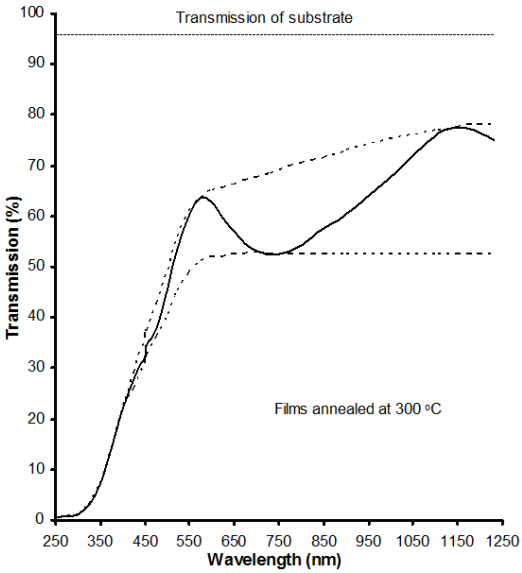

FIG. 6. Envelope of the transmission spectra of the $NaNbO_3$ films, annealed at 300 °C

4. Optical properties

Optical constants, such as, refractive index (n), optical band gap (E_g), absorption coefficient (α), extinction coefficient (k), and thickness of the films have been calculated, for $NaNbO_3$ films deposited on quartz (Qz) substrate ($n = 1.55$, transmittance $= 0.96$), using Swanepoel's envelope technique [18].

It is clear from Figs. 4 – 6 that the transmission in the film samples, deposited at the substrate temperature 300 °C, is lower than that the samples deposited at RT. It shows high absorption in the samples deposited at 300 °C substrate temperature, and thereby showing amorphous nature, which is in conformity with the results obtained from XRD patterns, Fig. 1. The film absorption has been reported to increase with high-level substrate temperature [12]. The absorption is low in the samples annealed at 300 °C, indicating good quality of $NaNbO_3$ films, Fig. 5. The low absorption in the films deposited at RT in comparison to that in the films annealed at 300 °C (as confirmed by XRD patterns, Fig. 2) may be attributed to the variation in the rate of re-crystallization, in these samples. Meanwhile, the peak transmission of all the films deposited in the present study is very much lower than that of the quartz substrate used, indicating very high absorption in these films. No many maxima and minima were observed in the transmission spectra of the present samples, which may be due to non-uniformity in the film thickness.

4.1. Refractive index (n)

According to Swanepoel's envelope technique [18], the refractive index (n), at wavelength λ, is given by

$$n(\lambda) = \left(N + \left(N^2 - n_s^2\right)^{1/2}\right)^{1/2},$$

where n_s is the refractive index of the substrate, at wavelength λ, and

$$N = \frac{2n_s\left[T_M(\lambda) - T_m(\lambda)\right]}{T_M(\lambda)\,T_m(\lambda)} + \frac{n_s^2 + 1}{2},$$

where $T_M(\lambda)$ and $T_m(\lambda)$ are the transmission maxima and minima, respectively, corresponding to wavelength λ obtained from the envelope, as shown in Figs. 3 – 5.

Figure 6 shows the calculated values of n with λ for the films deposited at different conditions. At 550 nm wavelength, the refractive index (n) values for films deposited at RT and 300 °C were 2.11 and 2.01, respectively; and 2.34 for the samples annealed at 300 °C. The degradation of n in the samples deposited at higher substrate temperature is due to sub-stoichiometry in the films due to preferential sputtering in the deposited films. Fig. 7 shows that n decreases with increasing wavelength for the films deposited at RT, and at 300 °C; while n remains almost constant for the samples annealed at 300 °C. The low value of packing density in the samples may be one of the reasons for the decrease in n with increasing wavelength, in the samples deposited at RT and at 300 °C, since

these samples may be oxygen deficient. In the samples annealed at 300 °C, in the ambient oxygen atmosphere, the oxygen stoichiometry and hence the packing density improves, and n remains constant with varying wavelength. Value of n has been reported 2.21 for the single crystal of $NaNbO_3$ [19], at 550 nm.

4.2. Optical band gap

The excellent transmission of dielectric materials in the visible region of the spectrum is found to terminate at shorter wavelengths with the onset of the UV absorption edge. The critical radiation wavelength, λ_c, at which this occurs, is given by $\lambda_c(\mu m) = 1.24/E_g$ (eV). These values physically correspond to electronic transitions from the filled valence band levels, across the energy gap E_g, to the unfilled conduction band states. Multiple peaks near the UV absorption edge indicate the complexity of these processes. At long wavelengths, the high optical transmission is limited by absorption due to the vibration of lattice ions in resonance with the incident radiation. The frequency of maximum absorption is related to the force constant and masses of vibrating anions and cations. The optical band gaps for the films deposited at RT and at 300 °C has been calculated to be 3.82 and 3.7 eV, respectively; and for the films annealed, at 300 °C, this value was found to be 3.81 eV. The band gap for single $NaNbO_3$ crystal has been reported 3.4 eV [20].

4.3. Film thickness

The thickness (d) of the film is given by [18]:

$$d = \frac{\lambda_1 \lambda_2}{4\left(n_1\lambda_2 - n_2\lambda_1\right)},$$

where λ_1 and λ_2 are the wavelengths of two successive maxima and minima; n_1 and n_2 are the refractive indices at λ_1 and λ_2, respectively.

The calculated thicknesses of the films deposited at RT and 300 °C were obtained as 3455 and 5182 Å, respectively, while a value of 3132 Å was obtained for the films annealed at 300 °C after depositing at RT. The lowering of the thickness in the annealed samples may be explained on the basis of reduction of voids between islands during the process. The voids are filled up by coalescence process, recrystallization and reorientation of the film crystallites.

4.4. Absorption and inter-band transitions

Absorption coefficient (α) of the film is given by [18]:

$$\alpha = -\frac{\log(x)}{d},$$

where,

$$x = \frac{E_m - \left[E_m^2 - \left(n^2-1\right)^3\left(n^2 - n_s^4\right)\right]^{1/2}}{\left(n-1\right)^3\left(n - n_s^2\right)},$$

with

$$E_m = \frac{8n^2 n_s}{T_M} + \left(n^2-1\right)\left(n^2 - n_s^2\right),$$

n is the refractive index of the film; T_m is the maximum transmission of the film, and d is the film thickness.

The absorption coefficient (α) was found to decrease with increased wavelength for all the $NaNbO_3$ films, deposited under different conditions. The calculated value of α was determined to be 4.67×10^3 /cm for the samples deposited at RT, at 550 nm wavelength. In the region of strong absorption, the interference fringes disappear. Values for n in strong absorption region were estimated by extrapolating the values calculated in the other parts of the spectrum [18].

The extinction coefficient (k), at wavelength λ, is given by:

$$k = \frac{\alpha\lambda}{4\pi}.$$

Observations, shown in Fig. 8, indicate that k decreases with increasing wavelength, for all the $NaNbO_3$ film samples, prepared under different conditions. Also, Absorption coefficient may be expressed as a function of the incident photon energy, $h\nu$, as [21]:

$$\alpha(h\nu) = A\left(h\nu - E_g\right)^m, \tag{1}$$

where A and m are constants, and the value of m decides the nature of transition. These observations may be analyzed according to this relation. The value of E_g has been calculated at and beyond the absorption edge. The variations of the absorption coefficient with the incident photon energy have been plotted for the estimation

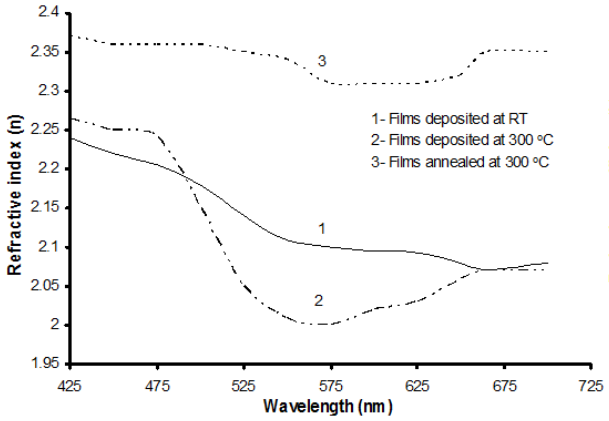

FIG. 7. Variation of refractive index with wavelength, of the $NaNbO_3$ films prepared at different conditions

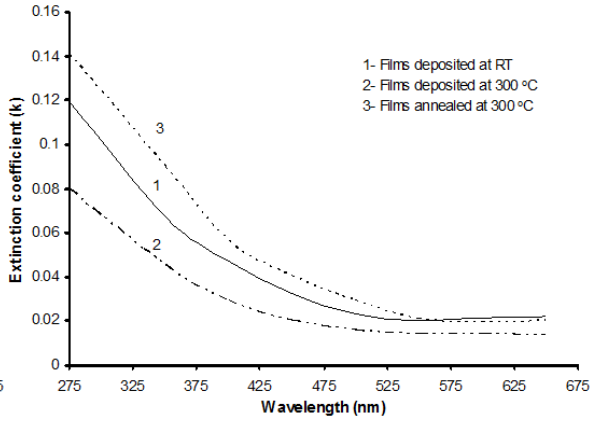

FIG. 8. Wavelength dependence of extinction coefficient of $NaNbO_3$ films, prepared at different conditions

of energy gap. The band gap was found to be composition dependent for dielectric films [22–25]. The radiation absorbed by a solid can be converted into elastic vibrations in it, and it may initiate photon-electron, photon-phonon and other interactions.

The photon-electron interaction leads to direct transition probability and this interaction satisfies Eq. (1) with $m = 1/2$. Figs. 9(a), 10(a) and 11(a) show α^2 *vs.* $h\nu$ curves, for the films deposited at RT, at 300 °C, and for the films annealed at 300 °C, respectively. Extrapolation of the straight portion of the curve, α^2 *vs.* $h\nu$, gives the direct allowed energy band gap of the film samples. The value for the direct allowed energy band gap was estimated from the intersection of the tangent, drawn near the absorption edge, in the α^2 *vs.* $h\nu$ plot (the straight line portion), with the energy axis. The direct allowed energy band gap values were obtained as 3.4 eV for the films deposited at room temperature and 300 °C, and 3.2 eV for the films annealed at 300 °C.

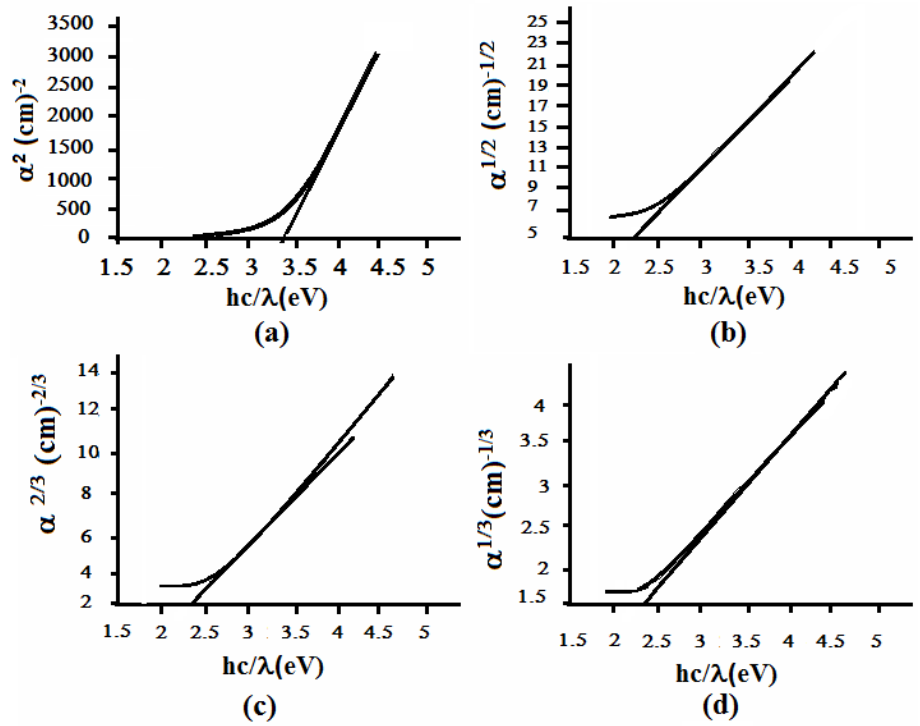

FIG. 9. α^m as a function of hc/λ, for different m values, in the samples deposited at RT

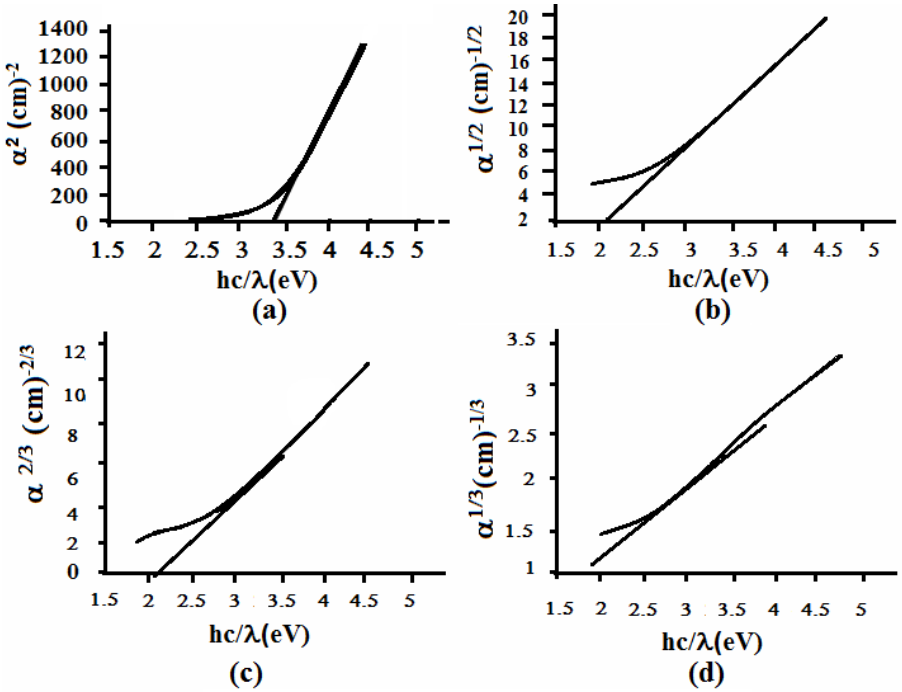

FIG. 10. α^m as a function of hc/λ, for different m values, in the samples deposited at 300 °C

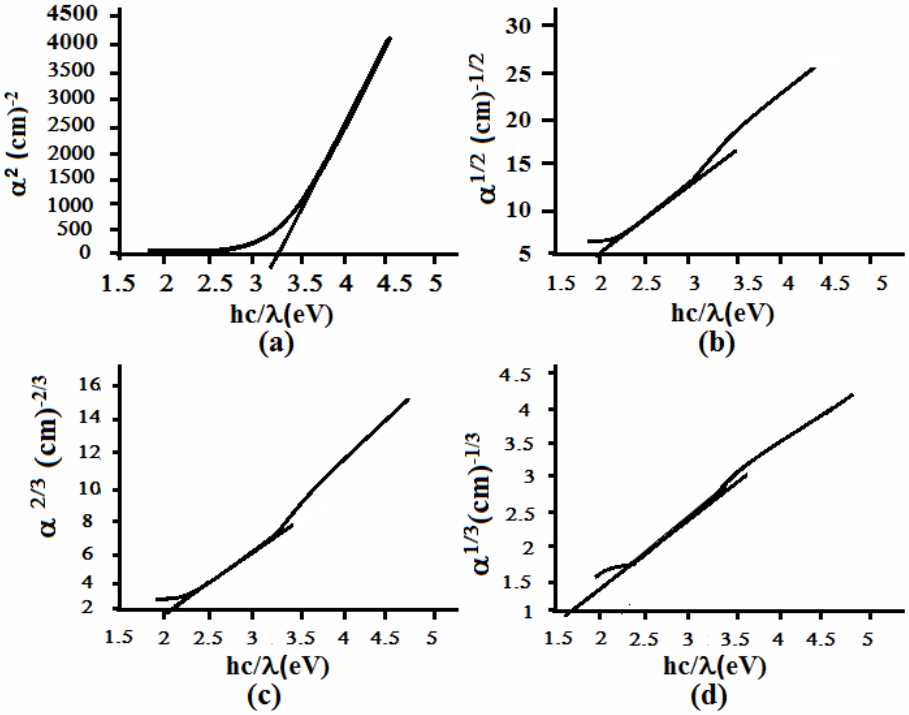

FIG. 11. α^m as a function of hc/λ, for different m values, in the samples annealed at 300 °C

The photon-phonon interaction leads to indirect allowed transition probability and is given by Eq. (1) with $m = 2$; and E_g is indirect allowed energy band gap. Figs. 9(b), 10(b) and 11(b) show the variation of $\alpha^{1/2}$ with $h\nu$. The indirect allowed energy band gap from the $\alpha^{1/2}$ *vs.* $h\nu$ plots is found to be 2.2, 2.09 and 2.0 eV; for the films deposited at RT, 300 °C, and for the films annealed at 300 °C, respectively.

In addition to the photon assisted electronic transitions there are phonon assisted interaction probabilities that give rise to the inter-band absorptions in the films corresponding to the energy levels in forbidden band. Excitons may be formed by direct photons only or by photon-phonon assistance. This direct absorption probability in the forbidden gap is given by Eq. (1) with $m = 3/2$; and the $\alpha^{2/3}$ *vs.* $h\nu$ plots are shown in Figs. 9(c), 10(c) and 11(c), for films prepared at different conditions. The values of direct forbidden gap energy (associated with this mechanism) were found to be 2.3, 2.06, and 2.12 eV, for the samples deposited at RT, at 300 °C substrate temperature, and for the samples annealed at 300 °C, respectively. Excitons may also be formed by photon-phonon interactions. The phonon assisted probabilities or indirect absorption probability in the forbidden gap is given by Eq. (1) with $m = 3$. Figs. 9(d), 10(d) and 11(d) shows $\alpha^{1/3}$ *vs.* $h\nu$ plot to obtain the indirect forbidden energy gap E_g, associated with this mechanism. The values of indirect forbidden energy gap E_g were found to be 2.24, 1.86, and 1.63 eV, for the samples deposited at RT, at 300 °C and for the samples annealed at 300 °C, respectively.

From these measurements, the most satisfactory representation is obtained for $\alpha^{1/3}$ *vs.* $h\nu$ plot, which suggests phonon assisted indirect forbidden transitions in the deposited $NaNbO_3$ films.

References

[1] Gunther P. Nonlinear optical crystals for optical frequency doubling with laser diodes. *Proc. SPIE*, 1981, **236**, P. 8–19.

[2] Okuyama M., Matsui Y., Nakano H., Hamakawa Y. $PbTiO_3$ ferroelectric thin film gate fet for infrared detection. *Ferrelectrctrics*, 1981, **33** (1), P. 235–241.

[3] Hewig G.H., Jain K. Frequency doubling in a $LiNbO_3$ thin film deposited on sapphire. *J. Appl. Phys*., 1983, **54** (1), P. 57–61.

[4] Baumert J.C., Hoffnagle J., Gunther P. Nonlinear optical effects in $KNbO_3$ crystals at $Al_xGa_{1-x}As$, dye, ruby and Nd:YAG laser. *Proc. SPIE*, 1984, **492**, P. 374–386.

[5] Iijimo K., Tomita Y., Takayama R., Ueda I. Preparation of C-axis orientated $PbTiO_3$ thin films and their crystallographic, dielectric, and pyroelectric properties. *J. Appl. Phys*., 1986, **60** (1), P. 361–367.

[6] Martin S.J., Butler M.A., Land C.E. Ferroelectric optical image comparator using PLZT thin films. *Electron. Lett*., 1988, **24** (24), P. 1486–1487.

[7] Krishnakumar S., Oguz V.H., et al. Deposition and characterization of thin ferroelectric lead lanthanum zirconate titanate (PLZT) films on sapphire for spatial light modulators applications. *IEEE Trans. Ultrason. Ferrelec. Freq. Contr*., 1991, **38** (6), P. 585–590.

[8] Ivey M., Mancha S., Carter R. Optical information storage and charge traps in PZT thin films. *IEEE Trans. Ultrson. Ferroelec. Freq. Contr.*, 1991, **38** (4), P. 337–343.

[9] Tamada H., Yamada A., Saitoh M. $LiNbO_3$ thin film optical waveguide grown by liquid phase epitaxy and its application to second-harmonic generation. *J. Appl. Phys*., 1991, **70** (5), P. 2536–2541.

[10] Gutmann R., Hullinger J., Hauert R., Mosser E.M. Auger electron and x-ray photoelectrons spectroscopy of monocrystalline layers of $KTa_{1-x}Nb_xO_3$ grown by liquid-phase epitaxy. *J. Appl. Phys*., 1991, **70** (5), P. 2648–2653.

[11] Polla D.I., Ye C., Tamagawa T. Surface-micromachined $PbTiO_3$ pyroelectric detectors. *Appl. Phys. Lett*., 1991, **59** (1), P. 3539–3544.

[12] Sreenivas K., Mansingh A., Sayer M. Structural and electrical properties of rf-sputtered amorphous barium titanate thin films. *J. Appl. Phys*., 1987, **62** (11), P. 4475–4481.

[13] Rabson T.A., Baumann R.C., Rost T.A. Thin film lithium niobate on silicon. *Ferroelectrics*, 1990, **112** (1), P. 265–271.

[14] Krupanidhi S.B., Mohan Rao G. Pulsed laser deposition of strontium titanate thin films for dynamic random access memory applications. *Thin Solid Films*, 1994, **249** (1), P. 100–108.

[15] Pignolet A., Mohan Rao G., Krupanidhi S.B. Rapid thermal processed thin films of reactively sputtered Ta_2O_5. *Thin Solid Films*, 1995, **258** (1–2), P. 230–235.

[16] Smith R.A. *Wave Mechanics of Crystalline Solids*. North Holland publication, Amsterdam, 1972.

[17] Rubio J.D., Albella J.M., Martinez-Duart J.M. Sputtered Ta_2O_5 antireflecting coating for silicon solar cells. *Thin Solid Films*, 1982, **90** (4), P. 405–408.

[18] Swanepoel S. Determination of the thickness and optical constants of amorphous silicon. *J. Phys. E: Sci. Inst*., 1983, **16** (12), P. 1214–1222.

[19] Landolt H., Börnstein R. et al. *Numerical Data and Functional Relationships in Science and technology*, **16**, Group III, *Crystal and Solid State Physics*. Springer Verlag Berlin, Heidelberg-New York, 1981.

[20] Raevskii I.P., Reznichenko L. Phase transitions and electrical properties of ferroelectric solid solution based on $NaNbO_3$. *Izestiva Akademii Nauk SSSR, Neorganicheskie Mater.,* 1979, **15** (5), P. 872–875.

[21] Sze S.M. *Physics of Semiconductor Devices*. Wiley publication, New York, 2000.

[22] Pankove J.J. *Optical Processes in Semiconductors*. Prentice Hall, New Jersey, 1956.

[23] Sze S.M. Current transport and maximum dielectric strength of silicon nitride films. *J. Appl. Phys*., 1967, **38** (7), P. 2951–2955.

[24] Kittel C. *Solid State Physics*. John Wiley and Sons, New York, 1970.

[25] Michael S. *Physics of Semiconductor Devices*. Prentice Hall of India Pvt. Ltd., New Delhi, 1995.

NANOSYSTEMS: PHYSICS, CHEMISTRY, MATHEMATICS, 2016, 7 (4), P. 592–594

In_4Mg_3 in In_xMg_3 ($x = 1 - 6$) series: a magic unit for future smart materials

Debesh R. Roy*, Majid Shaikh, Vipin Kumar

Department of Applied Physics, S. V. National Institute of Technology, Surat 395007, India

drr@ashd.svnit.ac.in

PACS 36.40.-c, 81.05.Dz, 61.46.Bc, 31.15.E **DOI 10.17586/2220-8054-2016-7-4-592-594**

Systematic investigation on the stability and electronic properties of a series of bimetallic (semiconductor-alkaline earth) clusters, viz., In_xMg_3 ($x = 1-6$) is performed, in the search for exceptionally and/or unusually stable motifs. A very popular hybrid exchange-correlation functional, B3LYP as proposed by A. D. Becke is employed for this purpose under the density functional formalism. The magic stability among the concerned clusters is explained using the jellium model. It is evident from the present study that the magic stability of In_4Mg_3 cluster arises due to the jellium shell closure and found as a potential building block for future novel semiconductor materials.

Keywords: Magic clusters, jellium model, density functional theory, smart materials.

Received: 27 January 2016. Revised: 16 May 2016.

1. Introduction

As a consequence of the discovery of fullerene [1], atomic and molecular clusters have gained immense attention as the potential candidates for designing novel nanomaterials [2–4]. The most important fact is that atomic clusters of sub-nano or nano-scale dimensions exhibits drastic differences in the physicochemical properties compared to their bulk counterparts, due to the effect of quantum confinement. This important behavior of nano-scale materials are found to be very useful in various technical applications over the last two decades or so [1–7].

In order to overcome the usual meta-stable nature of many clusters, one main focus of researchers is to search for the clusters with unusual or exceptional stability and/or useful physicochemical properties. The jellium is a quantum mechanical model of interacting electrons within an infinite volume of space and neutralized with an artificially assumed uniformly distributed background positive charge [8]. The jellium is usually treated within the density functional theory (DFT) [9, 10], since at zeroth temperature the properties of a jellium depend solely on electron density (ρ) [8]. Through an experimental mass spectra of a series of sodium clusters, W. D. Night et al. [11] have noticed that sodium clusters with a certain total number of valence electrons, viz., 2, 8, 18, 20, 34, 40, 52, ... etc. shows exceptional stability compared to their neighbors. Such exceptionally stable clusters are named as magic clusters, and based on the jellium model as mentioned above and similar to the electronic shell structure of atom, they have proposed a new cluster valence shell structure in terms of the total valence electrons of the magic clusters as $1S^2 1P^6 1D^{10} 2S^2 1F^{14} 2P^6$ .... Such cluster shell structure essentially represents the total valence electrons as observed for magic clusters with shell closure as $2(1S^2)$, $8(1S^2 1P^6)$, $18(1S^2 1P^6 1D^{10})$, $20(1S^2 1P^6 1D^{10} 2S^2)$, $34(1S^2 1P^6 1D^{10} 2S^2 1F^{14})$ etc. The exceptionally stable cluster motifs may have potency for utilizing them as the building blocks for designing novel cluster assembled materials.

The purpose of the present work is to perform a detailed study on the geometries, electronic properties as well as to search for any unusual and/or exceptionally stable cluster building motifs from the In_xMg_3 ($x = 1 - 6$) cluster series. The electronic properties include energy gain in adding an indium atom (ΔE_{In}) to the previous sizes, HOMO-LUMO energy gap (*HLG*), ionization potential (*I.P.*), chemical hardness (η) etc.

2. Theory and computation

The energy gain (ΔE_{In}) in forming In_xMg_3 clusters by adding an indium atom to the previous $In_{x-1}Mg_3$ ($x = 1 - 6$) size is given as:

$$\Delta E_{\mathrm{In}} = E\left(\mathrm{In}\right) + E\left(\mathrm{In}_{x-1}\mathrm{Mg}_3\right) - E\left(\mathrm{In}_x\mathrm{Mg}_3\right), \tag{1}$$

where $E(\mathrm{In}_x\mathrm{Mg}_3)$, $E(\mathrm{In}_{x-1}\mathrm{Mg}_3)$ and $E(\mathrm{In})$ are the total energies of the In_xMg_3, $In_{x-1}Mg_3$ clusters and of the In atom, respectively.

Using Koopmans' finite difference approximation, the ionization potential (*IP*) and electron affinity (*EA*) can be expressed in terms of the highest occupied (ϵ_{HOMO}) and the lowest unoccupied (ϵ_{LUMO}) molecular orbital energies as:

$$IP \approx -\epsilon_{HOMO}; \qquad EA \approx -\epsilon_{LUMO}. \tag{2}$$

The chemical hardness can be expressed in terms of ϵ_{HOMO} and ϵ_{LUMO} as follows:

$$\eta \approx \frac{IP - EA}{2} \approx \frac{\epsilon_{LUMO} - \epsilon_{HOMO}}{2}. \tag{3}$$

The theoretical investigations are carried out within the density functional theory (DFT) framework [9, 10]. A molecular orbital approach, using a linear combination of atomic orbitals, is applied to probe the electronic structure. The actual DFT based calculations are performed using GAUSSIAN 09 [12] program. We have used B3LYP exchange-correlation functional [13] and LANL2DZ basis sets [14] for our calculations. A large number of initial guesses in every possible way is considered for each of the In_xMg_3 ($x = 1 - 6$) clusters to predict their ground state structures. The geometries of optimized clusters are drawn with CHEMCRAFT [15] visualization software.

3. Results and discussion

The ground state structures of In_xMg_3 ($x = 1 - 6$) clusters along with the geometrical bond lengths and point groups is represented in Fig. 1. The point group of various structures is considered within the tolerance limit of 0.1 Å. The profile of energy gain (ΔE_{In}) in forming each clusters by adding one indium atom to an existing $In_{x-1}Mg_3$ ($x = 1 - 6$) cluster is provided in Fig. 2.

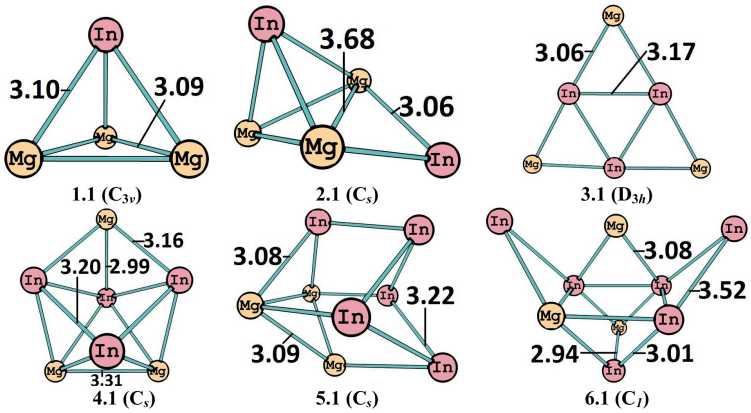

FIG. 1. Ground state structures and associated point groups of In_xMg_3 ($x = 1 - 6$) clusters. Isomer $x.n$ ($x = 1 - 6$) represents the clusters with x boron atoms in its lowest energy state ($n = 1$). The bold numbers on the cluster images show a few representative bond distances between In–In, Mg–Mg and In–Mg atoms in Angstroms (Å)

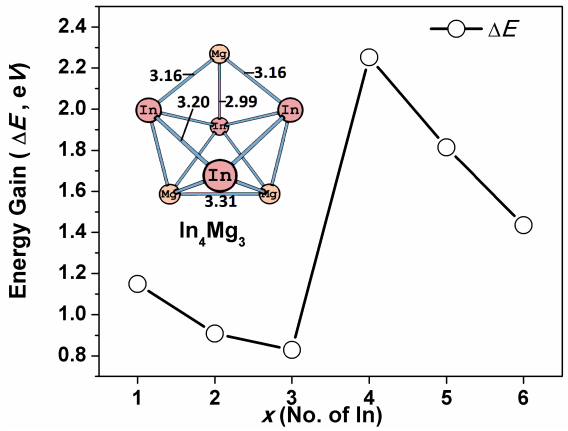

FIG. 2. Energy gain (ΔE) of In_xMg_3 clusters, in adding an indium atom to an existing $In_{x-1}Mg_3$ ($x = 1-6$) cluster. The bold numbers on the cluster image show few representative bond distances between In–In, Mg–Mg and In–Mg atoms in Angstroms (Å)

It can be noticed that, In_4Mg_3 cluster has very high energy gain (2.25 eV) compared to its neighboring clusters, implying its exceptional stability in the considered series. The stability of In_4Mg_3 is expected from the jellium framework since the number of valence electrons of the system is 18, which is a magic number with cluster electronic shell closure as $1S^2 1P^6 1D^{10}$. Table 1 provides the energy gain (ΔE_{In}), HOMO-LUMO energy gap (HLG), ionization potential (IP), electron affinity (EA) and chemical hardness (η) of the In_xMg_3 ($x = 1 - 6$) clusters. The maximum values of ΔE_{In} (2.25 eV) for In_4Mg_3 cluster justifies itself as the most stable motif in the series. The stability of the In_4Mg_3 cluster is further confirmed by its large I.P. (4.31 eV) value.

TABLE 1. Energy gain in adding an In atom (ΔE) to an existing $In_{x-1}Mg_3$ ($x = 1-6$), HOMO-LUMO energy gap (*HLG*), ionization potential (*IP*), electron affinity (*EA*) and chemical hardness (η) of the In_xMg_3 ($x = 1 - 6$) clusters

X	***ΔE (eV)***	***HLG (eV)***	***IP (eV)***	***EA (eV)***	***η (eV)***
1	1.15	2.20	4.36	2.16	1.10
2	0.91	1.23	3.58	2.35	0.62
3	0.82	0.85	3.71	2.86	0.42
4	2.25	1.19	4.31	3.12	0.60
5	1.82	1.95	4.34	2.39	0.98
6	1.44	1.55	4.26	2.71	0.77

In summary, In_4Mg_3 cluster is identified as a new magic cluster in the family of bimetallic magic clusters [16–18]. The possibility of utilizing In_4Mg_3 cluster as a potential building block for future cluster assembled materials by linking them with suitable inorganic/organic linkers is currently being investigated in our laboratory.

4. Conclusions

A detail theoretical study was performed in the search for exceptionally stable or magic clusters in the In_xMg_3 ($x = 1 - 6$) series. In_4Mg_3 shows magic stability with the effect of jellium shell closure. The significant energy gain, HOMO-LUMO energy gap (*HLG*), ionization potential, chemical hardness and electron affinity explain the origin of the extraordinary stability of In_4Mg_3 motif and imply its suitability to be considered as a building motif for novel inorganic nanomaterials. Also, the HLG value for In_4Mg_3 as 1.19 eV implies an initial classification for its suitability for application towards the design of novel semiconductor materials.

Acknowledgements

DRR is thankful to the SERB, New Delhi, Govt. of India, for financial support.

References

[1] Kroto H.W., Heath J.R., et al. C_{60}: buckminsterfullerene. *Nature*, 1985, **318** (6042), P. 162–163.
[2] *Handbook of nanotechnology* (3rd Ed.), Ed. Bhushan B., Springer, NY, 2010.
[3] Jena P., Castleman Jr A.W. *Nanoclusters: A Bridge Across Disciplines. A bridge across disciplines*, 2010, (Vol. 1), Elsevier.
[4] Song Y., Fu F., et al. The Magic Au_{60} Nanocluster: A New Cluster?Assembled Material with Five Au13 Building Blocks. *Angew. Chem. Int. Ed.*, 2015, **127** (29), P. 8550–8554.
[5] Chattaraj P.K., Roy D.R. Aromaticity in polyacene analogues of inorganic ring compounds. *J. Phys. Chem. A*, 2007, **111** (21), P. 4684-4696.
[6] Roy D.R. A DFT study on group III and V combined hexagonal clusters as potential building motifs for inorganic nanomaterials. *J. Mol. Struct.*, 2012, **1007**, P. 203–207.
[7] Lim S.Y., Shena W., Gao Z. Carbon quantum dots and their applications. *Chem. Soc. Rev.*, 2015, **44** (1), P. 362–381.
[8] Hughes R.I.G. Theoretical practice: the Bohm-Pines quartet. *Perspectives on science*, 2006, **14** (4), P. 457–524.
[9] Hohenberg P., Kohn W. Inhomogeneous electron gas. *Phys. Rev. B*, 1964, **136** (3), P. 864.
[10] Kohn W., Sham L.J. Self-consistent equations including exchange and correlation effects. *Phys. Rev. A*, 1965, **140** (4), P. 1133.
[11] Knight W.D., et al. Electronic shell structure and abundances of sodium clusters. *Phys. Rev. Lett.*, 1984, **52** (24), P. 2141.
[12] Frisch M.J., et. al. Gaussian 09, R-D.01. Gaussian, Inc., Pittsburgh PA, 2013.
[13] Becke A.D. Density-functional thermochemistry. III. The role of exact exchange. *The J. Chem. Phys.*, 1993, **98** (7), P. 5648–5652.
[14] Hay P.J., Wadt W.R. Ab initio effective core potentials for molecular calculations. Potentials for the transition metal atoms Sc to Hg. *J. Chem. Phys.*, 1985, **82** (1), P. 270–283.
[15] Chemcraft. Zhurko, G.A., Zhurko, D.A. `http://www.chemcraftprog.com`.
[16] Claridge S.A., Castleman A.W. Jr., et. al. Cluster-assembled materials. *ACS Nano*, 2009, **3**, P. 244–255.
[17] Castleman Jr.A.W., Khanna S.N. Clusters, Superatoms, and Building Blocks of New Materials. *J. Phys. Chem. C*, 2009, **113**, P. 2664–2675.
[18] Roy D.R., Singh P.K. Magic Stability of Ga_4Mg_3 Cluster in Ga_xMg_3 ($x = 1 - 6$) Series: A Density Functional Study. *Chem. Phys.*, 2013, **411**, P. 6–10.

NANOSYSTEMS: PHYSICS, CHEMISTRY, MATHEMATICS, 2016, 7 (4), P. 595–598

Structural and magnetic properties of $BaCo_{2-x}Ni_xFe_{16}O_{27}$ hexagonal ferrite prepared by a simple heat treatment method

Chetna C. Chauhan[1a], Rajshree B. Jotania[2b]

[1]Institute of Technology, Nirma University, Ahmedabad – 382 481, Gujarat, India
[2]Department of Physics, University School of Sciences, Gujarat University, Ahmedabad – 380 009, Gujarat, India

[a]chetna.chauhan@nirmauni.ac.in, [b]rbjotania@gmail.com

PACS 61.05.cp, 75.50.Vs, 75.60.Ej, 81.05.-t, 81.07.Wx **DOI 10.17586/2220-8054-2016-7-4-595-598**

A series of nickel-doped barium cobalt hexagonal ferrite samples with chemical composition $BaCo_{2-x}Ni_xFe_{16}O_{27}$ (x = 0.4, 0.8, 1.2, 1.6 and 2.0) were prepared using a simple heat treatment method. The dried precursor was calcined at 650 °C for 3 hours in a muffle furnace and slowly cooled to room temperature in order to obtain nickel-doped barium cobalt hexagonal ferrite powder. The prepared hexagonal ferrite powder samples were characterized using X-ray diffraction (XRD) and Vibrating Sample Magnetometer (VSM) techniques in order to study the effect of nickel substitution on structural and magnetic properties of barium cobalt hexagonal ferrites. The XRD analysis confirms the formation of mixed phases of W, M and spinel (S). The prepared powders exhibited single and multi-domain structures.

Keywords: Nickel doped barium cobalt hexagonal ferrites, heat treatment method, structural and magnetic measurements.

Received: 28 January 2016

Revised: 25 May 2016

1. Introduction

Barium hexaferrites possess magnetoplumbite crystal structure and have been extensively studied because of their large intrinsic uniaxial anisotropy and high Curie temperature, which make them widely used as permanent magnets, microwave devices and high density magnetic recording media, microwave absorbers, components and shielding [1–3]. Hexagonal ferrites are used in various components at high frequency range due to their high magnetic anisotropy, high Curie temperature, mechanical hardness, very low electrical conductivity, low dielectric loss, excellent chemical stability and corrosion resistance; their magnetic properties arise from the interactions between metallic ions occupying particular positions relative to the oxygen ions in its hexagonal crystalline structure [4, 5]. It is well known that structural and magnetic properties of barium hexaferrites strongly depend upon preparation method, substitution of Fe with other kind of ions and amount [6]. W-type hexagonal ferrites possess seven different sites ($4f_{IV}$, 2d, 12k, 6g, 4f, $4f_{VI}$ and 4e) in hexagonal crystal lattice, out of them five are magnetic sites. Iron ions are distributed among these sites of hexagonal crystal lattice [7]. Substitution of divalent or trivalent ions among various sublattices of hexagonal lattice can be used to improve intrinsic magnetic properties of barium hexaferrites [7]. During last decade various efforts have been made to improve structural and magnetic properties of barium hexaferrites by divalent and trivalent substitutions [8–10].

In the present investigation, a simple heat tratment method is adopted to prepare nickel substituted barium cobalt hexaferrite powder. The main objective of present investigation is to study the effect of nickel substitution on structural and magnetic properties of $BaCo_{2-x}Ni_xFe_{16}O_{27}$ (x = 0.4, 0.8, 1.2, 1.6 and 2.0) hexaferrite powder prepared by a simple heat treatment method and calcined at 650 °C for 3 hours.

2. Experimental

A series of $BaCo_{2-x}Ni_xFe_{16}O_{27}$ (x = 0.4, 0.8, 1.2, 1.6 and 2.0) hexaferrite is synthesized using high purity metal nitrate reagent as precursors, polyvinyl pyrrolidone (PVP) [$(C_6H_9NO)_n$] as a capping agent to reduce the agglomeration of the magnetic particles and deionized water was used as the solvent. The aqueous PVP solution is prepared by dissolving 3 g of polymer in 100 ml of deionized water and kept at 70 °C. Next, 1.6 mmol of iron nitrate [$(Fe(NO_3)_2)$], 0.1 mmol of barium nitrate [$Ba(No_3)_2$], 0.2 mmole of cobalt nitrate [$(CoN_2O_6{\cdot}6H_2O)$] and 0.4 mmole nickel nitrate [$Ni(NO_3)_2$] solution was added into PVP solution and then kept on a magnetic stirrer for 2 hours. The mixed solution was heated at 80 °C and the resulting orange thick slurry was recovered. The obtained slurry was heated at 650 °C for 3 hours to obtain nickel-doped barium cobalt hexaferrite powder, which was crushed in to fine powder using a mortar and pastel. The same procedure is repeated for x = 0.8, 1.2, 1.6 and 2.0 samples.

3. Results and discussion

3.1. Crystal Structure

A Bruker D. Z. Phaser diffractometer (PW 1830) revealed X-ray powder diffraction (XRD) pattern when using Cu-Kα radiation ($\lambda = 1.5405$ Å) with a step scan of 0.02 °C/min to determine the crystal structure of ferrite powder. Fig. 1 shows the XRD patterns of $BaCo_{2-x}Ni_xFe_{16}O_{27}$ ($x = 0.4, 0.8, 1.2, 1.6, 2.0$) powder samples. The XRD analysis reveals presence of W-ferrites (JCPDS No. 78-0135), M-ferrites (JCPDS No. 43-0002) and S-ferrites Fe_3O_4 (JCPDS file – PDF # 790417) in final product; both W and M possess hexagonal while S possesses spinel crystal structure. No traces of α-Fe_2O_3 was noted, as was observed in Ba-Ca hexaferrite [11, 12] prepared by the sol gel technique. It is reported [13] that the unit cell of W phase is closely related to the M-phase, the only difference is that the successive R blocks are inter placed by two S-blocks instead of one as in the M-phase. It has also been reported by other researcher [14] that W-type hexagonal ferrite is chemically unstable and some of W-phase decomposed with the M-phase.

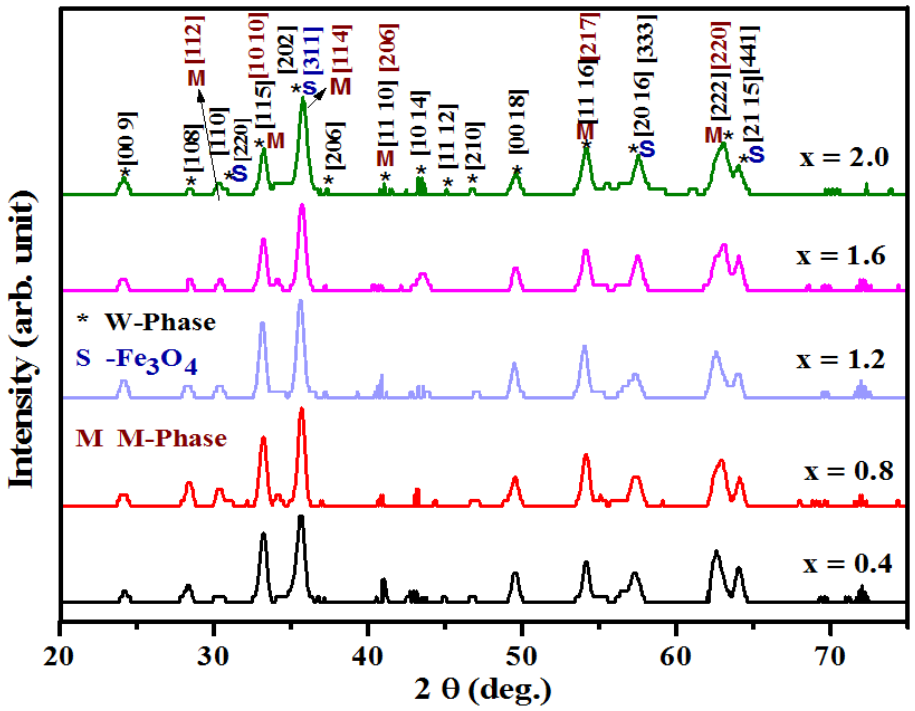

FIG. 1. X-ray diffraction patterns of $BaCo_{2-x}Ni_xFe_{16}O_{27}$ ($x = 0.4, 0.8, 1.2, 1.6, 2.0$) powder samples prepared using a simple heat treatment method and calcinated at 650 °C for 3 hours

The variation of lattice parameters a, c their ratio (c/a) and cell volume with the substitution of nickel are listed in Table 1. It is clear from Table 1 that value of (c/a) for all the samples remains constant. This behavior can be explained on the basis of ionic radii of the substituted ions. The ionic radius of Co^{+2} is 0.65 Å, which is nearly of the same order of that of Ni^{+2} ions (0.69 Å). This confirms that Ni^{+2} ions replaces Co^{+2} ions in the structure without disturbing the hexagonal symmetry. The average crystalline size (D_{xrd}) of the prepared $BaCo_{2-x}Ni_xFe_{16}O_{27}$ ($x = 0.4, 0.8, 1.2, 1.6, 2.0$) powder samples is calculated from the strongest Bragg peak [202] based on the Debye-Scherrer formula [15] shown in Table 2.

3.2. Magnetic Properties

The magnetic properties of the hexagonal ferrite powders are recorded at room temperature on a vibrating sample magnetometer (VSM) (Lake Shore, Model 7404). Fig. 2(a) shows the field dependence of the magnetization curves for $BaCo_{2-x}Ni_xFe_{16}O_{27}$ ($x = 0.4, 0.8, 1.2, 1.6, 2.0$) samples measured at room temperature under an applied field of 12.5 KOe. Saturation Magnetization (Ms), Coercivity (Hc), retaintivity (Mr) and squareness ratio (Mr/Ms) have been calculated from obtained hysteresis loops and listed in Table 2. The variation of Ms, Mr and Mr/Ms with nickel content (x) is shown in Fig. 2(b). The saturation magnetization and remanence values are found higher in $x = 0.8$ sample. The saturation magnetization and coercive field values were found

TABLE 1. Lattice constant a, c, ratio (c/a), volume of unit cell (V) and crystallite size (D_{xrd}) of $BaCo_{2-x}Ni_xFe_{16}O_{27}$ hexaferrite samples

Nickel Concentration (x)	Lattice Parameter a [Å]	Lattice Parameter c [Å]	(c/a)	Cell Volume V [Å]^3	Crystalline size D_{xrd} [nm]
0.4	5.885	33.100	5.624	992.747	15.55 ± 0.78
0.8	5.885	33.105	5.625	992.898	15.58 ± 0.78
1.2	5.885	33.109	5.626	993.018	15.09 ± 0.75
1.6	5.810	32.846	5.653	960.180	14.38 ± 0.72
2.0	5.819	32.995	5.670	967.526	13.19 ± 0.66

TABLE 2. Room temperature Magnetic parameters of $BaCo_{2-x}Ni_xFe_{16}O_{27}$ samples prepared by a simple heat treatment method and calcined at 650 °C for 3 hours

Ni concent (x)	*Ms* [emu/g]	*Mr* [emu/g]	*Hc* [KOe]	*R=(Mr/Ms)*
0.4	22.67	8.42	1.20	0.37
0.8	37.77	18.00	1.00	0.47
1.2	20.29	7.75	0.99	0.38
1.6	27.04	12.25	0.85	0.45
2.0	22.62	6.01	0.21	0.27

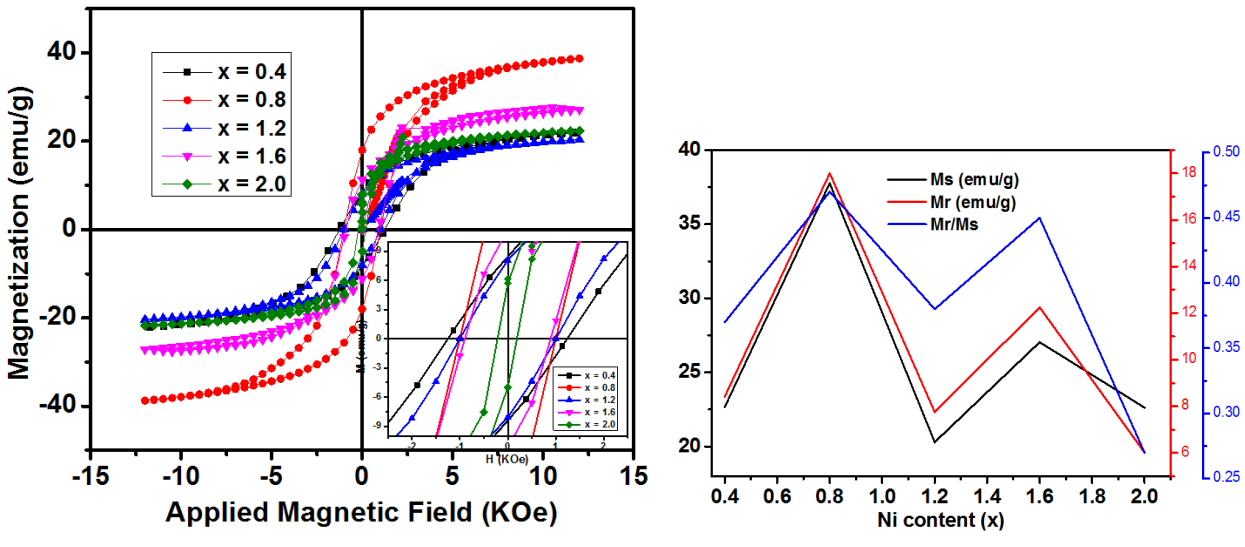

(a) (b)

FIG. 2. (a) Field Dependent magnetic properties and (b) variation of Mr, Ms and Mr/Ms for of $BaCo_{2-x}Ni_xFe_{16}O_{27}$ ($x = 0.4, 0.8, 1.2, 1.6, 2.0$) hexaferrite samples, prepared using a simple heat treatment method and calcinated at 650 °C for 3 hours

to be low in prepared samples compared to other doped barium hexagonal ferrites [8, 16]. The lower values of saturation magnetization and coercivity may be due to many reasons; surface effects, particle size and morphology, crystallographic defects, site occupancy of substituted ions in hexagonal lattice, phase impurity [17].

The ratio R of the remanence to the saturation magnetization (Mr/Ms) indicates the domain structure of prepared samples. A Mr/Ms value of ~ 0.5 is indicative of single domain and the lower value is associated with a multidomain structure [18]. In the present case, samples $x = 0.4, 1.2, 2.0$ show $R < 0.5$, indicating the formation of a multidomain structure, while samples $x = 0.8$ and 1.6 exhibited $R \cong 0.5$ confirming the formation of crystalline single domain structure. The hysteresis loops of $x = 0.4$ to 1.8 samples possessed hard magnetic character while the $x = 2.0$ sample showed soft ferrite behavior.

4. Conclusions

Nickel-doped barium cobalt hexagonal ferrites-$BaCo_{2-x}Ni_xFe_{16}O_{27}$ (x = 0.4, 0.8, 1.2, 1.6 and 2.0) were synthesized using a simple heat treatment method. X-ray diffraction analysis confirmed the formation of mixed phases of M, W (both hexaganal) and S (spinel). There was little change in the values of the lattice constants- a and c with addition of nickel in prepared barium cobalt hexaferrite powder. $BaNi_2Fe_{16}O_{27}$ hexaferrite exhibits soft ferrite nature, while other nickel substitutes barium cobalt ferrites show hard ferrite behavior.

Acknowledgements

One of the authors (Chetna C. Chauhan) acknowledge the funding support from Gujarat Council of Science and Technology (GUJCOST/MRP/2014-15/432, dated 30/06/2014) Gandhinagar. The work is also supported by DRS-SAP-Phase-I program of UGC (F.530/10/DRS/2010 (SAP-I)), New Delhi, India.

References

[1] Pullar R.C. Hexagonal Ferrites: A review of the synthesis, properties and applications of hexaferrite ceramics. *Prog. Mater Sci.*, 2012, **57**, P. 1191–1334.
[2] Vincent H., Sugg B., et al. Crystal growth, X-ray and magnetic studies of planar anisotropy M hexaferrites $BaFe_{12-2x}Ir_xMe_xO_{19}$ (Me=Zn, Co). *J. Mag. Mag. Mat.*, 1991, **101** (1-3), P. 170–172.
[3] Mendoza-Suarez G., Rivas-Vazquez L.P., et al. Magnetic properties and microstructure of $BaFe_{116-2x}Ti_xM_xO_{19}$ (M=Co, Zn, Sn) compounds. *Physica B: Cond. Mat*., 2003, **339** (2), P. 110–118.
[4] El-Saadawy M. Thermal conductivity and thermoelectric power of the $Zn_{2-x}Co_xBaFe_{16}O_{27}$ hexagonal ferrites system. *Mater. Lett.*, 1999, **39**, P. 149–152.
[5] Campbell P. *Permanent Magnet Materials and Their Application*. Cambridge University Press, Cambridge, 1994.
[6] Ong C.K., Fang H.C., Yang Z., Li Y. Magnetic relaxation in Zn-Sn-doped barium ferrite nanoparticles for recording. *J. Mag. Mag. Mat.*, 2000, **213**, P. 413–417.
[7] Wang L.X., Song J., et al. The microwave magnetic performance of Sm^{3+} doped $BaCo_2Fe_{16}O_{27}$. *J. Alloys Compd.*, 2009, **481**, P. 863–866.
[8] Huang K., Liu X., et al. Structural and magnetic properties of Ca-substituted barium W-type hexagonal hexaferrites. *J. Mag. Mag. Mat.*, 2015, **379**, P. 16–21.
[9] Pawar R.A., Desai S.S., et al. Ce^{3+} incorporated structural and magnetic properties of M type barium hexaferrites. *J. Mag. Mag. Mat.*, 2015, **378**, P. 59–63.
[10] Iqbal M.J., Khan R.A. Enhancement of electrical and dielectric properties of Cr doped $BaZn_2$ W-type hexaferrite for potential applications in high frequency devices. *J. Alloys Compd.*, 2009, **478**, P. 847–852.
[11] Jotania R.B., Chauhan C.C., Menon S.K., Kulkarni B.D. Synthesis and magnetic properties of barium?calcium hexaferrite particles prepared by sol-gel and microemulsion techniques. *J. Mag. Mag. Mat.*, 2008, **320**, P. 1095–1101.
[12] Chauhan C.C., Jotania R.B. Microstructual, Thermal and Magnetic proeprties of cobalt doped barium calcium hexaferrite prepared by a sol gle route. *Int. J. Adv. Eng. Tech (IJAET)*, 2012, **3** (2), P. 135–139.
[13] Smith J., Wijn H.P.J. *Ferrites.* Philips, Technical Library, Eindhoven, 1959.
[14] Lotgering F.K., Vromans P.H.G. Chemical instability of metal deficient hexagonal ferrite with W structure. *J. Am. Ceram. Soc.*, 1977, **40**, P. 416–418.
[15] Mandal K., Mandal S.P., Agudo P., Pal M. A study of nanocrystalline (Mn?Zn) ferrite in SiO_2 matrix. *Appl. Surf. Sci.*, 2002, **182**, P. 386–389.
[16] Castro S., Gayoso M., et al. Structural and Magnetic properties of barium hexaferrite nanostructured materials prepared by the combustion method. *J. Magn. Magn. Mater*, 1996, **152**, P. 61–69.
[17] Battle X., Obradors X., et al. Surface spin canting in $BaFe_{12}O_{19}$ fine particles. *J. Magn. Magn. Mater.*, 1993, **124**, P. 228.
[18] Jiles J.C. Recent advances and future direction in magnetic materials. *Acta Materiala*, 2003, **51** (19), P. 5907–5939.

NANOSYSTEMS: PHYSICS, CHEMISTRY, MATHEMATICS, 2016, 7 (4), P. 599–603

Dielectric studies of nanocrystalline calcium tungstate

N. Aloysius[1*], M. S. Rintu[2], E. M. Muhammed[2], T. Varghese[1,3]

[1]Department of Physics, Newman College Thodupuzha-685 585, Kerala, India
(Affiliated to M. G. University, Kottayam)
[2]Department of Physics, Maharajas College, Ernakulam-682 011, Kerala, India
[3]Nanoscience Research Centre (NSRC), Department of Physics, Nirmala College,
Muvattupuzha – 686 661, Kerala, India
*nanoncm@gmail.com

PACS 78.67.Bf, 81.16.Be, 73.63.-b **DOI 10.17586/2220-8054-2016-7-4-599-603**

Nanocrystalline samples of $CaWO_4$ were prepared at room temperature by simple chemical precipitation. The samples were characterized by X-ray diffraction and scanning electron microscopy. Energy dispersive X-ray analysis confirmed the elements present in the sample. The frequency and temperature dependence of the dielectric constant and ac electrical conductivity of the nanomaterial were investigated. Very low dielectric loss in nanocrystalline $CaWO_4$ powder was observed at high frequencies. The values of ac electrical conductivity calculated from the permittivity studies were found to increase as frequency increased, conforming to small polaron hopping.

Keywords: Chemical precipitation, dielectric constant, ac electrical conductivity, polaron hopping.

Received: 29 January 2016

Revised: 21 May 2016

1. Introduction

Nanocrystalline $CaWO_4$ has attracted particular interest because of its practical applications, such as laser host materials in quantum electronics and scintillators in medical devices [1–6]. It has been reported that $CaWO_4$ of scheelite-like structures is an excellent blue-emitting phosphor by their radiation of ultraviolet (UV) light [7]. Also, $CaWO_4$ has shown considerable promise as a fiber-matrix interlayer in oxide ceramic composites [8]. The lower dielectric constant and low loss make nanostructured $CaWO_4$ a promising candidate for applications as a low temperature co-fired ceramic (LTCC), substrate, and electronic packaging material [9]. Pullar et al. explained the microwave dielectric properties of AWO_4 (A = Mg, Zn, Ni and Co) compounds with extrinsic parameter, such as density [10]. Sreedevi et al. reported that Ag_2WO_4 nanoparticles can be a promising material for the high dielectric constant gate in Si-based complementary metal oxide semiconducting devices [11]. The influence of processing methods on the characteristics of $CdWO_4$ powders and the related microwave dielectric properties were reported by Bao-Chun Guo et al. [12]. The study of dielectric properties of samples as a function of temperature and frequency may help in identifying their potential applications [13]. The characterization of dielectric behavior is very important not only to the theory of the polarization mechanism but also from an application point of view, where knowledge of the temperature and the frequency dependence of dielectric constant are very important. The relative dielectric constant of the material determines its ability to store electrostatic energy.

Dielectric studies of $CaWO_4$ nanoparticles are incomplete and need further investigation. In the present work, we synthesized $CaWO_4$ nanoparticles by chemical precipitation followed by calcination. The samples were then characterized by X-ray diffraction (XRD) and scanning electron microscopy (SEM). The frequency and temperature dependence of dielectric properties of sintered pellets made out of the products were then investigated.

2. Materials and methods

Calcium nitrate $Ca(NO_3)_2{\cdot}4H_2O$ (99.8 %, Sigma Aldrich) and sodium tungstate $Na_2WO_4{\cdot}2H_2O$) (99.9 %, Alfa Aesar) analytical grade reagents were used for the preparation of $CaWO_4$ nanocrystals. The samples were prepared by reacting aqueous solutions of calcium nitrate and sodium tungstate (0.1 M each) at room temperature. The precipitate formed was centrifuged, filtered, washed with distilled water a number of times, and dried in an oven to get fine powders of calcium tungstate. S_1 and S_2 are samples of nanocrystalline $CaWO_4$ were calcined at 650 and 750 °C, respectively. XRD studies of these samples were conducted using Bruker D8 Advance X-ray diffractometer ($\lambda = 1.5406$ Å) with CuKα radiation in 2θ range from 20 to 80 °. The morphological analysis of $CaWO_4$ nanoparticles was carried out with a scanning electron microscope JEOL MODEL JSM-6390LV, operating at 20 kV measurements.

The calcined powder sample was cold pressed in the form of cylindrical pellets of diameter 13 mm and thickness $d \sim 1.5$ mm by applying a pressure of ~ 10 GPa using a hand operated hydraulic press. The pellets were then sintered at 500 °C. The density of the pellet was determined to be 4.88 g/cm^3. The circular faces of the pellets were made electrically conducting by coating with silver paste. Dielectric measurements as a function of frequency in the range of 100 Hz – 1 MHz were measured at various selected temperatures from 303 – 423 K using an LCR meter (Wayne Kerr H-6500 model) in conjunction with a portable furnace and temperature controller (± 1 K).

3. Results and discussion

The powder XRD spectra of $CaWO_4$ nanoparticle samples are shown in Fig. 1. Both the samples showed characteristic peaks of scheelite structure with tetragonal unit cell. The 'd' values taken from the JCPDS file No. 77-2235 for $CaWO_4$ are in close agreement with the observed 'd' values.

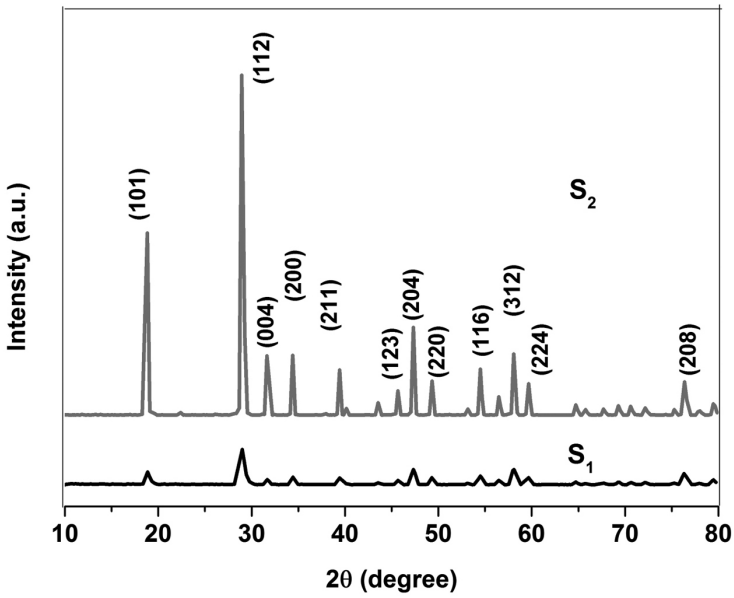

FIG. 1. XRD spectra of $CaWO_4$ samples

In general, the nanocrystallite size can be estimated from the Scherrer's formula: $D_{hkl} = K\lambda/(\beta \cos\theta)$, where λ is the x-ray wavelength (0.15405 nm), β the full-width at half maximum, θ the diffraction angle, K is a constant (0.89) and D_{hkl} the size along the (hkl) direction. From the analysis, the average crystallite size obtained was 39 nm for S_1 and 44 nm for S_2.

The SEM image of $CaWO_4$ nanoparticles calcined at 650 °C is shown in Fig. 2(a). They are clusters shaped like dumb-bells. The elemental analysis of the sample S_1 was done by energy dispersive X-ray (EDX) spectroscopy. Fig. 2(b) shows typical EDX spectrum of synthesized $CaWO_4$ nanoparticles. The peaks of the spectrum confirmed that the product contains Ca, W and O. The intense signal near at 1.774 keV indicates that W is the major element.

The dielectric constant and ac conductivity (σ_{ac}) were calculated by using equations $\varepsilon' = Cd/\varepsilon_0 A$ and $\sigma_{ac} = \varepsilon' \varepsilon_0 \omega \tan\delta$, respectively, where A is the face area, C the measured capacitance of the pellet, ε_0 the permittivity of vacuum, ω the angular frequency and tan δ the loss tangent. Fig. 3(a) shows the variation of dielectric constant with frequency for temperatures from 303 to 423 K of sample S_1. It is seen that the dielectric constant for all temperatures are high at low frequencies which decreased rapidly as frequency increased, attaining a constant value at higher frequencies. For 303 K, the value of ε was 24.74 at 100 Hz, which decreased to 7.11 at 1 MHz. At 393 K, the values were 30.08 (100 Hz) and 7.15 (1.0 MHz). The corresponding values for 423 K were 39.54 at 100 Hz and 7.20 at 1.0 MHz. Fig. 3(b) shows a similar variation for samples S_1 and S_2, at 393 K. At lower frequencies the dielectric constant is found to be higher for the sample having smaller grain size (S_1), but approaches a constant value beyond 0.1 MHz. When temperature is increased, more and more dipoles are oriented, resulting in an increase in the dielectric constant for a given value of frequency [14]. At very high frequencies (MHz), the charge carriers would have started to move before the field reversal occurs and ε' falls to a small value at higher frequencies.

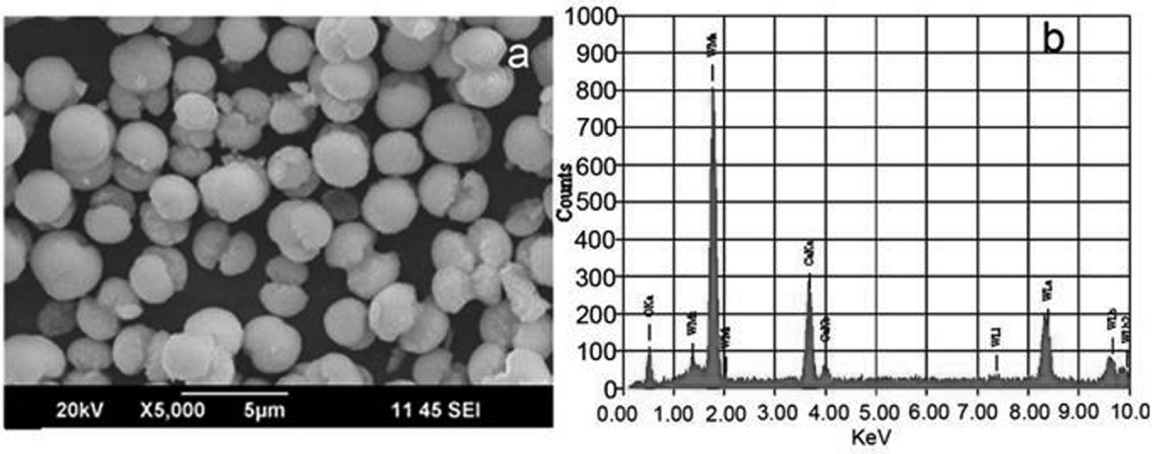

FIG. 2. (a) SEM image of $CaWO_4$ (S_1) and (b) EDX spectrum of $CaWO_4$

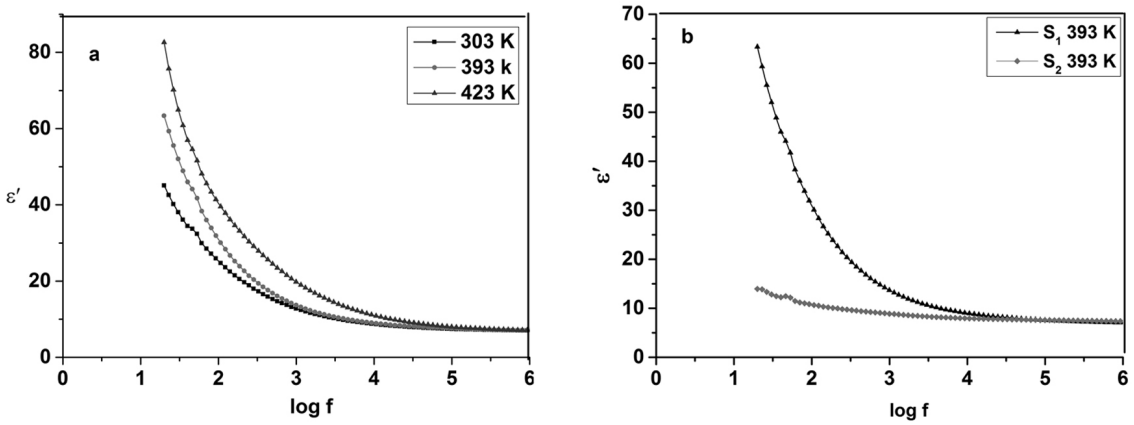

FIG. 3. The variation of dielectric constant with frequency of (a) sample S_1 at temperatures 303, 393 and 423 K and (b) samples S_1 and S_2 at 393 K

Space charge polarization and reversal of the polarization direction contributes much to the ε' [15]. With the increase in volume of the particle, the volume of the interfaces decreases. When volume increases, the contribution to ε' by electronic relaxation polarization inside the particles increases.

The frequency dependence of dielectric loss of sample S_1 is shown in Fig. 4(a). The loss factor represented by $\tan\delta$ has a value of 3.26 at 100 Hz which decreases slowly to zero at higher frequencies. At 393 K, the corresponding variation is not very different. For 423 K, $\tan\delta$ has a value of 9.53 at 100 Hz which gradually decreases almost to 0 at frequencies beyond 0.10 MHz. At 393 K the corresponding variation is not very different. The decrease in $\tan\delta$ takes place when the jumping rate of charge carriers lags behind the alternating electric field beyond a certain critical frequency.The inhomogeneities present in the interface layers in $CaWO_4$ nanocrystals produce an absorption current resulting in dielectric loss. This absorption current decreases with increase in frequency of the applied field. The hopping probability per unit time increases with increase in temperature. Correspondingly, the loss tangent also increases with increase of temperature [16]. The variation of $\tan\delta$ with frequency at 393 K for samples S_1 and S_2 with different grain sizes is shown in Fig. 4(b). At 100 Hz, the value is 3.4 for S_1 which decreases to 0.9 for S_2. This variation of $\tan\delta$ for different grain sizes is due to size effect [17]. The low value of $\tan\delta$ indicates its potential for microwave applications.

The loss in $CaWO_4$ can be explained using the electronic hopping model, which considers the frequency dependence of the localized charge carriers hopping in a random array. This model is applicable for materials in which the polarization responds rapidly to the appearance of an electron on any one site so that the transition may be said to occur effectively into the final state [17]. In the high frequency region $\tan\delta$ becomes almost zero because the electron exchange interaction (hopping) cannot follow the alternatives of the applied ac electric field beyond a critical frequency.

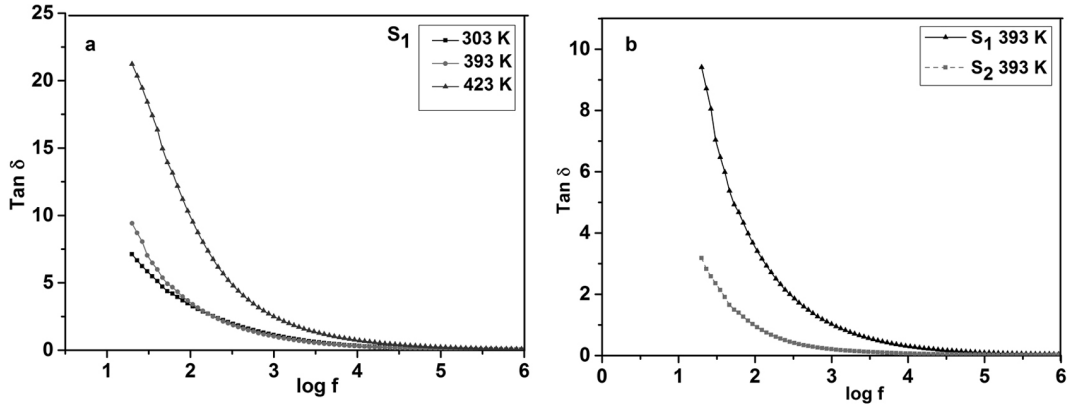

FIG. 4. The variation of loss tangent with frequency of (a) sample S_1 at temperatures 303, 393 and 423 K and (b) samples S_1 and S_2 at 393 K

Figure 5(a) shows the variation of ac conductivity (σ_{ac}) of sample S1with frequency. Initially, it has a small value which increased at higher frequencies. The nature of variation is similar for other temperatures, but the values are shifted upwards as the temperature is raised. For 303 K, σ_{ac} has a value of 5.001×10^{-7} S/m at 100 Hz which increased slowly at higher frequencies to 1.4×10^{-3} S/m at 0.10 MHz. At 393 K, the corresponding variation was not very different. For 423 K, the values were 2.236×10^{-6} S/m at 100 Hz and 2.781×10^{-5} S/m at 1.0 MHz. The variation of σ_{ac} with frequency at 393K for different grain sizes is shown in Fig. 5(b). At 100 Hz, σ_{ac} is found to be 5.002×10^{-7} S/m for S_1 which increased to 6.88×10^{-5} S/m at 1.0 MHz. For S_2, the corresponding values were 5.823×10^{-8} S/m and 7.671×10^{-6} S/m. It is clear from the figure that the conductivity increased as frequency increased conforming to small polaron hopping [18]. Also, there is a possibility of conduction due to impurities at low temperature. It is found that at given temperature and frequency, σ_{ac} is higher for particle having smaller size. According to Elliot's barrier hopping model, ac conductivity increases with hopping distance [19]. Therefore, it may be concluded that in $CaWO_4$ hopping distance increased with reduction in particle size.

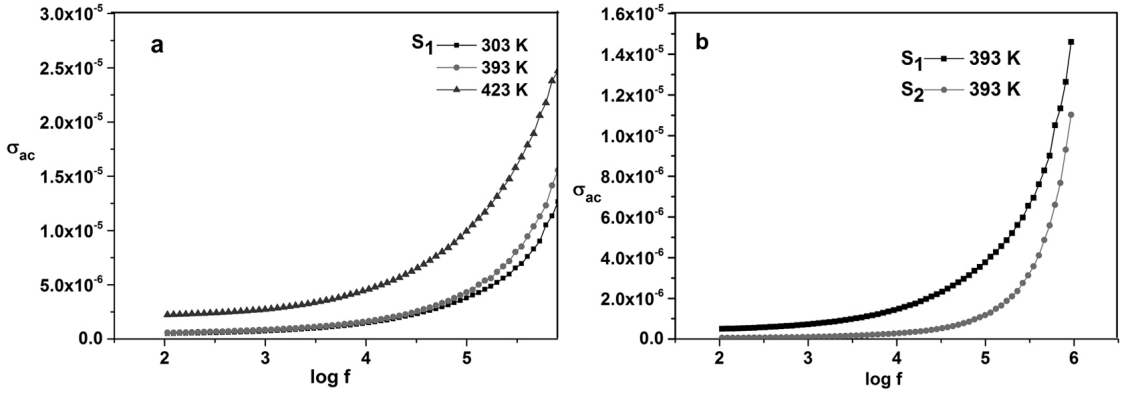

FIG. 5. The variation of ac electrical conductivity with frequency of (a) sample S_1 at temperatures 303, 393 and 423 K; (b) samples S_1 and S_2 at 393 K

4. Conclusion

The $CaWO_4$ nanoparticles were prepared at room temperature by simple chemical precipitation reaction without any catalyst, surfactant, or templates. The dielectric properties of $CaWO_4$ were determined as a function of frequency from 100 Hz to 1.0 MHz for temperatures ranging from 303 to 423 K. At lower frequencies, ε' and $\tan\delta$ have higher values while at higher frequencies the values reached steady lower values. Similar variation was observed when the temperature was raised but the values of ε' and $\tan\delta$ were elevated. The ac conductivity increased as frequency was increased conforming to small polaron hopping. The values of ε', $\tan\delta$ and σ_{ac} showed considerable increase as the particle size was reduced. The very low value of loss tangent obtained for

$CaWO_4$ nanocrystals suggests that it is potentially useful for microwave applications. It was found that the applied frequency, temperature and particles size affect the dielectric properties of the $CaWO_4$ nanocrystals.

Acknowledgements

The authors are indebted to NSRC, Nirmala College, Muvattupuzha and Newman College, Thodupuzha for the support to undertake this study. The financial support from the University Grants Commission, New Delhi, India (FIP/12th Plan/KLMG020 TF03) is greatly acknowledged.

References

[1] Kobayashi M., Ishii M., Usuki Y., Yahagi H. Scintillation characteristics of PbWO4 single crystals at room temperature. *Nuclear Instruments and Methods in Physics Research A*, 1993, **333** (2-3), P. 429–433.
[2] Katelnikovas A., Grigorjeva L., et al. Sol-Gel Preparation of Nanocrystalline $CaWO_4$. *Lithuanian J. of Physics*, 2007, **47** (1), P. 63–68.
[3] Phuruangrat A., Thongtem T., Thongtem S. Synthesis, characterization and photoluminescence of nanocrystalline calcium tungstate. *J. Exp. Nanosci.*, 2009, **5**, P. 263–267.
[4] Lou Z., Cocivera M. Cathodoluminescence of $CaWO_4$ and SrWO4 thin films prepared by spray pyrolysis. *Mater. Res. Bull*., 2002, **37**, P. 1573–1582.
[5] Nagirnyi V., Feldbach E., et al. Excitonic and recombination processes in $CaWO_4$ and $CdWO_4$ scintillators under synchrotron irradiation. *Radiat. Meas*., 1998, **29**, P. 247–250.
[6] Oishi S., Hirao M. Growth of $CaWO_4$ whiskers from KCl flux. *J.Mater.Sci., Lett*., 1989, **8** (12), P. 1397–1398.
[7] Liping L., Yiguo S., Guangshe L. Size-induced symmetric enhancement and its relevance to scheelite $CaWO_4$ nanocrystals. *J. Appl. Phys. Lett*., 2007, **90**, P. 054105–054107.
[8] Mogilevsky P., Parthasarathy T.A., Petry M.D. Anisotropy in room temperature microhardness and fracture of $CaWO_4$ scheelite. *Acta Materialia*, 2004, **52**, P. 5529–5537.
[9] Vidya S., Sam Solomon., Thomas J.K. Synthesis of Nanocrystalline $CaWO_4$ as Low-Temperature Co-Fired Ceramic Material: Processing, Structural and Physical Properties. *Journal of Electronic Materials*, 2012, **42**, P. 129–137.
[10] Pullar R.C., Farrah S., Alford N.M. $MgWO_4$, $ZnWO_4$, $NiWO_4$ and $CoWO_4$ microwave dielectric ceramics. *Journal of the European Ceramic Society*, 2007, **27**, P. 1059–1063.
[11] Sreedevi A., Priyanka K.P., et al. Nanophase α-Silver Tungstate for Potential Applications in Light Emitting Diodes and Gate Dielectrics. *Advanced Science, Engineering and Medicine*, 2015, **7**, P. 498–505.
[12] Bao-Chun Guo, Peng Liu, et al. Effect of Preparation Methods on Microstructures and Microwave Dielectric Properties of $CdWO_4$ ceramics. *Integrated Ferroelectrics*, 2015, **167**, P. 107–114.
[13] Chi Kao K. *Dielectric phenomena in Solids*. Elsevier, New York, 2004.
[14] Kar T., Choudhary R.N., Sharma S., Singh K.S. Structural and electrical properties of $Ba_2Na_3RNb_{10}O_{30}$ Ceramics. *Indian J. Phys. A*, 1999, **73** (4), P. 453-459.
[15] Ravinder D., Vijayakumar K. Dielectric behaviour of erbium substituted Mn–Zn ferrites. *Bull. Mater. Sci.*, 2001, **24** (5), P. 505–509.
[16] Potty S.N., Khader M.A. Dielectric Properties of nanophase Ag_2HgI_4 and Ag_2HgI_4–Al_2O_3 nanocomposites. *Bull. Mater. Sci*., 2000, **23** (5), P. 361–367.
[17] Murthy V., Sobhanadri J. Dielectric properties of some nickel-zinc ferrites at radio frequency. *Phys Status Solidi (a)*, 1976, **36** (2), K133–K135.
[18] Priyanka K.P., Sunny J., et al. Dielectric properties and a. c. conductivity of nanocrystalline titania. *J. Basic Appl. Phys.*, 2013, **2**, P. 105–108.
[19] Elliot S.R. Temperature dependence of a.c. conductivity of chalcogenide glasses. *Phil. Mag. Part B*, 1978, **37** (5), P. 553.

NANOSYSTEMS: PHYSICS, CHEMISTRY, MATHEMATICS, 2016, 7 (4), P. 604–608

Dynamic study of bismuth telluride quantum dot assisted titanium oxide for efficient photoelectrochemical performance

Pallavi B. Patil, Vijay V. Kondalkar, Kishorkumar V. Khot, Chaitali S. Bagade, Rahul M. Mane, P. N. Bhosale*

Materials Research Laboratory, Department of Chemistry, Shivaji University, Kolhapur–416004, India

*p_n_bhosale@rediffmail.com

PACS 82.45 Mp **DOI 10.17586/2220-8054-2016-7-4-604-608**

The 3D TiO_2 microflowers, sensitized by Bi_2Te_3 nanoparticles, having novel architecture were generated employing a two-step synthetic strategy, including a hydrothermal process and a potentiostatic electrodeposition technique. The design and synthesis of quantum dots (QDs) for achieving high photoelectrochemical performance is an urgent need for high technology fields

Keywords: Bi_2Te_3 QDs assisted TiO_2, 1D nanorods, PEC.

Received: 30 January 2016

Revised: 6 May 2016

1. Introduction

Quantum dot-sensitized solar cells (QDSCs) have received much attention because they are promising candidates for low cost and large area photovoltaic applications. Semiconductor quantum dot-sensitized solar cells (QDSSCs) have the advantages of being low cost and a simple fabrication process. The most attractive property of a semiconductor quantum dot is its ability to promote the photoconversion efficiency above Shockley-Queisser limit. The low efficiency of QDSSCs is attributed to the relatively low photovoltage in the cell compared to DSSCs and to the recombination paths induced by the electronic properties of the interfaces formed at TiO_2-QD-electrolyte triple junction [1]. Secondly, it is difficult to incorporate QDs into a TiO_2 mesoporous matrix to obtain a well-covered QD monolayer on the inner surface of the TiO_2 electrode. Other possible reasons include QD-electrolyte interfaces [2], electron loss occurring through charge recombination at the TiO_2-electrolyte interface [3]. To achieve higher performance photovoltaic solar cells, morphologies and structures of anode materials are also widely investigated [4]. In general, mesoporous TiO_2 nanoparticles are the most frequently used photoanodes in DSSCs and QDSSCs, due to their high internal surface area for sufficient sensitizer anchoring [5]. Unfortunately, mesoporous TiO_2 nanoparticles have some disadvantages, such as charge collection rate due to surface states and grain boundaries existing in the pathway of nanoparticles, which can lead to many unexpected trapping and de-trapping, and thus, inferior light scattering [6]. In this study, we successfully synthesized vertically aligned TiO_2 nanorods sensitized by Bi_2Te_3 nanoparticles. The photoelectrochemical performance of TiO_2 is greatly improved by sensitization of TiO_2 by Bi_2Te_3 nanoparticles [7]. The sensitization of TiO_2 by Bi_2Te_3 nanoparticles leads to a separation of the charge carriers. The charge separation leads to a reduction in the overall recombination in the solar cells and the enhancement of photogenerated carrier collection.

2. Method

First, TiO_2 can be prepared by our previously-reported hydrothermal method [7]. In detail 0.04 M TTIP was added in the solution containing 3M HCl and ethylene glycol stirred for some time. The clear transparent solution then poured into a Teflon-lined stainless steel autoclave maintained at 160°C for 2 h. The electrodeposition of Bi_2Te_3 nanoparticles on TiO_2 thin films was accomplished in a three electrode cell configuration containing aqueous solutions of 7 mM Bi $(NO_3)_3$ and 10 mM Te in 1M HNO_3. The deposition was carried out at -0.8 V vs Ag/AgCl. In this, TiO_2 nanorods act as working electrode, platinum as counter electrode and Ag/AgCl as reference electrode. The deposition time was fixed at 30 min. and the depositions were carried out at room temperature. In order to control the size of Bi_2Te_3 nanoparticles and prevent large particle formation, PVA was used as structure directing agent.

3. Results and discussion

3.1. Optical absorption spectra of Bi_2T_3 loaded TiO_2

The light absorption properties of Bi_2Te_3-loaded TiO_2 thin was evaluated using the UV-visible spectrophotometer (Shimadzu UV-1800 Japan). Figure 1 shows the Tauc plot of Bi_2Te_3 loaded TiO_2 thin films. The band gap energy of composite can be expressed by the Tauc relation. It is well known that there are fundamental optical transitions, namely directly-allowed (n=1/2) and indirectly-allowed (n=2) transition. It is also noteworthy that the band gap energy of Bi_2Te_3 loaded TiO_2 heterostructures was found to be 2.1 eV, indicating the optical absorption of the hybrid nanostructure has been extended from the UV region to the visible region.

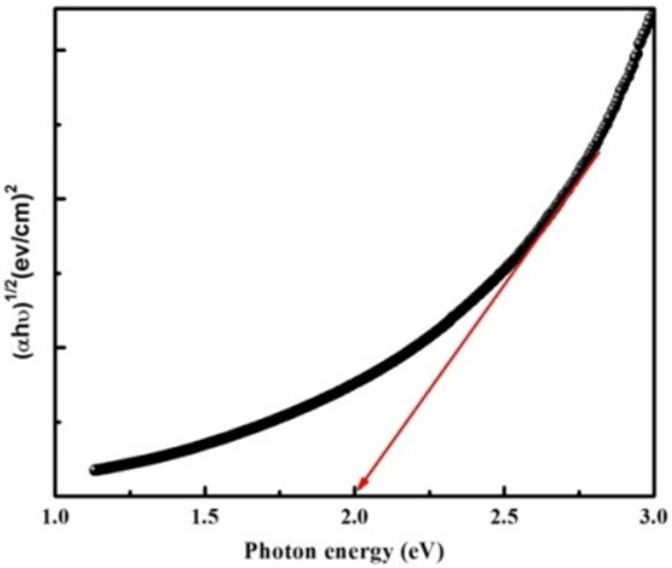

FIG. 1. Optical absorption spectra of Bi_2Te_3 loaded TiO_2 thin film

3.2. X-ray diffraction (XRD) pattern of Bi_2T_3 loaded TiO_2 thin film

The strong characteristic diffraction peak appeared at around 27.70° corresponds to (110) peak associated with rutile phase of TiO_2 (Space Group: P42/ mnm, JCPDS: 00-001-0562) (Rigaku, D/MAX Ultima III XRD spectrometer (Japan)). Furthermore, it should be noted that diffraction peak appearing at 27.67° corresponds to the (015) plane of Rhombohedral Bi_2Te_3 (JCPDS: 15-0863 space group R-3m) shown in Fig. 2. Due to overlap between (110) plane of TiO_2 and (015) plane of Bi_2Te_3, it is difficult to distinguish these two peaks in the XRD pattern. While the other peaks appeared at 2θ 27.70°, 36.22°, 41.35°, 54.58°, 56.97° and 65.54°, corresponding to the (110), (101), (111), (211), (220) and (221) crystal plane of tetragonal TiO_2 and 27.67°, 37.86°, 62.91° and 69.91° corresponding to the (015), (1010), (0213) and (0216) crystal planes of rhombohedral Bi_2Te_3.

It was found that the diffraction peak of the resulting deposit confirms the successful loading of Bi_2Te_3 nanoparticles on TiO_2. The crystallite size of the material was calculated by using Debye Scherrer formula, given in equation 1:

$$D = \frac{0.94\lambda}{\beta \cos\theta}, \tag{1}$$

where D is crystallite size, θ is Peak position of X-ray diffraction, β is Full Width at Half Maxima (FWHM) in radian, λ is Wavelength of X-ray used (0.154 nm). The XRD parameters are summarized in Table 1.

TABLE 1. XRD parameters.

Sample	Crystallite Size (D) (nm)	Microstrain(ε) 10^{-3} (lines m^{-2})	Dislocation density (δ)$\times 10^{-3}$ (lines^{-2} m^{-4})
Bi_2Te_3 loaded TiO_2	16.78	20156	3.5515

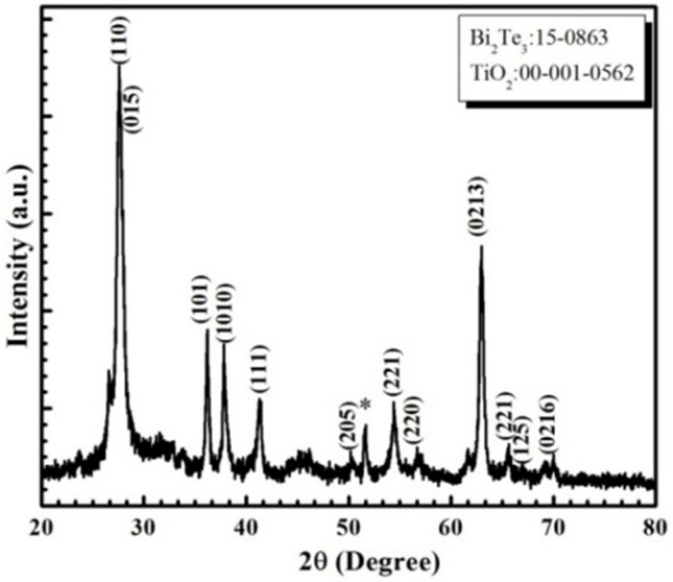

FIG. 2. X-ray diffraction pattern of Bi_2Te_3 loaded TiO_2 thin film

3.3. Field Emission Scanning Electron Microscopy (FESEM) of Bi_2T_3 loaded TiO_2 thin film

The morphological analysis of the synthesized material was carried out using field emission scanning electron microscopy (FESEM) (Hitachi, S-4700). Fig. 3 shows the low and high magnification field emission scanning electron microscopy (FESEM) images. The FESEM image shows that entire surface of FTO substrate is covered with well-aligned TiO_2 nanorods coated with Bi_2Te_3 nanoparticles. From the higher magnification of such nanorod arrays, the average diameter of the TiO_2 nanorod is 95–110 nm.

After Bi_2Te_3 quantum dot loading, the TiO_2 nanorods become rough, which means that the QDs have been successfully deposited on the surface of the TiO_2 nanorods after potentiostatic electrodeposition. The vertical alignment of the TiO_2 nanorods is beneficial for the improvement in the charge transfer of the solar cells. Such deep penetration of Bi_2Te_3 nanoparticles into the TiO_2 nanorods improves the charge separation and reduces recombination rate, which is beneficial for the photoelectrochemical performance of the solar cell.

3.4. Compositional analysis Bi_2Te_3 loaded TiO_2 thin film

Qualitative and quantitative analysis of the prepared Bi_2Te_3 loaded TiO_2 was carried out using energy dispersive X-ray spectroscopy (EDS).

The EDS spectrum confirms the presence of titanium, oxygen, bismuth and tellurium in prepared Bi_2Te_3 loaded TiO_2 thin film. From Figure 4, it is readily seen that the peaks at 4.5, 0.5, 2.4 and 3.7 keV confirm the presence of Ti, O, Bi and Te respectively in the Bi_2Te_3-loaded TiO_2 film.

3.5. Photoelectrochemical performance (PEC)

The typical J-V characteristic curve of Bi_2Te_3-loaded TiO_2 thin film was determined. The photoelectrochemical performance of the Bi_2Te_3-loaded TiO_2 thin film was carried out using a two electrode cell configuration (AUTOLAB PGSTAT100 FRA 32 potentiostat). In order to evaluate the photoelectrochemical performance, the Bi_2Te_3-loaded TiO_2 thin film acts as a photoanode, graphite as counter electrode with 0.5 polysulfide electrolyte. The cell configuration is as follows: Glass/ FTO/ Bi_2Te_3 loaded TiO_2/ 0.5M Polysulphide/G .

The photoelectrochemical performance i.e. fill factor (FF) and overall light to electric energy conversion efficiency (%) was calculated by equation (2) and (3):

$$FF = \frac{V_{max} J_{max}}{V_{oc} J_{sc}} \tag{2}$$

$$\eta_{\%} = \frac{V_{oc} J_{sc}}{P_{in} \times FF \times 100,} \tag{3}$$

where V_{oc} is open circuit voltage, J_{sc} is short circuit current, V_{max} is maximum voltage, J_{max} is maximum current, FF is the fill factor and P_{in} is the intensity of the incident light.

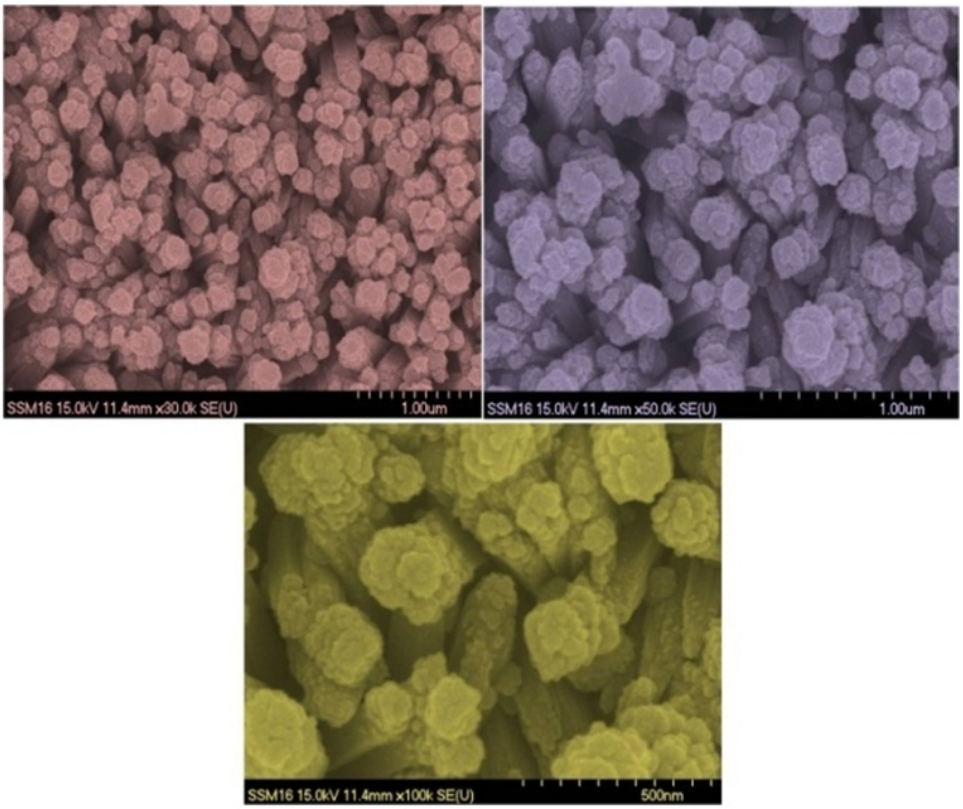

FIG. 3. Field emission scanning electron microscopy images of Bi_2Te_3 loaded TiO_2 thin film

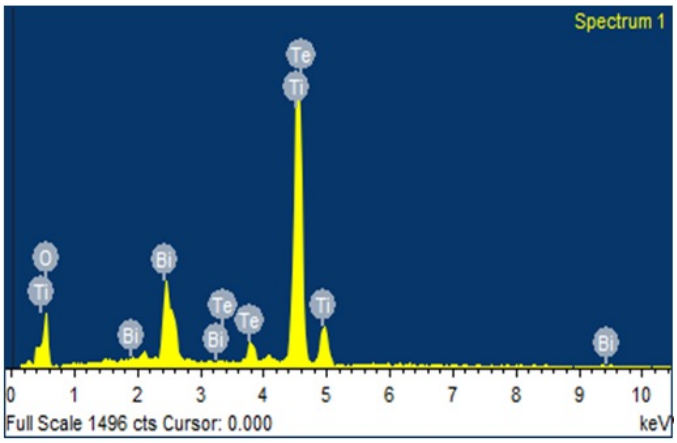

FIG. 4. EDS spectrum of Bi_2Te_3 loaded TiO_2 thin film

The detailed photovoltaic parameters are summarized in Table 2. The Bi_2Te_3-loaded TiO_2 thin film shows 0.026% photoconversion efficiency.

TABLE 2. Photoelectrochemical solar cell parameters of Bi_2Te_3 loaded TiO_2 thin film

Electrode	V_{oc} (mV)	J_{sc} (μA/cm^2)	R_s (Ω)	R_{sh} (Ω)	$\eta_{\%}$
Bi_2Te_3 loaded TiO_2	397.03	61	2660	4762	0.026

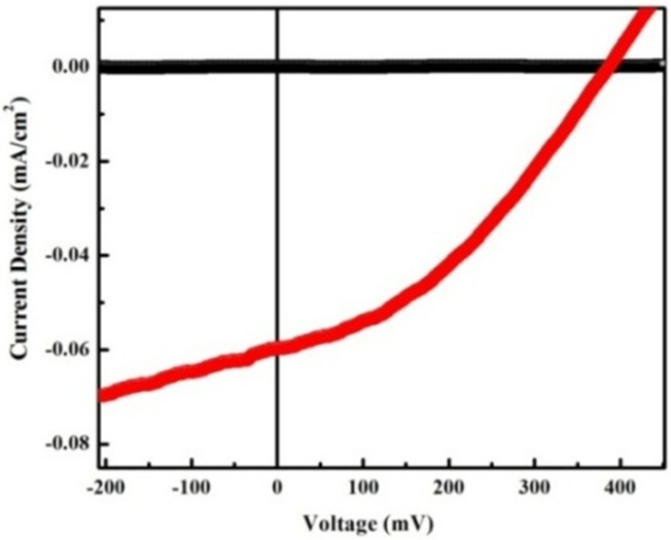

FIG. 5. J-V characteristic curve of Bi_2Te_3 loaded TiO_2 thin film

4. Conclusion

In summary, a Bi_2Te_3-loaded TiO_2 thin film was successfully prepared by a two-step synthetic strategy. 1D nanorods provided a unidirectional transport path for efficient charge, leading to high photoelectrochemical performance. Therefore, this novel combinatorial Bi_2Te_3 loaded TiO_2 thin film shows 0.026% photoconversion efficiency.

References

[1] Sero I., Gimenez S., Santiago F., Gomez R, Shen Q., Toyoda T., Bisquert J. Recombination in Quantum Dot Sensitized Solar Cells, *Acc. Chem. Res.*, 2009, **42**, P. 1848–1857.

[2] Diguna L., Murakami M., Sato A., Kumagai Y., Ishihara T., Kobayashi N., Shen Q., Toyoda T. Highly efficient CdS/CdSe-sensitized solar cells controlled by the structural properties of compact porous TiO_2 photoelectrodes. *J. Appl. Phys.*, 2008, **103**, P. 084304–084308.

[3] Lee Y., Chang C. Efficient polysulfide electrolyte for CdS quantum dot-sensitized solar cells. *J. Power Sources*, 2008, **185**, P. 584–588.

[4] Wu W., Xu Y., Su C., Kuang D. Ultra-long anatase TiO_2 nanowire arrays with multi-layered configuration on FTO glass for high-efficiency dye-sensitized solar cells. *Energy Environ. Sci.*, 2014, **7**, P. 644–649.

[5] Shiu J., Lan C., Chang Y., Wu H., Huang W., Diau Eric W. Size-Controlled Anatase Titania Single Crystals with Octahedron-like Morphology for Dye-Sensitized Solar Cells. *ACS Nano*, 2012, **6**, P. 10862–10873.

[6] Du J., Qi J., Wang D., Tang Z., Facile synthesis of Au@TiO_2 core-shell hollow spheres for dye-sensitized solar cells with remarkably improved efficiency. *Energy Environ. Sci.*, 2012, **5**, P. 6914–6918.

[7] Patil P., Mali S., Kondalkar V., Mane R., Patil P., Hong C., Bhosale P. Bismuth Telluride quantum dot assisted Titanium Oxide microflowers for efficient photoelectrochemical performance. *Mater. Lett.*, 2015, **159**, P. 177–181.

[8] Patil P., Mali S., Kondalkar V., Pawar N., Khot K., Hong C., Patil P., Bhosale P. Single step hydrothermal synthesis of hierarchical TiO_2 microflowers with radially assembled nanorods for enhanced photovoltaic performance. *RSC Adv.*, 2014, **4**, P. 47278–47286.

NANOSYSTEMS: PHYSICS, CHEMISTRY, MATHEMATICS, 2016, 7 (4), P. 609–612

Investigations on cycle time reduction, dynamic mechanical properties and creep for rotationally moldable nano composites of linear low density polyethylene and fumed silica

V. G. Chandran, S. D. Waigaonkar

BITS Pilani K.K. Birla Goa Campus, Department of Mechanical Engineering, NH-17B, Zuari Nagar, Goa, India, 403726

p2011407@goa.bits-pilani.ac.in, sdw@goa.bits-pilani.ac.in

PACS 81.05.Lg **DOI 10.17586/2220-8054-2016-7-4-609-612**

Composites of rotationally-moldable linear low density polyethylene (LLDPE) are becoming increasingly popular for rotational molding. In this study, the influence of fumed silica (FS) in pulling force requirement for demolding of rotationally moldable LLDPE is investigated. The dynamic mechanical analysis and creep studies were also performed to ascertain the reinforcement effects of FS in LLDPE matrix.

Keywords: LLDPE, FS, rotational molding.

Received: 31 January 2016

Revised: 9 June 2016

1. Introduction

The use of nanoparticles in rotational molding to enhance the melt characteristics and mechanical properties are increasing due to the limited choices of currently-available polymeric materials [1, 2]. Linear low density polyethylene (LLDPE) is the most commonly-used polymer for rotational molding. Normally, micro scale additives like anti oxidants, fillers, UV stabilisers, etc., are blended with LLDPE and pulverized to fine powder before molding to obtain the desired products. These additives are generally not nano-scale particles, and hence, do not provide reinforcement to polymer chains. Even though these additives provide desired properties, like UV resistance, reduced product cost, thermal stability, etc, they may adversely affect the mechanical properties [3]. The improvements in mechanical properties, such as tensile strength, impact toughness, creep, stress relaxation, etc. were reported with addition of nano fillers like, organo clays [4], metal nanoparticles [5], titanium oxide [6], zinc oxide [7], calcium carbonate [8] and silica nanoparticles in a polymer matrix [9]. Along with the improvements in mechanical properties, cycle time reduction for the molding process is also highly desired.

From our previous studies, it was observed that the nano-composites of LLDPE-FS up to 4 wt% FS provided acceptable melt flow characteristics for rotational molding [10]. In this study, nanoparticles of silica up to 4 wt% in the form of fumed silica (FS) having primary particle size in the range of 5–50 nm was dry mixed with LLDPE using a high speed mixer and was melt blended and pulverized in a commercial melt extruder and pulverizer. These blends (LLDPE-4%FS) were rotationally molded in a bi-axial rotational molding machine for studying the dynamic mechanical properties and cycle time. A unique fixture was made to study the mold release force at various temperatures and rates of pulling. The effect on maximum pulling force on commonly used mold materials, aluminum (grade 2024) and mild steel (grade S275), were studied with various LLDPE-FS blends. The PIAT (Peak internal air temperature) during rotational molding was studied using a Templogger, which records and transmits temperature readings wirelessly. The dynamic mechanical properties and viscoelastic creep was studied using DMA Q800 from TA instruments.

2. Results and discussion

The influence of FS nano particles, on the dynamic mechanical properties (DMA) viz. storage modulus (E'), loss modulus (E") and tan delta are given in Fig. 1. With the addition of FS (4%), an increase of 20% in storage modulus is observed at room temperature (30°C), while the loss modulus recorded an increase of 15%. The increasing trend of storage modulus and loss modulus is observed at all temperatures. Two distinct peaks are observed in the loss modulus curve, representing the glass transition temperatures (T_g). The first peak at -127°C represents the 'γ' T_g, which corresponds to small scale movements in polymer chains usually associated with inter- and intramolecular motions. The second peak at 46°C represents 'α' T_g , which corresponds to the onset of melting of low molecular weight polymer chains. The peak at -17°C in the loss modulus is analogus to the 'β' T_g observed in low density polyethylene (LDPE). Generally, the β transition is not observed in LLDPE. However, due

to the presence of fumed silica, the amorphous nature is increased in LLDPE, leading to entanglement of polymer chains [11]. The relaxation in polymer chains due to bending and twisting with the presence of FS, analogous to long side branches of LDPE, may be responsible for the presence of this β glass transition. At 4% FS, the concentration the shifts for 'α', 'β' and 'γ' T_g were not significant as compared to natural LLDPE.

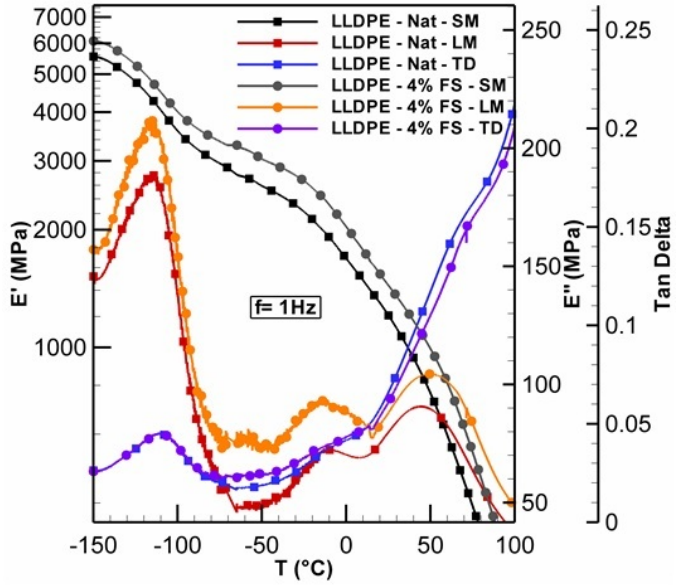

FIG. 1. Visco-elastic properties of LLDPE and LLDPE-4% FS blends

The proper dispersion of FS in LLDPE is required to achieve good mechanical properties. From our earlier studies, good dispersion was observed by both dry mixing and melt mixing until 2% FS concentration. Melt mixing is preferred for FS concentrations above 2% in LLDPE. The SEM micrograph of LLDPE −4% FS, as depicted in Fig. 2, shows good dispersion of FS for the samples tested. With the addition of FS, an increase in melt viscosity due to entanglement of polymer chains was observed, along with improvements in mechanical properties. The improvements in mechanical properties of LLDPE with the addition of FS can be attributed to the restricted movement of polymer chains due to partial entanglement and adhesion of FS to polymer chains. This provides higher resistance to shear in the polymer melt, thus increasing viscosity and polymer chain reinforcement, enhancing the product's mechanical properties. There also exists a structure, consisting of a hydrogen bonding network between the LLDPE chains and silica groups, which leads to improved mechanical properties [12].

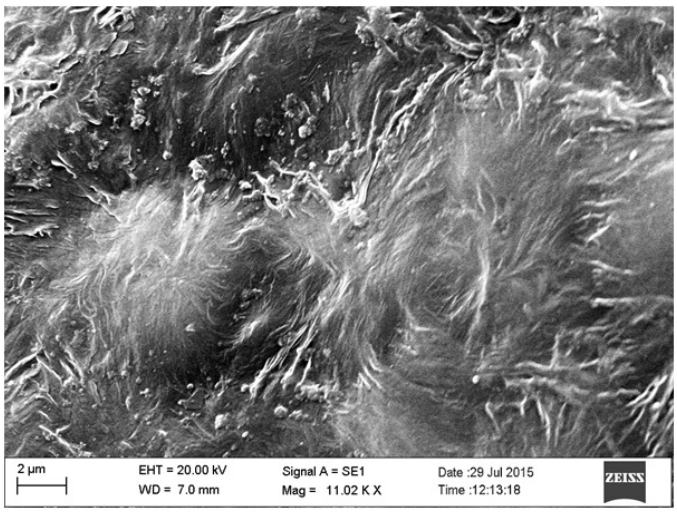

FIG. 2. Dispersion of FS in LLDPE - 4% FS blend

For stepped isothermal method (SIM), all the creep tests were done in single cantilever orientation at a constant stress of 0.5 MPa. The tests were done at increments of 10°C started from room temperature (30°C) to a maximum of 100°C providing a soak time of 5 minutes between every temperature step. The samples were loaded for 180 minutes at each temperature step (a dwell time of 10,000s is recommended by ASTM-D6992) for recording the creep strains. The SIM data were adjusted for thermal expansion and previous history of specimen by the change in temperature. The vertical shifting, rescaling and horizontal shifting were carried out to generate the creep master curves [13]. Creep master curves were generated for 40°C and 50°C and are shown in Fig. 3. As is readily seen from the graphs, the creep strains tend to decrease with the addition of FS. After an estimated loading of sample for one year (5.26×10^5 minutes) at 50°C nanocomposites with 4 wt% FS, exhibited 13% reduction in creep strains compared with natural LLDPE. Furthermore, the creep strains were reduced by as much as 13.5% for 4 wt% FS, which was predicted to be 5.26×10^7 minutes (around 100 years). The blends did not show significant variation in percentage of strain reduction with temperature. It was observed that, blends with 4 wt% FS showed 14% creep strain reduction at 40°C for an estimated loading of 1 year. The measurement of PIAT during rotational molding suggested a possible reduction of PIAT for LLDPE-FS blends. At 4% concentration, a PIAT of 175°C afforded products with good mechanical properties and minimum inner surface blow holes. This represents a reduction in cycle times and energy costs, as a PIAT of 210°C is preferred for natural LLDPE.

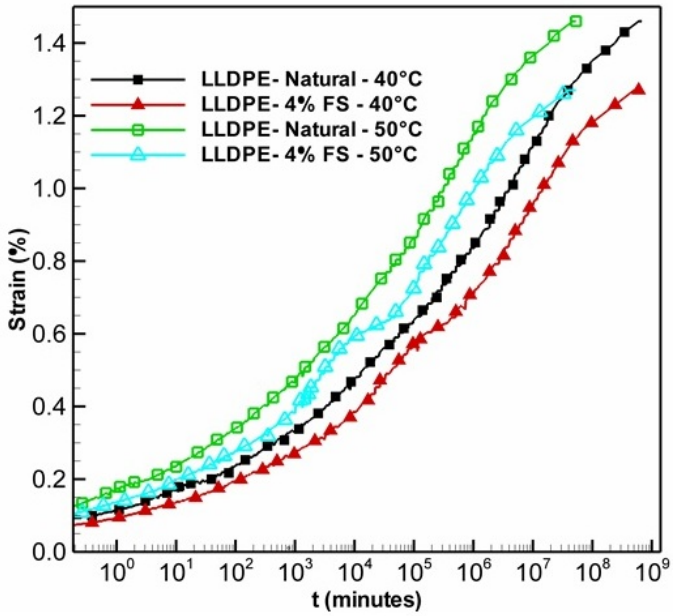

FIG. 3. Creep master curves of LLDPE and LLDPE-4% FS blends

Another important factor for cycle time reduction is mold release time. The adhesion of polymer to the mold and frictional resistance causes difficulty in the removal of products from a mold. Applying surface coatings and mold release agents reduces frictional resistance, however, applying mold release agents is time consuming and coating will deteriorate over time. Our investigations on pulling force required for removing the product from mold, as measured by a standard UTM using a unique fixture with mold cavity and internal heating is summarized in Fig. 4. It can be observed that the pulling force needed to remove the product from mold reduces with the addition of FS for both mild steel and aluminium molds. The minimum pulling force was observed at 80°C and thus it can be considered the ideal temperature to remove the product from the mold. The results show that the use of aluminium mold reduced the pulling force in comparison with that of steel molds at all temperatures. The reduction of pulling force ensures easy removal of the formed product, thereby reducing the cycle time.

3. Conclusion

In this study, rotationally moldable grade natural LLDPE and LLDPE-4%FS blends were used to study the dynamic mechanical characteristics of the parts produced by rotational molding. The improved viscoelastic behavior of LLDPE-4%FS blends ensures better rigidity and strength for rotomolded products. The reduced creep rates observed in LLDPE-4%FS blends ensure better product life. It was also observed that enhanced mold

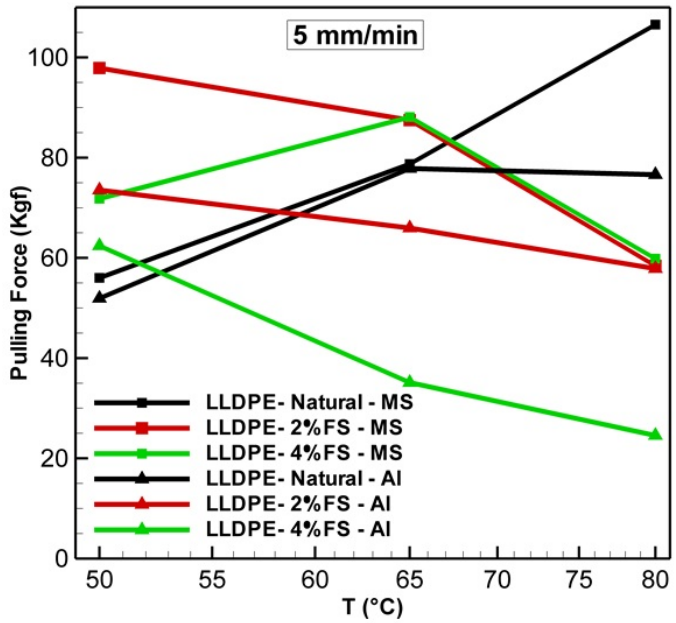

FIG. 4. Variation of pulling force

release and suggested reduction in PIAT considerably reduces the cycle time of the rotational molding process. In conclusion, LLDPE-4%FS blends make a better substitute for natural LLDPE in rotational molding applications.

References

[1] Therese L., Harkin-Jones E. An investigation into the relationship between the impact performance of rotationally molded polyethylene products and their dynamic mechanical properties. *Polymer Engineering & Science*, 2003, **43**, P. 905–918.
[2] Bellehumeur C.T., Tiang J.S. Simulation of Non-Isothermal Melt Densification of Polyethylene in Rotational Molding. *Polymer Engineering & Science*, 2002, **42**, P. 215–229.
[3] Jancar J., Douglas J.F., Starr F.W., Kumar S.K., Cassagnau P., et al. Current issues in research on structure-property relationships in polymer nano composites. *Polymer*, 2010, **51**, P. 3321–3343.
[4] Cassagnau P. Melt rheology of organoclay and fumed silica nanocomposites. *Polymer*, 2008, **49**, P. 2183–2196.
[5] Molefi J.A., Luyt A.S., Krupa I. Comparison of the influence of copper micro and nano particles on the mechanical properties of polyethylene/copper composites. *Journal of Material Science*, 2009, **45**, P. 82–88.
[6] Esthappan S.K., Kuttappan S.K., Joseph R. Thermal and mechanical properties of polypropylene/titanium dioxide nanocomposite fibers. *Materials & Design*, 2012, **37**, P. 537–542.
[7] Philippova O., Barabanova A., Molchanov V., Khokhlov A. Magnetic polymer beads: Recent trends and developments in synthetic design and applications. *European. Polymer. Journal*, 2011, **47**, P. 542–559.
[8] Karamipour S., Ebadi-Dehaghani H., Ashouri D., Mousavian S. Effect of nano-$CaCO_3$ on rheological and dynamic mechanical properties of polypropylene: Experiments and models. *Polymer. Testing*, 2011, **30**, P. 110–117.
[9] Cassagnau P., Mélis F. Non-linear viscoelastic behavior and modulus recovery in silica filled polymers. *Polymer*, 2003, **44**, P. 6607–6615.
[10] Chandran V.G., Waigaonkar S.D. Rheological and dynamic mechanical characteristics of rotationally moldable linear low-density polyethylene fumed silica nano composites. *Polymer. Composites*. In press, DOI: 10.1002/pc.23496.
[11] Nielsen L.E. Transitions in ethylene polymers. *Journal of Polymer Science*, 1960, **42**(140), P. 357–366.
[12] Dorigato A. Linear low density polyethylene/cycloolefin copolymer blends. *Express Polymer Letters*, 2010, **5**(1), P. 23–37.
[13] Achereiner F., Engelsing K., Bastian M., Heidemeyer P. Accelerated creep testing of polymers using the stepped isothermal method. *Polymer. Testing*, 2013, **32**, P. 447–454.

NANOSYSTEMS: PHYSICS, CHEMISTRY, MATHEMATICS, 2016, 7 (4), P. 613–617

Dielectric relaxation and charge transport process in $PrCrO_3$ nano-ceramic

Sujoy Saha[1], Alo Dutta[2*], P. K. Mukhopadhyay[2] and T. P. Sinha[1]

[1]Department of Physics, Bose Institute, 93/1, Acharya Prafulla Chandra Road, Kolkata-700009, India
[2]Department of Condensed Matter Physics and Material Sciences, S. N. Bose National Centre for Basic Sciences, Block-JD, Sector-III, Salt Lake, Kolkata-7000106, India

*alo_dutta@yahoo.com

PACS 61.05.cp, 77.22.Gm **DOI 10.17586/2220-8054-2016-7-4-613-617**

In this work we have investigated the frequency dependent dielectric properties of $PrCrO_3$ nano-ceramics using alternating current impedance spectroscopy. The material was synthesized by the sol–gel process. The Rietveld refinement of the X-ray diffraction data suggests single phase formation of the material with Pnma space group. The observed structure is substantiated by Raman spectrum of the sample. The ac conductivity follows the power law. The most probable relaxation frequencies at different temperatures were found to obey Arrhenius' law.

Keywords: Dielectric properties, sol-gel process, X-ray diffraction.

Received: 31 January 2016

1. Introduction

The rare-earth (R) transition-metal (M) oxides of perovskite structure with general formula RMO_3 have been the subject of investigation in recent years as they possess various interesting phenomena such as high temperature superconductivity, colossal magnetoresistance, and multiferroicity. Among these materials, rare–earth based orthochromites with general formula $RCrO_3$ have been investigated for their usefulness in several devices such as solid–oxide fuel cells and catalytic converters [1]. One of these orthochromites, $PrCrO_3$ (PCO), is an anti-ferromagnetic material with a Neel temperature of 237 K [2]. The Cr^{3+} spin structure is predominately G_x-type and a weak ferromagnetic moment lies along c-crystallographic axis at 4.2 K in PCO [2]. Prasad et al. [3] have investigated the relaxor ferroelectric like permittivity of bulk PCO ceramic having 30 nm grain size. Zhang et al. [4] have synthesized the cubic particle of orthorhombic PCO by hydrothermal process. Their results have showed that the molar ratio 1:1 of Pr and Cr can be obtained when the material is synthesized at 280 °C for 7 days using 8 M KOH solution.

The magnetic property of PCO is extensively studied, but to the best of our knowledge there is no report on the dielectric properties of PCO nano-ceramic till date. In the present work we have investigated the dielectric relaxation and ac conductivity of PCO nanoparticles synthesized by the sol-gel process.

2. Experimental

To prepare the PCO nano-ceramic, the metal nitrates with 1:1 molar ratio were dissolved in deionized water separately. Citric acid and ethylene glycol solution was added dropwise to the metal nitrates solution and stirred at 353 K for 6 h to form the gelled mass by auto combustion process. The dried gel was then calcined at 973 K in air for 4 h. The calcined sample was compressed into disc and sintered at 1023 K for 6 h. Scanning electron micrograph and energy dispersive X-ray spectrum were taken by a FEI QUANTA 200 scanning electron microscope. Transmission electron micrograph (TEM) was taken by TECNAI 200 kV transmission electron microscope. The X-ray diffraction (XRD) pattern of calcined PCO was taken by Rigaku Miniflex-II X-ray diffractometer. Raman spectrum was collected by Jobin-Yvon LABRAM-HR spectrometer using 488 nm line of an Ar-ion laser line. The frequency dependence capacitance and conductance of sintered pellet were measured by an LCR meter (Hioki) at frequencies ranging from 42 Hz to 1 MHz in temperature range from 303 – 673 K.

3. Results and disscussion

3.1. Structural Analysis

The Rietveld refinement of the room temperature XRD pattern of PCO with orthorhombic symmetry having Pnma (D_{16}^{2h}) space group using Full-prof code is shown in Fig. 1. The good agreement between the observed and calculated interplanar distances (d-values) of PCO indicates the single phase formation of the material in Pnma space group symmetry. The unit cell parameters, reliability factors, bond distances and bond angles obtained from

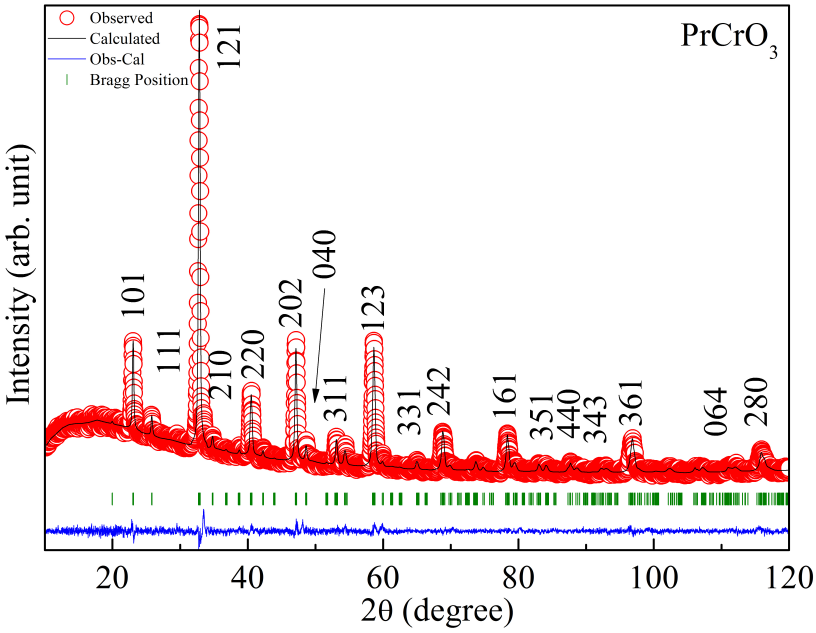

FIG. 1. Rietveld refinement of XRD profile of $PrCrO_3$ at room temperature

TABLE 1. Rietveld refinement data

Lattice parameters (Å)	Bond length(Å)	Bond angle
$a = 5.4721(5)$	$\langle \mathrm{Pr-OI} \rangle = 2.79$, $\langle \mathrm{Pr-OII} \rangle = 2.29$	$\mathrm{Cr-OI-Cr} = 154.3\ ^\circ$
$b = 7.7107(5)$	$\langle \mathrm{Cr-OI} \rangle$ 1.99, $\langle \mathrm{Cr-OII} \rangle = 1.96$	$\mathrm{Cr-OII-Cr} = 161.1\ ^\circ$
$c = 5.4445(5)$	$R_P = 3.76$, $R_{wp} = 4.93$, $R_{exp} = 5.23$, $\chi^2 = 0.891$	

Atom	x	y	z	Multiplicity	B_{iso} (Å^2)
Pr	0.5357(3)	0.25	0.4946(9)	4	0.429
Cr	0.25	0	0	4	0.087
OI	−0.0184(4)	0.25	0.5945(8)	4	0.705
OII	0.2891(7)	0.0235(5)	0.72077(7)	8	0.972

Rietveld refinement are given in Table 1. The mean size of coherent scattering regions, as calculated from the XRD data, was found to be 100 nm.

The high resolution TEM (HRTEM) image and selected area electron diffraction (SAED) pattern of PCO are shown in Fig. 2. The HRTEM image presented in Fig. 2(a) shows the well resolved lattice fringes of nanoparticles. The SAED pattern shows strong spots in regular positions indicating that particles are well crystalline in nature. The SEM image as shown in Fig. 2(c) indicates the compactness of the grains. The average grain size is found to be 92 nm. EDAX analysis shows that the atomic percentage of Pr, Cr and O in PCO is 19.09 %, 15.27 % and 65.64 % respectively.

We have studied the Raman spectrum of PCO to get a better understanding of the crystal structure and its consequence on the vibrational features of the material. The room temperature Raman spectrum of PCO as shown in Fig. 3 (Symbols are the experimental points) is typically matched with the Raman spectrum of perovskite having orthorhombic crystal structure. According to group theory, the orthorhombic Pnma structure has 24 Raman active modes ($7A_g$ + $5B_{1g}$ + $7B_{2g}$ + $5B_{3g}$) at the zone center. The antiphase tilt of the adjacent CrO_6 octahedra and the antiparallel displacements of Pr cations activate the Raman modes. The sum of 20 Lorentzian lines (violet solid lines in Fig. 3) is used to fit the experimental data. For the clarity of the figure, the frequency range is divided into two parts. Very weak intensity peaks are neglected during the Lorentzian fitting of the experimental data and thus a lesser number of peaks are obtained than the theoretical prediction.

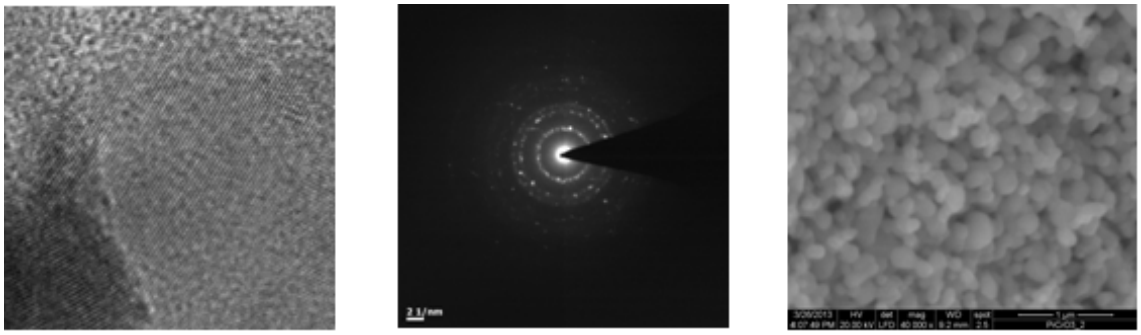

(a) (b) (c)

FIG. 2. HRTEM (a), SAED pattern (b) and SEM image (c) of $PrCrO_3$

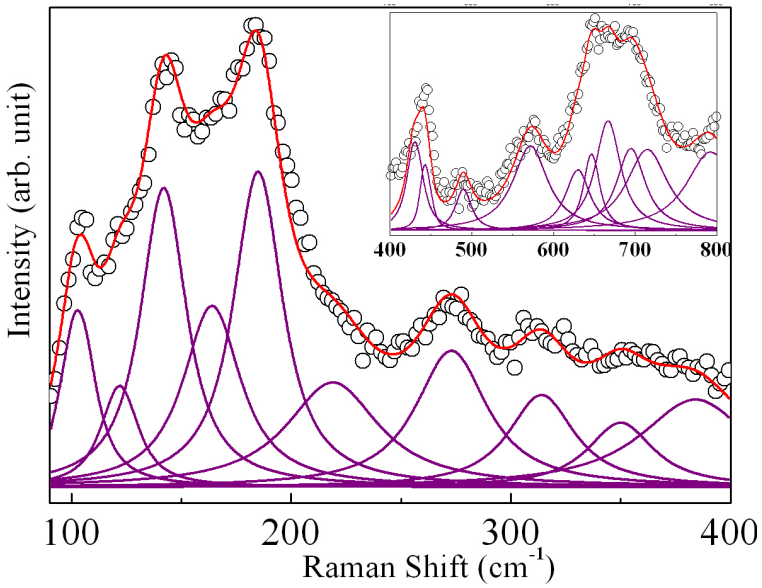

FIG. 3. Raman spectrum of $PrCrO_3$ at room temperature

3.2. Ac conductivity and dielectric relaxation

The angular frequency ($\omega = 2\pi\nu$) dependent log-log plots of ac conductivity (σ_{ac}) for PCO at different temperature are shown in Fig. 4. At each temperature, the conductivity decreases with decreasing frequency and becomes independent of frequency in the low frequency region. The extrapolation of this region towards $\omega = 0$ gives dc conductivity (σ_{dc}) which is attributed to the long range translational motion of the charge carriers. In this low frequency region, the electric field cannot perturb the hopping conduction mechanism of charged particles and hence, the conductance is approximately equal to the dc value. As the temperature is increased, the dc part of the conductivity spectra shifts to higher frequency side. The large value of dc conductivity at the higher temperature range with respect to the value in the lower temperature range indicates the generation of large number of thermally activated charge carriers in the experimental temperature range. The conductivity begins to increase after the frequency exceeds the critical frequency called hopping frequency (ω_H). The conductivity spectra of PCO follow the power law [5] as shown by the solid lines in Fig. 4. The temperature dependence of σ_{dc} obtained from the fitting of the experimental data to the power law at different temperatures follows Arrhenius' law (inset of Fig. 4) with an activation energy of 0.32 eV. The activation energy value indicates that polaron hopping may be responsible for conduction processes in PCO.

In Fig. 5 the frequency dependent dielectric constant (ε') and loss tangent ($\tan\delta$) of PCO as a function of temperature are shown. The observed peaks in $\tan\delta$ can be explained according to the fact that a strong correlation between the conduction mechanism and the dielectric behavior exists in PCO. For a thermally activated relaxation

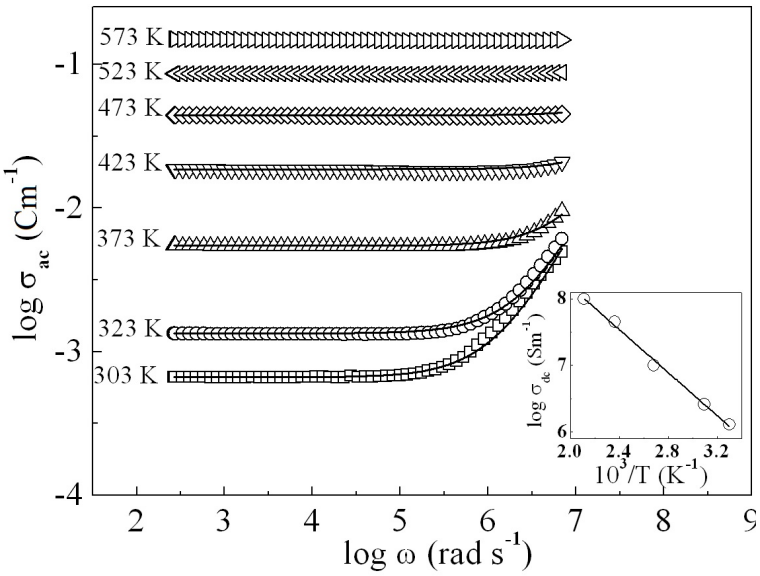

FIG. 4. Frequency dependent Ac conductivity. Inset is the temperature dependence of σ_{dc}

process, the relaxation time τ has the form $\tau_0 \exp(E/k_BT)$, where E and k_B are the activation energy for the relaxation process and the Boltzmann constant, respectively. Then the resonant condition is $\omega_{\max}\tau_0 \exp(E/k_BT) = 1$, where $\omega_{\max}$ is the frequency at which $\tan\delta$ has its maximum value. The temperature dependence of the most probable relaxation frequency ($\omega_{\max}$) follows Arrhenius' law (inset of Fig. 5), and a straight line fit to the experimental data gives an activation energy of 0.319 eV. This activation energy is equal to the activation energy obtained for the temperature dependence of σ_{dc}. This suggests that the dielectric loss in PCO is due to the conduction of charge carriers.

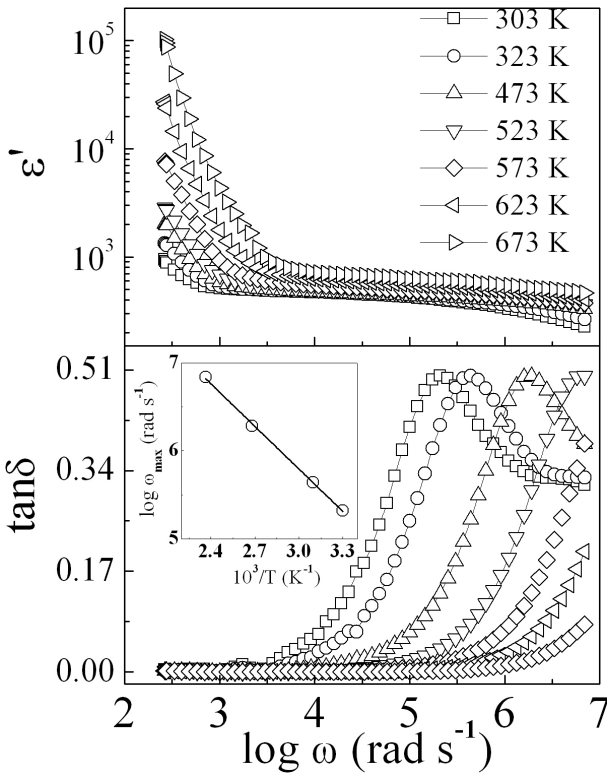

FIG. 5. Frequency dependence of ε' and $\tan\delta$. Inset is the Arrhenius plot of $\omega_{\max}$

4. Conclusions

The Rietveld refinement of XRD profile suggests the single phase formation of PCO with Pnma space group. The Raman spectrum fitted with 20 Lorentzian lines substantiates the orthorhombic crystal structure of PCO with space group Pnma. The dielectric properties of the sample have been investigated as a function of frequency and temperature. The frequency-dependent conductivity spectra follow the power law. The activation energy for charge carrier transport is found to be 0.32 eV, which indicates that polaron hopping plays the main role for the dielectric relaxation in PCO.

Acknowledgements

Alo Dutta thanks to Department of Science & Technology of India for providing the financial support through DST Fast Track Project under Grant No. SB/FTP/PS–175/2013.

References

[1] Shen Y., Liu M., San T.H., Jiang P. Preparation, Electrical Conductivity, and Thermal Expansion Behavior of Dense $Nd_{1-x}Ca_xCrO_3$ Solid Solutions. *J. Am. Ceram. Soc.*, 2009, **92**, P. 2259-?2264.

[2] Gordon G.D., Hornrcich R.M., Shtrikman S., Wanklyn B.M. Magnetization studies in the rare-earth orthochromites. V. $TbCrO_3$ and PrCrO. *Phys. Rev. B*, 1976, **13**, P. 3012–3017.

[3] Prasad B.V., Rao G.N., Chen J.W., Babu D.S. Relaxor ferroelectric like giant permittivity in $PrCrO_3$ semiconductor ceramics. *Mater. Chem. Phys.*, 2011, **126**, P. 918–921.

[4] Zhang Y., Yao C., Fan Y,. Zhou M. One-step hydrothermal synthesis, characterization and magnetic properties of orthorhombic $PrCrO_3$ cubic particles. *Mater. Res. Bull.*, 2014, **59**, P. 387–393.

[5] Jonscher A.K. *Universal relaxation law*. Chelsea Dielectrics Press, London, 1996.

NANOSYSTEMS: PHYSICS, CHEMISTRY, MATHEMATICS, 2016, 7 (4), P. 618–620

Influence of bismuth on the microstructure, hardness and dry sliding wear behavior of magnesium silicide reinforced magnesium alloy composite

D. E. Umesha[1], D. Shivalingappa[2], R. Kishore Kumar[2], Binto Tomy[2], D. Ramesh Rao[3]

[1]Bapuji Institute of Engineering and Technology, Davangere–577004, India

[2]Adhiyamaan College of Engineering, Hosur–635109, India

[3]M.S. Ramaiah Institute of Technology, Bangalore–560099, India

dsivadvg@gmail.com, kishore.rg7@hotmail.com

PACS 06.20.-f 12.60.Rc 61.10.Nz **DOI 10.17586/2220-8054-2016-7-4-618-620**

The modification effect of bismuth (Bi) on in-situ-formed magnesium silicide (Mg_2Si) reinforced magnesium-aluminium (Mg–Al) alloy is investigated using optical microscope, scanning electron microscope and X-ray diffraction. Processing of the in-situ composite was carried out through a stir casting technique. The size of Mg_2Si is significantly refined and the optimal modification effect was obtained when the Bi content in the composite is 1.4%. A slight decrease in hardness values and increase in wear resistance were observed in the study with bismuth addition.

Keywords: Mg–Al Alloy, bismuth, modifier, in-situ composite, wear resistance.

Received: 3 February 2016

Revised: 4 April 2016

1. Introduction

Increasing the fuel efficiency of a vehicle is one of the main considerations in automotive field, which in turn, is directly influenced by the weight of the vehicle. Magnesium alloys and composites are the lightest structural materials which can be used extensively in automotive industries. Magnesium metal matrix composites can be processed using both ex-situ and in-situ techniques. However, it has been noted that the in-situ method of processing results in improved grain structure, mechanical properties and wear properties for the final metal matrix composites [1, 2]. Magnesium alloys containing Mg_2Si particles seem to show high melting temperatures, low density, high hardness, low thermal expansion coefficients and reasonably high elastic moduli. Uniform morphology of Mg_2Si particles is difficult to obtain and moreover the size of these particles are larger in nature [3]. This can lead to poor mechanical properties for the composite. Modification is found to be a simple and effective technique for improving the morphology and size of Mg_2Si particles in Mg–Al alloys [4]. Modification of Mg_2Si can be also done by adding additives such as P, Li, Na, KBF4, Ca, La [5–8] etc. Bismuth is found to be one of the suitable additives that can be used for the modification of Mg_2Si particles.

The primary aim of the present study was to investigate the effect of Bi modification on the Mg_2Si phase in Mg–Al alloy. Based on these results, the hardness and dry sliding wear behavior of composites with different amounts of Bi were investigated.

2. Experimental Procedures

2.1. Materials and Processing

Commercially pure Mg ingot (99.3% purity), Al ingot (99.2% purity) and Si powder (99.9% purity) were used as the starting materials to prepare the Mg–Al/ Mg_2Si composites. The melting process was carried out in a steel crucible kept in a 2 kW electric resistance furnace under a protective atmosphere of argon gas. The furnace had a bottom pouring configuration and was also provided with an inert gas atmosphere.

The processing of composites was carried out in two stages by a stir casting technique. In the first stage, cast aluminium-silicon master alloy was synthesized by dispersing silicon particles into the molten aluminium. In the second stage, cast Al–Si master alloy was dissolved in the molten magnesium (760 °C) in such amounts so that the final mixture had 9 wt% Al in Mg–Al matrix alloy and 2.5 wt% Mg_2Si reinforcement. For refinement of Mg_2Si bismuth (0, 0.7, 1.4, 2 wt%) was added to the molten magnesium. Stirring was done at 600 rpm for 10 minutes for all samples. Finally, the composite slurry was poured into a 30mm$\times$50mm$\times$120mm steel mold.

2.2. Materials characterization and phase analysis

XRD analysis was carried out for powders from Mg–Al/ Mg_2Si composite containing 1.4 wt% Bi and Mg–Al/ Mg_2Si composite without Bi. Specimens for microstructure analysis were prepared using standard procedures and optical microscopy and SEM examination and EDS analysis were carried out.

2.3. Hardness and wear tests

The Brinell hardness test was used to measure the hardness of the specimens. Test specimens were indented with a 5 mm diameter hardened steel ball subjected to a load of 150 N applied for 10 seconds. Dry sliding wear tests were conducted according to the ASTM G99 standard using pin-on-disc machine. The wear tests for all specimens were conducted under two different loads (10 N and 20 N) and varying the disc rotating speeds of 300, 350, 400 and 450 rpm. Wear tests were carried out for a total sliding distance of approximately 1000 m. The pin samples were 30 mm in length and 8 mm in diameter.

3. Results and Discussion

3.1. Microstructural features

Figure 1 shows the XRD patterns of Mg–Al/ Mg_2Si composite without Bi content and with 1.4 wt. % Bi content respectively. The XRD pattern reveals that the processed in-situ composite contains α-Mg, β-$Al_{12}Mg_{17}$ and Mg_2Si phases. Some new peaks appear in the pattern with the addition of 1.4 wt. % Bi. The XRD pattern of the in-situ composite which was processed with the bismuth refinement material confirmed the presence of bismuth by showing the additional peaks corresponding to it.

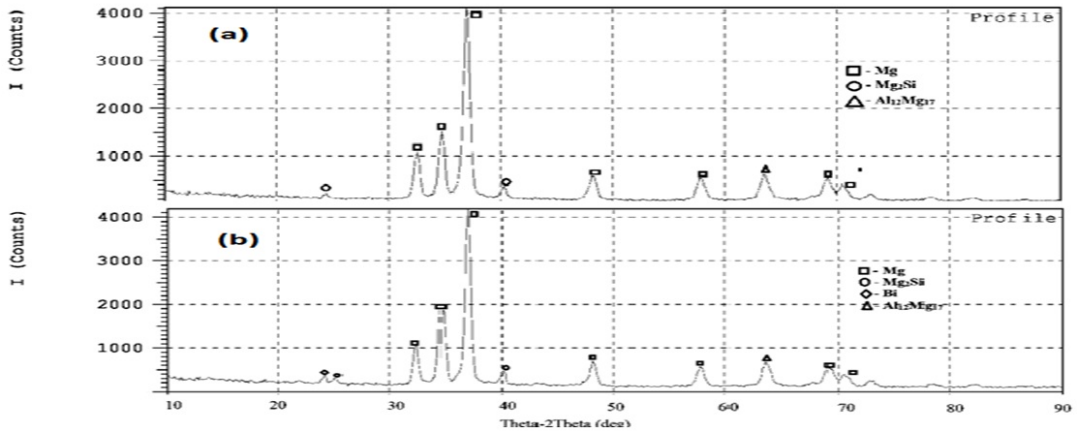

FIG. 1. XRD pattern of Mg–Al/ Mg_2Si composite (a) 0 wt% (b) 1.4 wt% Bi

The SEM micrographs, along with EDS patterns for in-situ composite with and without bismuth are shown in Figs. 2(a) and 2(b) respectively. The presence of bismuth was confirmed from the additional peaks, as is seen in Fig. 2(b) compared to peaks in Fig. 2(a). The larger size of the reinforcing Mg_2Si particles can be seen in the Fig. 2(a), whereas refined and smaller size of Mg_2Si phase can be seen in Fig. 2(b). Small white spots in Fig. 2(b) correspond to bismuth powder. The Mg_2Si particles in an unmodified sample were found to be clustered throughout as large particles.

The morphology was poor when compared to the 2% Bismuth modified specimen. As the percentage of bismuth increased, the Mg_2Si particles became divided, finally resulting in a unique particle distribution. However, it is also readily seen that the particles became coarser with more addition of bismuth.

3.2. Hardness and wear tests

Hardness tests revealed that Bi decreases the hardness value of the composites; however its variation is limited. The Mg–Al/ Mg_2Si composite showed better hardness properties than those Mg–Al/ Mg_2Si composites which were modified by varying amounts of bismuth. The hardness graph of the composite (Mg–Al/ Mg_2Si) with varying bismuth content is shown in Table 1.

Figure 3 shows the variation of wear rate for Mg–Al/Mg_2Si composite with Bi content. A decrease in wear rate can be seen with an increased Bi content and speed. However, the variation of decrease for wear rate can be seen more at higher loads (20N).

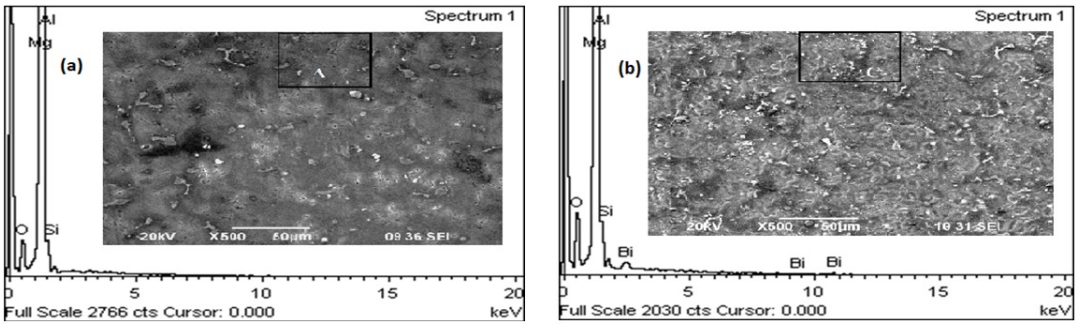

FIG. 2. SEM images with EDS of Mg–Al/ Mg_2Si (a)without and (b)with 1.4 wt% Bi

TABLE 1. Variation of hardness of Mg–Al/ Mg_2Si composite with Bi content

Bismuth (wt%)	0	0.7	1.4	2
Hardness (BHN)	72.9	69.3	69.3	71.5

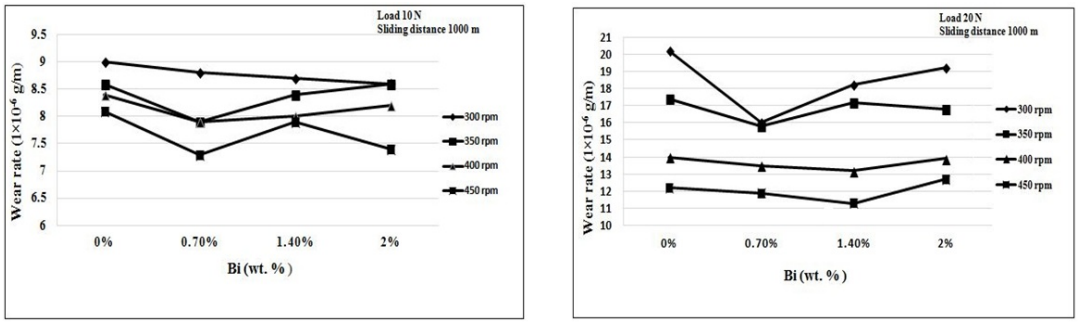

FIG. 3. Variation of wear rate of Mg–Al/ Mg_2Si composite with Bi content

4. Conclusion

From the research, it can be indentified that bismuth plays a significant role in modifying the morphology of Mg_2Si particles in Mg–Al/Mg_2Si composite. The size of the Mg_2Si particles and the hardness values decreased with the addition of bismuth (Bi). However, it was shown that Bi exerts a great influence on wear resistance, as that property was enhanced with increased bismuth content.

References

[1] Bhingole P.P., Chaudhari G.P., Nath S.K. Processing, microstructure and properties of ultrasonically processed in situ MgO-Al_2O_3–$MgAl_2O_4$ dispersed magnesium alloy composites. *Compos. Part A Appl. Sci. Manuf.*, 2014, **66**, P. 209–217.

[2] Shivalingappa D., Daniel B.S.S., Ray S. Effect of reinforcing phase inherited from another composite on the mechanical properties of cast magnesium base composite. *Mater. Sci. Eng. A*, 2012, **541**, P. 172–180.

[3] Hu Y., Rao L. Effect of particulate reinforcement on wear behavior of magnesium matrix composites. *Trans. Nonferrous Met. Soc. China*, 2012, **22**, P. 2659–2664.

[4] Hu J., Tang C., Zhang X., Deng Y. Modification of Mg_2Si in Mg–Si alloys with neodymium. *Trans. Nonferrous Met. Soc. China*, 2013, **23**, P. 3161–3166.

[5] Tang S., Zhou J., Tian C., Yang Y. Morphology modification of Mg_2Si by Sr addition in Mg-4%Si alloy. *Trans. Nonferrous Met. Soc. China*, 2011, **21**, P. 1932–1936.

[6] Qin Q.D., Zhao Y.G., Zhou W., Cong P.J. Effect of phosphorus on microstructure and growth manner of primary Mg_2Si crystal in Mg_2Si/Al composite. *Mater. Sci. Eng. A*, 2007, **447**, P. 186–191.

[7] Hadian R., Emamy M., Varahram N., Nemati N. The effect of Li on the tensile properties of cast Al-Mg_2Si metal matrix composite. *Mater. Sci. Eng. A*, 2008, **490**, P. 250–257.

[8] Emamy M., Khorshidi R., Raouf A.H. The influence of pure Na on the microstructure and tensile properties of Al-Mg_2Si metal matrix composite. *Mater. Sci. Eng. A*, 2011, **528**, P. 4337–4342.

NANOSYSTEMS: PHYSICS, CHEMISTRY, MATHEMATICS, 2016, 7 (4), P. 621–623

Effect of substrate temperature on microstructure and properties of nanocrystalline titania thin films prepared by pulsed laser deposition

G. Balakrishnan[1], S. Manavalan[2], R. Venkatesh Babu[3] and J. I. Song[4]

[1]Centre of Excellence in Patterned Multiferroics & Nanotechnology, Bharath Institute of Science and Technology, Bharath Institute of Higher Education and Research, Chennai – 73, India

[2]Department of Mechanical Engineering, Bharath Institute of Science and Technology, Bharath Institute of Higher Education and Research, Chennai – 73, India

[3]Department of Mechanical Engineering, Sri Lakshmi Ammal Engineering College, Chennai – 126, India

[4]Department of Mechanical Engineering, Chanwon National University, Changwon – 641773, South Korea

balaphysics76@gmail.com, manavalan.kannan@gmail.com, rvbaboo76@gmail.com, jisong@changwon.ac.kr

PACS 81.07. -b **DOI 10.17586/2220-8054-2016-7-4-621-623**

Titanium oxide (TiO_2) films were deposited on silicon (100) and quartz substrates at various substrate temperatures (300 – 873 K) at an optimized oxygen partial pressure of 3.0×10^{-2} mbar by pulsed laser deposition. The effect of substrate temperature on structure, surface morphology and optical properties of the films were investigated using X-ray diffraction (XRD), atomic force microscopy (AFM) and photoluminescence spectroscopy (PL) respectively. The XRD results showed that the films are polycrystalline in nature and have tetragonal structure. The film prepared at higher substrate temperature showed strong rutile phase. The results indicated that all the films possess both phases (anatase and rutile) of titania. The AFM shows the crystalline nature, dense, uniform distribution of the nanocrystallites with a surface roughness of 2 – 8 nm. The photoluminescence studies showed the asymmetric peak ~ 370 nm indicating the bandgap for the TiO_2 films.

Keywords: Titania, thin films, pulsed laser deposition, X-ray diffraction (XRD), atomic force microscopy (AFM), photoluminescence spectroscopy (PL).

Received: 5 February 2016

1. Introduction

Titania (TiO_2) exists in rutile, anatase and brookite phases. TiO_2 thin films are widely studied due to their interesting chemical, electrical and optical properties. TiO_2 thin films exhibit unique properties such as high dielectric constant, wide optical bandgap, high refractive index, photo catalytic, low absorption and high transparency with high chemical and thermal stabilities. Because of its excellent properties, it finds applications in heterogeneous catalysis, photocatalysts, self cleaning windows, solar cells, gas sensors, corrosion resistant coatings, optical coatings, metal oxide field effect transistors, varistors, Li-based batteries and electro chromic devices [1–3]. The occurrence of anatase and rutile phase of TiO_2 thin films mainly depends on the deposition method, process parameters and substrate temperature. Many techniques are used to deposit TiO_2 films, including sol-gel processes [4], reactive evaporation [5], chemical vapor deposition [6], sputtering [7, 8] and pulsed laser deposition (PLD) [9]. Among these techniques, pulsed laser deposition (PLD) is a simple technique to prepare high quality films from metal, semiconductors and ceramics. The rapid rate of ablation from target surface promotes the constituents of the target to evaporate congruently and to retain the stoichiometry in the film. There are many deposition parameters to be optimized to achieve the optimum properties. The oxygen partial pressure and the substrate temperature play an important role to produce high quality films by PLD. The preparation method and process parameters of TiO_2 films are of fundamental importance for obtaining the optimum properties for various applications. In the present work, nanocrystalline TiO_2 films were deposited on silicon and quartz substrates as a function of substrate temperature by PLD and their microstructure and optical properties were investigated.

2. Experimental details

TiO_2 powder was compacted into a pellet of 30 mm diameter and 5 mm thickness using a uni-axial press. The pellet was sintered ~ 1473 K for 8 hours and used as a target for the PLD. TiO_2 films were deposited on Si (100) and quartz substrates at various substrate temperatures from 300 K to 873 K. The films were deposited using KrF excimer laser ($\lambda = 248$ nm) with a repetition rate of 10 Hz. X-ray diffraction (XRD) studies were carried out using X'pert PW 3040 D-8 (PANalytical) diffractometer with $CuK_{\alpha 1}$ radiation. The surface topographies and roughnesses of the films were analyzed using atomic force microscope (XE-100 Park systems) in non-contact mode. The photoluminescent spectra of these films were recorded using a (Shimadzu, RF-5301PC) spectrofluorophotometer.

3. Results and Discussion

3.1. Microstructural studies

XRD pattern of the TiO_2 thin films is shown in Fig. 1. The XRD pattern shows the peaks at angles 25.8 ° and 37.9 °, corresponding to the anatase phase ((JCPDF # 21-1272), while the peaks at angles 27.5 °, 44.2 °, 56.5 °, 64.3 ° indicate the rutile phase (JCPDS # 21-1276) of titania. In the XRD pattern, A and R denotes the anatase and rutile phase of titania respectively [9]. The XRD results showed that the films were polycrystalline in nature and had tetragonal structure. The films deposited in the lower substrate temperatures (300 – 673 K), showed the small intense peaks corresponding to both anatase and rutile phases, while the films deposited at higher substrate temperatures (773 K and 873 K) indicated the strong peaks corresponding to the rutile phase. This indicated the higher rutile phase content and smaller anatase phase content in the films with increasing substrate temperature. The formation of rutile phase with temperature was due to the high energy of particles impinging on the substrate kept at higher temperature. The thickness of the films increased with increasing temperature. The anatase to rutile phase transformation takes place over a wide range of temperatures (from 823 to 1073 K). Ben Amor et al. [10] investigated the properties of TiO_2 films and observed the amorphous nature in the as-deposited condition, while the annealed films at 873 K showed anatase phase.

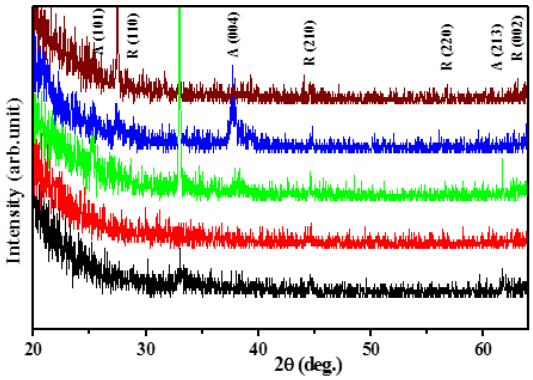

FIG. 1. XRD pattern of the TiO_2 thin films deposited on Si (100) at different substrate temperatures

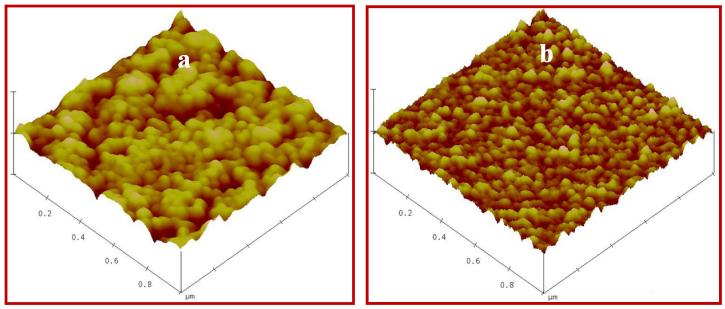

FIG. 2. AFM images of the TiO_2 films prepared at (a) 300 K and (b) 873 K

Figure 2 shows the AFM images of the typical films prepared at room temperature (300 K) and 873 K. The images showed the dense crystallites, uniform formation of the crystallites and smooth morphology. The mobility of the ad-atoms is higher at higher substrate temperatures and the film prepared at 873 K showed the coalescence of the crystallites. The surface roughness of the films were measured and found to be in the range 3 – 8 nm.

3.2. Photoluminescence studies

Figure 3 shows the photoluminescence (PL) spectra of the TiO_2 films deposited on silicon (100) substrates at various substrate temperatures. The PL spectra of the films were analyzed using 325 nm laser excitation wavelength. PL spectra showed broad and asymmetric peaks, indicating the presence of both anatase and rutile phases. At 873 K, two PL peaks were observed, indicating the clear anatase and rutile peaks. The small intense peak $\sim$ 470 nm (2.7 eV) is probably due to the structural defects, which are related to deep-level emissions like

oxygen vacancy [9, 11, 12]. The PL peak intensity of TiO_2 films with respect to substrate temperature is associated with its crystallinity and defects. The glancing incidence X-ray diffraction (GIXRD) results of the films showed more rutile phase (Fig. 1) at higher substrate temperatures. The PL peak intensity decreases systematically with the increased substrate temperature [9]. The variation of PL peak intensity is related to the formation of rutile and anatase phases at different substrate temperatures. The PL results are consistent with our XRD results [13]. All these results showed that the optical properties of TiO_2 films are dependent on their microstructure influenced by substrate temperature. Table 1 gives the details for the crystallite size, surface roughness and bandgap of the titania films with respect to the substrate temperature.

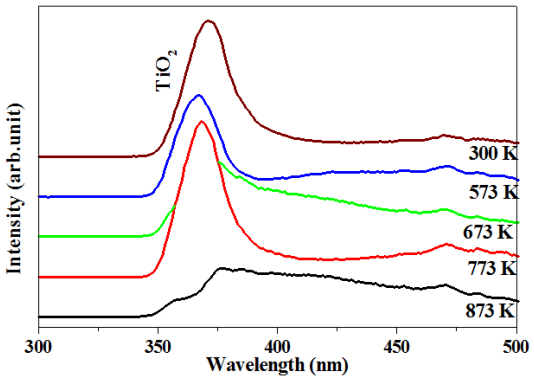

FIG. 3. Photoluminescence spectra of the TiO_2 films prepared at different temperatures

TABLE 1. Substrate temperature *vs* crystallite size, surface roughness and bandgap

Substrate Temp. (K)	Crystallite size Rutile (110) (nm)	Surface roughness AFM (nm)	Bandgap (eV) PL
300	—	3.0	3.35
573	—	5.2	3.37
673	—	6.5	3.37
773	30	7.2	3.37
873	48	8.0	3.30

4. Conclusions

The TiO_2 thin films were deposited on Si (100) and quartz substrates at various substrate temperatures by pulsed laser deposition. The XRD studies indicated small intense peaks corresponding to both anatase and rutile phases at low substrate temperatures, while the strong peaks indicated higher rutile phase content at higher substrate temperatures. The rutile phase content increased with increased substrate temperature. The AFM studies illustrated the dense, uniform distribution of the crystallites with smooth morphology. PL studies demonstrated the broad and asymmetric peaks $\sim$ 370 nm, indicating a bandgap of $\sim$ 3.30 – 3.37 eV.

References

[1] Gyorgy E., Socol G., et al. *Appl. Surf. Sci.*, 2005, **247** (4), P. 429–433.
[2] Tay B.K., Zhao Z.W., Chua D.H.C. *Mater. Sci. Eng. Rep.*, 2006, **52** (1), P. 178–182.
[3] Byun C., Jang J.W., et al. *Mater. Res. Bull.*, 1997, **32** (5), P. 431–440.
[4] Vorotilov K.A., Drlova E.V., Petrovsky V.L. *Thin Solid Films*, 1992, **207**, P. 135–144.
[5] Pulker H.K., Paesold G., Ritter E. *Appl. Opt.*, 1976, **15**, P. 2986.
[6] Lu J.P., Wang J., Raj R. *Thin Solid Films*, 1991, **204**, L13.
[7] Suhail M.H., Mohan Rao G., Mohan S.J. *Appl. Phys.*, 1992, **71** (3), P. 1421.
[8] Argelia Perez-Pacheco, Prieto C., Castaneda-Guzma R., Garcia-Lopez J. *Thin Solid Films*, 2009, **517**, P. 5415.
[9] Balakrishnan G., Vengala Rao Bandi, et al. *Mater. Res. Bull.*, 2013, **48**, P. 4901.
[10] Ben Amor S., Baud G., Besse J.P., Jacquet M. *Mater. Sci. Eng. B*, 1997, **47**, P. 110.
[11] Chung C.K., Liao M.W., Lai C.W. *Thin Solid Films*, 2009, **518**, P. 1415.
[12] Madhu Kumar P., Badrinarayanan S., Murali S. *Thin Solid Films*, 2000, **358**, P. 122.
[13] Gaurav Shukla, Pratima K. Mishra, Alika Khare. *J. Alloy Compd.*, 2010, **489**, P. 246.

NANOSYSTEMS: PHYSICS, CHEMISTRY, MATHEMATICS, 2016, 7 (4), P. 624–628

Study of Faraday effect on $Co_{1-x}Zn_xFe_2O_4$ nanoferrofluids

R. Karthick[1], K. Ramachandran[2], R. Srinivasan[3,*]

[1]Department of Physics, PSNA College of Engineering and Technology, Dindigul–624622, India

[2]School of Physics, Madurai Kamaraj University, Madurai–625021, India

[3]Department of Physics, Thiagarajar College, Madurai–625009, India

karthickr4584@gmail.com, thirumalchandran@gmail.com, *r_srini2067@yahoo.co.in

PACS 47.65.Cb, 63.50.Lm, 33.57.+c, 78.20.Ls **DOI 10.17586/2220-8054-2016-7-4-624-628**

Zinc doped cobalt ferrite$Co_{1-x}Zn_xFe_2O_4$ nanoparticles ($x = 0.1, 0.5, 0.9$) were synthesized by chemical co-precipitation method. The crystallite size, which was calculated from the full width half maximum (FWHM) value of the strongest peak (311) plane using Scherer approximation, was found to decrease with higher zinc content. The surface morphology of the powder samples was obtained using transmission electron microscopy (TEM). Magnetic properties, such as Saturation magnetization (M_s), Remanent Magnetization (M_r) and Coercivity of the powder samples, were measured using Vibrating Sample Magnetometer (VSM) at room temperature and were found to decrease with increased zinc content. Aqueous ferrofluids prepared from the powder samples were subjected to magnetic field to measure their Faraday rotation. Faraday rotation of the ferrofluids was found to increase with applied magnetic field and decrease with increasing zinc composition.

Keywords: nanoferrofluid, vibrating sample magnetometer, faraday rotation.

Received: 5 February 2016

Revised: 4 April 2016

1. Introduction

Ferrofluids are a colloidal suspension of single domain magnetic particles, with typical dimensions of about 10 nm, dispersed in a carrier liquid [1]. To avoid the aggregation of nanoparticles, they have to be covered with a suitable surfactant. Optical property of ferrofluids can be altered by external applied magnetic field [2]. Structural reorientation of the nanoparticles suspended in a magnetic colloid brings out magneto-optic properties [3], which are used in developing optical sensors [4], photonic devices [5], etc. The kinetics of particle aggregation in magnetic nanofluid have been studied using various techniques [6, 7]. The functional group adhered to the nanoparticles (stabilizers) can influence the kinetics of magnetic field induced chain like formation which influences their magneto-optic properties [8]. Among other influencing parameters, the dipolar interaction among nanoparticles is the main driving force for particle aggregation and field induced structural transitions [9]. Common methods of synthesis of ferrofluids employ co-precipitation [10], ball milling [11], sol-gel method [12] and micro emulsion [13]. Among these methods, co-precipitation is the low cost and less energy required for synthesis of ferrofluids.

2. Sample preparation

The chemical co-precipitation method was used to synthesize $Co_{1-x}Zn_xFe_2O_4$ nanoparticles for $x = 0.1$, 0.5 and 0.9. Stoichiometric ratios of $FeCl_{3.6}H_2O$, $CoCl_2$ and $ZnCl_2$ solution were mixed and added to NaOH solution under constant stirring. Diluted HCl was added until the pH reaches 9. In order to prevent agglomeration of the nanoparticles, oleic acid was added. The resultant precipitates were isolated by centrifugation and washed with de-ionized water, acetone and ethanol to remove impurities and then dried at 60 °C for 4 hours. Powder samples were used to carry out initial characterization such as XRD, TEM and VSM. Then, aqueous nanoferrofluids were prepared to study their magneto-optic effect.

3. Results and discussion

3.1. X-ray diffraction

The XRD pattern of the powder samples are shown in Fig. 1, which confirm the spinel structure (JCPDS no 22-1086) [14]. The crystallite size for each composition was calculated using the Debye-Scherer formula for the (311) plane. The crystallite size decreases from 11.4 nm to 5.6 nm with an increase in zinc content. In spinel ferrite, zinc ions have stronger preference to occupy tetrahedral site, iron ions preferentially occupy tetrahedral site while cobalt ions have octahedral site preference [15]. Increasing x values in $Co_{1-x}Zn_xFe_2O_4$ spinel ferrite causes

zinc ions to occupy tetrahedral sites preferentially, displacing iron ions from the octahedral sites [16]. Therefore, replacement of cobalt ions by zinc ions forces the transformation of inverse spinel into normal spinel structure.

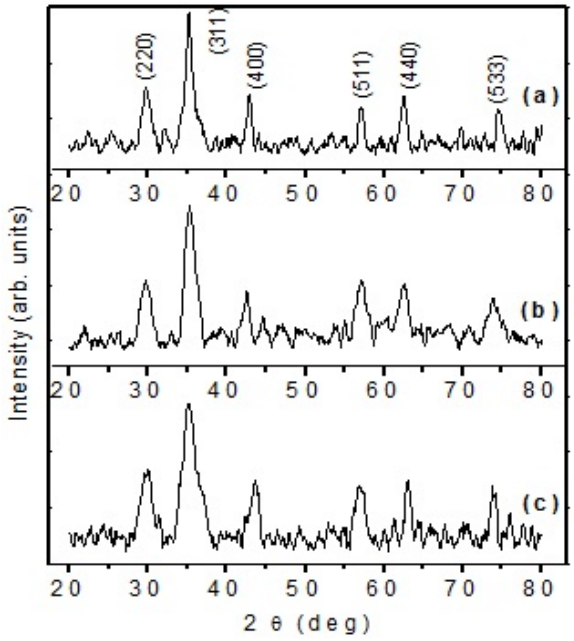

FIG. 1. XRD pattern of the samples (a) $Co_{0.9}Zn_{0.1}Fe_2O_4$, (b) $Co_{0.5}Zn_{0.5}Fe_2O_4$ and (c) $Co_{0.1}Zn_{0.9}Fe_2O_4$

3.2. Transmission electron microscopy

Figure 2 shows the transmission electron microscope (TEM) images of $Co_{1-x}Zn_xFe_2O_4$ nanoparticles. Physical particle sizes of the samples are found to be slightly larger than the crystallite size obtained by XRD. It was also observed that the presence of surfactant and decrease in the magnetic moment of particles reduced magnetic nanoparticle aggregation.

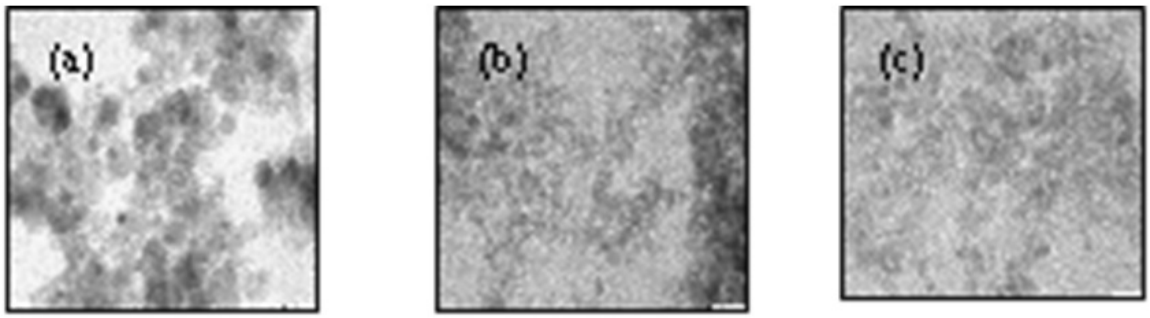

FIG. 2. TEM of the samples (a) $Co_{0.9}Zn_{0.1}Fe_2O_4$, (b) $Co_{0.5}Zn_{0.5}Fe_2O_4$ and (c) $Co_{0.1}Zn_{0.9}Fe_2O_4$

3.3. Magnetic measurements

M-H loop of the powder samples are shown in Fig. 3. Magnetization in a spinel ferrite arises as a result of dominant interaction existing between tetrahedral (A) site and octahedral (B) site mediated by oxygen A-O-B interactions [17]. Increasing zinc content in $Co_{1-x}Zn_xFe_2O_4$ spinel ferrite causes zinc ions to occupy tetrahedral sites and displaces iron ions to octahedral sites [16]. In octahedral sites, cobalt ions are replaced by iron ions [18]. Thus, the substitution of non-magnetic zinc ion varies the A-O-B interaction. Magnetic parameters, such as saturation magnetization (M_s), remanent magnetization (M_r) and coercive field (H_c), were found to vary with zinc content and are shown in Table 1. The values are in agreement with the literature [19]. Moreover, saturation magnetization of bulk cobalt ferrite is 65 emu/g [20]. Coercivity is a measure of magnetocrystalline anisotropy of

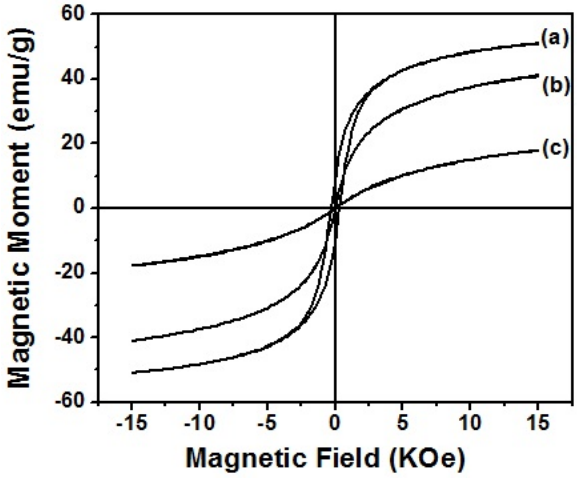

FIG. 3. M-H loop at room temperatureof the samples (a) $Co_{0.9}Zn_{0.1}Fe_2O_4$, (b) $Co_{0.5}Zn_{0.5}Fe_2O_4$ and (c) $Co_{0.1}Zn_{0.9}Fe_2O_4$

the samples [17]. Decreasing values of coercivity and remanence at room temperature indicate that the samples are approaching superparamagnetism [21]. Surface defects, such as formation of dead layer, canting of particle surface spins and deviation in cation distribution may reduce the magnetic properties [15].

TABLE 1. Magnetic parameter of the samples

Samples	Saturation Magnetization (emu/g)	Remanent Magnetization (emu/g)	Coercive Field (KOe)
$Co_{0.9}Zn_{0.1}Fe_2O_4$	50.95	9.4350	0.2878
$Co_{0.5}Zn_{0.5}Fe_2O_4$	41.04	0.0638	0.0044
$Co_{0.1}Zn_{0.9}Fe_2O_4$	17.89	0.0046	0.0013

3.4. FaradayrRotation

Faraday rotation of the samples was measured using standard technique, which includes electromagnet, polarizer, analyzer, cuvette and a monochromatic sodium vapor lamp. $Co_{1-x}Zn_xFe_2O_4$ nanoparticles were dispersed in de-ionized water and sonicated for 30 minutes. The volume fraction was kept as 0.005 for all the samples. Linearly polarized light from a polarizer was allowed to pass through the electromagnet, ferrofluid and an analyzer. In this set-up, a magnetic field applied is longitudinal to the polarized light. Light emerging out from analyzer was detected using a photodetector. The angle of rotation (θ_F) of plane polarized light is proportional to the product of applied magnetic field (B) and optical path length (l) of the ferrofluid through which the light passes:

$$\theta_F = VBl,$$

where, V is Verdet constant of the sample.

When a magnetic field is applied to the samples, degeneracy is lifted and the relative energies are determined by Lande g factor. During the transition of electrons between degenerate states, rotation of plane of polarization is accompanied by the development of an ellipticity of the originally polarized light [22]. Also, it was reported that Faraday rotation can be enhanced due to crystal field transitions and intervalence charge transfer transitions between neighboring ions [22, 23]. Varying the occupancy of tetrahedral and octahedral sites changes the Faraday rotation. The variation of Faraday rotation and Verdet constant are shown in Fig. 4 and Fig. 5. Variation of Verdet constant below 600 gauss for samples (a) and (b) indicates the need to increase the accuracy of measurement system at low fields.

4. Conclusion

$Co_{1-x}Zn_xFe_2O_4$ nanoparticles were synthesized by co-precipitation method using oleic acid as surfactant. The XRD diffraction patterns confirm the cubic spinel structure. The crystallite size decreases with increased zinc

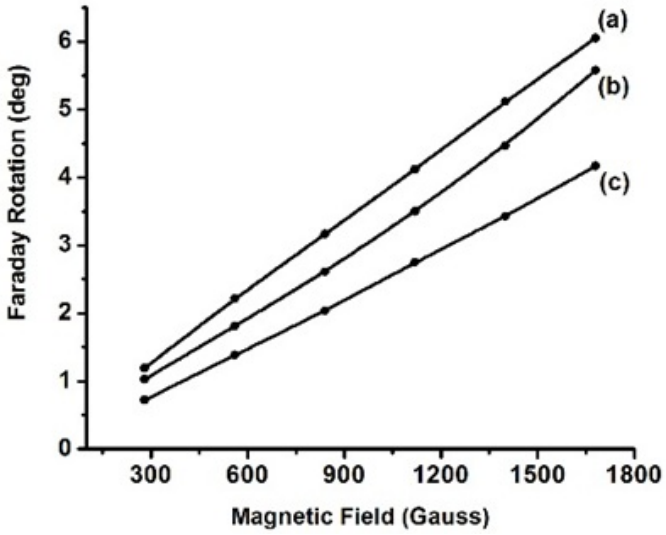

FIG. 4. Faraday rotation of the samples (a) $Co_{0.9}Zn_{0.1}Fe_2O_4$, (b) $Co_{0.5}Zn_{0.5}Fe_2O_4$ and (c) $Co_{0.1}Zn_{0.9}Fe_2O_4$

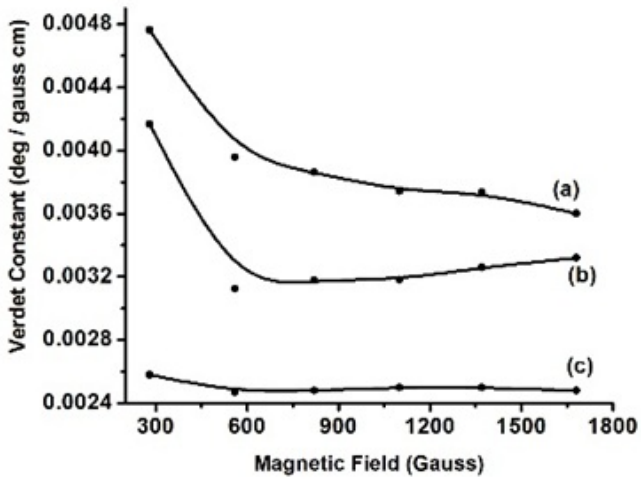

FIG. 5. Verdet constant vs magnetic field of the samples (a) $Co_{0.9}Zn_{0.1}Fe_2O_4$, (b) $Co_{0.5}Zn_{0.5}Fe_2O_4$ and (c) $Co_{0.1}Zn_{0.9}Fe_2O_4$

content. The magnetic properties and Verdet constant of $Co_{1-x}Zn_xFe_2O_4$ nanoparticles vary with the incorporation of zinc and cobalt ions into iron oxide spinel ferrite. The Faraday rotation and hence the Verdet constant decreases with increased zinc substitution.

Acknowledgement

The authors would like to thank SAIF, IIT Bombay for providing TEM facility.

References

[1] Ibrahim Sharifi, Shokrollai H., Amiri S. Ferrite based magnetic nanofluids used in hyperthermia applications. *Journal of Magnetism and Magnetic Materials*, 2012, **324**(6), P. 903–915.

[2] Masajada J., Bacia M., Drobczyński S. Cluster formation in ferrofluids induced by holographic optical tweezers. *Optics Letters*, 2013, **38**(19), P. 3910–3913.

[3] Bhatt H., Patel R. Optical transport in bidispersed magnetic colloids with varying refractive index. *Journal of nanofluids*, 2013, **2**(3), P. 188–193.

[4] Mahendran V., Philip J. Nanofluid based optical sensor for rapid visual inspection of defects in ferromagnetic materials. *Applied Physics Letters*, 2012, **100**(7), P. 073104.

[5] Fan C.Z., Wang G., Huang J.P. Magnetocontrollable photonic crystals based on colloidal ferrofluids. *Journal of Applied Physics*, 2008, **103**(9), P. 094107.

[6] Duncan P.D., Camp P.J. Aggregation kinetics and the nature of phase separation in two-dimensional dipolar fluids. *Physical Review Letters*, 2006, **97**(10), P. 107202.
[7] Ukai T., Maekawa T. Patterns formed by paramagnetic particles in a horizontal layer of a magnetorheological fluid subjected to a dc magnetic field. *Physical Review E*, 2004, **69**(3), P. 032501.
[8] Regmi R., Black C., Sudakar C., Keyes P.H., Naik R., Lawes G., Vaishnava P., Rablau C., Kahn D., Lavoie M., Garg V.K., Oliveira A.C. Effects of fatty acid surfactants on the magnetic and magnetohydrodynamic properties of ferrofluids. *Journal of Applied Physics*, 2009, **106**(11), P. 113902.
[9] Brojabasi S., Muthukumaran T., Laskar J.M., John Philip. The effect of suspended Fe_3O_4 nanoparticle size on magneto-optical properties of ferrofluids. *Optics Communications*, 2015, **336**, P. 278–285.
[10] Amighian J., Karimzadeh E., Mozaffri M. The effect on Mn^{2+} substitution on magnetic properties of $Mn_xFe_{3-x}O_4$ nanoparticles prepared by coprecipitation method. *Journal of Magnetism and Magnetic Materials*, 2013, **332**, P. 157–162.
[11] Yin H., Too H.P., Chow G.M. The effects of particle size and Surface coating on the cytotoxicity of nickel ferrite. *Biomaterials*, 2005, **26**(29), P. 5818–5826.
[12] VijayaBhasker Reddy P., Ramesh B., GopalReddy Ch. Electrical conductivity and dielectric properties of zinc substituted lithium ferrites prepared by sol-gel method. *Physica B*, 2010, **405**(7), P. 1852–1856.
[13] Woo K., Lee H.J., Ahn J.P., Park Y.S. Sol-gel mediated synthesis of Fe_2O_3 naorods. *Advanced Materials*, 2003, **15**(20), P. 1761–1764.
[14] Bragg W.H. The Structure of magnetite and the Spinels. *Nature*, 1915, **95**(2386), P. 561.
[15] BehshidBehdafar, Ahmad Kermanpur, HojjatSadeghi-Aliabadi, Maria del Puerto Morales, MortezaMozaffari. Synthesis of aqueous ferrofluids of $Zn_xFe_{3-x}O_4$ nanoparticles by citric acid assisted hydrothermal-reduction route for magnetic hyperthermia applications. *Journal of Magnetism and Magnetic Materials*, 2012, **324**(14), P. 2211–2217.
[16] VeenaGopalan E., Al-Omari I.A., Malini K.A., Joy P.A., Sakthi Kumar D., Yasuhiko Yoshida, Anantharaman M.R. Impact of zinc substitution on the structural and magnetic properties of chemically derived nanosized manganese zinc mixed ferrites. *Journal of Magnetism and Magnetic Materials*, 2009, **321**(8), P. 1092–1099.
[17] Yüksel Köseoğlu. Structural, magnetic, electrical and dielectric properties of $Mn_xNi_{1-x}Fe_2O_4$ spinel nanoferrites prepared by PEG assisted hydrothermal method. *Ceramics International*, 2013, **39**(4), P. 4221–4230.
[18] López J., González-Bahamón L.F., Prado J., Caicedo J.C., Zambrano G., Gómez M.E., Esteve J., Prieto P. Study of magnetic and structural properties of ferrofluids based on cobalt-zinc ferrite nanoparticles. *Journal of Magnetism and Magnetic Materials*, 2012, **324**(4), P. 394–402.
[19] Vaidyanathan G., Sendhilnathan S., Arulmurugan R. Structural and magnetic properties of $Co_{1-x}Zn_xFe_2O_4$ nanoparticles by co-precipitation method. *Journal of Magnetism and Magnetic Materials*, 2007, **313**(2), P. 293–299.
[20] Yeongll Kim, Don Kim, Choong Sub Lee. Synthesis and characterization of $CoFe_2O_4$ magnetic nanoparticles prepared by temperature-controlled coprecipitation method. *Physica B: Condensed Matter*, 2003, **337**(1-4), P. 42–51.
[21] Mathew D.S., Juang R.S. An overview of the structure and magnetism of spinel ferrite nanoparticles and their synthesis in microemulsions. *Chemical Engineering Journal*, 2007, **129**(1-3), P. 51–65.
[22] Prashant K. Jain, Yanhong Xiao. Ronald Walsworth and Adam E. Cohen. Surface Plasmon resonance enhanced magneto-optics (SuPREMO): Faraday rotation enhancement in gold coated iron oxide nanocrystals. *Nano Letters*, 2009, **9**(4), P. 1644–1650.
[23] Choi K.H. Magnetic behavior of Fe_3O_4 nanostructure fabricated by template method. *Journal of Magnetism and Magnetic Materials*, 2007, **310**(2), P. e861–e863.

NANOSYSTEMS: PHYSICS, CHEMISTRY, MATHEMATICS, 2016, 7 (4), P. 629–632

Preparation and characterization of porous silicon photoelectrode for dye sensitized solar cells

K. Gangadevi[1], K. Ramachandran[2], R. Srinivasan[1,*]

[1]Department of Physics, Thiagarajar College, Madurai–625009, India

[2]School of Physics, Madurai Kamaraj University, Madurai–625021, India

kdevi.ganga@gmail.com, thirumalchandran@gmail.com, *r_srini2067@yahoo.co.in

PACS 81.05.Rm, 82.33.Ln, 88.40.jr, 88.40.hj, 78.55.Mb

DOI 10.17586/2220-8054-2016-7-4-629-632

Nanostructured porous silicon (PS) samples were prepared by electrochemical anodic dissolution of doped silicon (p-Si) of (100) orientation at constant current density of 30 mA/cm^2 for different etching times 10 and 60 min. The samples were characterized by XRD and SEM. The particle size was calculated from XRD using Scherrer's approximation are in the range of 12 to 61 nm and the SEM images confirmed the difference in porosities of the sample. The samples were sensitized with chloroaluminium phthalocyanine (ClAlPc) to fabricate Dye-sensitized solar cells (DSSCs). The bandgaps from UV- Vis and photoluminescence measurements are in the range of 1.5 to 1.8 eV. The photocurrent and photovoltage of the cells were measured using Keithely source meter. The maximum conversion efficiency of 2.8% is observed and results are discussed.

Keywords: Porous silicon, Chloroaluminum Pc, dye sensitized solar cells, photoluminescence.

Received: 5 February 2016

Revised: 10 May 2016

1. Introduction

Dye-sensitized solar cells (DSSCs) are regarded as a promising low cost option to the conventional solid-state semiconductor solar cells, due to the use of relatively cheap materials and the easy manufacturing techniques. A very important component of DSSCs is the photoelectrode, which includes a nanocrystalline porous wide bandgap oxide semiconductor layer with large internal surface area. The Commercial solar cells are fabricated using crystalline silicon which is costly in nature, where the maximum efficiency of 24.5% is reported in literature [1]. In this work, we measured the conversion efficiencies of DSSCs prepared from porous silicon with different porosities.

2. Experimental

Porous silicon samples were prepared by electrochemical etching of p-type (100) silicon wafers (thickness 517 μm and resistivity 0.2–0.5 Ω cm) at a constant current density of 30 mA/cm^2 for etching periods of 10 and 60 minutes [2]. To sensitize the porous samples, the dye solution was prepared by mixing the synthesized ClAlPc dye [3] in 5 ml of ethanol and used for preparation of photoanode (ClAlPc/PS). The photoanodes were characterized by X–Ray Diffraction (XRD), Scanning Electron Microscopy (SEM), Ultraviolet-visible spectroscopy (UV-vis) and Photoluminescence (PL) techniques. The ClAlPc/PS photoanodes with different porosities were used to fabricate DSSCs.The I–V measurements were carried out to calculate the solar efficiencies using Keithley Source Meter 2400.

3. Results and discussion

3.1. XRD measurement

The XRD patterns of PS and ClAlPc/PS prepared at constant current density of 30 mA/cm^2 with etching times 10 and 60 min is shown in Fig. 1 A and B respectively.

In Fig. 1A, the characteristic peaks at 2θ = 24.82° and 64.77° depict the porous nature of silicon, which are identified as (111) and (404) plane respectively and are in agreement with JCPDS (27-1402) values [4]. The peak 2θ = 6.31° for ClAlPc in Fig. 1B agrees well with the reported value [5] and identified as the (2 0 0) plane of α–phase structure and the lattice spacing d = 12.88 Å. Additionally, it is noted that the intensities of the peaks increase with etching time and hence the porosity, as the porosity increases with etching time [6]. The broadened

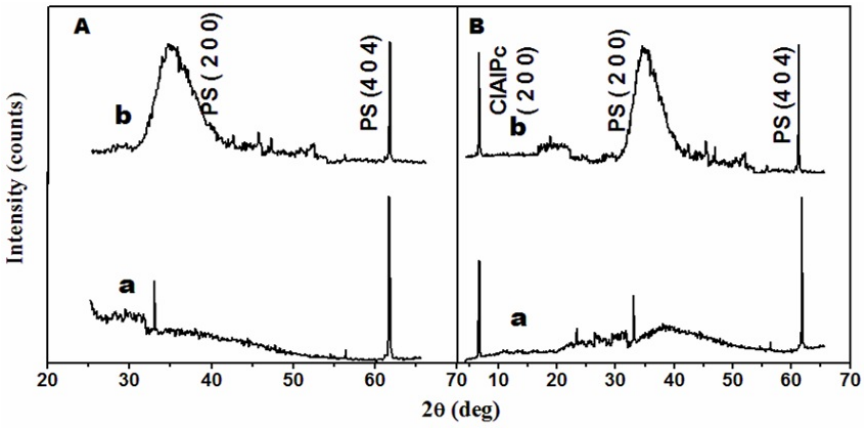

FIG. 1. XRD Pattern of the samples prepared at 30 mA/cm^2 for (a) 10 min (b) 60 min: (A) PS (B) ClAlPc/PS

peak shown by the sample prepared at 30 mA/cm^2, 60 min indicates that it is more nanostructured in nature. The crystallite sizes calculated from Scherrer's approximation are in the range from 12 to 61 nm.

3.2. Scanning electron microscope

The SEM image of the PS sample is shown in Fig. 2. The porosity of the sample increases with increasing etching time [6]. The porosities calculated from gravimetric method were shown to range from 55% to 78%.

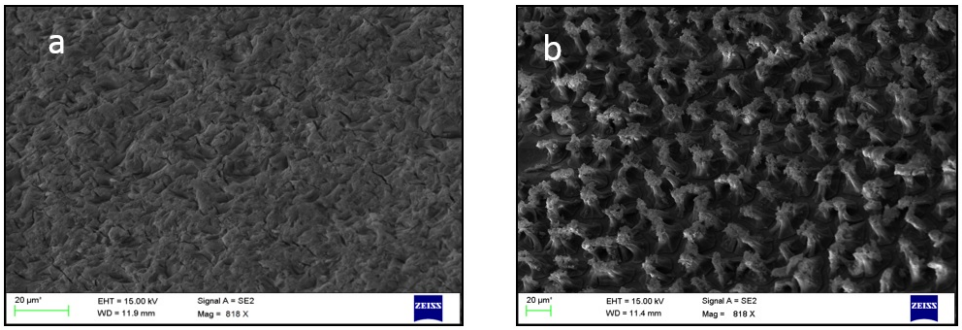

FIG. 2. SEM image of PS samples prepared at 30 mA/cm^2 for etching time (a) 10 min (b) 60 min

3.3. Optical measurements

The optical band gap measurements were carried out using UV absorption and PL emission for PS and ClAlPc/PS samples at room temperature. The PL emission spectra of PS and ClAlPc/PS samples are shown in Figs. 3A and 3B respectively. The calculated band gaps from PL and UV measurement are shown in Table 1. The values are in good agreement with each other.

The band gaps of the PS samples are blue shifted from the bulk silicon (1.1 eV). Also, the band gaps of the PS samples are slightly blue shifted with increased etching time. This shift in band gap (band gap widening) is because of quantum confinement due to reduction in the size of the Si nanocrystallites for increased etching time [7]. The decrease in crystallite size is attributed to the increase in porosity with increased etching time [8]. The PL intensity of the PS samples increases with increasing etching time due to the increase in the total volume of the nanocrystallites on the surface of the PS [9, 10].

For the dye sensitized PS (ClAlPc/PS), the PL emission is shifted to 735 nm (Fig. 3B(a)) compared to the PS sample which is attributed due to the presence of chlorine in the dye. The decrease in PL intensity shown by ClAlPc/ PS with increasing etching time is explained due to the enhanced absorption with an increase in porosity and confinement of particles into a lower dimension [11]. The minimum emission intensity shown by ClAlPc/PS at a current density of 30 mA/cm^2 with etching time of 60 min (Fig. 3B) indicates that it is a good absorber of radiation and can be used for solar cell application.

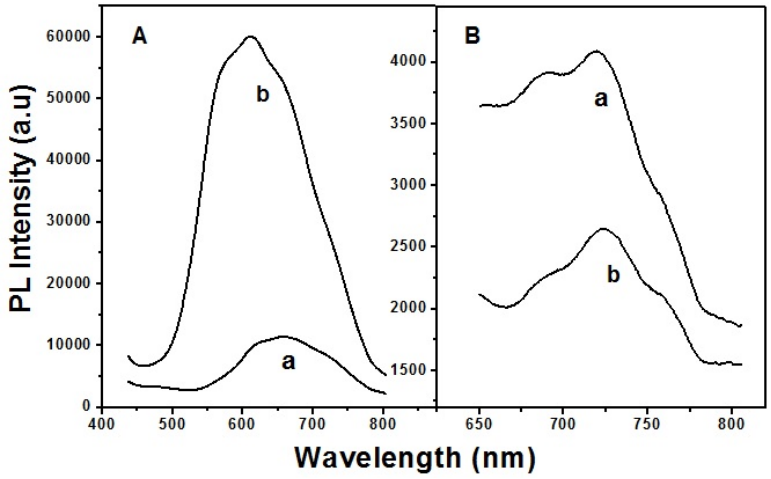

FIG. 3. Photoluminescence spectra of PS samples prepared at 30 mA/cm^2 for (a) 10 min (b) 60 min: (A) PS

TABLE 1. Bandgap of the samples

Etching time	Band gap (eV)			
	PS		ClAlPc/PS	
	PL	UV	PL	UV
a (10 min)	1.81	1.81	1.60	1.59
b (60 min)	2.02	2.05	1.76	1.77

3.4. I-V Measurements

Performance of DSSCs (1 cm^2 size) was analyzed by current–voltage (I–V) characteristics. Photocurrents and voltages were measured using a Keithely source meter 2400, with an 80 W halogen lamp and AM 1.5 G. The conversion efficiency of the samples is given in Table 2. The literature value of conversion efficiency of ClAlPc/TiO_2 is 2.1% [12].

TABLE 2. Conversion efficiency of the ClAlPc/PS samples (Current density 30 mA/cm^2)

	Porosity of PS (%)	Efficiency (%)
a (10 min)	55	0.84
b (60 min)	78	2.84

4. Conclusion

Nanostructured porous silicon (PS) samples were prepared at constant current density of 30 mA/cm^2 at etching times of 10 and 60 min. The samples were characterized by XRD, UV-Vis and PL emission techniques. The band gap increases with increased etching time. To study the effect of dye sensitizer, the surface of these PS samples was sensitized with derivative of Chloroaluminum Pc (ClAlPc). The dependence of absorption and emission intensities on these samples indicate that ClAlPc /PS prepared at current density of 30 mA/cm^2 with 60 min etching time is good absorber of radiations. The DSSC prepared by ClAlPc /PS shown a maximum conversion efficiency of 2.8% and can be used for solar cell applications.

Acknowledgement

The authors acknowledge the University Grant Commission (UGC), India, for financial support in the form of Major research project (F.No.41-941/2012 (SR)).

References

[1] Regan B.O., Gratzel M. Low-Cost, High Efficiency Solar Cell Based on Dye Sensitized Colloidal TiO_2 Film. *Nature*, 1991, **353**, P. 737–739.
[2] Smith R.L., Collins S.D. Porous silicon formation mechanisms. *Journal of Applied Physics*, 1992, **71**(8), P. R1–R22.
[3] Azim-Araghi M.E., Krier A. The influence of ammonia, chlorine and nitrogen dioxide on chloro-aluminium phthalocyanine thin films. *Appl. Surf. Sci.*, 1997, **119**, P. 260.
[4] Hadi H.A., Ismail R.A., Habubi N.F. Fabrication and characterization of porous silicon layer prepared by photo-electrochemical etching in CH_3OH:HF solution. *International Letters of Chemistry. Physics and Astronomy*, 2013, **3**, P. 29–36.
[5] Jafari M.J., Azim-Araghi M.E. Gholami M. Chemiresistive Electrical Properties Of Chloroaluminum Phthalocyanine Nanostructured Thin Films. *Optoelectronics And Advanced Materials*, 2012, **6**(9-10), P. 868–874.
[6] Khaldun A., Salman Z. Hassan., Khalid Omar. The effect of etching time of porous silicon on solar cell performance. *Journal of Superlattices and Microstructures – Elesvier*, 2011, **50**, P. 647–658.
[7] Azim-Araghi M.E., Karimi-Kerdabadi E., Jafari M.J. *Eur. Phys. J. Appl. Phys.*, 2011, **55**, P. 302–303.
[8] Srinivasan R., Jayachandran M., Ramachandran K. Photoacoustic studies on optical and thermal properties of p-type and n-type nanostructured porous silicon for (100) and (111) orientations. *Cryst. Res. Technol.*, 2007, **42**(3), P. 266–274.
[9] Kadhim Raheem G., Ismail Raid A., Abdulridha Wasna'a M. Structural, Morphological, Chemical and Optical Properties of Porous Silicon Prepared By Electrochemical Etching. *International Journal of Thin Films Science and Technology*, 2015, **4**(3), P. 199–203.
[10] Kim D.A., Shim J.H., Cho N.H.. PL and EL features of p-type porous silicon prepared by electrochemical anodic etching. *Appl. Surf. Sci.*, 2004, **234**, P. 256–261.
[11] Jayachandran M., Paramasivam M., Murali K.R., Trivedi D.C., Raghavan M. Synthesis Of Porous Silicon Nanostructures For Photoluminescent Devices. *Materphys. Mech.*, 2001, **4**, P. 143.
[12] Walter M.G., Rudine A.B., Wamser C.C. Porphyrins and phthalocyanines in solar photovoltaic cells. *J. Porphyrins Pthalocyanine*, 2010, **14**, P. 759–762.

NANOSYSTEMS: PHYSICS, CHEMISTRY, MATHEMATICS, 2016, 7 (4), P. 633–636

TiO_2 based dye-sensitized solar cell using natural dyes

J. Kalaivani[1], K. Renukadevi[2], K. Ramachandran[3], R. Srinivasan[1,*]

[1]Department of Physics, Thiagarajar College, Madurai–625009, India

[2]Department of Physics, G. Venkataswamy Naidu College, Kovilpatti–628502, India

[3]School of Physics, Madurai Kamaraj University, Madurai–625021, India

renu_kritto@yahoo.com, thirumalchandran@gmail.com, *r_srini2067@yahoo.co.in

PACS 88.40.hj, 83.80.Mc, 78.66.Qn **DOI 10.17586/2220-8054-2016-7-4-633-636**

Nanostructured TiO_2 thin films were prepared for various thicknesses on fluorine – doped tin oxide (FTO) conductive glass by the spin coating method. Anthocyanin dye was used to sensitize the sample. The structural characterization was done by XRD. The bandgaps from UV–Vis and photoluminescence measurements are in the range of 2.41 to 2.59 eV. The photocurrent and photovoltage of the cells was measured using Keithley source meter. A maximum conversion efficiency of 0.27 % was observed and the results were discussed.

Keywords: Dye sensitized solar cells, natural dyes, TiO_2 film.

Received: 5 February 2016

Revised: 20 June 2016

1. Introduction

Dye-sensitized solar cells (DSSC) are expected to be used for future clean energy [1, 2] and are usually composed of a dye-capped nanocrystalline porous semiconductor electrode, a metal counter electrode, and a redox electrolyte containing iodide and triiodide ions. The performance of the cell is primarily dependent on the material and quality of the semiconductor electrode and the sensitizer dye used for the fabrication of the cell. In DSSC, the sensitizer (dye) plays a key role in absorbing sunlight and transforming solar energy into electric energy. Numerous metal complexes and organic dyes have been synthesized and utilized as sensitizers. By far, the highest efficiencies for DSSC have been obtained using Ru-containing sensitizer compounds absorbed onto Nano crystalline TiO_2 reached 11–12 % [3, 4]. Although, such DSSC have provided a relatively high efficiency, they are costly, as the resources are limited in quantity. On the other hand, organic dyes are cheaper and are reported to attain efficiencies as high as 9.8 % [5]. The advantages of natural dyes include their easy availability, environmental friendliness and low cost. In this paper, we report the performance of natural anthocyanin, obtained from black rice extraction. This compound would be used as the dye, since anthocyanin has good chemical bonding with titanium dioxide [6].

2. Experimental procedure

The solvent used to extract dye was prepared by using ethanol, acetic acid and distilled water with molarity ratio about 3:2:1. The blackrice was mixed in the solvent, then the mixture was stirred at 50 °C for 30 minutes, the solution formed was filtered by filter paper, to obtain dark-red solution of anthocyanin dye. TiO_2 nanoparticles of 0.2 g is blended using an agate mortar with 0.4 ml nitric acid solution (0.1 M), 0.8 g polyethylene glycol (MW–10,000) and one drop of nonionic surfactant (Triton X–100) to obtain porous TiO_2 film on FTO plate [7]. The blending process was continued using an ultrasonic bath for 30 minutes until it forms thick paste without any clots. A piece of conductive glass (FTO) is selected and placed on a metal sheet. A scotch tape at four sides was used as masking material on the conductive layer restricts the thickness and area of the paste. Then various thicknesses of TiO_2 thin films are coated over FTO plate by spin coating method for various rpm rates (3000, 4000, 5000 and 6000). Later, the plate is sintered at 450 °C for 2 hours under thermal furnace module. The thicknesses of the sample were measured using optical thickness profilometer and the sintered TiO_2 thin films were immersed in natural dyes for 24 hours, allowing the natural dye molecules to be adsorbed onto the surface of TiO_2 nanoparticles. The DSSC photo electrode (TiO_2/anthocyanin) is ready for testing. The samples were characterized by XRD, PL and UV techniques. Finally, the DSSCs were fabricated with platinum as a counter electrode and potassium iodide as liquid electrolyte.

3. Results and discussion

3.1. Structural characterization (XRD)

Various thickness of TiO_2 on FTO plate were deposited using spin coating method and it was found that the thickness of the sample decreases with increased rpm. The XRD patterns of the samples TiO_2 and TiO_2/anthocyanin for various thicknesses are shown in Fig. 1A and 1B respectively. The thickness of the samples was measured using an optical thickness profilometer. In Fig. 1A, the characteristic peaks at 27 °(110), 37 °(301) and 54 °(211) reveal the formation of ructile phase of TiO_2 (JCPDF card No: 73-1765) [8]. The nature of XRD peaks reflect that the nanoparticles are crystalline. Furthermore, the intensity of peak corresponding to (1 1 0) plane decreases with decreased thickness (Fig. 1A). After the absorption of anthocyanin dye, the peak corresponding to the plane (2 2 1) disappears and the peak corresponding to (1 1 0) decreases due to the formation of chemical bonding between TiO_2 and anthocyanin dye molecules (Fig. 1B) [6]. The thickness and XRD parameters are listed in Table 1.

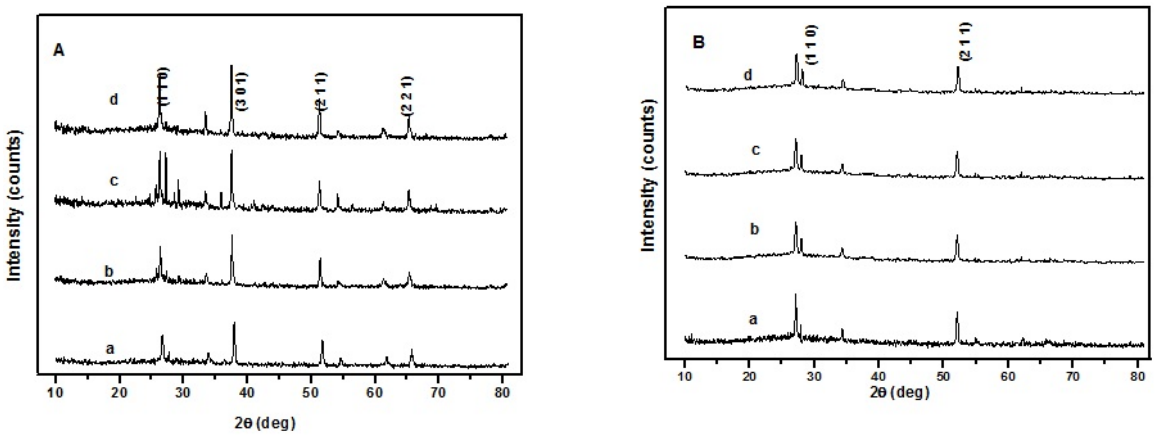

FIG. 1. XRD pattern of the samples prepared at the rpm of a) 3000; b) 4000; c) 5000; d) 6000: A) TiO_2; B) TiO_2/anthocyanin

TABLE 1. Thickness, Lattice Constant, Crystallite size of TiO_2 sample prepared at different rpm

Rotation per minute	Thickness (μm)	Lattice constant (Å)	Crystallite size (nm)
3000	18.62	4.58	27
4000	10.18	4.57	25
5000	7.36	4.56	22
6000	4.78	4.55	21

3.2. Optical measurements

The PL spectra of TiO_2/anthocyanin samples are shown in Fig. 2. The bandgaps, calculated from UV – absorption and Photoluminescence emission spectra of the samples, are given in Table 2. The bandgaps of the prepared samples (2.59 to 2.41 eV) lie in the required range of preparation for solar cells. The intensity of the PL spectra increases with increase in rpm, whereas the bandgaps of the samples decrease due to the decrease in crystallite size [9].

3.3. I–V characterization

The photovoltaic tests of the prepared DSSCs using natural dye extracts as sensitizer were carried out by I–V measurements. Photocurrents and voltages were measured using a Keithley source meter 2400, with a 80 W halogen lamp and AM 1.5 G. The quality of the solar cell is determined by a parameter called solar cell efficiency, which is simply defined by a ratio:

$$\eta = \frac{P_{max}}{P_L} \tag{1}$$

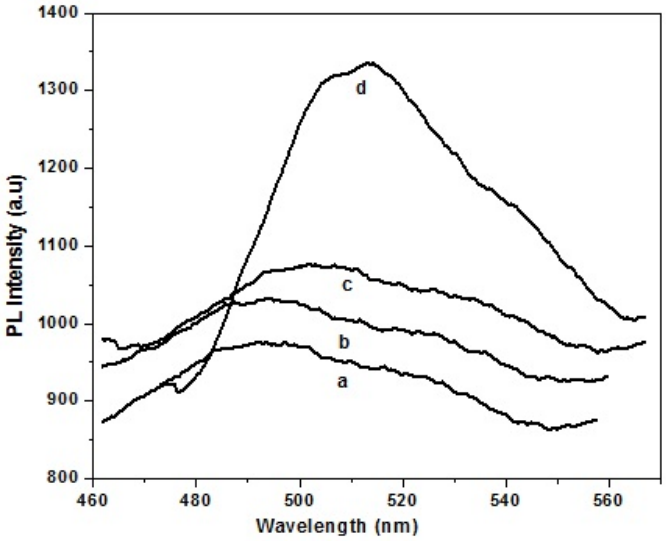

FIG. 2. PL spectra of TiO_2/anthocyanin samples prepared at the rpm of a) 3000; b) 4000; c) 5000; d) 6000

TABLE 2. Bandgap values of TiO_2/anthocyanin samples from PL and UV measurement

Rotation per minute	Band gap (eV)	
	PL	UV
3000	2.57	2.59
4000	2.52	2.52
5000	2.47	2.46
6000	2.41	2.41

where P_{max} is the maximum solar cell power and P_L is power of the incident light. Thus, solar cell efficiency and P_{max} are associated by a linear dependence. The conversion efficiencies were measured and calculated, the results are summarized in Table 3. The fill factor of the sample increases with decrease in thickness of the sample. This increase in fill factor causes increase in efficiency of the DSSCs.

TABLE 3. Conversion Efficiencies of the DSSCs prepared by Natural dyes

Rotation per minute	Thickness (μm)	Fill Factor	Conversion Efficiency (%)
3000	18.62	0.46	0.12
4000	10.18	0.58	0.13
5000	7.36	0.70	0.20
6000	4.78	4.28	0.27

4. Conclusion

The synthesized nanostructured porous TiO_2 samples were sensitized using anthocyanin dye. The structural characterization was done by XRD. The XRD pictures showed the features of TiO_2 and the effect of anthocyanin dye (blackrice). The bandgaps calculated from the UV absorption spectrum are in the range 2.41 to 2.59 eV, which is in agreement with PL measurements. The bandgap decreases with increased RPM's. The suitability of these samples for solar cell applications and sensors were studied and the samples were optimized using UV absorption. The DSSC prepared at the ratio 6000 rpm showed the highest efficiency of 0.27 %.

References

[1] Grätzel M. Dye-sensitized Solar cells. *J. Photochem. Photobiol., C. Photochem. Rev.*, 2003, **4**, P. 145–153.
[2] Law M., Greene L.E., Johnson J.C., Saykally R., Yang P. Nanowire dye-sensitized solar cells. *Nat. Mater.*, 2005, **4,** P. 455–459.
[3] Chiba Y., Islam A., Watanabe Y., Komiya R., Koide N., Han L.Y. Dye-Sensitized Solar Cells with Conversion Efficiency of 11.1%. *Jpn. J. Appl. Phys.*, 2006, **45**, P. L638–L640.
[4] Buscaino R., Baiocchi C., Barolo C., Medana C., Grätzel M., Nazeeruddin Md.K., Viscardi G. A mass spectrometric analysis of sensitizer solution used for dye-sensitized solar cell. *Inorg. Chim. Acta*, 2008, **361**, P. 798–805.
[5] Zhang G., Bala H., Cheng Y., Shi D., Lv X., Yu Q., Wang P. High efficiency and stable dye-sensitized solar cells with an organic chromophore featuring a binary π-conjugated spacer. *Chem. Commun.*, 2009, P. 2198–2200.
[6] Hao S., Wu J., Huang Y., Lin J. Natural dyes as photosensitizers for dye-sensitized solar cell. *Solar Energy*, 2006, **80**(2), P. 209–216.
[7] Kim S., Lee J.K., Kang S.O., Ko J.J., Yum J.H., Fantacci S., De Angelis F., DiCenso D., Nazeeruddin Md.K., Grätzel M. Molecular Engineering of Organic Sensitizers for Solar Cell Applications. *Journal of American Chemical Society*, 2006, **128**, P. 16701–16707.
[8] Sanjay Chakane, Anisha Gokarna, Bhoraskar S.V. Metallophthalocyanine coated porous silicon gas sensor selective to NO_2. *J.Sensors and Actuators B*, 2003, **92**, P. 1–5.
[9] Azim-Araghi M.E., Karimi-Kerdabadi E., Jafari M.J. *Eur. Phys. J. Appl. Phys.*, 2011, **55**, P. 302–303.

NANOSYSTEMS: PHYSICS, CHEMISTRY, MATHEMATICS, 2016, 7 (4), P. 637–642

ZnS nanoparticles decorated graphene nanoplatelets as immobilisation matrix for glucose biosensor

G. Suganthi[1], T. Arockiadoss[2], T. S. Uma[1*]

[1]Bio products laboratory, Central Leather Research Institute, Adyar, Chennai 600 036, Tamil Nadu, India
[2]Department of physics, Madurai Kamaraj University, Madurai 625021, Tamil Nadu, India
Shugankarthick@gmail.com, arockiados@gmail.com, tsuma@clri.res.in

PACS 87 **DOI 10.17586/2220-8054-2016-7-4-637-642**

A glucose biosensor has been fabricated by using ZnS nanoparticle-substituted graphene nanosheets. Thermally exfoliated graphene nanosheets act as a suitable support for the deposition of ZnS nanoparticles. In this work, graphene was functionalized with ZnS nanoparticles by a simple chemical reduction method. The synthesized G/ZnS nanoparticles have been characterized using X-ray diffractometry (XRD), Transmission electron microscopy (TEM), scanning electron microscopy (SEM), energy dispersive spectroscopy (EDS), FT-IR techniques. Aditionally, the Glucose biosensor has been constructed by drop-casting G/ZnS over a conductive carbon support followed by the deposition of Glucose oxidase (GOx) over a G/ZnS electrode. The performance of the biosensor was investigated by an electrochemical method. The resultant bioelectrode retains its biocatalytic activity and offers fast, highly-sensitive glucose quantification and a shelf-life of about 10 weeks under refrigerated conditions.

Keywords: Glucose oxidase, ZnS nanoparticles, graphene, enzymatic, biosensor.

Received: 5 February 2016

1. Introduction

Estimation of glucose level in blood is considered as very important for patients suffering from diabetes, heart diseases, chronic kidney failure and other disorders that require continuous glucose monitoring [1, 2]. Hence, in recent years, the demand has grown in the field of medical diagnostics for simple and disposable devices that also demonstrate fast response time, user-friendliness, cost-efficiency, and are suitable for mass production [3, 4]. Biosensor technologies offer the potential to fulfill these criteria through an interdisciplinary combination of approaches from nanotechnology, chemistry and medical science. Among the various analytical methods, enzymatic methods offer several advantages in terms of rapid determination, sensitivity and selectivity [5].

The immobilization of enzymes is the most critical step in biosensor fabrication, and thus, confers many operational advantages including high selectivity and possible modulation of the catalytic properties. Carbon-based nanomaterials are popularly used in electrochemical method due to its large surface area, excellent electrical and mechanical properties for enzyme loading and direct electron transfer to obtain low detection limits [6, 7]. Glucose oxidase (GOx), a highly specific enzyme, is most widely employed of all enzyme-based glucose biosensors. It catalyzes the oxidation of glucose to gluconolactone and hydrogen peroxide.

Among the various metal nanoparticles, zinc sulfide nanoparticles are an interesting material with a high isoelectric point that allows easy immobilization of an enzyme (with a low Isoelectric point) through electrostatic interaction [8, 9]. Furthermore, its high chemical stability and non-toxic nature, as well as its biocompatibility and high electron transfer capability make ZnS a promising material for building an enzymatic sensor by immobilizing the appropriate biomolecules without electron mediators [10, 11].

Graphene, a nanostructure of carbon, is a two-dimensional honeycomb crystalline single layer lattice of carbon [12, 13]. It has received enormous interest in various areas of research owing to its large specific surface area, extraordinary electrical and thermal conductivities, high mechanical stiffness, good biocompatibility and low manufacturing cost. The biocompatibility, high conductivity, and the large surface area of graphene have made it an ideal candidate in the development of bio-electronic devices. The large surface area and excellent electrical conductivity of graphene allow it to act as an "electron wire" between the redox centers of an enzyme or protein and an electrode's surface. Rapid electron transfer facilitates accurate and selective detection of biomolecules [14, 15].

Currently, a wide variety of electrode devices are available for electrochemical determination. Toray Carbon paper (GDL) has received much attention in several electrochemical applications such as biofuel cells, super-capactiors, batteries and biosensors, owing to its large surface-volume ratio, high porosity and good electrical conductivity [16].

Herein, we present the design and fabrication of Carbon paper (CP) macro-substrate/Graphene(G)/ZnS based electrodes. The results show good performance, fast response times, nice stability and reproducibility, and low

detection limits for the ZnS/G nanocomposite based on the reduction of H_2O_2 by immobilized glucose oxidase on the composite.

2. Materials and Methods

2.1. Materials

Glucose oxidase (GOD, type x-s from Aspergillus niger), D-(+)-glucose, Flake graphite powder (99.99 % SP-1, Bay carbon, average particle size 45 mm), were purchased from Sigma Aldrich. Carbon paper (TGPH-60) was obtained from Toray Ind., Hydrogen peroxide (H_2O_2, 30 % wt/V) was purchased from Fisher scientific. Concentrated sulfuric acid (H_2SO_4, 99 %), concentrated nitric acid (HNO_3, 98 %), potassium permanganate ($KMnO_4$) were obtained from Rankem Chemicals, India and used without further purification. Zinc sulfide nanoparticles were prepared by an aqueous chemical method using zinc chloride ($ZnCl_2$) and Sodium Sulfide (Na_2S). 0.1M phosphate buffer solution (PBS, pH 7) prepared using were prepared by mixing stock standard solution of K_2HPO_4. The aqueous stock solution of KH_2PO_4 was prepared using deionized water (DI water). The common chemicals used for the preparation of buffers, etc., were of analytical reagent grade. All the electrochemical studies and synthesis were performed using deionized (DI) water.

2.2. Synthesis of Graphene (G)

Graphene was synthesized according to thermal exfoliation method using GO as the precursor [12]. Thermal exfoliation was done in a quartz tube at 800 °C. For dispersing metal nanoparticles over graphene, the as-prepared graphene (G) was functionalized by continuous stirring in a solution of concentrated sulfuric and nitric acids (3:1) for 30 min.

2.3. Synthesis of ZnS/G nanocomposite

Zinc chloride and sodium sulfide was taken such that the ratio between the ZnS produced and the f-G is 3:7. In a typical preparation, functionalized graphene and 1 M zinc chloride was prepared in 100 ml of deionized water. Then solution of 1 M sodium sulfide was added dropwise to the magnetically stirred mixture at 70 °C, which resulted in formation of ZnS/f-G nano-colloid. The suspension was filtered and washed several times with DI water and finally the residue was dried in a vacuum oven at 60 °C.

2.4. Materials characterization techniques

The crystallinity of the synthesized material was characterized by X-ray diffraction technique using PANalytica X'pert pro X-ray diffractometer with Cu-Kα as the X-ray source. The surface morphology of the sample was examined by SEM (FEI, Quanta 3D) and TEM (TECNAI G F20,S-TWIN). Electrochemical studies were carried out by CH Instrument, electrochemical workstation with a three-electrode electrochemical cell comprising a ZnS/G modified carbon paper electrode as the working electrode, a Pt wire as the counter electrode and a Ag/AgCl (1 M KCl solution) as the reference electrode. PBS was used as the supporting electrolyte for all the electrochemical studies at ambient temperature.

2.5. Fabrication of the Bioelectrodes

The bioelectrode was fabricated over the Carbon paper electrode (CPE). The electrode was modified by a simple drop casting method. First, 1 mg/ml graphene (G) solution was prepared by ultrasonication of 1 mg of G in 1 ml of 0.5 % nafion solution. Nafion gives better dispersion as well as stability to the graphene (G). About 15 μl of the solution was dropped over the surface of carbon paper electrode and allowed to dry at room temperature. 10 μl of GOD was film cast over the dried G film. Finally, another 5 μl layer of NA was dropped and allowed to dry and kept at 4 °C to preserve the enzyme activity. The similar procedure was used for fabricating ZnS/G electrode. The fabricated electrodes will be termed as f-G/GOD/NA/CPE and Au/f-G/GOD/NA/CPE from here onward.

3. Results and discussion

3.1. XRD and FT-IR studies of the samples

The XRD pattern of the hybrid composite has been compared with the starting material. Fig. 1 depicts the XRD pattern of (a) ZnS and (b) ZnS-G. Well resolved crystalline peaks appear at 13.15 °, 21.8 °, 26.6 °, 31.6 °, 40.5 ° and 55 ° corresponding to ZnS nanoparticles [10]. Fig. 1(b) shows the diffraction peaks appear at 29.0 °, 33.5 °, 48.1 ° and 57.0 ° (JCPDS No. 05-0566) corresponding to ZnS nanostructure along with C (002) peak. This indicates the successful functionalization of graphene with ZnS nanoparticles.

The compatibility study was carried out using a Perkin Elmer FTIR spectrophotometer in the region of 4000 to 500 cm^{-1}. Spectra for ZnS, graphene and their admixture were obtained and compared. In the Fig. 2(b) FTIR spectra exhibit strong bands appearing in 643, 947, 1129, 1410, 1629 and 3419 cm^{-1}, corresponding to ZnS nanoparticles [11]. The peak at 612 cm^{-1} is assigned to the ZnS band (i.e., corresponding to sulfides). The O–H bending region due to absorbed water appear at 1629 cm^{-1} and O–H stretching at 3419 cm^{-1}. From FT-IR spectroscopy shown in Fig. 2(c), it is clear that several types of functional groups, particularly carbonyl and hydroxyl groups have been generated on acid-oxidized graphene sheet surfaces as expected [13]. Examination on surfaces of acid oxidized graphene was carried out using a Fourier transform infrared (FT-IR) spectrophotometer to ensure formation of desired surface functional groups. The absorption spectra at 3441 cm^{-1} exhibit OH stretching and OH-bending at 1624 cm^{-1}. Hence, the information provided there indicates uniform distribution of ZnS nanoparticles on the graphene surface.

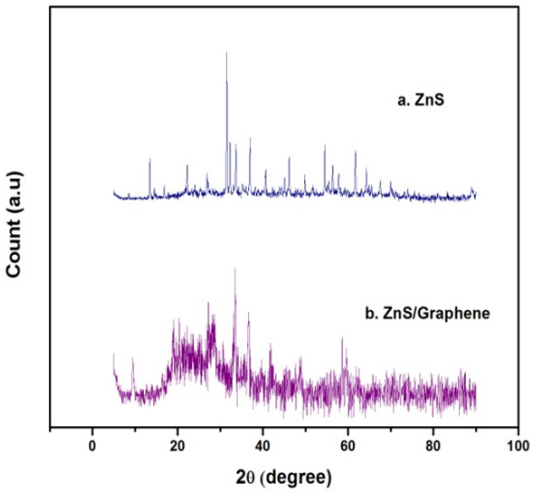

FIG. 1. XRD of ZnS and ZnS/Graphene

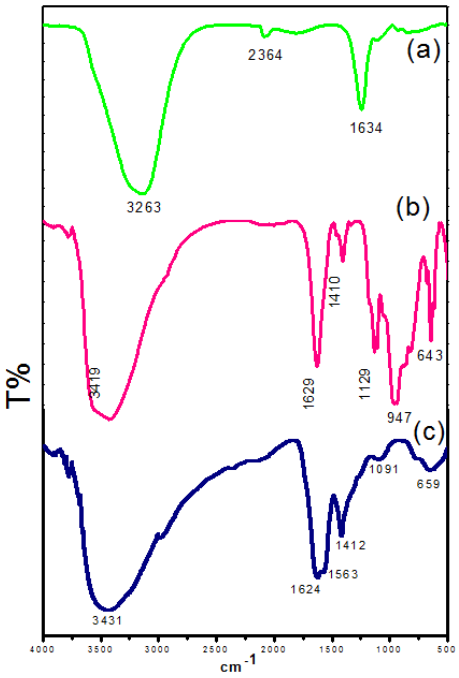

FIG. 2. FTIR spectra of (a) ZnS/G (b) ZnS and (c) G

3.2. SEM and TEM analysis of the samples

The surface morphology of the samples was studied by electron microscopy. SEM and TEM images of G and ZnS/G composites at different resolutions reveal the 2D structure of G sheets and the uniform distribution of ZnS nanoparticles on the surface of G with low and high magnification, as shown in Figs. 3 & 4. Energy dispersive X-ray analysis (EDX) results demonstrate the presence of ZnS in the corresponding samples [10].

Figure 5(a) illustrates that EDX of graphene shows the weight percentage of carbon 93.64 % and oxygen 06.36 % and Fig. 5(b) shows the edax of ZnS decorated graphene nanocomposites shows the weight percentage of carbon 71 %, oxygen 3 %, Zinc 22 % and Sulphur 4 % present in the corresponding samples.

The EDX results explains the composition of elements such as C, O, S and Zn for the corresponding samples and discussed above.

3.3. Electrochemical activity towards H_2O_2

The collective electro-catalytic effect of nanoparticles and graphene towards H_2O_2 is well-documented in the literature. In the present study, the enzymatic generation of hydrogen peroxide is achieved in the reaction layer of the G or (G/ZnS) film. In order to investigate the electro-catalytic performance towards the electrochemical reaction of hydrogen peroxide at the G or (G/ZnS) film, cyclic voltammetry (CV) has been performed. The CVs with ZnS and G/ZnS film modified CPE before and after addition of 10 μM H_2O_2 in 0.1 M phosphate buffer solution (pH 7) are shown in Figs. 6 and 7. The two electrodes show only a small background current in the

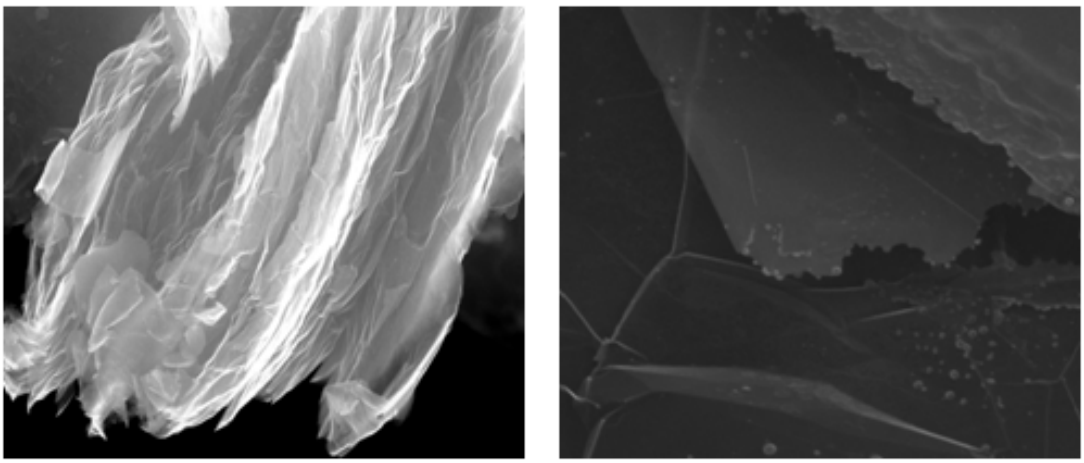

(A) (B)

FIG. 3. SEM images of (A) G and (B) ZnS/G

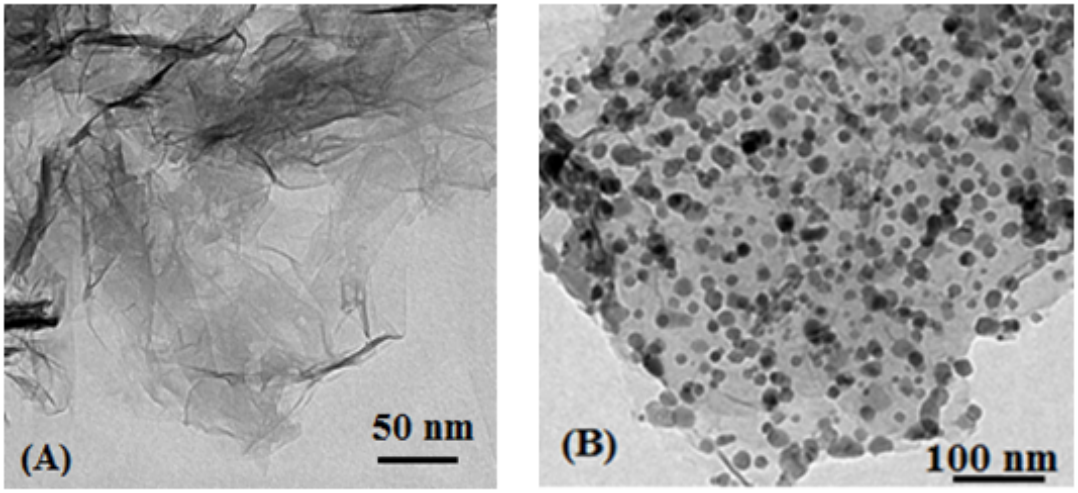

FIG. 4. TEM Images of (A) G and (B) ZnS/G

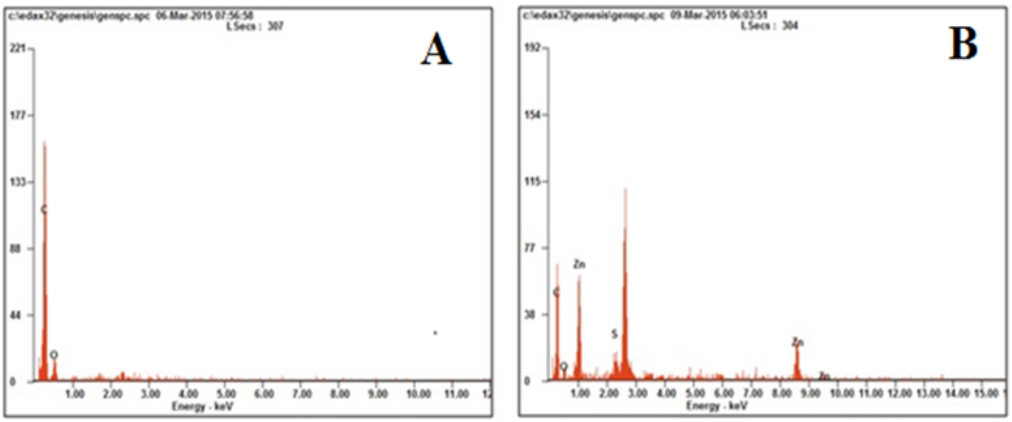

FIG. 5. EDX spectra of (A) G and (B) ZnS/G

absence of hydrogen peroxide. Upon addition of hydrogen peroxide, the CV of G/ZnS modified electrode changed with obvious increase of the current relative to that of G. A pair of well-defined redox peaks appears with G/ZnS electrode. This is due to the high electron transfer rate of the G/ZnS/GOD/NA/CP electrode, high aspect ratio and huge working surface area of the nanocomposite.

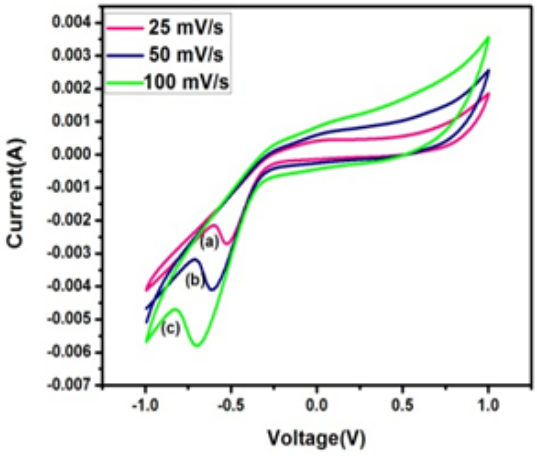

FIG. 6. CV of G/GOD/NA/CPE in 0.1 M PB solution (pH 7) containing 0.3 mM H_2O_2 at a scan rate of (a) 25 mV/s; (b) 50 mV/s; (c) 100 mV/s

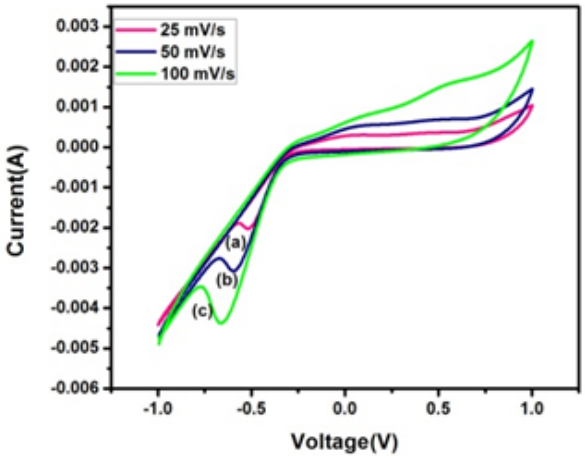

FIG. 7. CV of ZnS/G/GOD/NA/CPE in 0.1 MPB solution (pH 7) containing 0.3 mM H_2O_2 at a scan rate of (a) 25 mV/s; (b) 50 mV/s; (c) 100 mV/s

3.4. Electrochemical activity towards glucose

Figures 8 & 9 illustrates the CV responses of G/GOD/NA/CPE and G/ZnS/GOD/NA/CPE with the addition of 100 μM glucose recorded at a scan rate of 25, 50 and 100 mV/s. G/ZnS/GOD/NA/CPE exhibits a couple of redox peaks versus Ag/AgCl reference electrode, showing the potential characteristic of graphene. An increase in current has also been observed from the CV curve of ZnS/G/GOD/NA/CPE with glucose in PBS compared to ZnS/ChOx/NA/GCE with glucose in PBS. The origins of well-defined redox peaks from the CV curve of G/ZnS/GOD/NA/CP electrode in PBS with 100 μM glucose is due to the H_2O_2 generation during the oxidation of glucose by GOD. In addition to this, because of high surface area of G/ZnS, GOD attached to the surfaces of G/ZnS facilitates the fast and direct electron transfer between the active sites of immobilized GOD and electrode surface which leads to well-defined peaks. Therefore, glucose is efficiently detected with the G/ZnS/GOD/ NA/CPE.

4. Conclusions

Graphene nanosheets have been successfully substituted with ZnS nanoparticles and GOD has been immobilized on the G-ZnS/CP electrode. The incorporation of Graphene into the electrode increases the surface area and serves as an excellent support for ZnS nanoparticles that effectively catalyze redox reactions involving H_2O_2. In addition, the combination of G and ZnS nanoparticles facilitates the low potential amperometric detection of glucose and exhibits both good reproducibility and long-term stability of the biosensor, thereby providing a suitable platform for biosensor design and other biological applications.

Acknowledgements

We are grateful to The Director, CLRI, Chennai, for his kind permission to publish this work.

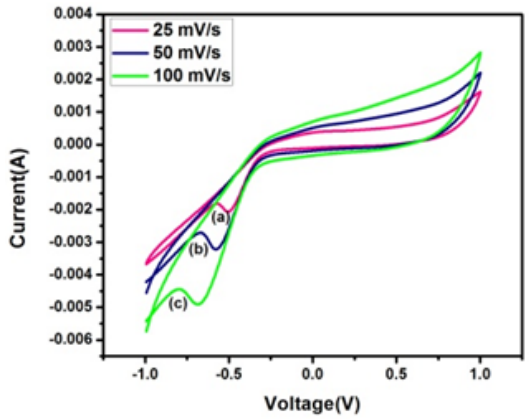

FIG. 8. CV of G/GOD/NA/CPE in 0.1 M PB solution (pH 7) containing 100 μM cholesterol at a scan rate of 25, 50 and 100 mV/s

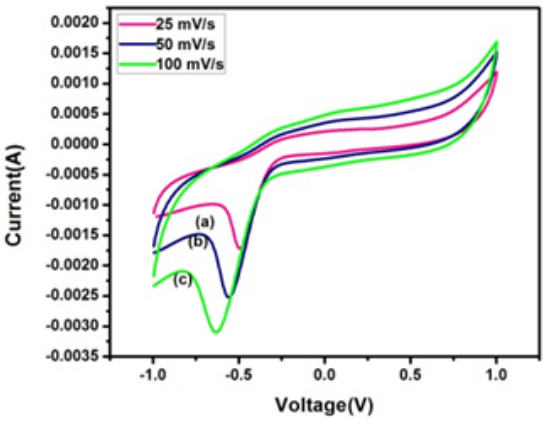

FIG. 9. CV of ZnS/G/GOD/NA/CPE in 0.1 M PB solution (pH 7) containing 100 μM cholesterol at a scan rate of 25, 50 and 100 mV/s

References

[1] Wild S., Roglic G., et al. Global prevalence of diabetes estimates for the year 2000 and projections for 2030. *Diabetes Care*, 2004, **27** (5), P. 1047–1053.
[2] American Diabetes Association. Diagnosis and classification of diabetes mellitus. *Diabetes Care*, 2003, **36** (Suppl 1), S67–S74.
[3] Bakker E., Qin Y. Electrochemical sensors. *Anal. Chem.*, 2006, **78** (12), P. 3965–3984.
[4] Luo X., Morrin A., Killard A.J., Smyth M.R. Application of nanoparticles in electrochemical sensors and biosensors. *Electroanalysis*, 2006, **18** (4), P. 319–326.
[5] Heller A., Feldman B. Electrochemical glucose sensors and their applications in diabetes management. *Chem. Rev.*, 2008, **108** (7), P. 2482–2505.
[6] Dungchai W., Chailapakul O., Henry C.S. A low-cost, simple, and rapid fabrication method for paper-based microfluidics using wax screen-printing. *Analyst*, 2011, **136** (1), P. 77–82.
[7] Nie Z.H., Nijhuis C.A., et al. Electrochemical sensing in paper-based microfluidic devices. *LabChip*, 2010, **10** (4), P. 477–483.
[8] Wang F., Hu S. Electrochemical sensors based on metal and semiconductor nanoparticles. *Microchim Acta*, 2009, **165** (2), P. 1–22.
[9] Wang J. Nanomaterial-based electrochemical biosensors. *Analyst*, 2005, **130** (4), P. 421–426.
[10] Rita J., Sasi S. Florence optical, structural and morphological studies of bean-like Zns nanostructures by aqueous chemical method. *Chalcogenide Letters*, 2010, **7** (4), P. 269–273.
[11] Xu J.F., Ji W., et al. Preparation of ZnS nanoparticles by ultrasonic radiation method. *Appl. Phys. A*, 1998, **66**, P. 639–641.
[12] Konstantin K.N., Ozbas B., et al. Raman Spectra of Graphite Oxide and Functionalized Graphene Sheets. *Nano Lett.*, 2008, **8** (1), P. 36–41.
[13] Schniepp H.C, Li J.L., et al. Functionalized single graphene sheets derived from splitting graphite oxide. *J. Phys. Chem. B*, 2006, **110** (17), P. 8535–8539.
[14] Yang W., Ratinac K.R., et al. Carbon nanomaterials in biosensors: should you use nanotubes or graphene? *Angew. Chem., Int. Ed.*, 2010, **49** (12), P. 2114–2138.
[15] Zhu Z., Garcia G.L., et al. A Critical Review of Glucose Biosensors Based on Carbon Nanomaterials: Carbon nantubes and graphene. *Sensors*, 2012, **12** (5), P. 5996–6022.
[16] Kuwahara T., Ohta H., Kondo M., Shimomura M. Immobilization of glucose oxidase on carbon paper electrodes modified with conducting polymer and its application to a glucose fuell cell. *Bioelectrochemistry*, 2008, **74** (1), P. 66–72.

NANOSYSTEMS: PHYSICS, CHEMISTRY, MATHEMATICS, 2016, 7 (4), P. 643–646

Bistable electrical switching and performance of a pentacene-based write once/read many memory device

A. G. Gayathri, C. M. Joseph

Department of Physics, Dayananda Sagar College of Engg, Shavige malleswara Hills, Kumaraswamy layout, Bangalore-560076, India

gaythri305@yahoo.com, cmjoseph@rediffmail.com

PACS 72.80.Le, 73.61.Wp, 73.61.Ph, 85.25.Hv **DOI 10.17586/2220-8054-2016-7-4-643-646**

In this paper, the performance of a pentacene-based write once/read many memory device is reported. The IV characteristics of a pentacene device deposited at 5 Å/s on an ITO-coated glass substrate was studied. This device showed a stable switching from ON to OFF state with an ON-OFF current ratio of nearly 10^3 and a retention time of 5×10^4 s with a switching threshold voltage of 3.9 V. The irreversible switching of this device makes it suitable for write once/read many memory devices. The structural studies of pentacene thin films on glass substrate were also done and the dependence of device performance on grain size is reported. Improved performance of this device due to the addition of C_{60} layer is also discussed.

Keywords: Organic semiconductor, pentacene, thin films, vacuum thermal evaporation, WORM memory.

Received: 5 February 2016

1. Introduction

In recent years, organic memory devices with an active layer sandwiched between two electrodes have attracted much attention as future information storage devices [1–5]. The demand on organic non-volatile memory devices increases rapidly due to their simplicity in device structure, good scalability, low cost potential, low power operation and large capacity for data storage. Electrical bistable switching phenomena have been observed and reported for a variety of organic materials and device structures [1–10]. Several conductance mechanisms are also reported to explain this switching phenomenon.

Different types of organic memory devices are: random access memory, re-writable memory and write once/read many memory (WORM). WORM memory is a type of non volatile memory that is capable of storing data permanently and being read from repeatedly. Thus it is potentially applicable for permanent data storage, such as wireless identification tags, smart cards, etc. Lidan Wang et al. [11] demonstrated a non volatile organic WORM memory device based on CuPc/F_{16}CuPc p–n junction. Shengwei Shi et. al. [12] fabricated an organic electrical memory device with a simple structure based on a single layer pentacene film embedded between Al and ITO electrodes. Bin Li et. al. [13] reported the impact of electrode metals on a pentacene based WORM device. They found that devices with Fe electrodes have lower threshold voltages. However, in terms of application, organic memory devices are often characterized by their performance and materials with good reliability need to be developed.

In this work, we fabricated a write once/read many memory device with vacuum evaporated pentacene on ITO coated glass substrate with aluminium as the top electrode and the performance of the fabricated device was studied and compared with a device with an additional layer of C_{60}.

2. Experimental

Figure 1(a) shows the chemical structure of pentacene molecule. Thin films of pentacene (99.999 % source powder purchased from Aldrich) were thermally deposited onto chemically cleaned glass substrates under vacuum ($\sim 2 \times 10^{-6}$ Torr) using a HIND HIVAC coating unit (Model no. 12A4D). For the devices, films were coated on to pre-cleaned ITO coated glass substrates kept at room temperature. Source material was evaporated from a molybdenum boat at a deposition rate of 5 Å/s to get a thickness of around 90 nm. Finally, aluminium was deposited thermally at a deposition rate of 20 Å/s from a tungsten basket to complete the device as in Fig. 1(b). The deposition rates and thicknesses of the deposited thin films were controlled by a quartz crystal thickness monitor. The layered structure of the device was Glass/ITO/Pentacene (5 Å/s, 90 nm)/Al (150 nm). For comparison, a layer of C_{60} was deposited on pentacene layer at a deposition rate of 5 Å/s to get a thickness of 60 nm. The overlap between the electrodes defined the dimensions of the memory cell (9 mm^2). The distance between molybdenum

source and substrate holder was about 13 cm. The electrical measurements of the fabricated device were measured using a Keithley 2400 source meter and an Agilent B1500A semiconductor device analyzer.

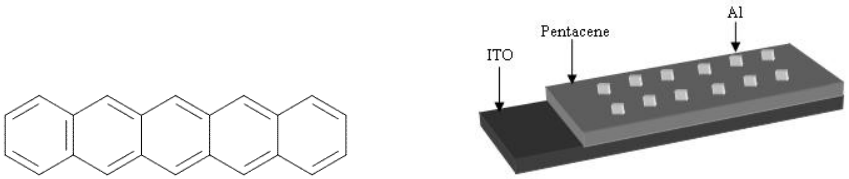

(a) (b)

FIG. 1. Chemical structure of pentacene (a) and schematic view of the fabricated pentacene device (b)

The structural studies were done using a Rigaku X-ray diffractometer. All the electrical tests were conducted at ambient conditions, without any device encapsulation and the measurements were done with a probe dimension of around 14 μm.

3. Results and discussion

3.1. Structural studies of pentacene thin films

An XRD spectrum of the pentacene thin films deposited at 5 Å/s is shown in Fig. 2. XRD pattern exhibits crystalline nature with the major diffraction peaks indexed and matches with the previous results [14, 15]. The peak was observed at $2\theta = 5.80$ which corresponds to α phase triclinic pentacene in the (001) plane. Average crystallite size was calculated using Debye-Scherrer formula [16] and was found to be 200 Å. The dislocation density was also evaluated using Williamson and Smallman's formula [16] for the deposited films and was found to be 2.5×10^{15} m^{-2}.

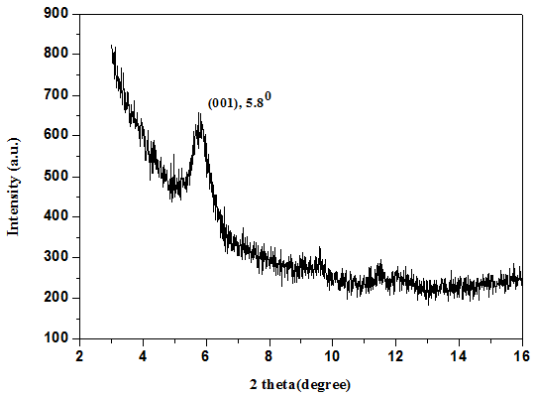

FIG. 2. X-ray diffraction patterns of pentacene thin films grown at 5 Å/s

3.2. IV characteristics of fabricated device

Figure 3(a) shows the IV plot of the device ITO/pentacene (5 Å/s)/Al for a forward and a reverse voltage sweep for 8 continuous voltage sweep cycles. The voltage was scanned from 0 V to 15 V and back to 0 V. Initially the device stayed in the high current state which is usually referred to as ON state. At a threshold voltage V_T of 3.9 V, the resistance increased suddenly from kiloohms to megaohms, indicating a sudden transition from ON state to OFF state. This hysteresis loop clearly shows the bistability of the device. The ratio of the conductivities achieved between the two states was about 10^3. After this transition, the device remained in the same state even after turning off of the power as shown in the second voltage scan. This revealed the non-volatile nature of this pentacene device. One of the important features of this device was that the switching was irreversible as reported [12, 13] and never returned to the initial off state even by applying a negative voltage pulse. This property makes it potentially suitable for a write-once/read many memory (WORM) device. For the ON state, the sweep voltage is between 0 V and 1.5 V, and the current can be measured very stably at a constant low voltage as long as the current transition has not occurred. For the high resistance state, the sweep voltage is between 0 V and 15 V.

After switching to the low current state, the device will stay in the OFF state with the next voltage sweep cycle. The voltage sweep cycles can be more for both ON and OFF states. The stability of the device under stress was evaluated in a continuous bias condition (@1V). The device showed a good performance for 5×10^4 s retention time test as shown in the Fig. 3(b).

Figure 4 compares the device performance of the device with and without C_{60} layer. Addition of C_{60} layer improved the device performance with an ON-OFF ratio 10^8 and $V_T = 3.17$ V.

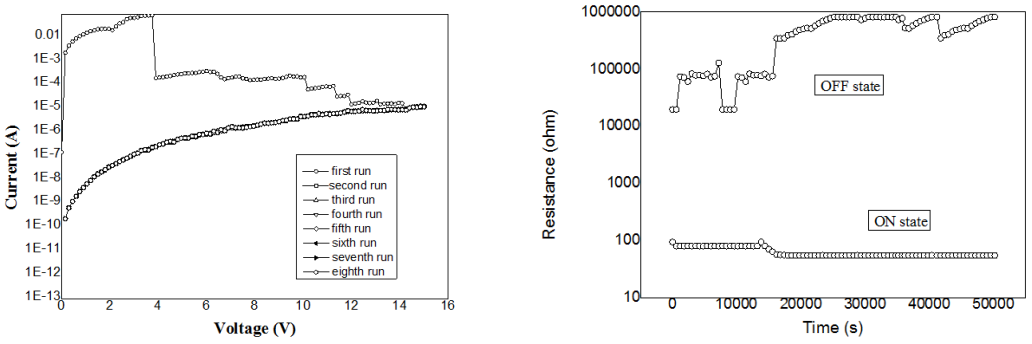

FIG. 3. (a) IV characteristics of ITO/ pentacene (5 Å/s)/Al with eight continuous voltage sweep cycles. Inset shows retention time measurements both in the ON state and OFF state (@1V). (b) Retention time measurements both in the ON state and OFF state (@1V).

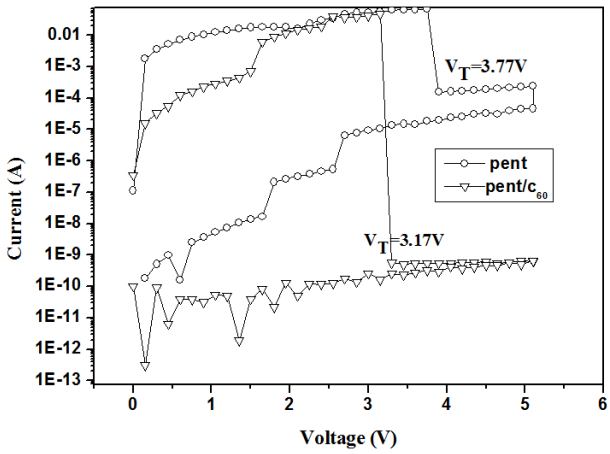

FIG. 4. Comparison of IV characteristics of ITO/Pentacene/Al and ITO/Pentacene/C_{60}/Al

The conducting mechanism of a pentacene-based WORM devices were reported earlier [11, 12]. In those devices with a structure Al/pentacene/Al, Al/pentacene/Fe and ITO/pentacene/Al, the top metal atom diffuse in to the pentacene layer under positive bias forming conductive channels responsible for high ON state. P. Aruna et al. reported the effect of fullerene doping on the electrical properties of P3HT-PCBM layers [17]. Salaoru I. et al. [6] successfully demonstrated a new donor acceptor small organic molecular pair with tetrathiafulvalene (TTF) as an electron donor and tetracyanoethylene as an electron acceptor element that determined memory behavior. The initial ON state of our devices can be explained on the basis of grain size calculation. The grain size of the films deposited at 5 Å/s was found to be more. Due to this large grain size, the metal will be diffused into the active layer, which leads to the formation of huge interface dipole layer at the electrode interface resulting in an initial high ON state. However, this interface dipole is destroyed for a large space field resulting in the decrease of the current. Addition of C_{60} layer significantly improves the device performance due to the molecular storage capability of the fullerenes, significantly enhancing the storage density capability as previously reported [5].

4. Conclusions

Bistable electrical switching of pentacene devices was studied and compared to that of a device with a C_{60} layer. The irreversible switching of these devices makes it suitable for a write once read many memory device applications. The devices with pentacene deposited at 5 Å/s showed a stable switching from low resistance state to a high resistance state. This is because as the grain size increases, the penetration of Al increases, resulting in an initial OFF state. ON-OFF ratio of the films increases from 10^3 to 10^8 with the addition of C_{60} layer. Threshold voltage decreases from 3.77 V to 3.17 V with the addition of C_{60} layer.

Acknowledgements

Financial support by Visvesvaraya Technological University (VTU), Belgaum, Karnataka, India through a grant is gratefully acknowledged. Financial support by Vision Group on Science and Technology (VGST), Department of Information Technology, Biotechnology & Science and Technology, Government of Karnataka, India through a CISE grant is also acknowledged.

References

[1] Ma L., Xu Q., Yang Y. Organic non-volatile memory by controlling the dynamic copper-ion concentration within organic layer. *Appl. Phys. Lett.*, 2004, **84**, P. 4908–4910.
[2] Pyo S., Ma L., et al. Experimental study on thickness related electrical characteristics in organic/metal-nanocluster/organic systems. *J. Appl. Phys.*, 2005, **98**, P. 054303(1–6).
[3] Ouyong J., Chu C.W., et al. Programmable polymer thin film and non-volatile memory device. *Nature materials*, 2004, **3**, P. 918–922.
[4] Konno K., Sakai H., Matsushima T., Murata H. An organic nonvolatile memory using space charge polarization of a gate dielectric. *Thin solid films*, 2009, **518**, P. 534–536.
[5] Alokik K., Shashi P., Manish C. Organic memory devices using C_{60} and insulating polymer. *Mater. Res. Soc. Symp. Proc.*, 2005, **830**, D7.2.1–D7.2.5.
[6] Salaoru I., Paul S. Memory devices based on small organic molecules donor-acceptor system. *Thin Solid Films*, 2010, **519**, P. 559–562.
[7] Li Y., Chu Y., et al. Synthesis and memory characteristics of polyimides containing noncoplanar aryl pendant groups. *Polymer*, 2012, **53**, P. 229–240.
[8] Thanh Dao T., Matsushima T., Murata H. Organic nonvolatile memory transistors based on fullerene and an electron-trapping polymer. *Org. Electronics*, 2012, **13**, P. 2709–2715.
[9] Min Kim D., Ko Y.G., et al. Digital memory behaviors of aromatic polyimides bearing bis(trifluoromethyl)-and bithiophenyl-triphenylamine units. *Polymer*, 2012, **53**, P. 1703–1710.
[10] Ling Q.D., Liaw D.J., et al. Polymer memories: Bistable electrical switching and device performance. *Polymer*, 2007, **48**, P. 5182–5201.
[11] Wang L., Su Z., Wang C. Interfacial dipole in organic p/n junction to realize write-once/read-many-times memory. *Org. Electronics*, 2013, **14**, P. 1163–1169.
[12] Shi S., Peng J., Lin J., Ma D. Write-once read-many-times memory based on a single layer of Pentacene. *Electron. Dev. Lett.*, 2009, **30**, P. 343–345.
[13] Bin L., Kao C.Y., Arthur J.E. Impact of electrode metals on a pentacene-based write-once read-many memory device. *Letter/Synth. Met.*, 2010, **160**, P. 2385–2388.
[14] Puigdollers J., Voz C., et al. Pentacene thin films obtained by thermal evaporation in high vacuum. *Thin solid films*, 2003, **427**, P. 367–370.
[15] Girtan M., Dabos-Seignon S., Stanculescu A. On morphological, structural and electrical properties of vacuum deposited pentacene thin films. *Vacuum*, 2009, **83**, P. 1159–1163.
[16] Onlaor K., Tunhoo B., et al. Electrical bistable properties of copper phthalocyanine at different deposition rates. *Solid-State Electronics*, 2012, **72**, P. 60–66.
[17] Aruna P., Suresh K., Joseph C.M. Effect of fullerene doping on the electrical properties of P3HT/PCBM layers. *Materials Science in Semiconductor Processing*, 2015, **36**, P. 7–12.

NANOSYSTEMS: PHYSICS, CHEMISTRY, MATHEMATICS, 2016, 7 (4), P. 647–649

Investigations on tri manganese tetra oxide nano particles prepared by thermal decomposition

C. Sagi Rani[1], P. Athira[1], N. Joseph John[2]

[1]Department of Physics, Noorul Islam Centre for Higher Education, Noorul Islam University, Kumaracoil, Tamil Nadu, India
[2]Department of Physics, Govt. Arts College, The Nilgris, Tamil Nadu, India

sagirani.c@gmail.com, athira01011993@gmail.com

PACS 81.07.-b, 81.07.Bc **DOI 10.17586/2220-8054-2016-7-4-647-649**

Oxides of manganese have large number of applications in the field of sensors, piezoelectric crystals etc. In the present work, Mn_3O_4 nano materials were synthesized by using manganese acetate, adopting the method of thermal decomposition. The Nano materials thus prepared were characterized by employing various techniques like PXRD, FTIR, UV and Thermal analyses. The average particle size, calculated using Debye-Scherrer formula, was found to be in the range of 51 – 62 nm. The presence of Mn_3O_4 is also confirmed from FTIR. Thermal studies were also carried out. The optical band gap for the prepared nano materials was obtained from the UV-spectroscopic studies.

Keywords: Nano particles, thermal decomposition, PXRD, FTIR, UV, thermal studies.

Received: 5 February 2016. Revised: 31 May 2016.

1. Introduction

Nanotechnology provides the ability to create new materials or devices with new functions and properties. The current age is characterized by increased technological advances and rapid nanotechnology development [1]. Technologies with such a system of materials having at least one of its dimensions within 100 nm are referred to as nanoscience. The fundamental, physical, chemical and natural properties of materials are considerably altered as the size of their consistent grains is decreased to the nanometer scale. Most of the nanostructured materials have properties significantly different from those of the bulk materials due to the factors such as large fraction of surface atoms, high surface energy and reduced imperfections [2, 3].

It is evident that nanostructured materials are expected to have improved optical properties compared with bulk materials, as these properties depend on their size, shape and local dielectric environment [4]. In recent years, the synthesis of semiconductor materials with specific size and morphology has attracted a lot of interest due to their significant mechanical, electrical, optical and magnetic properties for potential applications in various fields [5]. Nanoscience and nanotechnology find applications in almost every branch of science and technology, electronics, astrophysics and in medical science. Recent progress in the preparation and characterization of materials on nanometer scale has introduced a new point of view for scientists in reduced dimensions. This will change the crystalline and electronic structure considerably [2].

Transition metal oxide nanoparticles are very attractive due to their variety of applications [6]. Mn_3O_4 is an important transition metal oxide due to its extensive applications in magnetic, electrochemical, lithium ion batteries, catalytic applications, super capacitors and dilute magnetic semiconductors etc. [7]. It is one of the most stable oxides of manganese [6]. Due to its nanometer size and large surface area, different morphologies are expected to display better performance in all the above mentioned applications [6]. The optical properties are the most fascinating and very useful properties of nano metal oxides. Oxides of manganese have optical properties which are associated with the intrinsic and extrinsic effect. The optical transition between the electrons in the conduction band and holes in the valence band causes the intrinsic effect. Mn_3O_4 is a direct band gap semiconductor and a transparent conducting material. By using a large number of techniques such as optical absorption, photo-reflection, photoluminescence etc. the optical transitions can be widely used in variety of applications.

In the present study, Mn_3O_4 nanoparticles were prepared using the thermal decomposition technique. Manganese oxide nanoparticles are water insoluble, brownish black powder and have no odor. Mn_3O_4 has the spinel structure [3], where the oxide ions are cubically closed packed and the Mn^{II} ions occupy tetrahedral sites whereas the Mn^{III} occupy the octahedral sites [3, 7].

2. Experimental procedure

Tri manganese tetra oxide nanoparticles were prepared by adopting the method of thermal decomposition. The required quantity of manganese acetate tetra hydrate [$(CH_3COO)_2Mn{\cdot}4H_2O$] in its dry form is taken in a ceramic container and is heated in a muffle furnace for a period of 24 hrs, maintained at a temperature of 950 °C. As a result, a brownish black powder of Mn_3O_4 particles was obtained and collected for further characterization.

3. Result and discussion

3.1. XRD characterization

The prepared Mn_3O_4 nanomaterials were characterized by powder X-ray diffraction. X-ray powder diffraction measurements were performed using the X-ray diffractometer operating with Cu-Kα radiation ($\lambda = 0.15406$ nm). Fig. 1 shows the X-ray diffraction spectra for the prepared Mn_3O_4 nanoparticles.

Figure 1 shows the crystalline structure with several significant peaks that can be readily indexed as (112), (200), (103), (211), (004), (220), (105), (224), (312) and (400) crystal planes respectively, which is in good agreement with the standard value, JCPDS No. 024-0734. All the peaks in the pattern can be indexed to a tetragonal phase with lattice constants $a = b = 5.7621$ Å, $c = 9.4696$ Å.

The particle size is calculated according to Debye-Scherrer formula:

$$2d = \frac{0.9\lambda}{\beta cos\theta},$$

where λ is the wave length of Cu-Kα radiation, β is the full width at half maximum, corresponding to the diffraction angle 2θ. The crystal size for the prepared Mn_3O_4 nano particle was found to be 51 – 62 nm.

3.2. FTIR characterization

Figure 2 shows the FTIR spectra of the prepared Mn_3O_4 nano particles which show several significant absorption peaks that help to understand various chemical bonds present in it.

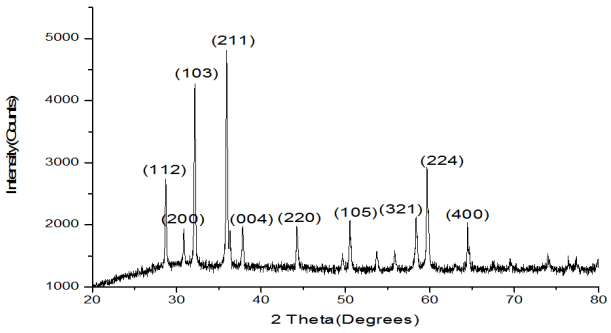

FIG. 1. XRD Spectra for the prepared Mn_3O_4 nano particles

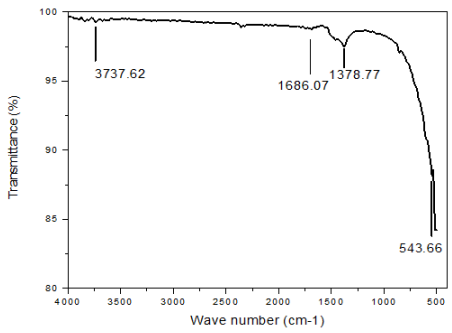

FIG. 2. FTIR Spectra for the prepared Mn_3O_4 nano particle

The vibration frequency located at 543 cm^{-1} corresponds to the vibration of Mn–O stretching modes. Moreover, the broad band at 3738 cm^{-1} and the narrow one at 1666 cm^{-1} correspond to O–H vibrating mode of the adsorbed water. Thus, FTIR provides concrete evidence for the presence of manganese oxide.

3.3. Thermal analysis (TGA/DTA)

The thermal stability of the prepared Mn_3O_4 nano particles was carried out between 250 – 1050 °C.

Figure 3 represent the TGA/DTA spectra for the prepared Mn_3O_4 nano particles. In the temperature range up to 300 °C a weight loss of 2.85 % can be related to the release of weakly adsorbed water molecules. It is found that the sample was completely decomposed within the given range.

3.4. UV characterization

The UV absorption spectra for the prepared Mn_3O_4 nano particle is shown in Fig. 4. The optical absorption peak intensity was found to be 316.507 nm. The optical band gap of the sample is calculated using the formula, $E_g = hc/\lambda$, where E_g – energy gap, c – velocity of light and λ – wave length. The optical band gap for the prepared Mn_3O_4 nano particle was found to be on the order of 3.824 eV.

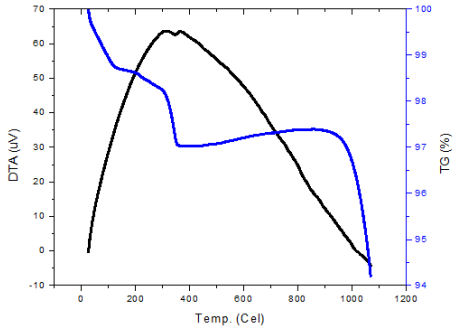

FIG. 3. TGA/DTA Spectra for the prepared Mn_3O_4 nano particle

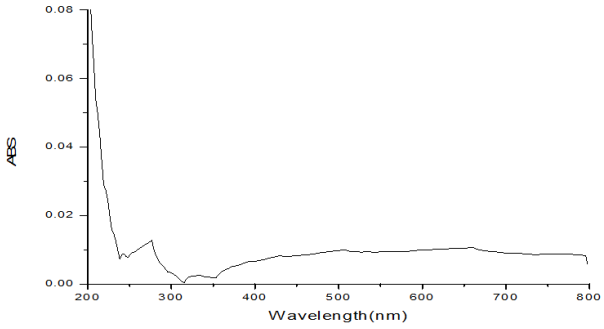

FIG. 4. UV Spectra for the prepared Mn_3O_4 nano particles

4. Conclusions

Mn_3O_4 nano particles were successfully synthesized by using manganese acetate by adopting the method of thermal decomposition. The nano materials thus prepared were characterized by adopting various techniques like XRD, FTIR, UV and thermal analysis. The average particle size is calculated using Debye-Scherrer formula as 56 nm. Presence of Mn_3O_4 is also confirmed from FTIR. Thermal studies were also carried out. The optical band gap for the prepared nanomaterials was found to be 3.824 eV.

Acknowledgements

We would like to acknowledge The University of Kerala X-RD Laboratory (DST-PURSE) Kariavattom Campus, Trivandrum for the XRD characterization. The facilities provided by the research laboratories of Department of Physics as well as the department of Nanotechnology, Noorul Islam Centre for Higher Education were also greatly acknowledged.

References

[1] Shanmugam S. *Nanotechnology*, MJP publishers. 2011.
[2] Usha K., Mahadevan C.K. Structure, Morphology and Electrical properties of Mn_3O_4 nanocrystals. *Scholars Research Library, Archives of Physics Research*, 2011, **2** (1), P. 75–80.
[3] Sherin J.S., Thomas J.K., Suthagar J. Combustion Synthesis and Magnetic Studies of Hausmannite, Mn_3O_4, nanoparticles. *International Journal of Engineering Research and Development*, 2014, **10** (7), P. 34–41.
[4] Hassouna Dhaouadiet, Hassouna Dhaouadi, et al. Mn_3O_4 Nanoparticles: Synthesis, Characterization, and Dielectric Properties. *International Scholarly Research Network Spectroscopy*, 2012, Article ID 706398, 8 p.
[5] Mote V.D., Dargad J.S., Dole B.N. Effect of Mn doping concentration on structural, Morphological and optical studies of ZnO Nano-Particles. *Nanoscience and Nano engineering*, 2013, **1** (2), P. 116–122.
[6] Vijaya Lakshmi S., Pauline S., Maria Vinosel V. Microstructural Characteriztion of Trimanganese Tetra Oxide (Mn_3O_4) Nanoparticle by Solvothermal Method and Its Dielectric Studies. *International journal of engineering sciences & research technology*, 2014, **3** (11), P. 123–131.
[7] Shrividhya T., Ravi G., Mahalingam T., Hayakawa Y. Synthesis and Study on Structural, Morphological and Magnetic properties of nanocrystalline Manganese Oxide. *International Journal of Science and Engineering Applications*, Special Issue NCRTAM ISSN-2319-7560, 2013. DOI: 10.7753/IJSEANCRTAM.1004.
[8] Harish Kumar, Manisha, Poonam Sangwan. Synthesis and Characterization of MnO_2 Nanoparticles using Co-precipitation Technique. *International Journal of Chemistry and Chemical Engineering*, 2013, **3** (3), P. 155–160.
[9] Wang Z.H., Geng D.Y., et al. Magnetic properties and exchange bias in Mn_2O_3/Mn_3O_4 nanoclusters. *Journal of applied physics*, 2009, **105**, 07A315.
[10] Yanyan Yang, Lifen Xiao, Yanqiang Zhao, Fengyun Wang. Hydrothermal Synthesis and Electrochemical Characterization of α-MnO_2 Nanorods as Cathode Material for Lithium Batteries. *Int. J. Electrochem. Sci.*, 2008, **3**, P. 67–74.
[11] Jianghong Wu, Hongliang Huang, Li Yu, Junqing Hu. Controllable Hydrothermal Synthesis of MnO_2 Nanostructures. *Advances in Materials Physics and Chemistry*, 2013, **3** (3), P. 201–205.
[12] Pradeep Kumar B.M., Shivaprasad K.H., et al. Preparation of MnO_2 nanoparticles for the adsorption of environmentally hazardous malachite green dye. *International Journal of Application or Innovation in Engineering & Management (IJAIEM)*, 2014, **3** (12), P. 102–106.
[13] Hansung Kim, Branko N. Popov. Synthesis and Characterization of MnO_2-Based Mixed Oxides as Super capacitors. *Journal of the Electrochemical Society*, 2003, **150** (3), D56–D62.
[14] Hiromichi Hayashi, Yukiya Hakuta. Hydrothermal Synthesis of Metal Oxide Nanoparticles in Supercritical Water. *Materials*, 2010, **3**, P. 3794–3817.
[15] Edelsten A.S., Cammarata R.C. *Nanomaterials synthesis properties and applications*. Novel research laboratory, Washington, 1988.

NANOSYSTEMS: PHYSICS, CHEMISTRY, MATHEMATICS, 2016, 7 (4), P. 650–656

Superhydrophobic coatings using nanomaterials for anti-frost applications – review

S. V. Laturkar, P. A. Mahanwar

Department of Polymer and Surface Engineering, Institute of Chemical Technology,
Matunga, Mumbai, 400019, India

supriyalaturkar13@gmail.com, pa.mahanwar@ictmumbai.edu.in

PACS 82.35.Np, 68.03.Cd **DOI 10.17586/2220-8054-2016-7-4-650-656**

Frost formation and accretion on various outdoor structures like aircraft, wind turbines, heat exchanger coils etc. as well as on glass doors of indoor refrigerators is a serious issue as it presents economic as well as safety challenges. Most of the research done on anti-frost coatings is based on the theme of making the surface super hydrophobic (contact angle $> 150\ ^\circ$, Sliding angle $< 10\ ^\circ$) mimicking a lotus leaf which provides low or zero ice adhesion. Nanomaterials have played a significant role in such coatings as they help in tuning the surface properties which are surface roughness and surface energy. In this paper, we have tried to investigate why all superhydrophobic surfaces may not be ice-phobic and how nanomaterials improve super hydrophobicity of the surface, in turn, making them anti-frosting. This paper is a detailed study of anti-frosting strategies based on nanosystems which have been developed to date.

Keywords: Anti-frost coatings, superhydrophobic, icephobic, nano fillers, surface roughness, surface energy, contact angle.

Received: 5 February 2016

Revised: 21 April 2016

1. Introduction

When moist air comes in contact with a cold surface, whose temperature is below the triple point of water, frosting or icing takes place on the surface [1].

Considering the phase equilibrium of water-system, if pressure is applied to the system at the triple point (where all the three phases coexist); the effect of applying pressure will be to cause condensation of vapor to liquid or solid phase. Ultimately, the vapor phase will disappear and only two phases, solid and liquid, will stay and further application of pressure will cause increase of pressure with change of temperature along the fusion curve on phase diagram [2]. This implies that pressure exerted by humid air is responsible for frosting or icing on many outdoor structures in colder regions such as wind turbines, aircrafts, heat exchangers (air-conditioners/heaters), as well as domestic and industrial refrigerators/freezers. Thus, frosting is a condensation phenomenon and temperature of the (cold) surface, percent relative humidity (% RH) and temperature of air, are the factors which influence frosting and defrosting.

Frost formation and accretion on various infrastructures is a serious issue as it presents economic as well as safety challenges. For example, the ice accretion on aircraft results in drag increase and sometimes may lead to dangerous loss of lift force, which may cause tragic crashes [3]. Ice accretion on wind turbine blades can cause a production loss of as much as 50 % of the annual production [4]. Furthermore, frost and ice accumulation in refrigerators and heat exchangers results in a decrease of heat transfer efficiency up to 50 – 75 % [5].

Several conventional defrosting/de-icing techniques include electric heating which accelerates ice melting or breaking the accretion by direct scrapping which neither safe nor efficient. In addition, Automatic robots, electromagnetic forces [6] are reported for the de-icing of overhead transmission lines. Thus, most of these conventional anti-frosting strategies are often inefficient, energy-consuming, high-cost, or environmentally harmful. Applying an anti-frost or defrosting coating on the cold surface has been found as the most promising and interesting method in the past two decades, realizing the objective of preventing frosting and saving energy.

Initially freezing point depressants such as Ethylene glycol were incorporated into the resin or a hydrophilic polymer was impregnated with an anti-freeze, for defrosting in heat exchangers [7]; which was later replaced by- developing an ‘ice-phobic’ surface where the substrate is mostly made superhydrophobic which exhibit water contact angles exceeding 150 °C, mimicking a lotus leaf. Today, many such anti-frosting strategies have been developed by incorporating various nanomaterials in the coating formulation.

This paper clarifies the terms ‘superhydrophobicity’ and ‘ice-phobicity’. It reviews the significance of nanomaterials for tuning the surface properties of a glass or a metal substrate so as to make it ‘anti-frost’; along with some important anti-frosting strategies which have been developed till date.

2. Superhydrophobicity and ice-phobicity

The wettability of a flat surface is directly related to the surface energy and is expressed by contact angle (CA) θ of a water droplet given by Young's equation:

$$\cos\theta = \frac{\gamma_{SV} - \gamma_{SL}}{\gamma_{LV}}, \tag{1}$$

where, γ_{SV}, γ_{SL}, γ_{LV} refer to the interfacial surface tensions with S(solid), L(liquid) and V(gas) respectively. Surfaces with water contact angles (CA's) greater than 150 $^\circ$ are considered superhydrophoic or ultraphobic. The dynamic CA's are measured during the growth (advancing) and shrinkage (receding) of a water droplet as contact angle hysteresis CAH ($\triangle\theta = \theta a - \theta r$). The values of $\triangle\theta$ can be as low as below 10 $^\circ$ on some surfaces, whereas many surfaces show much larger hysteresis, due to chemical heterogeneity and roughness [8].

The superhydrophobic surfaces are usually covered with micro- or nanoscale asperities (rough). Water can either penetrate the asperities (Wenzel state: wet-contact mode) or be suspended above the asperities (Cassie Baxter state: nonwet-contact mode). In either case, much higher contact angles are observed than those obtained for the corresponding flat surface. For a hydrophobic surface, in the Wenzel's regime, the contact angle and its hysteresis increase as the roughness factor increases until it exceeds 1.7, from where the CAH starts to decrease. The decrease in the contact angle hysteresis is attributed to the switching from the Wenzel to the Cassie–Baxter state due to the formation of hierarchical rough morphology with sufficient air trapped in the gap to reach Cassie state of suspension of water droplet on top of the asperities as shown in Fig. 1 [8,9].

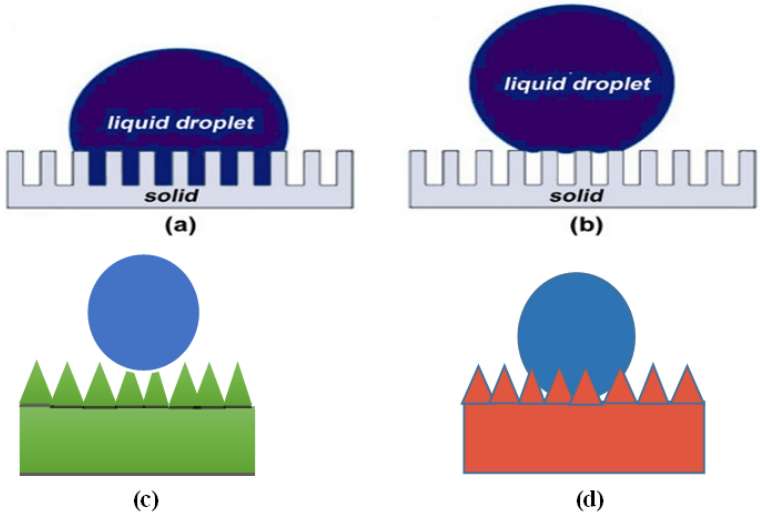

FIG. 1. Wenzel model (a); Cassie-Baxter model (b); Behaviour of a liquid droplet on lotus leaf (Cassie state) (c); Behaviour of a liquid droplet on rose petal (Cassie impregnating wetting state) (d)

Thus, when a rough surface reaches 'Cassie' state it can show the 'self-cleaning' effect from where the dust particles or frost roll off when surface is slightly tilted, mimicking a Lotus leaf. (Also known as 'lotus effect' characterized by high CA and low CAH). Another special case of Cassie state is 'rose petal' inspired surfaces where the water droplets enter into the larger scale grooves of the petal but not into the smaller ones, thus forming a Cassie impregnating wetting state (characterized by high CA and high CAH due to adhesive property of the petal). These two effects can be attributed to difference of the microstructures and chemical composition between the petal and the lotus leaf [9].

Now, talking about ice-phobicity, a surface should be called ice-phobic if it delays frost formation from incoming water (moisture) or delays ice formation from condensed droplets (frost crystals) in the situation where normally ice would form and/or there is low adhesion force between ice and the solid surface [10]. Considering this definition, it is clear that to achieve ice-phobicity or anti-frost property on a cold surface, the surface can be made superhydrophobic with low adhesion force i.e. low CAH so that the incoming water droplets (moisture) roll off as soon as they condense and before converting into the frost; thus, frost accumulation can also be avoided due to low or non-adhesion.

This implies that lotus leaf inspired surfaces (high CA, low CAH) can show ice-phobicity and not the rose petal inspired ones. However, it has been also studied that every superhydrophobic surface which shows self-cleaning behavior (lotus effect) may not necessarily show ice-phobicity. There are several other parameters, such as surface roughness, mechanical robustness of the surface so as to maintain the same superhydrophobicity at sub-zero temperatures and with subsequent icing /de-icing events. This can be explained by the following example:

S. A. Kulinich et al. studied the ice-releasing properties of rough hydrophobic coatings based on different materials with different surface topographies [11]. Three samples were investigated for ice-phobic properties: 1. Etched aluminium alloy coated with an organosilane (ODTMS). 2. TiO_2 nanopowder functionalized with perfluoroalkyl methacrylic copolymer (Zonyl) applied on the substrate by spin coating. 3. TiO_2-Zonyl applied by spray coating. Fig. 2 shows both CA and CAH values obtained for the above three samples. Table 1 shows root mean square roughness values for the three samples at various icing-de-icing events. From Table 1 and Fig. 2 it can be seen that sample 3 though maintains high roughness after 6 de-icing cycles, high CAH 80 ° leads to high ice adhesion strength. Sample 1 and 2 show higher contact angles 153 ° and 152 ° respectively along with low CAH values (5.7 ° and 6.1 ° respectively).

TABLE 1. Variation in surface roughness with subsequent icing-deicing events

Sample Number	Sample Description	Root-mean-square roughness (nm) at event:					
		1	2	3	4	5	6
1	Etched Al/ODTMS	240	238	237	237.5	232	230
2	TiO_2 spin	210	200	170	168	167	165
3	TiO_2 spray	310	290	300	302	305	305

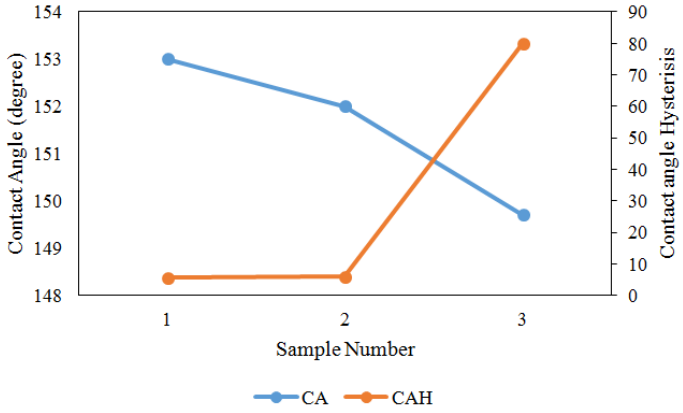

FIG. 2. Contact angle and contact angle hysteresis for three different samples

However, there is a gradual decrease in roughness for sample 2 due to the sharper and much taller asperities which were believed to be gradually damaged during icing/de-icing cycles, whereas sample 1, also having sharp and tall asperities, seemed to be more resistant to damage during icing/de-icing. This was likely due its more rigid asperities (built of Al_xO_y) compared to those in sample 2 (based on fluoropolymer heavily loaded with TiO_2 nanoparticles). Thus, the more robust nanostructured surface prepared by etching the aluminium substrate maintained the ice-releasing properties better compared to its counterparts.

3. Role of nanomaterials

Nanomaterials play a significant role in the tuning of surface properties of the substrate which is desired to be superhydrophobic and also ice-phobic. As mentioned in section 2, to achieve ice-phobicity, the surface has to reach the Cassie state (high CA, low CAH), which can be accomplished by increasing the surface roughness. Nanomaterials such as carbon nanotubes, hydrophobic nanosilica, ZnO nanorods etc. are often used both as fillers and for functionalization, to impart roughness to the surface, and also to improve the mechanical properties of the surface.

Qitao Fu et al. prepared mechanically robust sol-gel type of ice-phobic coatings and once again clarified the significance of nanofillers in designing superhydrophobic surfaces and also that all superhydrophobic surfaces may not be ice-phobic [12]. Two sets of samples were prepared, one having coating samples prepared by using MTEOS, GLYMO and varying amounts (5 – 20 wt %) of silica nanoparticles; and the other having coating samples prepared by adding varying amounts of FAS (4 – 16 wt %) to the above formulations. The first set of samples showed increase in water CA i.e. increase in superhydrophobocity with an increase in nanofiller content as a result of increased surface roughness. However, such samples with high silica content failed in maintaining the superhydrophobicity below room temperature (high ice adhesion). On the other hand, a second set of samples containing a low surface energy fluoroalkylsilane showed ice-phobocity to temperatures as low as -10 °C. With 0.31 – 0.35 μmol/gm of FAS in sol and 16 wt % silica nanoparticles, the surface maintained CA ~ 170 °, SA ~ 4.4 ° at -10 °C. The samples containing only FAS without nanofiller or with up to 8 % nanofillers were able to give CAs up to 120 ° and higher sliding angles (60 – 80 °) and therefore failed to show both superhydrophobicity and ice-phobicity.

Carbon nanotube-based composite materials have been investigated for superhydrophobic coatings to improve mechanical strength. Yoonchul Sohn et al. developed an anti-frost coating with reliable thermal cyclic properties [13]. A superhydrophobic multi-walled carbon nanotube (MWCNT)–silicone composite film (Cassie structure) that can endure over 4000 thermal cycles (-30 °C to room temperature, 40 % RH) was fabricated by controlling the composition and microstructure of the composite. The nanofiller content of this coating was 20 vol %, showing thermo-mechanical reliability without significant change in the contact angle (~ 160 °). A composite structure having higher nanofiller content (20 – 30 %), which contains numerous pores, can accommodate high levels of thermal stress. The stress relaxation can reach 48 % and 84 % of the reference point for the 20 and 30 vol % MWCNT specimens, respectively. Since the coefficient of thermal expansion (CTE) of silicone (310 ppm °C) is much larger than that of MWCNTs (7 ppm °C), the large expansion and shrinkage of silicone matrix compared to MWCNT fillers resulted in cracking of specimens containing lesser nanofiller content, after 1000 thermal cycles. Though the 30 vol % MWCNT-silicone film is better for stress relaxation, the 20 vol % film shows superior ice-phobic properties (lower CAH).

Thus nanopores in superhydrophobic coatings, constituting air pockets in a Cassie structure, are of great importance not only for wetting characteristics but also for superior reliability induced by stress relaxation. Although a more open structure can help relax more stress arising from a CTE mismatch, the composition of a superhydrophobic coating should be carefully selected to optimize its wetting characteristics while maintaining its mechanical reliability.

4. Superhydrophobic anti-frost coatings using nanotechnology

Min He et al. also developed anti-frost coatings for glass substrates. They prepared superhydrophobic surfaces using ZnO nanorod arrays, which could maintain superhydrophobicity to condensed micro-droplets at temperatures below the freezing point. ZnO nanorod arrays were employed because of their controllable morphologies. Materials with different ZnO nanorod arrays were fabricated by the method of low-temperature wet chemical bath deposition and modified with a fluoroalkylsilane (FAS-17) to obtain super-hydrophobicity, even at temperatures lower than 0 °C [14]. Firstly, ZnO seeds layer was obtained on the cover glass by treating it with zinc acetate and then it was immersed into an equimolar solution of $Zn(NO_3)_2$ and hexamethylenetetramine, and kept sealed at a temperature of 90 °C for different times (t_{ZnO}) to control the growth (size) of the ZnO nanorods. Table 2 shows the change in contact angle with t_{ZnO} at room temp., -5 °C and -10 °C. The values of sliding angle have been mentioned only at room temperature as 1 °, 1 ° and 2 ° for t_{ZnO} 1 h, 2 h and 3 h respectively. The ice-phobic behavior when compared with that of a hydrophobic glass surface, it has been observed that the time of condensed droplets maintaining a liquid state is much longer on the superhydrophobic ZnO nanorod array surfaces. Furthermore, the shorter growth time (t_{ZnO}) of ZnO nanorods, increases the time period for maintaining condensed droplet in the liquid state, thus providing better anti-frost performance.

Hao Wang et al. fabricated anti-frosting copper surfaces for evaporator coils of industrial refrigerators and air-conditioners. This coating was based on nanosized $CaCO_3$ particles modified with heptadecafluorodecyl trimethoxysilane mixed in an ordinary polyacrylate binder [15]. The coating, when applied on glass, showed superhydrophobic behavior (with $CA = 155$ °) and maintained the same superhydrophobicity on copper plate for subsequent 10 frosting-thawing treatments at temperature -7.2 °C and 55 % humidity. In this case, frost formation was not totally inhibited, but the rate of frosting was greatly reduced as compared to bare copper or ordinary hydrophobic surfaces and formed frost was able to roll off the plate when mounted vertically as a result of roughness (nano $CaCO_3$) and low surface energy FAS.

Yanfen Huang et al. developed ice-phobic coatings to protect aluminium ground wires and phase conductors of overhead power lines from icing [16]. The coating was prepared by a simple, inexpensive method using silica/fluorinated acrylate copolymers. The nano silica sol was mixed with fluorinated acrylic copolymers in different weight ratios. The films showed good hydrophobicity (CAs up to 141.7 °C) and especially excellent mechanical properties of adhesion strength and pencil hardness as compared to other superhydrophobic surfaces. The coated Al surface can delay icing for 90 min. compared with the glass surface at -5.6 °C.

Hyomin Lee et al. prepared a zwitter-wettable surface, i.e. one that has the ability to rapidly absorb molecular water from the environment while simultaneously appearing hydrophobic when probed with water droplets [17]. This can be prepared by using hydrogen-bonding-assisted layer-by-layer (LbL) assembly of poly (vinyl alcohol) (PVA) and poly(acrylic acid) (PAA). An additional step of functionalizing the nano-blended PVA/PAA multilayer with poly (ethylene glycol methyl ether) (PEG) segments produced a significantly enhanced antifog and frost-resistant behavior. The addition of the PEG segments was needed to further increase the non-freezing water capacity of the multilayer film. The desirable high-optical quality of these thin films arises from the nanoscale control of the macromolecular complexation process that is afforded by the LbL processing scheme. The author justifies the inhibition of frost formation on glass due to this type of coating by the fact that in this case, the water molecules are presumably molecularly dispersed as a result of strong polymer-water hydrogen bonding interactions and hence are not capable of freezing at the usual temperature. Also, the above-prepared nanoscale LbL assembly ensures that crystallisation of PVA molecules will be limited or non-existent, which is helpful to accommodate more amount of non-freezing water.

William Tong et al. designed transparent glass windows with antifrost/anti-fog capabilities in order to maintain the aesthetic appearance of glass windows for vehicles and modern buildings [18]. The nanostructured metamaterials can be coated on the window's outside surface. A tungsten-silica-tungsten (at nanoscale) metamaterial coating was used as the solar absorber to coat on window's outside surface. The top layer of the absorber is a 1D tungsten planar stack, the dielectric SiO_2 spacer works as optical cavity and the bottom tungsten film as non-perfect or perfect mirrors. The profile of this three-layer structured coating can be designed by adjusting the thickness of bottom and top layers in such a way that sufficient visible light transmits through the window glass for enough lightening in the room, while maximum infrared waves can be absorbed for heating. The coating was deposited using closed field magnetron sputtering (CFM). This nanoscale metamaterial structure with periodic metal-dielectric interfaces efficiently absorbs solar radiation and with proper design, the window surface temperatures can be well controlled which is useful for efficient anti-frosting and anti-fogging. The transparency can be adjusted by changing the tungsten layer thickness ($\sim$ 300 nm) meanwhile the absorption performance of the solar absorber has no significant variation.

Aeree Kim et al. fabricated a 'nanostructured' and therefore superhydrophobic Al surface for anti-frosting applications due to its property of enhanced self-propelled jumping by condensate droplets. This Al surface was fabricated in three following steps: 1. Alkali treatment (0.05 M NaOH) to produce an aluminium hydroxide ($Al(OH)_3$) layer. 2. Boiling the specimens in deionized water to induce formation of nanostructures. 3. A self-assembled monolayer (SAM) of fluorochlorosilane was applied to render it superhydrophobic as well as ice-phobic. It can be seen from Fig. 3 that the time for which the specimens are immersed in boiling water governs the surface's nanostructure and hence, the CA and CAH. All four specimens were alkali treated for the same time (5 min) and coated with SAM layer, however, different CA and CAH values were obtained for those samples having different boiling times. Samples had higher CA and lower CAH for 5 – 30 minutes boiling, as shown in Fig. 3. Self-Propelled Jumping (SPJ) by condensate droplets that occurs on superhydrophobic surface, shows significant dependency on the super saturation $S = PV/PW$, where PV is the vapor pressure and PW is the saturation pressure that corresponds to the specimen surface temperature. Frost formation on the above 'nanostructured' aluminium was delayed more than 4 times at $S = 3.41$ and $S = 6.39$ compared to smooth Al surface [19].

TABLE 2. Effect of t_{ZnO} on contact angle

	Contact angle		
$t_{\mathbf{ZnO}}$	**Room temp.**	**-5 °C**	**-10 °C**
1 hr	170.9 °	167.9 °	163.4 °
2 hr	166.1 °	160.3 °	158.2 °
3 hr	165.8 °	154.6 °	155.4 °

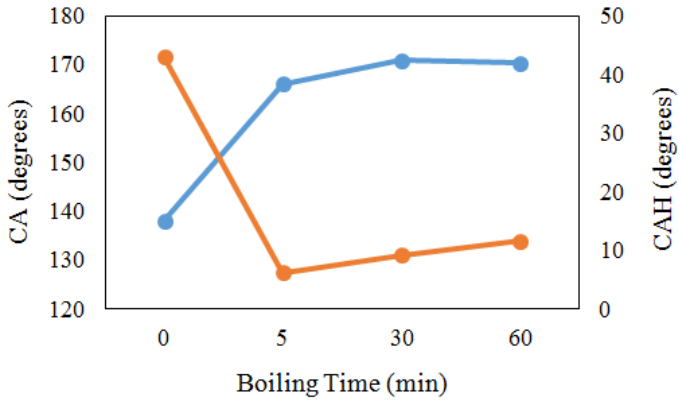

FIG. 3. Effect of boiling time on CA and CAH

The lotus leaf-inspired superhydrophobic surfaces show promising ice-phobicity but at high humidity conditions, they may fail. Due to their high surface area and increased nucleation site density to condensing droplets, they may induce ice nucleation at an even faster rate than smooth surfaces of the equivalent materials at high humidity conditions [20]. Slippery liquid infused porous surfaces (SLIPS) have attracted great interest as anti-icing coatings. The 'pitcher plant' inspired slippery surfaces capable of repelling condensing water droplets have been created by infiltrating a micro/nanoporous substrate with a lubricating liquid to produce a thin, ultra-smooth lubricating layer that repels almost any immiscible materials. Such SLIPS have been fabricated on industrially-relevant metals like aluminium and thus can be used as antifrosting surfaces for aircraft, refrigeration etc. The criteria for designing SLIPS are: 1) the lubricating fluid repellent fluid (e.g. water, oil) have to be immiscible; 2) the chemical affinity between the lubricating fluid and the solid should be higher than that between the repellent fluid and the solid; 3) the solid surface should preferably have roughened nanostructures to provide increased surface area for the adhesion and retention of the infiltrated lubricating fluid [21].

Kim et al. developed aluminium based SLIPS by the electrodeposition of highly textured polypyrrole (PPy) on Al substrates followed by fluorination of the structured coating and infiltration with the lubricant. PPy/Al surfaces having rough and globular morphology were fluorinated with a fluorochlorosilane and infiltrated with a low viscosity perfluorinated lubricating fluid which has freezing point less than −70 °C, immiscible with water and strong chemical affinity to the modified solid substrate. The contact angle hysteresis (CAH) which decides the surface retention force was found to be lowest as below 3 ° for the SLIPS-Al specimens when compared with the bare Al, hydrophobically modified Al and even with superhydrophobic PPy coated Al (without lubricant). While checking the ice-phobic behavior, it has been observed that SLIPS-Al surface delays frost formation. After 100 min of freezing (at −2 °C, 60 % RH), only 20 % surface is covered with ice. After a prolonged exposure to deep freezing, ice accumulates on the surface, however, during the defrost cycle, the large ice patches slide off the surface immediately upon melting at the interface, leaving the surface clean and ready for the next cooling cycle within 1 minute. The average ice adhesion strength on SLIPS/Al has been reported as 15.6 kPa. This low adhesion strength is attributed to the ultrasmooth solid-liquid interface present at the SLIPS surface which has significantly fewer defects/ heterogeneities/pinning points than the solid-solid interface found in conventional superhydrophobic surfaces [22].

Though SLIPS are promising for anti-icing, the most challenging point is their durability. Water tolerance, lubricant retention ability after subsequent icing-deicing cycles are the parameters to be considered while designing a SLIPS. Q Liu et al. developed hierarchically micro structured high temperature vulcanized silicone rubber (HTV) infiltrated with a perfluoropolyether lubricant to form SLIPS. These surfaces showed water contact angle more than 162 ° and lubricant contact angle nearly 0 °, which suggests that the lubricant can infiltrate completely into the substrate. As the no. of icing/deicing cycles increased the freezing and thawing times accelerate which is related to the lubricant depletion. The lubricant retention rate (LRR) at −14 °C, 80 % RH and air at 18 °C for the above surface was found to be nearly 37 % after 4 cycles. Also, these samples showed best results for delayed ice formation. Ice adhesion strength was nearly 250 kPa up to 5 cycles and maximum 700 kPa for 20 cycles [23].

Recently, Chanda et al. studied and compared the advantages and disadvantages of superhydrophobic and hydrophilic surfaces with respect to their anti-frosting properties and came to the conclusion that neither purely (super)hydrophobic polymeric surfaces, nor 'antifreeze' hydrophilic ones provide an ideal solution for the problem of icing [24].

5. Conclusion

Frost formation and accretion on various infrastructures is a serious issue, as it presents economic as well as safety challenges. Considering the current anti-frosting strategies based on superhydrophobic surfaces, it should be made very clear that superhydrophobicity and ice-phobicity are different phenomena as far as practical applications are concerned. Nanotechnology is the backbone of such coatings which helps in tuning the morphology of the surface by providing the required surface roughness for a coating's superhydrophobic nature and mechanical strength. The amount of nanofillers to be incorporated or the procedures to be followed while fabricating a nanostructured surface are also important in order to obtain the desired anti-frosting properties.

There is still scope for development of more bio-inspired anti-frosting strategies, such as grafting nanomaterials on smart interface materials, the use of different binder combinations for naofiller, fluorinated system or simplifying the design methods for 'slippery' surfaces.

References

[1] Zhongliang L., Hongyan W., Xinhua Z. An experimental study on minimizing frost deposition on a cold surface under natural convection conditions by use of a novel anti-frosting paint. Part I. *International Journal of Refrigeration*, 2006, **29**, P. 229–236.
[2] Puri B.R., Sharma L.R., Pathania M.S. *Principles of Physical Chemistry*. Vishal publications, Jalandhar, 2002, 281 p.
[3] Gent R.W., Dart N.P., Cansdale J.T. Aircraft icing. P*hil. Trans. R. Soc. Lond. A*, 2000, **358**, P. 2873–2911.
[4] Botta G., Cavaliere M., Holttinen H. Ice accretion at acqua spruzza and its effects on wind turbine operation and loss of energy production. *BOREAS IV*, 1998, 31 March – 2 April, Hetta, Finland, P. 77–86.
[5] Huang Lingyan, Zhongliang Liu, et al. Experimental Study on Frost Release on Fin-and-Tube Heat Exchangers by Use of a Novel Anti-Frosting Paint. *Experimental Thermal and Fluid Science*, 2009, **33** (7), P. 1049–1054.
[6] Dalili N., Edrisy A., Carriveau R. A Review of Surface Engineering Issues Critical to Wind Turbine Performance. *Renewable and Sustainable Energy Reviews*, 2009, **13**, P. 428–438.
[7] Ostin R., Johannesson G. A Polymeric Approach to Counteract Frosting in Air-to-Air Heat Exchangers. *Heat Recovery Syst. CHP*, 1991, **11** (5), P. 415–421.
[8] Li X.M., Reinhoudt D. What do we need for a superhydrophobic surface? A review on the recent progress in the preparation of superhydrophobic surfaces. *Chem. Soc. Rev.*, 2007, **36**, P. 1350–1368.
[9] Feng L., Zhang Y., Xi J., Zhu Y. Petal effect: A superhydrophobic state with high Adhesive force. *Langmuir*, 2008, **24** (8), P. 4114–4119.
[10] Hejazi V., Sobolev K., Nosonovsky M. From Superhydrophobicity to Icephobicity: Forces and Interaction Analysis. *Scientific reports*, 2013, **3**, P. 2194.
[11] Kulinich S.A., Farzaneh M. On Ice-Releasing Properties of Rough Hydrophobic Coatings. *Cold Regions Science and Technology*, 2011, **65** (1), P. 60–64.
[12] Fu Q., Kumar D., et al. Development of sol-gel icephobic coatings: effect of surface roughness and surface energy. *ACS Applied Materials and Interfaces*, 2014, **6**, P. 20685–20692.
[13] Sohn Y., Kim D., Lee S., Yin M. Anti-frost coatings containing carbon nanotube composite with reliable thermal cyclic property. *Journal of Materials Chemistry A*, 2014, **2**, P. 11465–11471.
[14] He M., Wang J., Li H., Song Y. Super-hydophobic surfaces to condensed micro-droplets at temperatures below the freezing point retard ice/frost formation. *The Royal Society of Chemistry*, 2011, **7**, P. 3393–4000.
[15] Wang H., Tang L., Wu X., Dai W. Fabrication and anti-frosting performance of supehydrophobic coating based on modified nano-sized calcium carbonate and ordinary polyacrylate. *Applied Surface Science*, 2007, **253**, P. 8818–8824.
[16] Huang Y., Hu M., et al. Preparation and characterisation of silica/fluorinated acrylate copolymers hybrid films and the investigation of their icephobicity. *Thin Solid Films*, 2012, **520**, P. 5644–5651.
[17] Lee H., Alcaraz M., Rubner M.F., Cohen R.E. Zwitter-wettability and anti-fogging coatings with frost resisting capabilities. *ACS NANO*, 2013, **7** (3), P. 2172–2185.
[18] Tong W., Tong A. Anti-frost and energy saving transparent glass windows manipulated through solar absorbing metamaterial coatings. *Global Advanced Research, Journal of Engineering, Technology and Innovation*, 2015, **4** (3), P. 31–40.
[19] Kim A., Lee C., Kim H., Kim J. Simple approach to superhydrophobic nanostructured Al for practical anti-frosting applications based on Enhanced self-propelled jumping droplets. *ACS Applied Materials and Interfaces*, 2015, **7**, P. 7206–7213.
[20] Jung S., Dorrestjin M., et al. Are superhydrophobic surfaces best for icephobicity? *Langmuir*, 2011, **27**, P. 3059–3066.
[21] Wong T.S., Kang S.H., et al. Bioinspired self-repairing slippery surfaces with pressure-stable omniphobicity. *Nature*, 2011, **477**, P. 443–447.
[22] Kim P., Wong T.S., Alvarenga J., Kreder M.J. Liquid infused nanostructure surfaces with extreme anti-ice and anti-frost performance. *ACS NANO*, 2012, **6** (8), P. 6569–6577.
[23] Liu Q., Wang Y., et al. Durability of a lubricant infused electrospray silicon rubber surface as an anti-icing coating. *Applied Surface Science*, 2015, **346**, P. 68–76.
[24] Chanda J., Lonow L., Kirillova A., Synytska A. New insight into icing and de-icing properties of hydrophobic and hydrophillic structured surfaces based on core-shell particles. *Soft matter*, 2015, **11**, P. 9126–9134.

NANOSYSTEMS: PHYSICS, CHEMISTRY, MATHEMATICS, 2016, 7 (4), P. 657–661

Electro chemical and photo catalytic studies of MnO_2 nanoparticle from waste dry cell batteries

M. Mylarappa[1,2], V. Venkata Lakshmi*[1], K. R. Vishnu Mahesh**[3], H. P. Nagaswarupa[4], S. C. Prashantha[4], D. M. K. Siddeswara[4] and N. Raghavendra[5]

[1]Research Centre, Department of Chemistry, AMC Engineering College, Bengaluru-560083, Karnataka, India
[2]Department of Studies and Research in Chemistry, Tumkur University, Tumkur-572103, Karnataka, India
[3]Department of Chemistry, Dayananda Sagar College of Engineering, Bengaluru-560083, Karnataka, India
[4]Research Centre, Department of Science, East West Institute of Technology, Bengaluru-560091, Karnataka, India
[5]CMRTU, RV College of Engineering, Bengaluru-560059, Karnataka, India
*laxmimurthy@rediffmail.com, **vishnumaheshkr@gmail.com

PACS 82.47.-a **DOI 10.17586/2220-8054-2016-7-4-657-661**

The objective of the existing research was essentially focused on recovery of MnO_2 nanoparticles from consumed dry cells by employing adapted hydrometallurgical process. Experimental tests for the recovery of MnO_2 present in the dry cell batteries have been carried out by an acidic reductive leachant, namely oxalic acid. The elemental compositions of the recovered metals from dry cells were confirmed by Energy Dispersive X-ray analysis (EDAX). Surface morphology of the recovered metals was examined using Scanning Electron Microscopy (SEM). Phase composition of the recovered metals from dry cell batteries were confirmed from X-ray Diffract meter (XRD). Cyclic Voltammetry (CV) studies were carried out to clarify the reversibility of the reactions. The obtained MnO_2 catalyst was applied for the degradation of different non-volatile dye compounds such as Indigo carmine (IC) and Rhodamine B (RB). The performance of MnO_2 shows fast degradation of dyes of high concentration.

Keywords: Dry cell batteries, recovery, Zn, Mn, electrochemical, catalytic activity.

Received: 5 February 2016

1. Introduction

Dry cell batteries are used in radios, recorders, toys, remote controls, watches, calculators, cameras, and in many other objects. The waste batteries present serious problems due to their toxicity, abundance and longevity in the environment [1]. The hydrometallurgical methods are the most popular process in all over the world because of its environmental suitability and economical coasts for treating even low zinc and manganese containing materials on small scale with high purity and low energy requirements [2, 3]. Hence, the treatment of these wastes for the recovery of manganese is vigorous for discarded material to raw material recycling. Two different acid-reductive leaching agents have been investigated; sulfuric acid - oxalic acid and sulfuric acid- hydrogen peroxide. MnO_2 is economically and commercially-important with applications in different fields, such as battery industry, catalysis, water treatment plants, steel industry and chemicals. In this study, we show how to recover manganese as MnO_2 from consumed dry cell using a hydrometallurgical process, without altering the concentration of zinc in solutions that can be recovered by precipitation or electro winning [4]. The aim of this work is to study the applicability of electrochemical and photocatalytic enactment of MnO_2 using a hydrometallurgical process and the catalytic action of MnO_2 is due to its high efficiency in the reduction/oxidation cycles [1]. The effects of the recovered conditions and crystallinity of MnO_2 on the catalytic performance in degradation of high concentration dyes (methylene blue indigo carmine and Rhodamine B) were intensively evaluated [5].Nanostructured materials have received enormous interest in recent years because of their unusual properties when compared with bulk materials. Nanoscale one-dimensional (1D) structures such as nanotubes, nanowires and nanorods have attracted much interest because of their unique electronic, optical and mechanical properties due to the low dimensionality and the quantum confinement effect. For example, the electrons interact differently in one dimensional (1D) and three-dimensional structures (3D). The 1D system is the smallest dimensional structure that can be used for efficient transport of electrons and optical excitations, and is thus expected to be critical to the function and integration of nanoscale devices. 1D nanostructure provides a good system for investigating the electrical and thermal transport properties in size and shape reduction [6–8]. The aim of this work is to study the applicability of electrochemical and photocatalytic enactment of MnO_2 using a hydrometallurgical process and the catalytic action of MnO_2 is due to their high efficiency in the reaction/oxidation cycles [1]. The effects of the recovered conditions and crystallinity of MnO_2 on the catalytic performance in degradation of high concentration dyes (methylene blue indigo carmine and Rhodamine B) were thoroughly evaluated [5].

2. Experimental

The waste dry cell batteries in an amount of 100 g were collected from different manufacturers. A series of mechanical processing is conducted in the following sequence to yield enriched Zn and Mn particles. The waste dry cell batteries were fed to a hammer mill for dismantling. Magnetic separator removed the magnetic fractions and the non-magnetic fraction was screened in a 2 mm sieve. A second magnetic separation was carried out to remove the ferrous materials which remain in the sample. The sieved powder was later washed with deionized water and finally dried at 100 °C for 24 hrs. The washed powder (20 g) was subsequently dissolved in 100 mL, 3 M H_2SO_4 followed by addition of 5.94 g Oxalic acid dehydrated as leaching agent. The leaching was continued for 5 hrs at 90 °C with continuous stirring. Recovery of MnO_2 particle from the leaching solution is possible at room temperature without special purification of the solution, and preserving a high efficiency. After the complete reductive acid leaching process, the required quantity of leached solution in a 500 ml beaker and a solution of 4 M NaOH was added slowly to the beaker with constant magnetic stirring. At the end of the precipitation, the solution in the beaker was filtered and the solid residue remaining in the filter paper was dried in an oven at 100 °C for 24 hours. MnO_2 was formed as dark precipitate at the bottom of the cell. The recovered sample was investigated by means of the EDX, SEM and XRD to analyze elemental composition, morphology and phase composition of the powder.

3. Result and discussion

Energy Dispersive X-ray analysis (EDX) was carried out to obtain the elemental composition of the metals in powder sample. The accurate size and morphology of the MnO_2 studied from the Scanning Electron Microscopy (SEM) and X-ray diffraction spectroscopy (XRD). Fig. 1(a) shows that manganese and oxygen contents were detected in that point, indicating the presence of high manganese hydroxide content [9]. The leaching residue showed almost similar particle size compared to that before leaching. Particles are well distributed throughout with little agglomeration; particle sizes ranged from 5 to 30 μm. In Fig. 1(b), the average particle size of MnO_2 is found to be 9 nm, indicating good crystallinity.

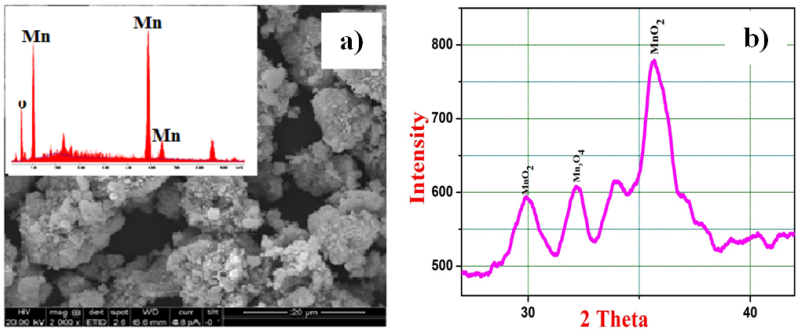

FIG. 1. EDAX/SEM and XRD spectra of MnO_2 from dry cells

4. Cyclic voltammetry studies

The MnO_2 electrode was prepared as a commixture with 10 wt.% of MnO_2 powder as active material with 90 wt.% of graphite. The constituents were mixed along with 3 drops of silicone oil to obtain uniform composition. Electrochemical activity of MnO_2 is often assessed by CV and electrochemical impedance spectra (EIS). An electrochemical measurement utilizes a three-electrode system having working electrode, Ag/AgCl reference electrode and a platinum wire as counter electrode. Cyclic voltammetry (CV) and EIS were performed in potential between $+0$ to -1 V using 0.5 M KCl, NaOH, Na_2SO_4 and NaCl electrolytes at a constant scan rate [6, 10]. To evaluate the electrochemical reversibility (E_R) of the sample, the potential window of CV was changed from $+0$ to -1 V and sweep rate 10 mV as shown in Fig. 2(a). A smaller the value of $E_0 - E_R$ shows the reversibility of the electrode reaction is greater. In Figs. 2(a) and 2(b), it is clearly shown that the smaller the value of $E_0 - E_R$, the greater the reversibility of the electrode reaction is. Samples having lower solution resistance values (Rs) are going higher conductivity values. In Figs. 2(a) and 2(b), it is readily seen that the MnO_2 sample using 0.5 M NaOH has lower E_R compare to different electrolytes, indicating the higher conductivity. The comparative cyclovoltammetric results of electrode in several electrolytes at a scan rate of 10 mV/s are tabulated in Table 1. Fig. 3(a) to (d) show the different scan rates with different electrolytes. The effect of scan rate is presented in Fig. 3. As the

TABLE 1. Electrochemical reversibility

Electrolytes	E_0 (mV)	E_R (mV)	$E_0 - E_R$	Rct (ohm)	$C(F) \times 10^{-5}$
0.5 M KCl	0.3951	0.3373	0.0578	15.75	0.0282
0.5 M NaOH	0.3040	0.3261	0.0221	15.15	0.01594
0.5 M Na_2SO_4	0.4443	0.3939	0.0504	22.28	0.01285
0.5 M NaCl	0.8268	0.3569	0.4699	19.26	0.01414

scan rate increases, the CV profile deviates from the ideal capacitive behavior. This is mainly because the redox reactions depend on the insertion-deinsertion of the alkali ion or protons from the electrolyte. At slower scan rates, the diffusion of ions from the electrolyte can gain access to almost all available pores on the electrode surface, leading to a complete insertion reaction, indicating excellent capacitive behavior and a low contact resistance However, the curve shape is gradually distorted from rectangular to quasi-rectangular with an increase of the scan rate from 10 mV/s to 50 mV/s. The experimental information shows the redox reactions for all electrolytes, as indicated by the moderately large $E_0 - E_R$ and Rct. However, the $E_0 - E_R$ of electrode in 0.5 M NaOH was merely 0.0221 mV and 15.15 Ω, as shown in Fig. 4(a) to (d), which is smaller than that of the different electrolytes as seen the Table 1. This indicates that the capacitive behavior of the given electrode in 0.5 M NaOH is better than the other electrolytes.

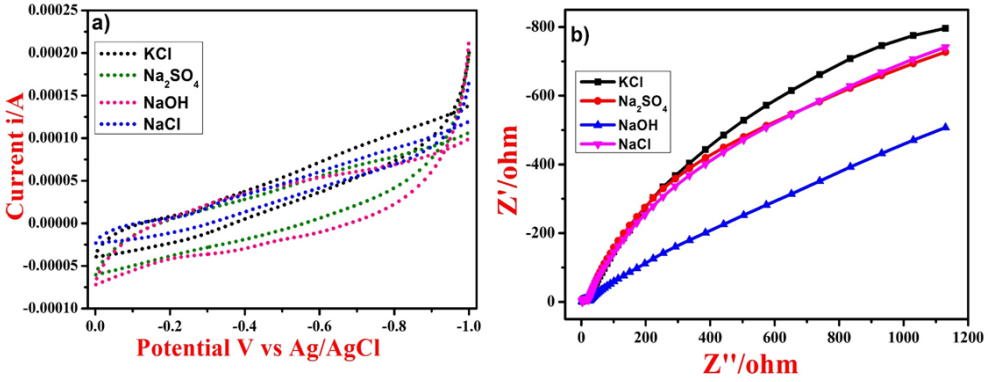

FIG. 2. a) Cyclic voltagramms of MnO_2 different electrolytes; b) Impedance spectra of MnO_2 electrode

5. Photocatalytic Activity of MnO_2

The photocatalytic enactment of the as-prepared sample was assessed through the photocatalytic degradation of Rhodamine-B (RB) and Indigo carmine(IC) under visible light irradiation. In these experiments, 60 mg of MnO_2 was dispersed in 250 ml IC (20 ppm) and similarly Rhodamine-B aqueous solutions respectively. The mixed suspensions were first magnetically stirred in the dark for 30 min to reach the adsorption-desorption equilibrium. Under stirring at ambient conditions, the mixed suspensions were exposed to visible light irradiation produced by a 400 W metal Philips lamp (wavelength: 254 nm). At certain time intervals, 5 ml aliquots of the mixed suspensions were extracted. The filtrates were analyzed by recording UV-vis spectra of RB and IC using a Spectratreats 3.11.01 Release 2A UV–vis spectrophotometer.The UV-vis absorption of MnO_2 show an intense absorption band in the range 200 to 220 nm. In Fig. 5 shows the UV-vis absorption spectra of RB and IC as a function of the catalytic reaction time [11]. Both RB and IC solutions turns colorless after 30 min, which indicates complete degradation of the dye molecules by MnO_2. After 30 min of reaction, the MnO_2 showed a higher efficiency in degradation of IC compared to RB. During the process of IC and RB degradation, the MnO_2 is reduced to Mn^{2+}, and leaches into the water and 74 % degradation is achieved under optimal conditions. It was determined that using the as-recovered MnO_2 Nano particle from waste dry cells, the dye solutions with concentration 60 mg/L can be degraded up to 74 % and mineralized up to 24 % in 45 minutes.

6. Conclusion

In this study, an aqueous technique was utilized to recover MnO_2 nanoparticles from waste dry cells by hydrometallurgy. Highly porous nano-MnO_2 is effectively recovered. Electrochemical estimations meant that the

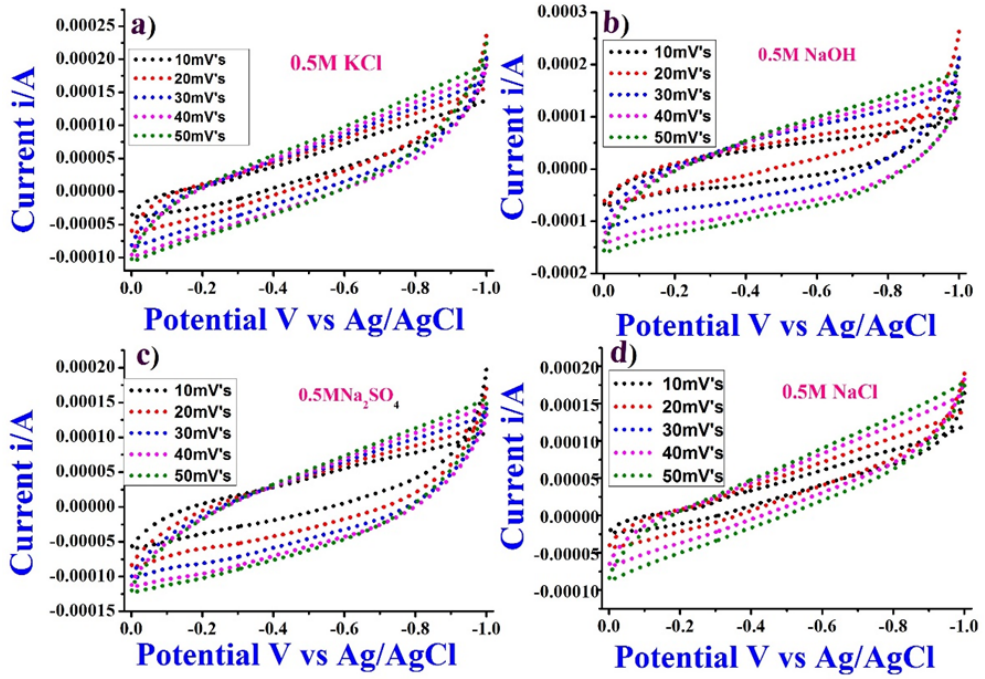

FIG. 3. Different scan rate of MnO_2 in different electrolytes

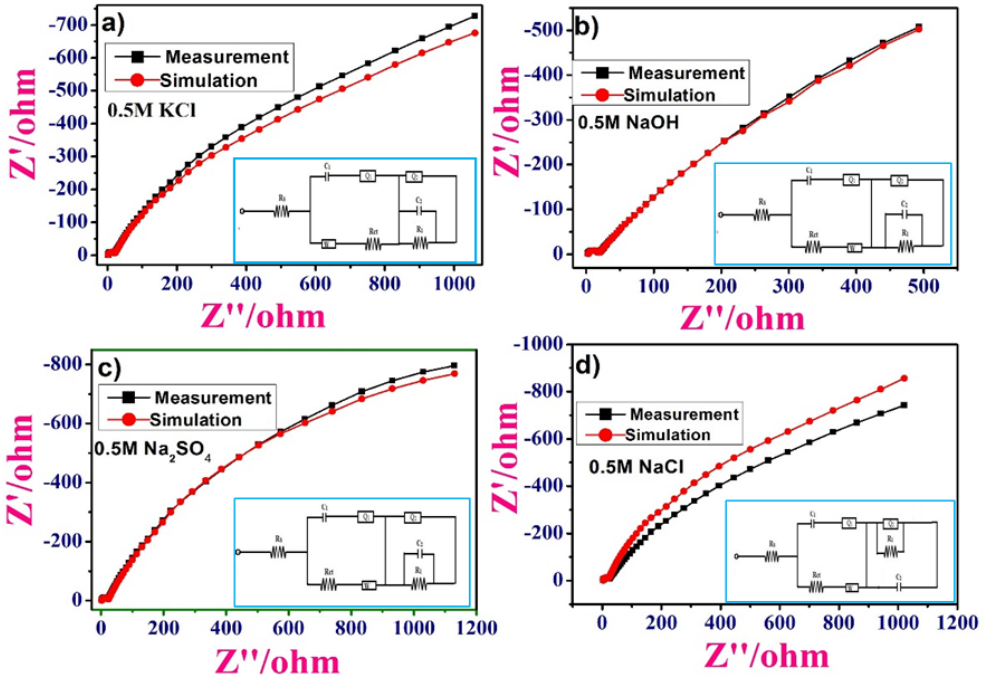

FIG. 4. Nyquist plots and equivalent circuit for MnO_2 electrode in different electrolytes

MnO_2 obtained displayed high electrochemical activity when the precipitates are kept at 100 °C for 24 hrs. The electric limit of this example demonstrated to be superior in correlation with the business tests. This showed that the MnO_2 had the best electrochemical execution at a high sweep rate of 10 mV/s. The recovered specimen displayed low charge exchange resistance (Rct) and high capacitive authorization. The morphology and crystallinity of MnO_2 improve in catalytic enactment in degradation of RB and IC. Using the as-obtained MnO_2, the IC solution with concentration 60 mg/L was shown to be degraded up to 74 % and mineralized up to 24 % and RB up to 72 % in 45 minutes.

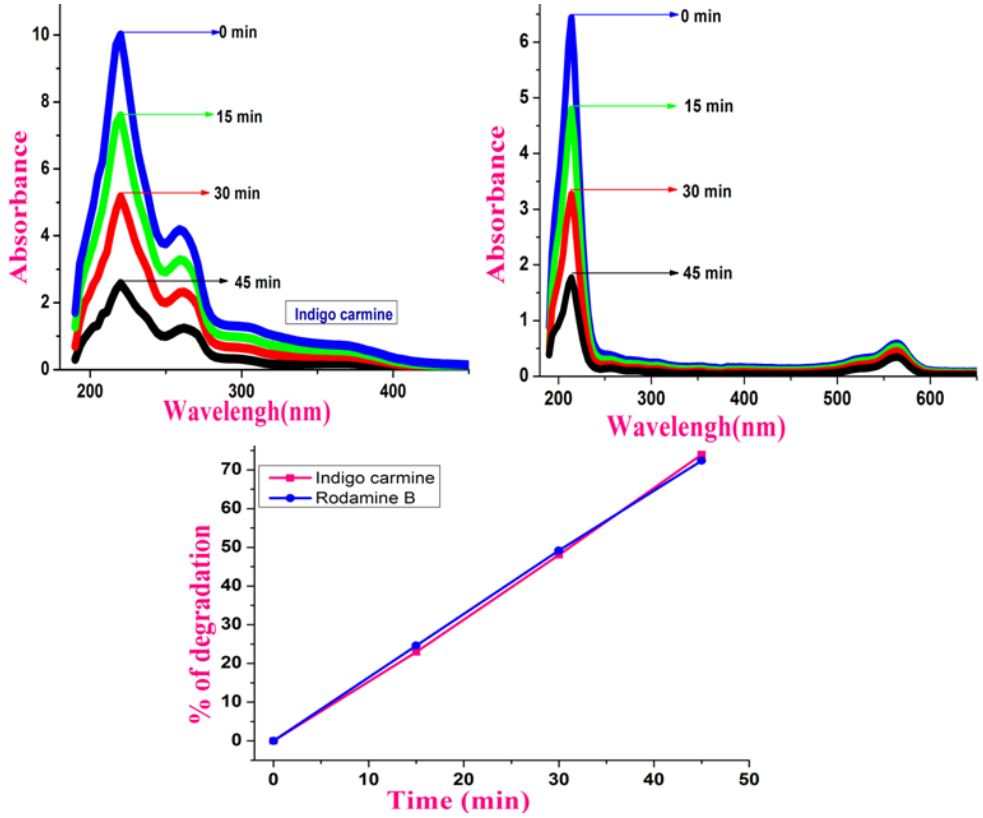

FIG. 5. UV-vis absorption spectra of RB and IC as role of time catalyzed by MnO_2

References

[1] Gallegos M.V., Falco L.R., et al. Recovery of manganese oxides from spent alkaline and zinc-carbon batteries. An application as catalysts for VOCs elimination. *Waste Management*, 2013, **33**, P. 1483–1490.

[2] Sobianowska-Turek A., Szczepaniak W., Zab-locka-Malicka M. Electrochemical evolution of reducers – Recovery of Mn from Zinc-Mn and Zinc-C battery waste. *Journal of Power Sources*, 2014, **270**, P. 668–674.

[3] Baba A.A., Adekola A.F., Bale R.B. Development of a combined pyro-and hydro-metallurgical route to treat spent Zinc-carbon batteries. *Journal of power sources*, 2009, **171**, P. 838–844.

[4] Macolino P., Manciulea A.L., et al. Manganese recovering from alkaline spent batteries by ammonium peroxodisulfate. *Acta Metallurgica Slovaca*, 2013, **19** (3), P. 212–222.

[5] Andrade Tacca C.A., Duart M.M.E. Acid leaching and electrochemical recovery of manganese from spent alkaline batteries. 2nd Mercosur Congress on Chemical Engineering and 4th Mercosur Congress on Process Systems Engineering.

[6] SiXu Deng, Dan Sun, et al. Synthesis and electrochemical properties of MnO_2 nanorods/graphene composites for supercapacitor applications. *Electrochimica Acta*, 2013, **111**, P. 707–712.

[7] Devreese J.T., Evrard R.P., Van Doren V.E. *Highly Conducting One-DimensionalSolids*. Plenum, New York, 1979.

[8] Pandey B.K., Shahi A.K., Gopal R. Synthesis, optical properties and growth mechanism of MnO nano structures. *Applied Surface Science*, 2013, **283**, P. 430–437.

[9] Kursunoglu S., Kavya M. Dissolution and precipitation of Zinc and Manganese obtained from spent Zinc-carbon and alkaline battery powder. *Physicochem. Probl. Miner Process*, 2014, **50**, P. 39–53.

[10] Buzatu M., Aceanu S.S., et al. Recovery of zinc and manganese from spent batteries by reductive leaching in acidic media. *Journal of power sources*, 2014, **247**, P. 612–617.

[11] Chanhlin Yu, Gao Li, et al. Fabrication,characterization of β-MnO_2 micro rod catalysts and their performance in rapid degradation of dyes of high concentration. *Catalysis Today*, 2014, **224**, P. 154–162.

NANOSYSTEMS: PHYSICS, CHEMISTRY, MATHEMATICS, 2016, 7 (4), P. 662–666

Synthesis and characterization of nano ZnO and MgO powder by low temperature solution combustion method: studies concerning electrochemical and photocatalytic behavior

K. N. Shravana Kumara[1,2], H. P. Nagaswarupa[1*], K. R. Vishnu Mahesh[3,4], S. C. Prashantha[1], M. Mylarappa[5,6], D. M. K. Siddeshwara[7,2]

[1]Research Centre, Department of Science, EWIT, Bengaluru-560091, India
[2]Research and Development Centre, Bharathiar University, Coimbatore-641046, India
[3]Department of Chemistry, Dayananda Sagar College of Engineering, Bengaluru-78, India
[4]Dr. Premachandra Sagar Center for Advance Functional Materials, DSCE, Bengaluru-78, India
[5]Research Centre, Department of Chemistry, AMC Engineering College, Bengaluru-83, India
[6]Department of Studies and Research in Chemistry, B.H Road, Tumkur University Tumkur, Karnataka, India
[7]Department of Chemistry, Jyothi Institute of technology, Bengaluru-560062, India

*nagaswarupa77@gmail.com

PACS 81.07. -b **DOI 10.17586/2220-8054-2016-7-4-662-666**

The objective of the research was mainly focused on the synthesis of ZnO and MgO nanoparticle by low temperature solution combustion method using Urea as fuel. The accurate size and morphology of the nanoparticles were studied from Transmission Electron Microscopy (TEM) to assess the structure of the ZnO and MgO particles. The phase composition of the Synthesized ZnO and MgO nanoparticles were confirmed from powder X-ray diffractometer (PXRD). The electrochemical impedance spectroscopy (EIS) shows the charge transfer capacity was more in the electrode with zinc oxide compared to magnesium oxide. Cyclic voltammetry studies were performed to ascertain the electrochemical reversibility of electrode.We evaluate the photocatalytic activity of nanoparticles shows rapid color removal and reduction in the concentration of dyes.

Keywords: Synthesis, ZnO, MgO, electrochemical and photo catalytic behavior.

Received: 5 February 2016

Revised: 1 May 2016

1. Introduction

The photocatalytic degradation efficiency and mineralization degree of dyes are limited because of the slow interfacial electron transfer. In recent years, the light-converting materials have attracted tremendous attention for photocatalysis and solar energy collection which can be easily absorbed by a given dye and thus effectively excite the dye to generate more electron-hole pairs, resulting in the improvement of the self-sensitized dye degradation. In this work, we report the photocatalytic degradation of Methylene Blue (MB) and Methyl Orange (MO) under visible light irradiation by using ZnO/MgO nanoparticles synthesized by a solution combustion method [1]. It was found that ZnO/MgO particles exhibited high enhancement of visible light photocatalytic performance in the degradation of MB and MO.

Currently, inorganic nano metal oxides (TiO_2, MgO, CaO and ZnO) are attracting research interest due to their safety, stability and multifunctional properties [2]. Design of materials which can be efficiently trapped and transfer energy in the form of charges is a major challenge in photocatalysis, photoluminescence (PL) and solar energy conversion fields. However, less progress has been made for nanomaterials, which often exhibit their unique size dependent physical/chemical properties due to their large surface-to-volume ratio and quantum confinement effects. Zinc oxide finds a wide range of applications as photocatalyst, lasers, white light emitting diodes (WLEDs), sensors, antireflection coatings, antibacterial, antifungal, solar cell material, varistors, optical devices, piezoelectric devices, optoelectronic devices, photonics etc [3].

The aim of the work is the synthesis of ZnO and MgO Nanoparticle with Urea as a fuel by using low cost solution combustion method. The cyclic voltammetry and photocatalytic activity were carried out to predict the properties of prepared samples.

2. Experimental

2.1. Synthesis of ZnO/MgO nano particles

In a synthesis, according to the stoichiometric ratio and molar mass of Zinc Nitrate ($ZnNO_3{\cdot}6H_2O$), Magnesium Nitrate ($MgNO_3{\cdot}6H_2O$) and Urea (NH_2CONH_2) were dissolved in a small amount of distilled water. Then, the solution was heated in a furnace 10 to 15 minutes at 450 °C. After the reaction was complete, the resulting white product was crushed into a fine powder. Then, the as-synthesized products were calcined at 500 °C for 4 h in air to obtain ZnO/MgO nanoparticles [4]. Stoichiometric compositions of the metals nitrates (oxidizers) and urea (fuel) were calculated using the total oxidizing and reducing valences of the components which serve as numerical coefficients for stoichiometric balances.

$$6Zn(NO_3)_2 + 10NH_2CONH_2 \rightarrow 6ZnO + 10CO_2 + 20H_2O + 16N_2, \tag{1}$$

$$6Mg(NO_3)_2 + 10NH_2CONH_2 \rightarrow 6MgO + 10CO_2 + 20H_2O + 16N_2. \tag{2}$$

2.2. Characterization

X-Ray diffraction analyses were carried out using a high resolution X-ray Diffractometer Maxima-7000 (Shimandzu) at a scanning rate of 2 $^\circ min^{-1}$ using CuKα radiation ($\lambda = 1.54$ Å) operating at 40 kV and 30 mA. TEM was used to study the accurate size and morphology of the ZnO/MgO. TEM images of the ZnO/MgO were obtained at 80 kV under high resolution TEM instrument (JEOL, Japan, and JEM-1011). Cyclic voltammetry and electrochemical impedance were measured by Electrochemical workstation CHI604E. The samples were analyzed by recording UV–vis spectra of MB and MO, using a Spectra treats 3.11.01 Release 2A UV–vis spectrophotometer.

3. Result and discussion

3.1. X-Ray diffraction

The average crystalline size, structure and phase of sample were determined using XRD in the 2θ range from 20 – 700 at a scanning rate of 2 $^\circ min^{-1}$. Using the peak width at half maximum height and peak position (2θ) in the XRD spectra, the inter layer space can be calculated utilizing Bragg's law:

$$n\lambda = 2d \sin\theta, \tag{3}$$

where λ is wave length of X-ray radiation used in the diffraction experiments, d is the space between layers in the clay lattice and θ is the measured diffraction angle.

The XRD form of ZnO/MgO nanoparticles obtained from solution combustion synthesis were as shown in Figs. 1(a) and 1(b). The peaks at 2θ values of 31.71, 34.41, 36.21, 47.46, 56.57, 62.76 and 67.94 ° corresponded to the crystal planes of (100), (002), (101), (102), (110), (103) and (112) of zinc oxide nano particles. The diffraction peaks could be referring to the spherical phase, which was evaluated with the data from JCPDS card No. 89-7102. The strong and narrow peak denotes that the product particles have a well-formed crystalline nature. The particle average size was calculated by the Scherrer formula and found to be in the range of 38 nm. In Fig. 1(b), the XRD results of MgO revealed that the structure was in cubic structure and these results were matched with JCPDS card number 75-1525. Peaks were absorbed at 36.8, 42.8, 62.1, 74.6 and 78.5 ° along with miller indices values (111), (200), (220), (311) and (222) respectively. As the width of the peak increases, the size of particle size decreases, which appears to make the present material in the nano range. The average crystallite size was measured as 40 nm.

3.2. Transmission electron microscopy

Transmission Electron Microscopy (TEM) is useful to understand if amorphous or crystalline sized particles are smaller. The TEM images of ZnO and MgO nano particles were shown in the Figs. 2(a) and 2(b) respectively. From Fig. 1(a), it is clearly shown that, ZnO exhibits nearly circular/spherical like structure and Fig. 1(b) indicating MgO exhibits the hexagonal shape and very homogeneous crystal structures without any observable pores.

3.3. Cyclic voltammetry studies

Cyclic voltammetry (CV) and electrochemical impedance measurements were carried out using CHI604E electrochemical workstation. For cyclic voltammetry studies, the test electrode was prepared by grinding the combination of 20 % prepared ZnO/MgO Nano powder, 70 % graphite powder and 10 % silicone oil used as binder and resulting pasted on a disk electrode. A platinum foil was used as a counter electrode; Ag-AgCl electrode as a reference electrode and 0.5 M Na_2SO_4 solution as electrolyte. All measurements were carried out at room temperature. The representative CV curves for ZnO/MgO are shown in Figs. 3(a,c,d) with different scan

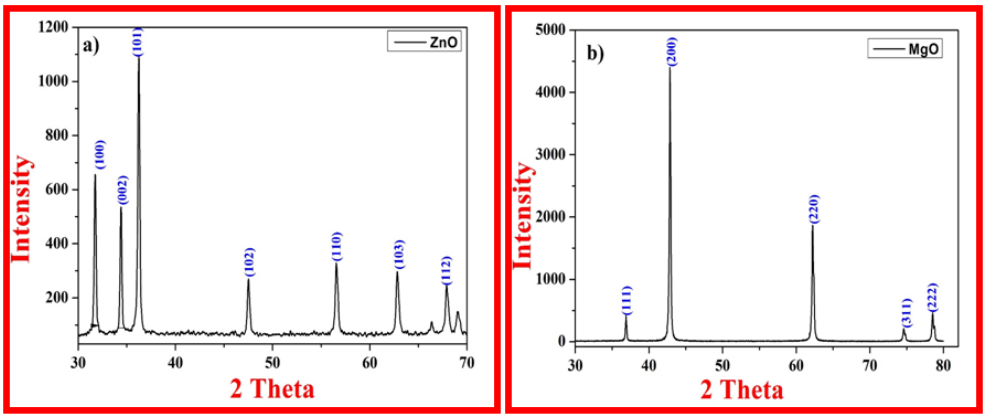

FIG. 1. XRD images of ZnO and MgO nano particles

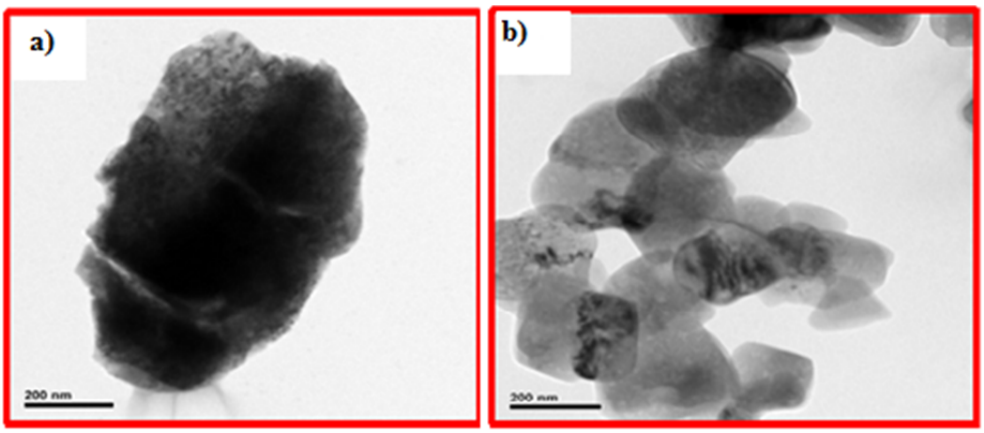

FIG. 2. TEM images of ZnO and MgO nano particles

TABLE 1. Electrochemical reversibility and EIS of ZnO/MgO Electrodes

Electrode	**Electrolyte**	$\mathbf{E_0}$ **(V)**	$\mathbf{E_R}$ **(V)**	$\mathbf{E_0 - E_R}$	$\mathbf{Rct(\Omega)}$	$\mathbf{C(F) \times 10^{-5}}$
ZnO	Na_2SO_4	0.2988	0.2739	0.0249	12.01	2.801
MgO	Na_2SO_4	0.2986	0.2639	0.0347	16.09	0.0326

rates. Increasing the scan rate from 10 mv to 50 mv, increases the oxidation and reduction of peaks for ZnO/MgO samples. The comparative CV results of electrodes ZnO/MgO at a scan rate of 0.01 V/s are tabulated in Table 1. The data there confirm that the electrochemical reversibility of ZnO is superior than that of MgO. Therefore, ZnO is more suitable for electro and photo catalytic activity applications. These results indicate that the charge and discharge process of the ZnO pasted electrode shows better electro chemical reversibility than MgO pasted electrodes. Fig. 3(b) represents the electrochemical impedance spectra (EIS) of the ZnO/MgO pasted electrodes. The impedance spectra of all these electrodes display a depressed semicircle considerable from charge transfer resistance (Rct) in the high-frequency region, corresponding to Rct in parallel connection with the capacitance (C) and the line at low frequency regions corresponds to Warburg impedance (W) of proton diffusion. A decrease in the charge transfer resistance and an increase in the capacitance indicate that ZnO-paste electrode shows more surface electrochemical activity than that of MgO-paste electrode.

3.4. Photocatalytic studies

In the current work, Methylene blue (MB) and Methyl orange (MO) dyes were used as pollutants in our models to assess the photocatalytic activity of ZnO/MgO under UV light irradiation. 60 mg of ZnO/MgO was spread in 250 ml MB (20 ppm). The mixed suspensions were first magnetically stirred in the dark for 30 min

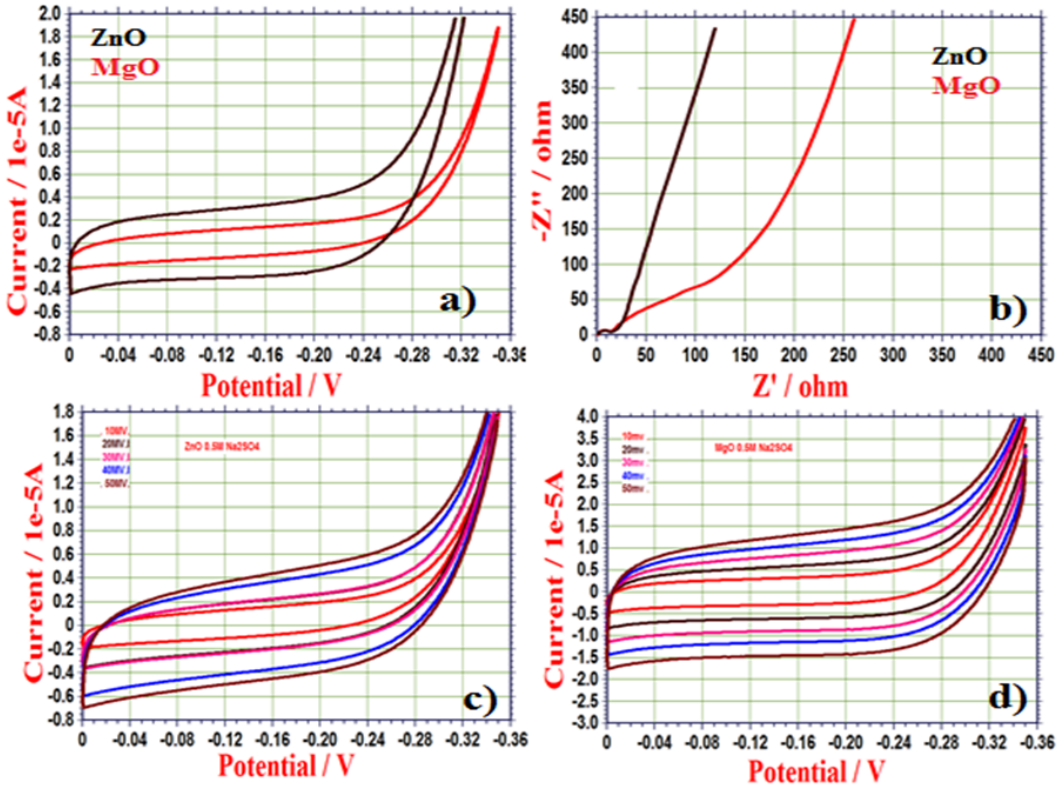

FIG. 3. Cyclic voltagramms and EIS of a) ZnO b) MgO with different scan rate

to reach the adsorption-desorption equilibrium. Under the ambient conditions and stirring, the mixed suspensions were open to visible light irradiation created by a 400 W metal Philips lamp (wavelength: 254 nm). At certain time intervals, 5 ml aliquots of the mixed suspensions was extracted. The filtrates were analyzed by recording UV-vis spectra of MB and MO using a Spectratreats 3.11.01 Release 2A UV-vis spectrophotometer. In UV light, RGO/ZnO can absorb UV light (254 nm) and generate electron-hole pairs. These photo-produced electron and hole pairs can travel into the catalyst surface and react with surface adsorbed O_2 to form active oxygen species. Photo degradation of MB and MO by ZnO/MgO nanoparticles was studied. In Figs. 4(a) to (b) show the UV-vis absorption spectra of MB and MO as a function of the catalytic reaction time. Both MB and MO solutions turns colorless after 60 min that specifies that complete degradation of the dye molecules by ZnO/MgO. After 60 min of reaction, the ZnO/MgO, Showed a good catalytic degradation of MO. It was observed that by using prepared composite material, the MB solution with concentration of 60 mg/L can be degraded up to 93 % in 60 minutes, whereas the MO was degraded up to 76 % using ZnO particle. Additionally, 98 % and 91 % of MB and MO respectively were degraded using MgO nanoparticles.

4. Conclusion

In the present work, ZnO and MgO were prepared by simple and low cost solution combustion method at low temperatures (400 °C). The average grain sizes of ZnO and MgO nanoparticles were found to be 38 nm and 40 nm, which are confirmed by XRD results. The ZnO pasted electrode showed better electro chemical reversibility than the MgO pasted electrode. A decrease in the charge transfer resistance and an increase in the capacitance indicate that ZnO pasted electrode shows more surface electrochemical activity than that of MgO pasted electrode. The photocatalytic activity of ZnO/MgO nanoparticles showed a good catalytic degradation of MB and MO. This indicates that using as-prepared composite material, the MB and MO solution with concentration 60 mg/L can be degraded up to 98 % and 93 %, MO degraded up to 91 % and 76 % in 60 minutes using ZnO and MgO particles.

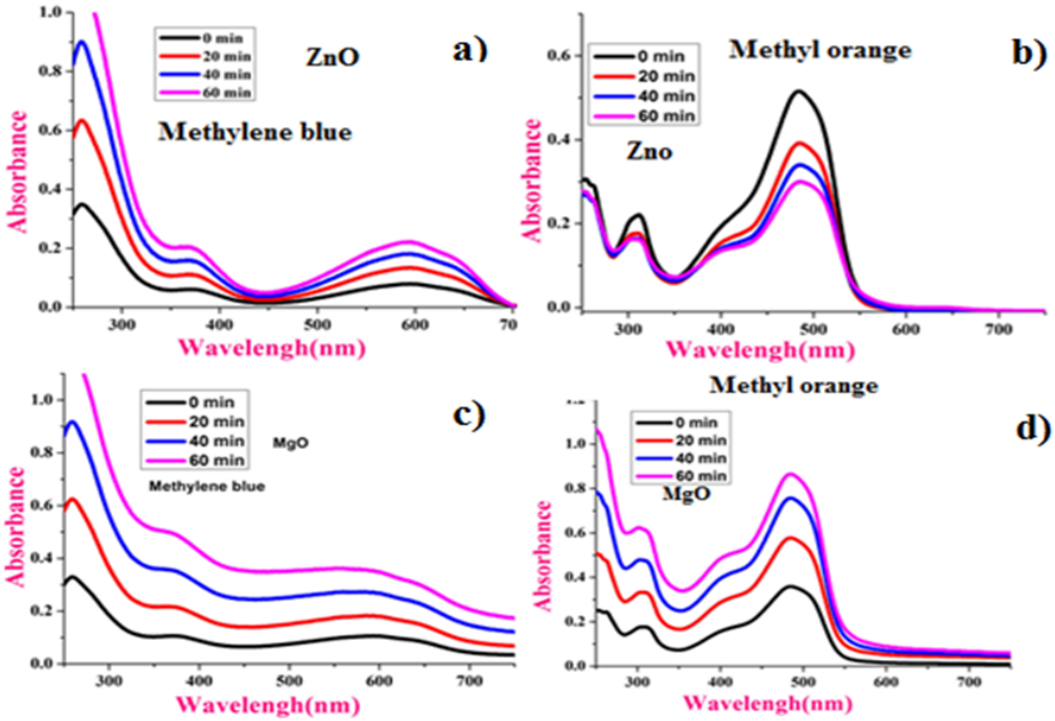

FIG. 4. UV-visible absorption spectra of MB and MO catalysed by ZnO and MgO

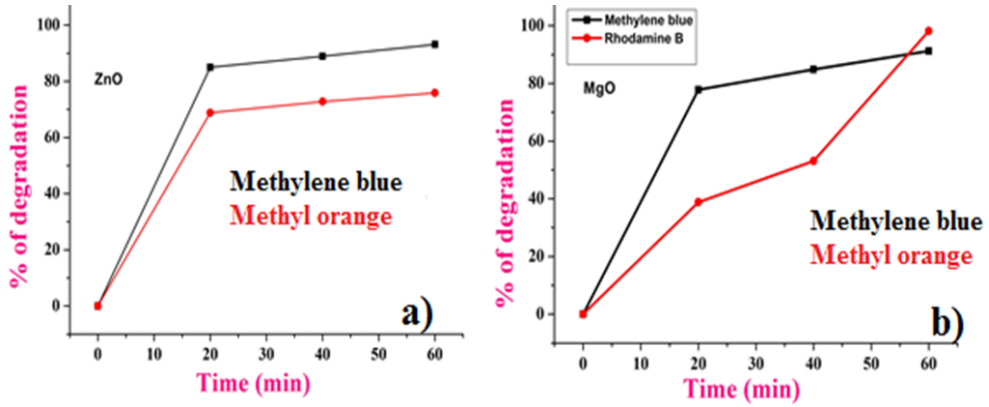

FIG. 5. Effect of Degradation of MB and MO by ZnO and MgO

References

[1] Park J.Y., Lee Y.J., et al. Chemical synthesis and characterization of highly oil dispersed MgO nanoparticles. *J. Ind. Eng. Chem.*, 2006, **12**, P. 882–887.

[2] Naik R., Prashantha S.C., et al. Low temperature synthesis and photoluminescence properties of red emitting Mg_2SiO_4: Eu^{3+} nanophosphor for near UV light emitting diodes. *Sensors Actuators B*, 2014, **195**, P. 140–149.

[3] Anilkumar M.R., Nagaswarupa H.P., et al. Bio-inspired route for the synthesis of spherical shaped MgO:Fe^{3+} nanoparticles: Structural, photoluminescence and photocatalytic investigation. *Spectrochimica Acta Part A: Molecular and Biomolecular Spectroscopy*, 2015, **149**, P. 703–713.

[4] Patil K.C., Hegde M.S., Tanu Rattan, Aruna S.T. *Chemistry of Nanocrystalline Oxide Materials, Combustion Synthesis, Properties and Applications*. World Scientific Publishing Co. Pt. Ltd., UK, 2008.

NANOSYSTEMS: PHYSICS, CHEMISTRY, MATHEMATICS, 2016, 7 (4), P. 667–674

Preparation of chitosan/different organomodified clay polymer nanocomposites: studies on morphological, swelling, thermal stability and anti-bacterial properties

B. H. Nanjunda Reddy[1,a], V. Venkata Lakshmi[*,2], K. R. Vishnu Mahesh[**,3], M. Mylarappa[2,a], N. Raghavendra[4] and T. Venkatesh[5]

[1]Department of Chemistry, Amrita School of Engineering, Bengaluru, Campus, Amrita Vishwa Vidyapeetham University, Bangalore–560035, Karnataka, India

[a]Department of Studies and Research in Chemistry, B.H̃ Road, Tumkur University, Tumkur–572103, Karnataka, India

[2]Research center, Department of Chemistry, AMC Engineering College, Bengaluru–560083, India

[3]Department of Chemistry, Dayananda Sagar College of Engineering, Sahvige Malleshwara Hills, Kumara Swamy Layout, Bangalore–560083, Karnataka, India

[4]CMRTU, RV College of Engineering, Bengaluru–560059, Karnataka, India

[5]Department of Chemistry, ACS College of Engineering, Bengaluru–560074, Karnataka, India

*laxmimurthy@rediffmail.com, **vishnumaheshkr@gmail.com

PACS 83.80.-k **DOI 10.17586/2220-8054-2016-7-4-667-674**

In the current study, chitosan films were prepared by dispersing different commercially-modified nanoclays, such as C-Na, C-10A, C-15A, C-30B, and C-93A. The exfoliation and morphology were studied using XRD and SEM. The C-15A, C-30B and C-93A nanoclays/Cts BNCs (Bionanocomposites) showed very good uniform exfoliation compared to that of other clays. The thermal analyses were evaluated using DSC and TGA. These results also confirmed that because of exfoliation, the thermal properties were improved in the case of C-15A, C-30B and C-93A nanoclays/Cts BNCs. The swelling capacity of a chitosan/clay films were studied. Increasing the chitosan content in the film increased the swelling capacity significantly; the decreasing order of swelling capacity of Cts/Clay films is in accordance with the decrease in clay content. Greater swelling capacity is shown by films Cts, C-Na and C-10A is because of the presence of greater hydrophilic agencies in the film makeup, which assist in improving the swelling characteristics of the films. The antibacterial activities of Cts/clay were also investigated against Gram-negative and Gram-positive bacteria (*E. coli* and *S. aureus*) according to the zone of inhibition in the disc diffusion method.

Keywords: chitosan, clay, bio-nanocomposites, swelling property and anti-bacterial property.

Received: 5 February 2016

Revised: 11 May 2016

1. Introduction

In the most recent decade, polymer/clay composites have received much attention because of their astonishing ability to improve most of the properties and are an essential alternative to standard polymer composites. The intercalation of polymers into the gallery of the clays brings greater characteristics to hybrid materials [1–4]. In comparison to the vast research on polymer/clay composites, the quantity of biopolymer/clay composites research is comparatively smaller [5–7]. Chitosan (Cts) is a polysaccharide that consists of N-acetyl-glucosamine and N-glucosamine units and it is largely insoluble at neutral and alkaline pH, given that its pKa within the variety of 6.2–7.0 is one of the second most plentiful natural polymers after cellulose in the world, naturally obtained and is derived by deacetylation of chitin present in crustaceous species [8, 9]. In addition to its unique properties such as biocompatibility, biodegrability and non toxicity, it is widely used in biotechnology, pharmaceuticals, cosmetics, textiles agriculture fields due to its antifungal and antimicrobial activities [10]. Unmodified chitosan is not antimicrobially energetic at pH 7, since it does not dissolve or include a large number of charges on the amino groups. The antimicrobial activity of chitosan also increases with increasing degree of deacetylation, due to the increasing number of basic amino groups.

Montmorillonite (MMT) is a member of the smectite group minerals which has a layered shape or platelets. Because of its high aspect ratios and excessive surface area, if clay particles are properly dispersed in a polymer matrix at a loading level of 1–5 % (w/w), precise mixtures of physical and chemical properties may be enhanced, and in turn those composites become more attractive for making films and coatings for a multiplicity of commercial applications, such as drug delivery systems and antimicrobial systems due to their natural abundance and the

propensity with which they can be chemically and physically modified for drug delivery applications [11, 12]. Montmorillonite has been appreciably implemented for prolonged release of drugs as it could hold large amounts of drug due to its excessive cation exchangeability. The surface adsorption of various drugs like griseofulvin, indomethacin and prednisone to montmorillonite clay improves their dissolution rate. The hydrophilic and swelling properties of montmorillonite in aqueous media help to facilitate the wetting of hydrophobic drug substances. This clay ultimately improves the bioavailability of drugs.

Cts are capable of engaging with negatively charged clay, which has a silicate layer shape. When Cts dispersions have been blended with clays, the zeta potentioability of clays and the viscosities of the composite dispersion have been changed [13]. The dry fabric acquired from those composite dispersions is called a nanocomposite if the Cts intercalates into the silicate layer of the clay. Different types of clays, such as montmorillonite and rectorite, have all been used to prepare nanocomposite substances with Cts [14–17]. Within the practice method of these substances, it is necessary to use a heating treatment on the composite dispersion to initiate the nanocomposite formation [15, 18] Furthermore, the clay content material stimulated thermal stability and mechanical properties of the nanocomposites [16, 18]. Cts-clay nanocomposites have been developed and characterized for use as biosensors, packaging materials and superabsorbent substances [19–21]. Furthermore, Cts–clay films should retard the release of a bioactive agent integrated into the films. The current objective of these studies, in particular, targeted the impact of various organo-modified nanoclays on the properties of chitosan (Cts) based Bio-Nanocomposites (BNCs).

2. Experimental

2.1. Materials

Low molecular weight chitosan (CS) used in this work was bought from Sigma Aldrich Chemicals, Bangalore, and Karnataka, India. The Clays such as C-Na, C-10A, C-15A, C-30B, and C-93A were procured form Southern Clay Products, USA. Acetic acid and sodium hydroxide were obtained from Sigma Aldrich Chemicals, Bangalore, and Karnataka, India.

2.2. Preparation of clay/chitosan nanocomposites

The 2 % wt/vol of chitosan solution was prepared by dissolving it in 1 % acetic acid (pH=4.0) with continuous magnetic stirring for 30 min. and then allowed to sit overnight for complete dissolution, or alternatively, 3 % wt/vol ratio of clay (based on the chitosan wt.) was used. Therefore, an appropriate quantity of different clays were dispersed in 10 ml of 1 % acetic acid and magnetically stirred continuously for 24 hours at room temperature and ultrasonicated for about 30 minutes, for this solution, the as already prepared chitosan solution was transferred very slowly and this mixture was stirred for an additional 4 hours using magnetic stirrer. The resulting solution was carefully poured into Teflon-coated glass plates and kept overnight in a 60 °C oven. The resulting composite films were soaked in 1 % NaOH solution for 30 minutes to remove excess acidic content, followed by washed with distilled water several times to effect the removal of NaOH. Then, the composite films were peeled off from the glass plates and the resulting films again oven dried. Films were packed in air tight polyethylene pouches for further characterizations. A similar procedure was followed for the other clay sample dispersion in a chitosan matrix.

3. Results and discussion

3.1. X–Ray diffraction

The Fig. 1 shows the XRD patterns of neat Cts, Cts/C-Na, Cts/C-10A, Cts/C-15A, Cts/C-30B and Cts/C-93A nanocomposites with addition of 3 wt% of above commercial clays. The XRD pattern of Cts suggests the characteristic crystalline peaks at round 20 °. In line with the literature, after incorporation of clay inside Cts matrix the basal plane of Cts/C-Na at 2θ=7.2 ° which disappears and which will be substituted by new peak at around 6 ° whose d-spacing d=1.47 nm. The shift of the basal reflection of C-Na to a lower angle indicates the formation of an intercalated nanostructure, even as the peak broadening and lower depth most likely indicate a disordered intercalated or partially-exfoliated structure, in the case of unmodified C-Na, the inter space distance (d001) turned into enlarged from 1.23 to 1.47 nm (information required for specific composites Cts/93A, 15A, 30B)(approximate d-spacing values for C93A, C30B, C15A, C10A are 3.68, 3.53, 3.4, 3.27 respectively in accordance with graph). According to the XRD report, partial exfoliation is achieved only in the sample containing 3 % C-Na unmodified clay but no uniform exfoliation was noted for the composites of C-15A, C-30B and C-93A. However, according to SEM reports, partial exfoliation was achieved for the sample Cts/C-10A and same trend was observed in Fig. 1.

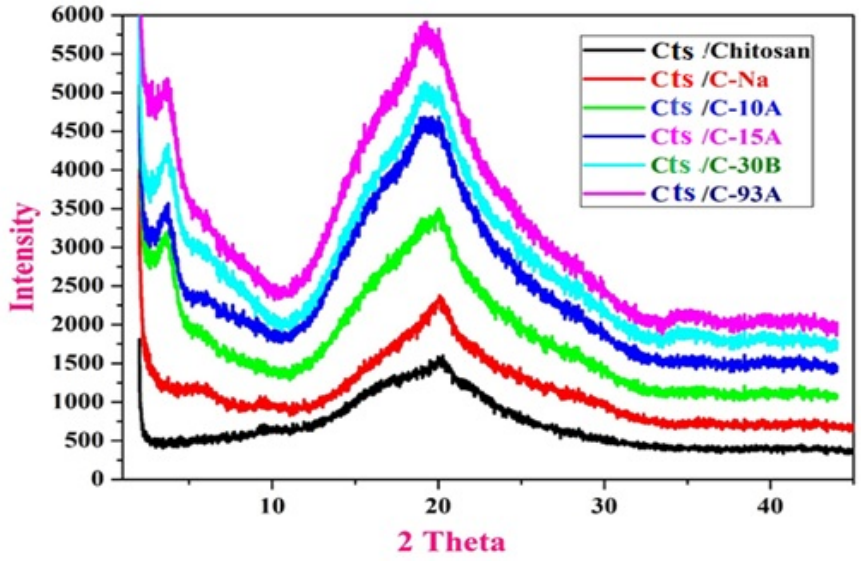

FIG. 1. XRD Pattern of chitosan with different organo modified clay

3.2. Fourier transfer infrared spectroscopy

FTIR was used to characterize the chemical interactions with Cts and clay in the nanocomposites. The organic cations in the clay may additionally comprise diverse useful functional groups that react with chitosan resin to improve interfacial adhesion among clay monolayer and polymer matrix, hence, this cation exchange effect is characterized by the enhancement of the magnitude of the 3193–3187 cm^{-1} band in conjunction with a reduction of intensities because of Si-O and Al-O. The enhanced intensity of the 3193–3187 cm^{-1} band displays the increased hydrogen bonding among the lattice hydroxyls and organic groups. Whilst the protons inside the chitosan are hydrogen bonded oxygen species of Si-O and Al-O segments, Si-O and Al-O bonds might be weakened and the tetrahedral symmetry of these moieties may be distorted. The FTIR spectrum of the clay shows the characteristic bands at 1662 cm^{-1} because of H-O-H bending, 1000 and 1182 cm^{-1} due to Si-O stretching 819 and 670 cm^{-1} due to (Al Mg)-OH vibration modes, while the IR spectra of Cts/C-10A showed additional peaks, including 1725 cm^{-1} (N-H bending), 1590 cm^{-1} (N-H bending) and 1455 cm^{-1} (C-H bending). The absorption band of the carbonyl(C=O) stretching for the secondary amide (amide first band) was observed at 1488 cm^{-1}. At 2356 cm^{-1}, the stretching frequency gradually increased from that of pure chitosan to C93A composite sample with the variation of the type of clay. FTIR was also used to study the polymer/clay interaction, since a shift in the δ_{NH3} vibration might be expected when $-\delta_{NH3}$ groups interact electrostatically with the negatively-charged sites of the clay. In fact, a shift of the δ_{NH3} band towards a lower frequency is noted in all the chitosan/clay films, as is shown in Fig. 2. However, this shift is higher for chitosan/clay films with the lowest amounts of chitosan, while the chitosan/clay films with the highest amounts of biopolymer show a frequency value the trend observed in the films of pure chitosan (Ct). This fact may be related to the $-\delta_{NH3}$ groups that do not interact electrostatically with the clay substrate (Fig. 2). The absorption frequency of pure chitosan in the range of 1721 to 1644 cm^{-1} was related to the vibrations of carbonyl bonds (C=O) of the amide group CONHR (secondary amide, ν_1 = 1721 cm^{-1}) and to the vibrations of protonated amine group (δ_{NH3}, $\nu_2 = 1644$ cm^{-1}).

3.3. Thermal analysis of Cts/clay composites using DSC and TGA

DSC showed two broad peaks for Cts/clay composites, one is an endothermic broad peak and the other one is an exothermic broad peak. The endothermic broad peaks for Cts, Cts/C-Na, Cts/C-10A, Cts/C-30B and Cts/C-93A composite films (as shown in Fig. 3) are: 273, 281, 297.5, 300, 271 and 292 °C respectively. The first temperature region is situated at high temperature in DSC curves because of heating rate used was higher 20 °C min^{-1}. The first peak could be assigned to the water loss, while the second to the decomposition of system components. It is bearing related to the thermal stability of nanocomposites. From these data, it can be concluded that nanocomposites of Ct/C-Na, Ct/C-10A, Ct/C-15A, Ct/C-30B and Ct/C-93A improved the thermal stability of chitosan. Additionally, for the degradation and deacetylation of chitosan and remaining residue at 270 °C and above, the decomposition in air is highly exothermic for the samples Ct/C-30B, Ct/C-93A. This may be due to

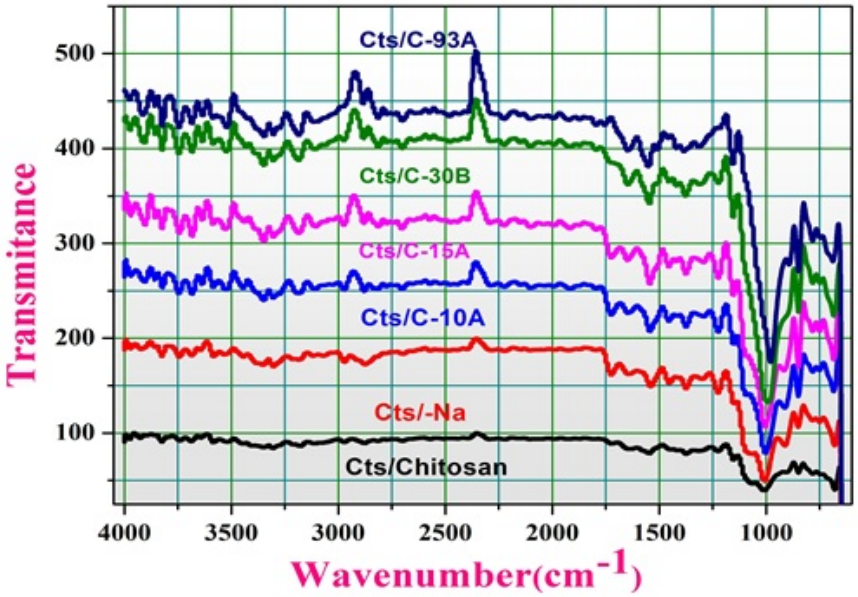

FIG. 2. FTIR patterns of chitosan with different organo modified clay composites

the surfactants used during the modification of these cloisites (C-30B, C-93A) and the same phenomenon was observed in the Fig. 4 (decomposition of intercalated Ct/C-30B and Ct/C-93A layers occurred in the vicinity of 270 °C with significant weight loss). It has been observed that the melting points and exothermic broad peaks all the composite films were 90, 75, 88, 95, 92, 83 °C respectively. The TG, glass transition behavior of Cts and Cts/clay bio-composite films were measured by the DSC evaluation. The TG and melting endothermic height of Cts 3 wt% of Cts/clay has been shifted from approxi. 50–130 °C. The DSC does not detect any traces of thermal transitions for 3 wt% of MMT/clay. The melting endothermic peak of Cts was observed at 140 °C at the same time as the height of Cts/Clay bio composites shown at 150–250 °C, the melting temperature expanded with increased clay content (3 wt%) within the Cts. For these composites, one can find two peaks in TGA curves. In the first stage, a smaller loss in weight 10–12 % was observed compared to the second stage (40 %).

The addition of nanoclays produces a thermal barrier and decreases the weight loss, thus inorganic particles are found to enhance the thermal stability of the chitosan composites. As can readily be seen, better thermal stability was observed for Cts/C-10A, Cts/C-15A, Cts/C-30B, Cts/C-93A composites. This is linked with more intercalation and exfoliation of the chitosan and inorganic fillers (clay). In air flow, another degradation step at 63 °C for the samples Cts/C-10A and Cts/C-93A was observed, the cause of which may be assigned to the oxidative degradation of carbonaceous residue formed during second step. The carbonaceous residue is greater in these samples because of the nature of the modifiers/surfactants which were used in the modification of cloisites.

3.4. Morphological study using SEM

The morphology of surfaces with different surface structure between MMT (clay) and chitosan films are shown in Figs. 5(a-f) using SEM data. The surface of Cts exhibits a smooth laminated structure; comparatively, the surface of composite films seems to be course, indicating an improved intercalation of Cts chains in the clay platelets. Thus, SEM analysis results agreed with the XRD analysis results that produced increase in basal spacing value which was relatively small. This small increase indicated that most of chitosan were on clay (MMT) surface because of formation of hydrogen bonds and intermolecular interactions of these polymers. The exfoliated structure was observed in XRD results. Those outcomes have been corroborated with the aid of SEM effects. The homogenous dispersion of nanoparticles and homogenous matrix in SEM photographs give proof for an exfoliated structure.

3.5. Swelling study

The swelling capacity of a chitosan/clay films performs an essential function regarding the antibacterial activity, wound recovery potential and for biomedical packaging because of their excessive water/solvent retaining potential. The Cts, Cts/C-Na, Cts/C-10A showed higher swelling capacity than Cts/C-15A, Cts/C-30B and Cts/C-93A films, and, among the all these samples, Cts/C-15A showed lowest swelling capacity. This may be because of more

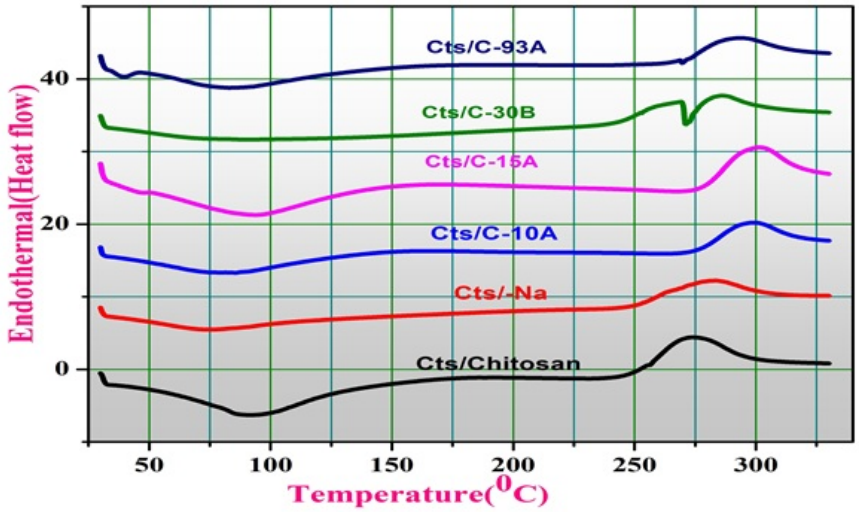

FIG. 3. DSC micrographs of chitosan with different organo modified clays

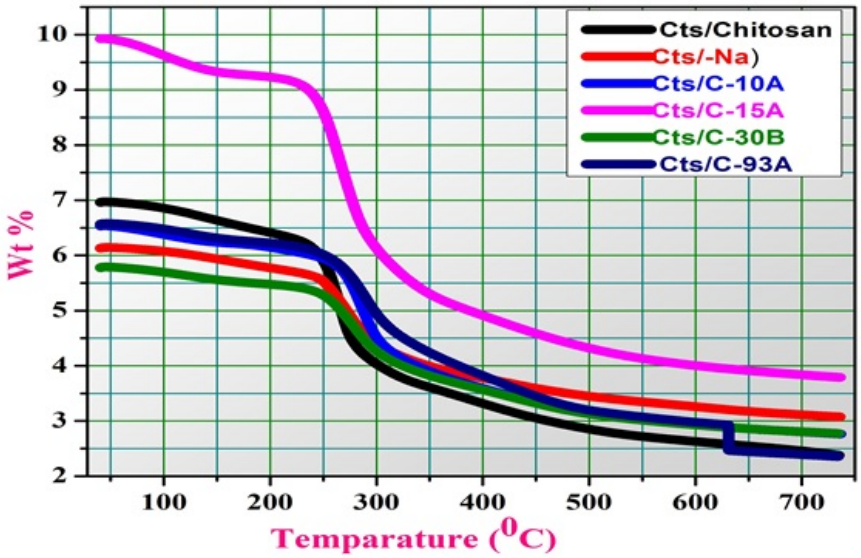

FIG. 4. TGA of chitosan with different organo modified clays

cross linking /interaction of clay with chotosan polymer chains for example, the swelling capacities of the samples were as follows: Cts-1.8 g/g; Cts/C-Na-1.85 g/g; Cts/C-10A 1.75g/g. The other films had the following values: Cts/C-15A-1.58 g/g; Cts/C-30B-1.5 g/g; Cts/C-93A-1.35 g/g respectively. The lowering of the swelling potential is attributed to the clay binding with Cts chains, i.e. the interplay of negative charges on the clay with 'O' and N–atoms of hydroxyl and amine groups present in Cts chains. This produces an additional cross links inside the chain networks. The higher degree of cross-linking with the film restricts the penetration of water for swelling. The increase in chitosan content in the film increases the swelling capacity significantly, the decreasing order swelling capacity of Cts/Clay films is in accordance with Cts/C-15A(1.35 g/g)< Cts/C-93A(1.5 g/g)< Cts/C-30B(1.58 g/g) ,Cts/C-10A< Cts/C-Na(1.7 g/g)< Cts(1.78 g/g) more swelling capacity is showed by films Cts,Cts/C-Na and Cts/C-10A is due to the presence of greater hydrophilic agents within the film network which assist in improving the films' swelling properties (Fig. 6).

4. Antibacterial tests

The antimicrobial activity of chitosan and chitosan-based nanocomposite films were examined qualitatively via an inhibition zone method. In this technique, specific pathogenic microorganism such as *S. aureus* and *Escherichia*

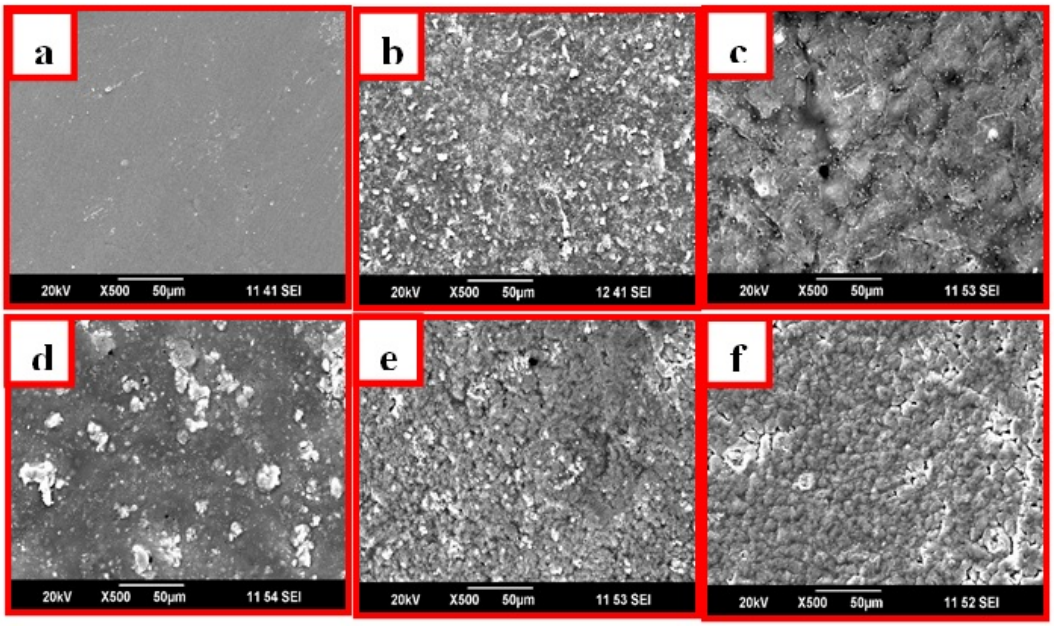

FIG. 5. SEM images of a) Pure Cts, b) Cts/C-NA, c) Cts/ C-10A, d) Cts/C-15A e) Cts/C-30B and f) Cts/C-93A

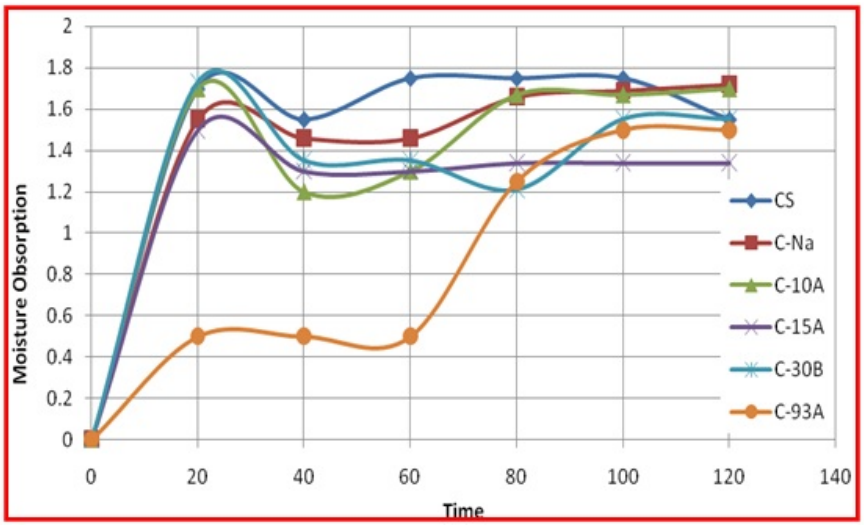

FIG. 6. Swelling behavior of chitosan with different organo modified clays

coli were used to assess the antimicrobial activity of the chosen two films. Both traces of *S. aureus* and *E. coli* were cultivated on tryptic soy (TS) agar (Difco Lab) at 30 °C for two days. All the stock cultures were saved at 4 °C. For the qualitative size of antimicrobial activity, the film samples were punched to make disks (diameter) 6 mm), and the antimicrobial activity present determined the use of a modified agar diffusion assay (disk check). The plates were examined for feasible clean zones after incubation at 37 °C for two days. The presence of any clear zone that shaped across the movie disk at the plate medium was recorded as an illustration of inhibition towards the microbial species. The qualitative antimicrobial activity of the films became determined the use of a quarter inhibition technique for testing pathogenic bacteria.

Pure chitosan film did not show any antibacterial properties. This effect of chitosan may be related fact that chitosan does not diffuse through the adjusted agar media in the agar diffusion test method, so that the only organism in direct contact with the active site of chitosan are inhibited [22–24]. The inhibition zone diameters for the Cts/C-15A sample is better than those of Cts/C93A sample, and it has also been observed that *S. aureus* is more sensitive to Cts/C15A than *E. coli*. This may be attributed to the antimicrobial activity of the quaternary

ammonium silicate layer of Ct/C-15A incorporated film. The effectiveness of such groups bearing alkyl substituents in disrupting bacterial cell membranes (especially for *S. aureus*) and causing cell lysis has been well documented in the literature [25–28]. In the case of Cts/C93A, greater activity was noted against *E. coli* than *S. aeureus*. There are some suggestions that the antimicrobial activity of polymer clay nano composites depends on super molecular organization of the surfactants and the nanostructure of the components. Cts/C-93A has most activity against *E. coli* despite having the lowest surfactant content in the organoclay, that is, 90 % of the surfactants with respect to CEC(Cationic exchange capacity) whereas Cts/C-15A has highest surfactant content in the organo clay and has highest activity against *S. Aureus* (Fig. 7).

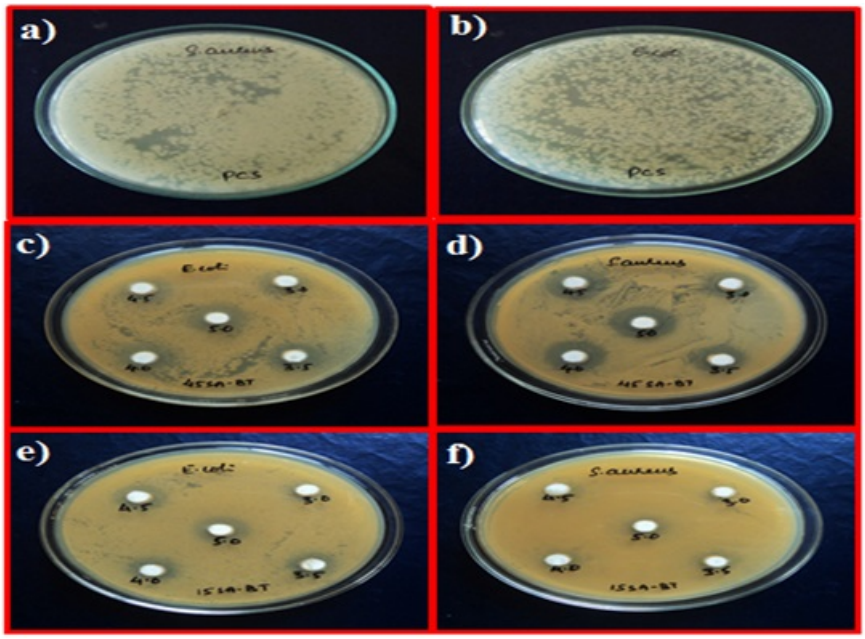

FIG. 7. Antimicrobial activity of a) pure Ct for E coli., b) Pure Ct for S aureus, c) Ct/C-93A for E coli, d) Ct/C-93A S aureus, e) Ct/C-15A for E coli, f) Ct/C-15A for S aureus

5. Conclusion

The effect of different organo-modified nanoclays on the properties of chitosan (Cts) based bio-nanocomposites (BNCs) was evaluated. The exfoliated structure was observed in XRD results. These results were corroborated by SEM results. The homogenous dispersion of nanoparticles and homogenous matrix in SEM images provided evidence for the BNC's exfoliated structure. The addition of nanoclays produces a thermal barrier and decreases the weight loss, thus inorganic particles are found to enhance the thermal stability of the chitosan composites. The increase in chitosan content in the film increased the swelling capacity significantly; the decreasing order swelling capacity of Cts/Clay films was due to the presence of more hydrophilic groups in the film network, which assist in improving the swelling characteristics of the films. The chitosan with different organo-modified clays exhibited optimum antibacterial activity against *E. coli.* and *S. aureus*.The inhibition diameters of these complexes were slightly smaller and the amount of antibiotic explains the smaller inhibition halos that the adsorption complexes showed in comparison to those of the antibiotic solutions.

References

[1] Ray S.S., Okamoto M. Polymer/layered silicate nanocomposites: a review from Preparation to processing. *Prog in Polym Sci.*, 2003, **28**, P. 1539–1641.

[2] Pavlidou S., Papaspyrides C.D. A review on polymer-layered silicate nanocomposites, *Prog in PolyM Sci.*, 2008, **33**, P. 1119–1198.

[3] Wilson B., Samanta M.K., Santhi K., Sampath Kumar K.P., Ramasamy M. Suresh Chitosan nanoparticles as a new delivery system for the anti-Alzheimer drug tacrine. *Nanomedicine: Nanotechnology, Biology, and Medicine*, 2010, **6**, P. 144–152.

[4] Dev A., Binulal N.S., Anitha A., Nair S.V., Furuike T., Tamura H., Jayakumar R. Preparation of poly (lactic acid)/chitosan nanoparticles for anti-HIV drug delivery applications. *Carbo Poly.*, 2010, **80**, P. 833–838.

[5] Wang X., Du Y., Luo J., Lin B., Kennedy J.F. Chitosan/organic rectorite nanocomposite films: structure, characteristic and drug delivery behavior. *Carbohydrate Polymers*. 2007, **69**, P. 41–49.

[6] Depan D., Pratheep Kumar A., Singh R.P. Cell proliferation and controlled drug release studies of Nano hybrids based on chitosan-g-lactic acid and montmorillonite. *Acta Biomater.*, 2009, **5**, P. 93–100.
[7] Wang X., Du Y., Yang J., Wang X., Shi X., Hu Y. Preparation, characterization and antimicrobial activity of chitosan/layered silicate nanocomposites. *Polymer.*, 2006, **47**, P. 6738–6744.
[8] Mizushima Y., Ikoma T., Tanaka J., Hoshi K., Ishihara T., Ogawa Y., Ueno A. Injectable porous hydroxyapatite micro particles as a new carrier for protein and lipophilic drugs. *J Cont Rele.*, 2006, **110**, P. 260–265.
[9] Xu Q.G., Czernuszka J.T. Controlled release of amoxicillin from hydroxyapatite-coatedpoly (lactic-co-glycolic acid) microspheres. *J Control Release*, 2008, **127**(2), P. 146–153.
[10] Real R.P., Padilla S., Vallet-Regí M. Gentamicin release from hydroxyapatite/poly (ethyl Methacrylate) composites. *J. Biomed Mater Res.*, 2000, **52**, P. 1–7.
[11] Han Y.S., Lee S.H., Choi K.H., Park I. Preparation and characterization of chitosan-claynanocomposites with antimicrobial activity. *Jour of Phys and Chem of Solids.*, 2010, **71**, P. 464–467.
[12] Katti K.S., Turlapati P., Verma D., Gujjula P.K., Katti D.R. Static and dynamic mechanical behavior of hydroxyapatite-polyacrylic acid composites under simulated body fluid. *Ameri Jour Biochem Biotechno*, 2006, **2**, P. 73–79.
[13] Ebru Günister, Dilay Pestreli, Cüneyt H. Ünlü, Oya Atıcı, Nurfer Güngör. Synthesis and characterization of chitosan-MMT biocomposite systems. *Carbohydrate Polymers*, 2007, **67**(3), P. 358–365.
[14] Alexandre M., Dubois P. Polymer-layered silicate nanocomposites: Preparation, properties and uses of a new class of materials. *Materials Science and Engineering*, 2008, **R28**, P. 1–63.
[15] Margarita Darder, Montserrat Colilla. Eduardo Ruiz-Hitzky Chitosan-clay Nano composites: application as electrochemical sensors. *Applied Clay Science*, 2005, **28**, P. 199–208.
[16] Wang S.F., Shen L., Tong Y.J., Chen L., Phang I.Y., Lim P.Q., Liu T.X. *Polymer Degradation and Stability*, 2005, **90**, P. 123–131.
[17] Sadok Letaïef, Pilar Aranda, Eduardo Ruiz-Hitzky. Influence of iron in the formation of polypyrrole-clay nanocomposites. *Applied Clay Science*, 2005, **28**(1-4), P. 183–198.
[18] Xiaoying Wang, Yumin Du, Jianhong Yang, Xiaohui Wang, and Xiaowen Shi, Ying Hu. *Polymer*, 2006, **47**, P. 6738–6744.
[19] Rhim J., Hong S., Park H., Perry K.W. Preparation and characterization of chitosan-based nanocomposite films with antimicrobial activity. *Journal of Agricultural and Food Chemistry*, 2006, **54**, P. 5814–5822.
[20] Fan J., Hanson B. *Inorg. Chem.*, 2005, **44**, P. 6998–7008.
[21] Fan J., Slebodnick C., Angel R., Hanson B.E. *Inorg. Chem.*, 2005, **44**, P. 552–558.
[22] Ojagh S.M., Rezaei M., Razavi S.H., Hosseini S.M. Effect of chitosan coatings enriched with cinnamon oil on the quality of refrigerated rainbow trout. *Food Chemistry*, 2010, **120**, P. 193–198.
[23] Zivanovic S., et al. Antimicrobial Activity of Chitosan Films Enriched with Essential Oils. *Journal of Food Science*, 2005, **70**(1).
[24] Choma C., Clavel T., Dominguez H., Razafindramboa N., Soumille H., Nguyen-the C., Schmitt P. Effect of temperature on growth characteristics of Bacillus cereus TZ415. *International Journal of Food Microbiology*, 2000, **55**, P. 73–77.
[25] Hugo W.B., Russel A.D. Types of antimicrobial agents. In Principles and Practice of Disinfection. Preservation and Sterilization; Russel A.D., Hugo W.B., Ayliffe G.A.J., Eds. Blackwell Scientific Publications: Oxford, U.K, 1992, P. 7–68.
[26] Kim C.H., Choi J.W., Chun H.J., Choi K.S. Synthesis of chitosan derivatives with quaternary ammonium salt and their antibacterial activity. *Polym. Bull*, 1997, **38**, P. 387–393.
[27] Gottenbos B., Van der Mei H.C., Klatter F., Nieuwenhuis P., Busscher H.J. In vitro and in vivo antimicrobial activity of covalently coupled quaternary ammonium silane coatings on silicone rubber. *Biomaterials*, 2002, **23**, P. 1417–1423.
[28] Kim J.Y., Lee J.K., Lee T.S., Park W.H. Synthesis of chitosan oligosaccharide derivative with quaternary ammonium group and its antimicrobial activity against Streptococcus mutans. *Int. J. Biol. Macromol.*, 2003, **32**, P. 23–27.

NANOSYSTEMS: PHYSICS, CHEMISTRY, MATHEMATICS, 2016, 7 (4), P. 675–677

Superparamagnetism in FeCo nanoparticles

P. P. Pradyumnan

Department of Physics, University of Calicut, Kerala 673 635, India

drpradyumnan@gmail.com

PACS 75.75.+a, 81.16 Be **DOI 10.17586/2220-8054-2016-7-4-675-677**

Superparamagnetism is an important physical property of a certain kinds of nanoparticles and these particles have attracted interest because of their applications in the technological world and medical fields. In this work, the author reports the synthesis of iron cobalt ($Fe_{60}Co_{40}$) and Manganese (Mn) incorporated FeCo compound nanoparticles by a simple inert atmosphere reductive decomposition method. The synthesized nanoparticles were characterized by transmission electron microscopy (TEM), X-ray diffraction technique (XRD), selected area electron diffraction (SAED), energy dispersive X-ray analysis (EDX) and Fourier transform infrared (FTIR) spectroscopic method. The magnetic properties of the particles have been studied with a magnetometer (SQUID).

Keywords: Nanoparticle, soft magnetic, $Fe_{1-x}Co_x$ compound, reductive decomposition, TEM, SQUID.

Received: 5 February 2016

Revised: 24 April 2016

1. Introduction

Nanoparticles have now turned from theoretical interest to application in the technological world. In these years nanomagnetic particles have drawn special attention because of their recording ability and use as perpendicular magnetic memory and biomedical applications such as hyperthermia, magnetic resonance contrast enhancement and drug delivery etc. [1]. The nanoparticles, which show high magnetic moment are a better candidate, as far as the applications are concerned. The FeCo nano particle has such ability, but the main task is its preparation and stability. Many investigators have prepared nanoparticles of FeCo compounds using different techniques.

They have used chemical and physical methods for the growth of nanoparticles. Most of the physical methods require substrates [2–6]. For the fabrication of perpendicular recording media, substrate is applicable, but for the biological application individual nanoparticles are more reliable.

This paper reports the preparation of multifunctional nanoparticles of $Fe_{1-x}Co_x$ and Mn-incorporated compounds by a reductive decomposition-based reflux method using suitable stabilizers and surfactants. We have prepared three compositional compounds containing iron and cobalt as well iron, cobalt and manganese. All these synthesized materials were characterized by X-ray diffraction (XRD), selective area electron diffraction (SAED), Fourier transform infrared spectroscopy (FTIR), energy dispersive X-ray (EDX) and transmission electron microscopy (TEM). The magnetic properties of the materials studied using SQUID magnetometer.

2. Synthesis

The $Fe_{1-x}Co_x$ compounds, Mn incorporated nanoparticles were prepared using a modified method reported by Sun et al. [2]. Here, we used $Fe(acac)_3$ and $Co(acac)_2$, $Mn(acac)_2$ as precursors. Reductive decomposition of these was achieved by using benzyl ether as solvent medium, 1-octadecene as reducing agent and oleic acid as surfactant and oleylamine as stabilizer. The growth temperature was fixed at 240 °C. To avoid oxidation during nanoparticle growth, the reaction chamber was blanketed with argon. Care has been taken for the collection of the nanoparticles and washing of the nanoparticles to avoid the surfactants and stabilizers. But it was found to be very difficult to completely rinse the surfactants and stabilizers from the nanoparticles.

The shape of the nanoparticles depended on the growth temperature, whereas it had nothing to do with the composition and size of the particles. But it is very difficult to control the size of all the particles in this case. In our studies, we have fixed the above temperature for obtaining the maximum product. In all the compositions, the particle size found was to be less than 10 nm.

3. Experiments

3.1. X-ray diffraction (XRD)

XRD is the most primary technique to analyze the crystalline nature of the material. A Rigaku X-ray diffractometer has been utilized for the studies. All the three compounds shows the crystal structure is body centered cubic (bcc). Since the particle size is too small, the spectral broadening is evident. The peaks at (110) and (200) peaks are visible. TEM-electron diffraction studies were also utilized to confirm the crystalline nature of the compounds.

3.2. Infrared Spectroscopy

During the preparation of the compounds, organic chemicals like oleic acid and oleylamine were utilized. Even though proper washing has been done for the particles, there is a finite possibility that these molecules can be found on the surface of the nanoparticles. The IR spectrum of all the particles shows, the absorption bands. It is very difficult to wash out all the surfactants, and there is a strong attachment between the compound particles and these molecules. Fig. 1 shows the IR spectrum for one sample of the compounds.

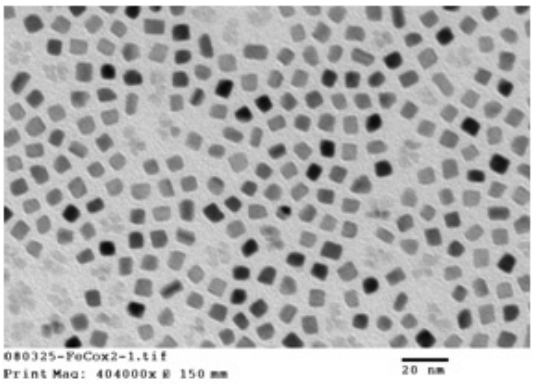

FIG. 1. TEM image of FeCo nano particles

For oleic acid, whose formula is $(CH_3(CH_2)_7CH = CH(CH_2)_7COOH)$, the following pattern was observed: the vibration is assigned at C–C (either COOH- or CH_3-sided) stretching. The difference observed is probably due to C=C bonding. In the spectrum of the broad, strong band at 1161 cm^{-1} flanked by weaker bands at 1238 and 1118 cm^{-1}.

3.3. Energy Dispersive X-ray Analysis (EDX)

The percentages of the Fe and Co present in all the prepared compound nanoparticles were measured using EDX technique. During synthesis we have approximated the ratio by varying the molar ratio of the precursors. Table 1, gives the ration of the final compositions of the $Fe_{1-x}Co_x$ compounds. From these results, we observed that the Fe ion is dominant in the compound formation and the single phases will be observed during these ratios only.

TABLE 1. Ration of the expected and actual compositions for $Fe_{1-x}Co_x$ compounds

No of compound combinations	Molar ratio of the metal precursors used		Molar ratio of the metal actually present in the compounds as per EDX	
	Fe	Co	Fe	Co
1	0.60	0.40	0.65	0.35
2	0.50	0.50	0.60	0.40
3	0.40	0.60	0.55	0.45

3.4. Transmission Electron Microscopic Studies (TEM)

The TEM images of the prepared nano particles are shown in Fig. 1. The $Fe_{1-x}Co_x$ compounds ($x = 0.35$, 0.40, 0.45).

The coercivity was found to be 0. Fig. 2 shows the room temperature hysteresis loops of the $Fe_{60}Co_{40}$ compound nanoparticles. We took same weight (0.1 mg) of both compound particles for SQUID studies It is found that due to the incorporation of Mn, the magnetic behavior of the materials were drastically changed and the magnetic moment was reduced, due to the incorporation of Mn ions. Fig. 2 shows the M/Ms Vs H graph of synthesized materials.

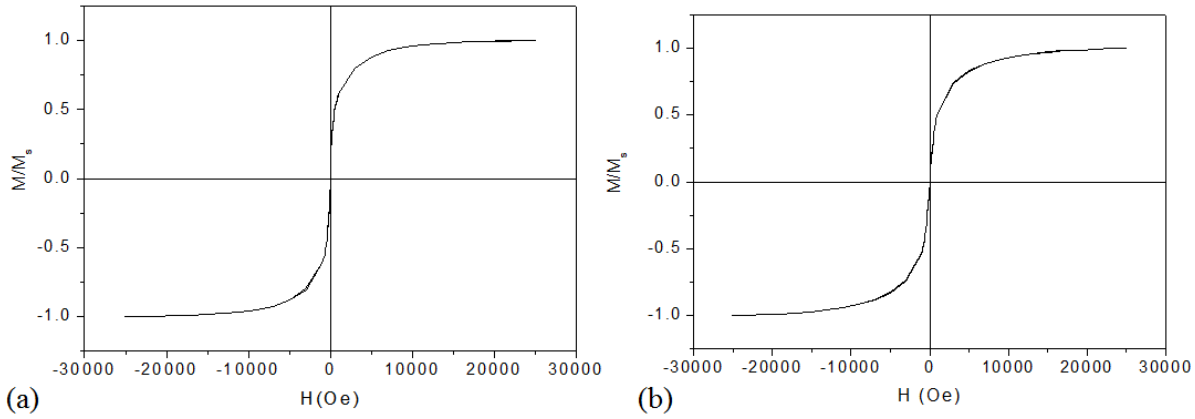

FIG. 2. Hysteresis loop of (a) $Fe_{60}Co_{40}$ and (b) $Fe_{65}Co_{30}Mn_5$ compound nanoparticle (size: 4 – 5 nm)

4. Conclusion

Well defined nanoparticles of FeCo and Mn incorporated FeCo compound were synthesized by a reductive decomposition-based reflux method. Uniformly sized nanoparticles of size 4 – 5 nm have been well characterized. The magnetic properties were attenuated due to the incorporation of Mn ion. Both the compound particles showed super paramagnetic behavior at room temperature.

Acknowledgements

Author grateful to SERB, Govt. of India for major research project funding SB/EMEQ-002/2013 and DST-FIST, Department of Physics, University of Calicut for experimental facilities.

References

[1] Reiss G., Hutten A. Magnetic nanoparticles-applications beyond data storage. *Nature materials*, 2005, **4** (10), P. 725–726.

[2] Don Keun Lee, Young Hwan Kim, et al. Preparation of monodisperse Co and Fe nanoparticle using precursor of M^{2+}-oleate$_2$ (M = Co, Fe). *Curr. Appl. Phys.*, 2006, **6**, P. 786–790.

[3] Soo Ja Shin, Young Hwan Kim, et al. Preparation of magnetic FeCo nanoparticles by coprecipitation route. *Curr. Appl. Phys.*, 2007, **7**, P. 404–408.

[4] Yun Hao Xu, Jianmin Bai, Jian-Ping Wang. High-magnetic-moment multifunctional nanoparticles for nanomedicine applications. *J. Magn. Magn. Mater.*, 2007, **311**, P. 131–134.

[5] Wen J.Z., Goldsmith F.C., et al. Detailed Kinetic Modeling of Iron Nanoparticle Synthesis from the Decomposition of $Fe(CO)_5$. *J. Phys. Chem. C*, 2007, **111**, P. 5677–5688.

[6] Shousheng Sun, Murrey C.B., et al. Monodisperse FePt Nanoparticles and Ferromagnetic FePt Nanocrystal Superlattices. *Science*, 2000, **289**, P. 1989–1992.

NANOSYSTEMS: PHYSICS, CHEMISTRY, MATHEMATICS, 2016, 7 (4), P. 678–682

ZnO decorated graphene nanosheets: an advanced material for the electrochemical performance and photocatalytic degradation of organic dyes

D. M. K. Siddeswara[1], K. R. Vishnu Mahesh[2*], S. C. Sharma[3], M. Mylarappa[4], H. Nagabhushana[5], K. S. Ananthraju[2], H. P. Nagaswarupa[6], S. C. Prashantha[6], N. Raghavendra[7]

[1]Department of Chemistry Jyothy Institute of Technology, Bengaluru-560082, Karnataka, India
[2]Department of Chemistry, Dayananda Sagar College of Engineering, Kumara Swamy Layout, Bengaluru, 560078, Karnataka, India
[3]Department of Mechanical Engineering, DSCE, Provost, Dayananda Sagar University, Bangalore, 560078, India
[4]Research Center, Department of Chemistry, AMC Engineering College, Bengaluru-83, Karnatak,India
[5]Prof. C. N. R. Rao Centre for Advanced Materials, Tumkur University, Tumkur, 572 103, India
[6]Research Center, 4Department of Science and Humanities, EWIT, Bengaluru-91, India
[7]CMRTU, RV College of Engineering, Bangalore-59, India

*vishnumaheshkr@gmail.com

PACS 81.07.-b **DOI 10.17586/2220-8054-2016-7-4-678-682**

The objective of the current research was mainly focused on synthesizing the Reduced Graphene Oxide (RGO) using modified Hummers method and ZnO functionalized reduced graphene oxide (RGO) composite was fabricated by a one-pot approach. The ZnO functionalized graphene nanosheets were characterized by X-ray diffractometer (XRD) and surface morphology was examined using Transmission Electron Microscopy (TEM). Electrochemical characteristics of the ZnO/RGO composite were investigated through cyclic voltammetry and electrochemical impedance spectroscopy (EIS). The composite was capable of delivering a high specific capacitance with excellent cycling stability. The ZnO decorated RGO catalyst was also applied to degrade different nonvolatile compounds such as Methyl Blue (MB) and Indigo carmine (IC). The performance of RGO/ZnO shows rapid degradation of dyes of high concentrations.

Keywords: Reduced graphene oxide, ZnO, Mn_2O_3, electrochemical, catalytic activity.

Received: 5 Febraury 2016

1. Introduction

Graphene is one-atom thick two-dimensional sheet of carbon atoms fashioned in a honeycomb lattice and is considered as the future revolutionary material [1]. An exponential growth after 2004 in graphene-related research is reflected in the number of publications. Graphene is highly anticipated to be an excellent electrode material due to its notable characteristics such as high surface area to volume ratio, good electrical conductivity, good flexibility, fast electron mobility and good thermal and electrochemical properties [2–4].

Because of its outstanding mechanical properties compared to other carbon materials, has attracted enormous interest. Considering the excellent properties of graphene, ZnO and Mn_2O_3, a combination of graphene with ZnO and Mn_2O_3 nanoparticles (NPs) might provide enhanced performance. Several methods have been carried out to produce graphene/ZnO and graphene/Mn_2O_3 composites. Other researchers have also synthesized graphene/ZnO and graphene/Mn_2O_3, as they appear to be promising materials for pseudocapacitors due to their superior electrochemical performance, environmental friendliness, and lower production costs [5]. The present research is mainly focused on synthesizing Reduced Graphene Oxide (RGO) by using Hummer's method. RGO and metal oxides such as ZnO and Mn_2O_3 composite were fabricated by a one-pot approach. The obtained RGO with metal oxides were characterized using X-ray Diffractometry (XRD) and ZnO and Mn_2O_3 composites were concerning to electrochemical and photocatalytic activity [6–11].

In this report, a simple and facile synthetic route is developed to prepare graphene-ZnO composite as an electrode material and photocatalyst for the organic dyes. Initially, graphene oxide (GO) was synthesized using the well-known modified Hummer's method. ZnO nanorods are inserted between the graphene nanosheets layer-by-layer rather than simply appended to the surface of graphene during the GO hydrothermal reduction process. This strategy provides a novel method for preparing highly active materials (ZnO nanorods) directly grown on Gr surface that avoids the restacking of Gr sheets, which show high electrochemical activity at higher scan rates and superior long-term cycle stability applied in an all solid-state supercapacitor device. Such excellent electrochemical properties provide important prospects for graphene- ZnO hybrid to be widely used as electrode material in supercapacitor [12, 13].

2. Experimental

2.1. Materials

Graphite, zinc nitrate hexahydrate ($Zn(NO_3)_2{\cdot}6H_2O$), sodium nitrate ($NaNO_3$), sulfuric acid (H_2SO_4), hydrochloric acid (HCl), potassium permanganate ($KMnO_4$), hydrogen peroxide (H_2O_2), hydrazine hydrate ($N_2H_4{\cdot}H_2O$) and potassium chloride (KCl) were purchased from Sigma-Aldrich and used without additional purification.

2.2. Synthesis of Graphene Oxide

GO was prepared from natural graphite using a modified Hummers method. In a typical experiment, graphite (1.5 g), $NaNO_3$ (1.5 g) and H_2SO_4 (70 mL) were mixed and stirred in an ice bath. Subsequently, 9 g $KMnO_4$ was added slowly. In a particular reaction condition, water was added slowly, followed by the slow addition of 10 mL 30 % H_2O_2. The above mixture was centrifuged and purified, the sample was dispersed in deionized water to obtain highly exfoliated GO sheets. This as-prepared GO was reduced to obtain RGO.

2.3. Synthesis of RGO/ZnO Composite

Pure ZnO Nano rods were synthesized by hydrothermal method. In a typical experiment, 100 mg of $Zn(NO_3)_2$ was first dispersed into 30 ml deionized water. Then, 15 μl of hydrazine hydrate was added dropwise under stirring, followed by ultrasonication for 30 min. Then, the solution was transferred to a 50 ml Teflon-lined autoclave and heated at 160 °C for 12 h. Finally, the RGO/ZnO nanostructures were collected after washing and centrifugation.

3. Result and Discussion

3.1. X-Ray Diffractometer

Crystalline structure of the materials were examined by an X-ray diffractometer (XRD). It can be seen (Fig. 1) that the ZnO XRD patterns of the nanocomposites with different mass ratios are similar to that of pure zinc oxide, indicating that no other impurity peaks were detected. It can be readily assigned to pure ZnO with hexagonal structure [2]. The XRD pattern confirms the crystalline nature of the as-prepared RGO/ZnO material and the Transmission electron microscopy (TEM) images indicate the presence of nanosheets around the centers.

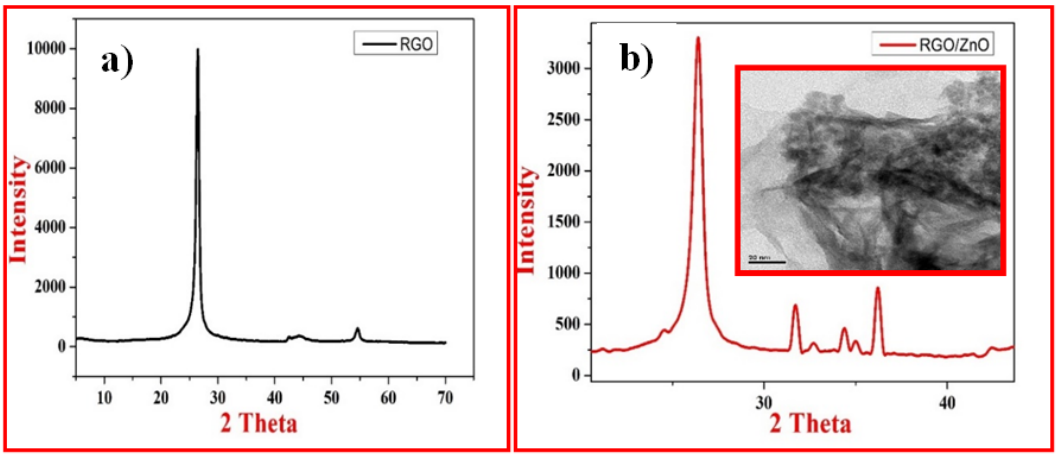

FIG. 1. XRD of a) RGO; b) XRD and TEM image of RGO/ZnO

3.2. Electrochemical Studies

The electrochemical activities of RGO and RGO/ZnO were assessed by cyclic voltammetry, which can provide additional information for material characterization from the shape, the number and the position of the different peak like the redox processes. The obtained black paste was immersed into a homemade disk electrode with glass walls and graphite bar as current collector. A CHI604E work station was used for all electrochemical measurements. Electrochemical measurement utilized three electrode system having working electrode, Ag/AgCl reference electrode and a platinum wire as counter electrode. Cyclic voltammetry (CV) studies were performed in potential between $+0$ to -1 V using electrolytes at constant scan rate. Cyclic voltammetry was used to determine the influence of RGO/ZnO on the overall charge capacity of the electrode. The value of $E_0 - E_R$ measures

the electrode reversibility (E_R), which is one of the predominant factors influencing the power capabilities of electrodes in 0.5 M Na_2SO_4 electrolyte. In Fig. 2(a) the smaller value of $E_0 - E_R$ indicates greater reversibility for the electrode reaction. In the current studies, several scan rates ranging from 10 to 50 mVs^{-1} were used. The effect of scan rate is presented in Fig. 2(b). As the scan rate increased, the CV profile deviated from the ideal capacitive behavior. A smaller the value of RGO/ZnO showed greater reversibility for the electrode reaction. Decreased solution resistance (Rs) values indicate greater conductivity values for the sample. In Fig. 3(a), one can clearly see that the sample RGO/ZnO in 0.5 M Na_2SO_4 shows lower charge transfer resistance (Rct) than the RGO electrode, indicating the enhanced conductivity and confirming that the capacitive behavior is faster, as is shown in Table 1. The simulation of RGO/ZnO is shown in Fig. 3(b).

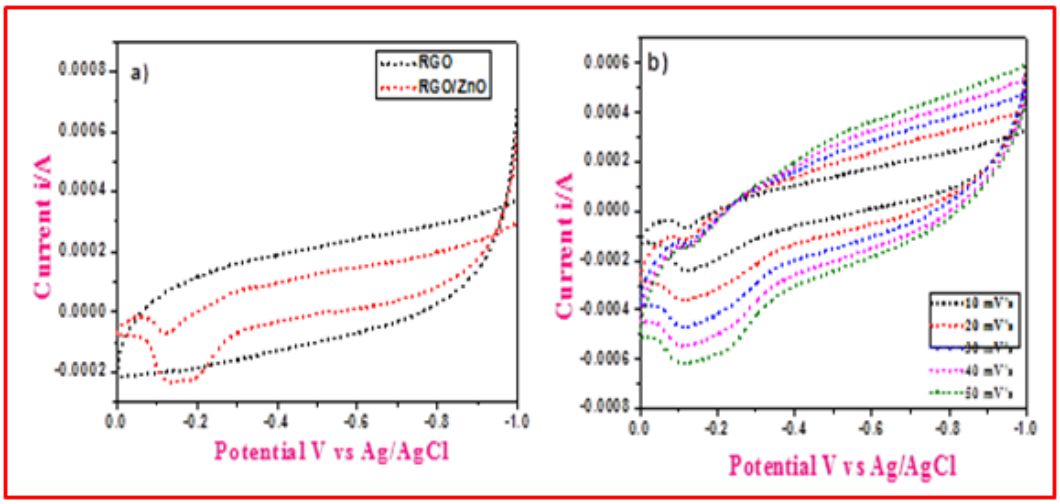

FIG. 2. a) Cyclovoltagramms of RGO and RGO/ZnO; b) different scan rate of RGO/ZnO

TABLE 1. Electrochemical reversibility and EIS of RGO, RGO/ZnO and RGO/Mn_2O_3 electrodes

Electrodes	$\mathbf{E_0(V)}$	$\mathbf{E_R(V)}$	$\mathbf{E_0 - E_R}$	$\mathbf{Rct(\Omega)}$	$\mathbf{C(F) \times 10^{-4}}$
RGO	0.8675	0.4480	0.4195	23.7	0.01
RGO/ZnO	0.3963	0.3077	0.0886	36.74	2.021

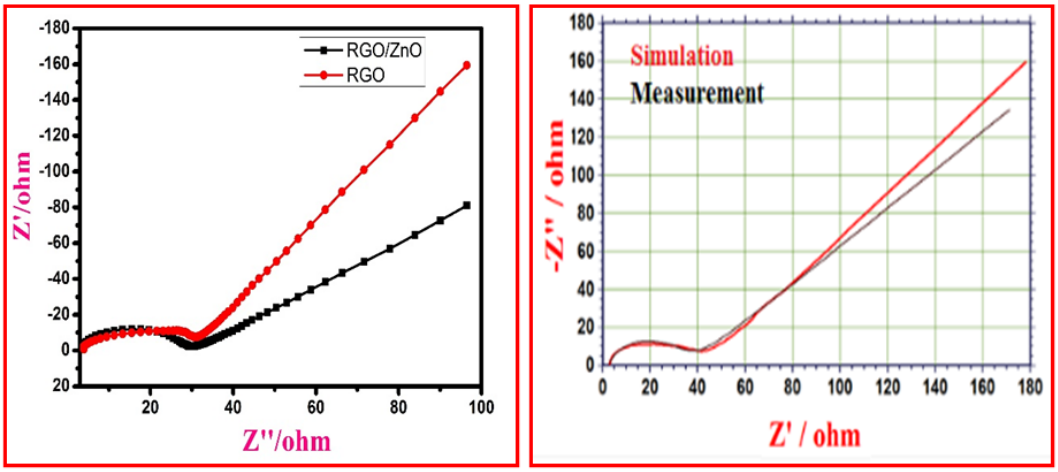

FIG. 3. a) Nyquist plots of RGO and RGO/ZnO; b) fitted simulation of RGO/ZnO

3.3. Photocatalytic Activity

In the existing work, Methylene blue (MB) and Indigo carmine (IC) dyes were used as ideal pollutants to estimate the photocatalytic activity of RGO/ZnO under UV light irradiation [12, 13]. In an experiment, 60 mg of RGO/ZnO was dispersed in 250 ml MB (20 ppm). The mixed suspensions were first magnetically stirred in the dark for 30 min to reach the adsorption–desorption equilibrium. Under ambient conditions and stirring, the mixed suspensions were exposed to visible light irradiation produced by a 400 W metal Philips lamp (wavelength: 254 nm). At certain time intervals, 5 ml aliquots of the mixed suspensions were extracted. The filtrates were analyzed by recording UV–vis spectra of MB and IC using a Spectratreats 3.11.01 Release 2A UV–vis spectrophotometer. In UV light, RGO/ZnO can absorb UV light (254 nm) and generate electron–hole pairs. These photo-generated electron and hole pairs can migrate into the catalyst surface and react with surface adsorbed O_2 to form active oxygen species. The photo degradation of MB and IC by RGO/ZnO nanoparticles and the effect of various parameters, like initial catalyst loading, initial dye concentration etc., were thoroughly investigated. RGO/ZnO nanomaterials exhibited the highest photocatalytic activity.

Figure 4 shows the UV-vis absorption spectra of MB and IC as a function of the catalytic reaction time. Both MB and IC solutions turned colorless after 80 min, indicating complete degradation of the dye molecules by RGO/ZnO. After 80 min of reaction, the RGO/ZnO showed good catalytic degradation of IC. When using the as-prepared composite material, the MB solution with concentration 60 mg/L can be degraded up to 79.9 % and mineralized up to 21 % in 80 minutes, as is shown Fig. 5.

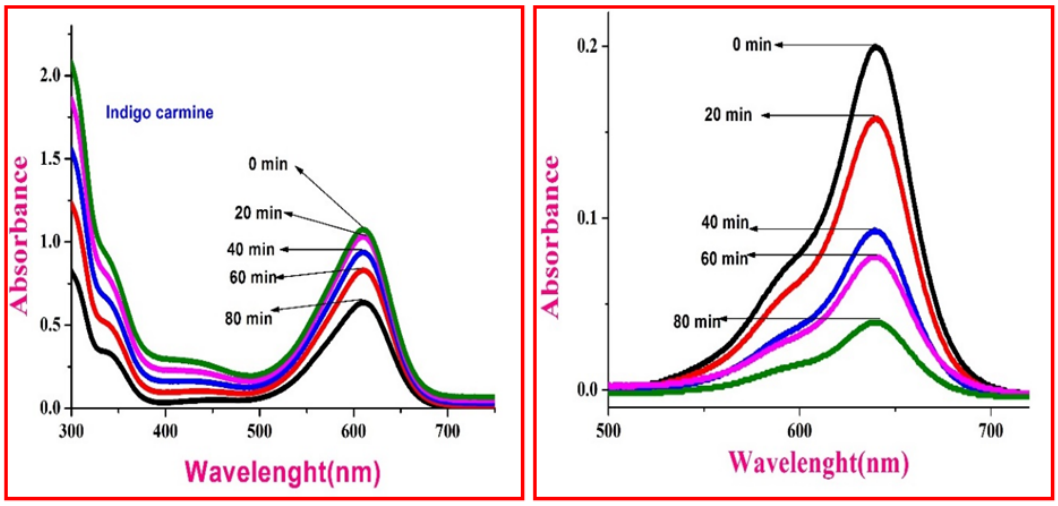

FIG. 4. Time-dependent UV-vis absorption spectra of RGO/ZnO in IC and MB

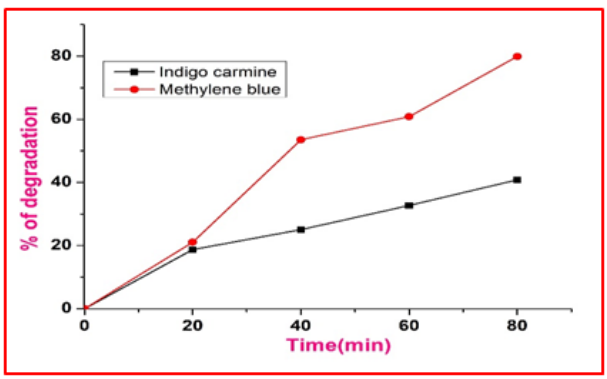

FIG. 5. UV-visible spectra of IC and MB degradation

4. Conclusion

RGO and RGO/ZnO composites were successfully prepared and their applications as electrode materials for electrochemical applications and photocatalytic activities were investigated. Cyclic voltammetry showed ideal capacitive behavior for RGO and RGO/ZnO hybrid nanosheets. Table 1 shows RGO/ZnO having less $E_0 - E_R$ and hence electrochemical reversible reactions will be more, and RGO/Mn_2O_3 having lesser Rct value and hence capacitance will be more. The photocatalytic activity was assessed through UV-Visible spectra, from which, we conclude that RGO/ZnO showed a good catalytic degradation of IC. This test showed that using the as-prepared composite material, the MB solution with concentration 60 mg/L can be degraded up to 79.9 % and mineralized up to 21 % and IC degraded up to 40.85 in 80 minutes.

References

[1] Yuvaraj Haldorai, Walter Voit, Jae-Jin Shim. Nano ZnO @reduced graphene oxide composite for high performance super capacitor. *Green synthesis in supercritical fluid Electrochemical Acta.*, 2014, **120**, P. 65–72.

[2] Ejikeme Raphael Ezeigwe, Michelle T.T. Tan, Poi Sim Khiew, Chiu Wee Siong. One-step green synthesis of graphene/ZnO nanocomposites for electrochemical capacitors. *Ceramics International*, 2015, **41**, P. 715–724.

[3] Zhou Y.K., He B.L., Zhang F.B., Li H.L. Hydrous manganese oxide/carbon nanotube composite electrodes for electrochemical capacitors. *Solid State Electrochem.*, 2004, **8**, P. 482.

[4] Subramanian V., Zhu H., Wei B. Alcohol-assisted room temperature synthesis of different nanostructured manganese oxides and their pseudocapacitance properties in neutral electrolyte. *Chem. Phys. Lett.*, 2008, **453**, P. 242–249.

[5] Zijiong Li, Zhihua Zhou, et al. High-performance solid-state supercapacitors based on graphene-ZnO hybrid nanocomposites. *Nanoscale Research Letters*, 2013, **8**, P. 473.

[6] Li B., Liu T., Wang Y., Wang Z. ZnO/graphene-oxide nanocomposite withremarkably enhanced visible-light-driven photocatalytic performance. *J. Col-loid Interface Sci.*, 2012, **377**, P. 114.

[7] Tingting Liu, Guangjie Shao, Mingtong Ji, Guiling Wang. Synthesis of MnO_2-graphene composites with enhanced super capacitive performance via pulse electrodeposition under supergravity field. *Journal of Solid State Chemistry*, 2014, **215**, P. 160–166.

[8] Xichuan Lia, Xiaoyang Xua, et al. Electrochemically active MnO_2/RGO nanocomposites using Mn powder as the reducing agent of GO and the MnO_2 precursor. *Electro chimica Acta*, 2014, **130**, P. 305–313.

[9] Yongchuan Liu, Dawei He, et al. Synthesis of MnO_2/graphene/carbon nanotube nanostructured ternary composite for supercapacitor electrodes with high rate capability. *Materials Chemistry and Physics*, 2014, **147**, P. 141–146.

[10] Conway B.E. *Electrochemical Supercapacitors: Scientific Fundamentals and Technological Applications*. Kluwer Academic/Plenum, New York, 1999.

[11] Muhammad Mohsin Hossaina, Bon-Cheol Kub, Jae Ryang Hahna. Synthesis of an efficient white-light photo catalyst composite of graphene and ZnO nanoparticles: Application to methylene blue dye decomposition. *Applied Surface Science*, 2015, **354**, P. 55–65.

[12] Prathap Anu M.U., Kaur B., Srivastava R. Hydrothermal synthesis of CuO micro-/nanostructures and their applications in the oxidative degradation of methylene blue and non-enzymatic sensing of glucose/H_2O_2. *J. Colloid Interface Sci.*, 2012, **370**, P. 144–154.

[13] SiXu Deng, Dan Sun, et al. Synthesis and electrochemical properties of MnO_2 nanorods/graphene composites for supercapacitor applications. *Electrochimica Acta*, 2013, **111**, P. 707–712.

NANOSYSTEMS: PHYSICS, CHEMISTRY, MATHEMATICS, 2016, 7 (4), P. 683–686

Characterization studies on the novel mixed thin films

P. Ramasundari[1], S. Ganeshan[2] and R. Vijayalakshmi[3]

[1]P. G. & Research Department of Physics, S. V. N. College, Madurai, India
[2]Department of Physics, Vivekananda College, Madurai, India
[3]P. G. & Research Department of Physics, Thiagarajar. College, Madurai, India

ramprof62@gmail.com, ramyarv@rediffmail.com

PACS 68 **DOI 10.17586/2220-8054-2016-7-4-683-686**

Among electrochemical processes having a considerable impact on technical development, the mixed thin film (Mo-Ni oxide) plays an important role, due to its better mechanical, anticorrosive and thermal stability characteristics. The mixed films have been prepared by dip spin coating. The films are grown on substrates like Indium Tin Oxide (ITO) and are well adherent on the substrates, pinhole free and transparent. The X-ray diffraction analysis of the films confirms they are polycrystalline in nature. The morphological study reveals that the uniform distributions have flower-like structure. From the compositional analysis, the EDAX spectra show the presence of molybdenum and nickel. The optical band gap was found to be 1.36 eV and band assignments for Fourier Transform Infrared (FTIR) spectra are comparable to reported values.

Keywords: Dip Spin Coating, EDAX, SEM, X-Ray Diffraction.

Received: 5 February 2016

Revised: 27 April 2016

1. Introduction

The optical properties of thin films are very important for many applications. Researchers have shown considerable interest in Ni–Mo oxide films, because of their applications such as hydrogen evolution catalysis [1,2] and anticorrosion treatment [3]. Transition metal oxides, like nickel oxides have found application due to their anti-ferromagnetic semiconducting properties with a wide band gap of 3.6 eV [4,5]. This provides opportunities for use in electrochromic devices [6], fuel cells [7] or other applications. Electrodeposition-prepared transition metal oxide films exhibit good electrochromic properties. For electrodeposited Mo–Ni oxide films, it has been shown that as Mo content increases, certain peaks in XRD broaden and disappear due to a decrease in grain size [8,9]. Even though there are reports for the optical properties, structural characteristics, band assignments and electrical properties by dip spin coating Indium Tin Oxide (ITO) plates, values are reported only for Indium Tin Oxide (ITO) substrates in this paper.

2. Experimental

The concentrations of 0.05 N (of MoO_3 and $NiSO_4$ mixture) at 330 K by dip spin coating under optimized conditions. The coating was performed at 3000 rpm for 30 mins as optimized parameters to obtain the mixed oxide thin film. The coated samples were investigated by conventional XRD with Cu$K\alpha$ radiation using XPERT-PRO diffractometer. FTIR measurements in the range of 400 – 4000 cm^{-1} were carried out by JASCO CANVAS. The SEM photographs were recorded using HITACHI S-3400.

3. Results and Discussion

3.1. XRD Analysis

The structural properties of these films were analyzed by the X-ray diffractometer. Fig. 1 shows the diffraction pattern of Mo–Ni mixed oxide thin film which is deposited on the Indium Tin Oxide (ITO) plate. From the surface analysis, it was found that the mixed thin films exhibit uniform thickness. The diffracting angles were set to 20 $^\circ$ to 80 $^\circ$ with a low scanning speed and in continuous mode. Diffraction peaks were observed at $2\theta = 28.450$, 39.430, 44.720, 47.320 and 65.560, corresponding to the (0 0 2), (-2 -2 2), (1 2 2), (1 -1 3), (-1 -5 1) planes of the mixed thin films respectively. XRD pattern of Mo–Ni mixed oxide thin films showed polycrystalline wurzite structure with a preferential (1 2 2) orientation peak and the peaks are comparable to reported values [10].

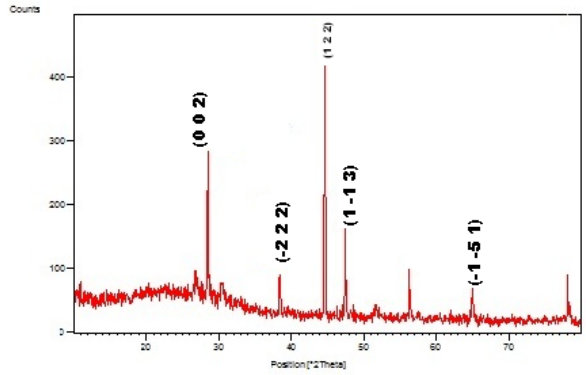

FIG. 1. XRD pattern of as deposited Mo–Ni oxide film on ITO substrate

3.2. SEM Analysis

The film deposited on the Indium Tin Oxide (ITO) substrate showed flower-like structure. The EDAX, which was used in conjunction with SEM, confirmed the elemental composition of the film as deposited on the substrate, revealing the presence of molybdenum and nickel (89.52 % Mo & 5.42 % Ni) as well as impurities like copper and zinc.

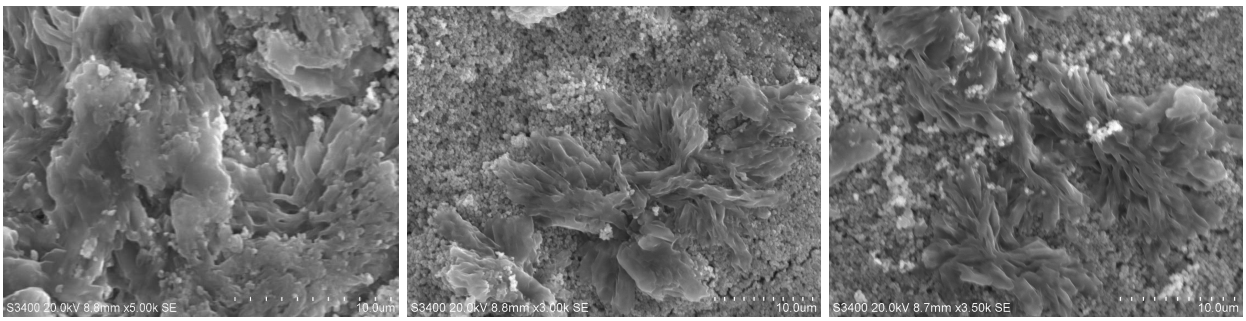

FIG. 2. SEM images of as deposited Mo–Ni oxide film on ITO substrate

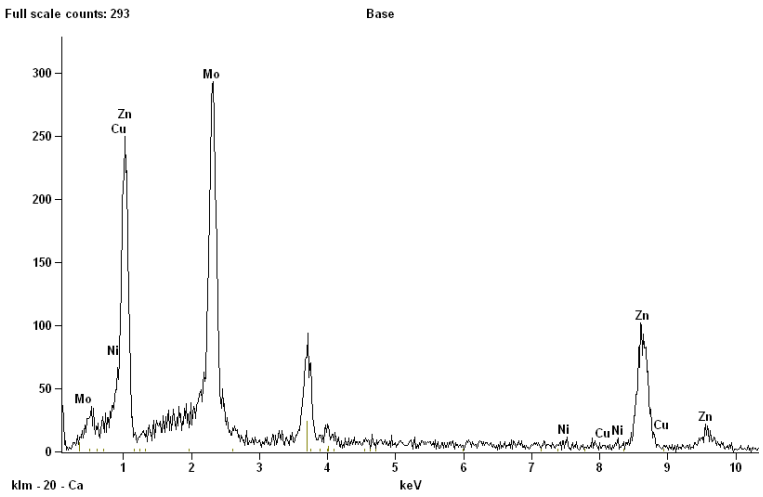

FIG. 3. EDAX spectra of as deposited mixed Mo–Ni oxide film on ITO substrate

3.3. FTIR Spectra

Fourier transform infrared spectroscopy provides information about a particular compound's functional groups, molecular geometry and inter/intramolecular interactions. The bands at 3425 cm^{-1}, 1614 cm^{-1} in Fig. 4 were attributed to the surface absorbed water in the mixed Mo–Ni oxide thin films. The band 3780 cm^{-1} and 3932 cm^{-1} are due to O–H stretching vibrations of water molecules. The vibration absorption peaks at 875 cm^{-1} were due to Mo–O–Mo stretching [11].

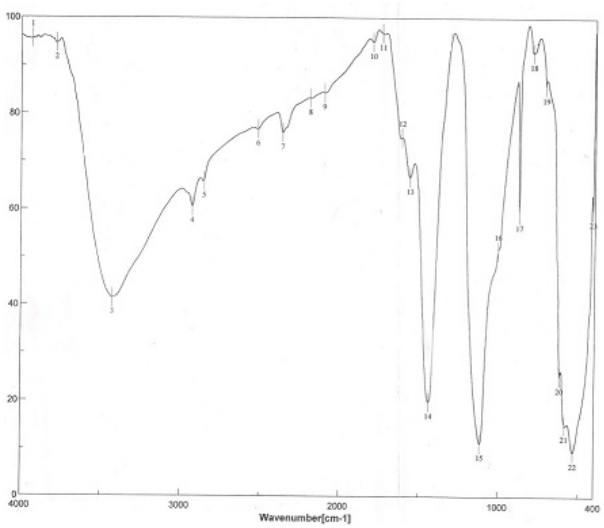

FIG. 4. FTIR Spectra of as deposited mixed Mo–Ni oxide film

3.4. Optical Studies

Optical absorption characterisitcs were studied in the 200 – 1100 nm range. The absorption spectrum for the as-deposited mixed Mo–Ni oxide film is shown in Fig. 5. The UV-Visible spectrum shows a sharp peak centered at 360 – 376 nm with a long tail towards longer wavelength side. Absorption has very high value in the UV region and decreases with increasing wavelength, becoming constant towards the visible region, which indicates a high transparency in the visible region. The optical band gap of mixed Mo-Ni thin film was found to be 1.36 eV.

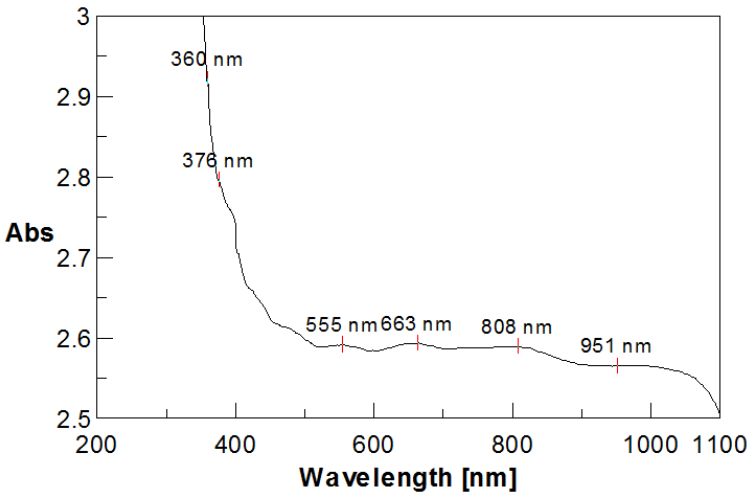

FIG. 5. Absorprtion Spectra for as deposited mixed Mo–Ni oxide film on ITO substrate

4. Conculsion

Electrochromic materials, like mixed Mo–Ni oxide thin film, were deposited on ITO under optimized conditions. The dip spin coated films are white in color and are transparent. The films are well adherent on the substrates, pinhole-free and transparent. X-ray diffraction shows that the films are polycrystalline in nature and are comparable to JCPDS data. SEM images reveal that the films are without any pinholes or cracks and cover the substrate well. The optical absorption spectrum reveals that the material has a direct band gap nature and its energy is in agreement with the reported values.

References

[1] Mihailov L., Spassov T., Kanazirski I., Tsvetnaov I. Electrocatalytic behavior of Ni-based amorphous alloys for hydrogen evolution. *J. Mater. Sci.*, 2011, **46**, P. 7068–7073.

[2] Kirk D.W., Thorpe S.J., Suzuki H. Ni-base amorphous alloys as electrocatylst for alkaline water electrolysis. *Int. J. Hydrogen Energy*, 1997, **22**, P. 493–500.

[3] Chassaing E.E., Portail N.N., Levy A.F., Wang G. Electrodeposition and Characterization of Nanocrystalline Ni-Mo Catalysts for Hydrogen Production. *J. Appl. Electrochem.*, 2004, **34**, P. 1085–1091.

[4] Adler D., Fainleb J.J. Electrical and optical properties of 'Narrow?Band Materials'. *Phys. Rev. B*, 1970, **2** (8), P. 3112–3134.

[5] Zollner M., Kipp S., Becker K.D. Reactive Processes of Nickel Oxide on oxidic Substrates as observed by Scanning Force Microscopy. *Crystal Research and Technology*, 2000, **35** (3), P. 299–305.

[6] Purushothaman K.K., Muralidharan G. Nanostructured NiO Based All Solidstate electrochromicdevice. *Journal of Sol-Gel Science and Technology*, 2008, **46**, P. 190–197.

[7] Shaigan N., Ivey D.G., Chen W. Metal?Oxide Scale Interfacial Imperfections and Performance of Stainless Steels Utilised as interconnects in Solid Oxide Fuel cells. *Journal of The Electrochemical Society*, 2009, **156** (6), P. 765–770.

[8] Beltowaka-Lehman E., Bigos A., Indykaand P. Electrodeposition and characterisation of nanocrystalline Ni-Mo coatings. *Surf. Coat. Technol.*, 2012, **211**, P. 67–71.

[9] Beltowaka-Lehman E., Indyka P.P. Kinetics of Ni-Mo electrodepsotion from Ni-rich citrate baths. *Thin Solid Films*, 2012, **520**, P. 2046.

[10] Masatoshi Saitou. Characterization of Electrodeposited Ni and Ni?Mo Thin Films by X-ray Diffraction. *Int. J. Electrochem. Sci.*, 2014, **9**, P. 6033–6042.

[11] Sulma Marisela Fernandez-Valverde, Eduardo Ordonez-reqil, Gerardo cabanas-Moreno, Omar Solorza-feria. Electrochemical Behavior of Ni-Mo Electrocatalyst for Water Electrolysis. *J. Mex. Chem. Soc.*, 2010, **54** (3), P. 169–174.

NANOSYSTEMS: PHYSICS, CHEMISTRY, MATHEMATICS, 2016, 7 (4), P. 687–690

Optical and structural studies of vanadium pentoxide thin films

S. Ganeshan[1], P. Ramasundari[2], A. Elangovan[3] and R. Vijayalakshmi[4]

[1]Department of Physics, Vivekananda College, Madurai
[2]P. G. & Research Department of Physics, S. V. N. College, Madurai
[3]P. G. & Research Department of Chemistry, Thiagarajar College, Madurai
[4]P. G. & Research Department of Physics, Thiagarajar College, Madurai
sganeshanmdu@gmail.com, ramyarv@rediffmail.com

PACS 81.15 Pq, 74.25 Gz, 61.05 Cp **DOI 10.17586/2220-8054-2016-7-4-687-690**

Recently, transition metal oxides like Vanadium pentoxide have become a subject of intensive studies. The particular physical and chemical properties of these materials allow a wide range of practical applications such as electrochromic devices, cathode electrodes for lithium batteries, humidity sensors. The V_2O_5 film was prepared by an electrodeposition technique. The structural and optical properties were studied by X-Ray Diffraction (XRD), scanning electron microscopy (SEM), UV-Visible and Fourier Transform Infrared Spectroscopy (FT-IR). XRD spectra recorded has been observed and compared with the JCPDS values. SEM images showed very smooth surface morphology and the elemental compositions of the film were confirmed by EDAX. The transmittance of the V_2O_5 films showed 75 % at 425 nm for the as-deposited substrate. The energy band gap of the films was found to be 2.45 eV and the band assignments of the V_2O_5 film are comparable with the reported values.

Keywords: Electrodeposition, optical properties, X-ray diffraction.

Received: 5 February 2016

Revised: 11 May 2016

1. Introduction

V_2O_5 is an important material among other transition metal oxides from the view point of its novel electronic and optical characteristics in thin film form, leading to applications in lithium solid state micro batteries, gas sensors and electrochromic display devices [1,2].The vanadium-oxygen system has been intensively studied by theoretical and experimental techniques. Vanadium oxide is used in thermal sensing and switching. Vanadium pentoxide films have been prepared using various physical and chemical techniques, such as thermal evaporation, electron beam evaporation, sol-gel, electrochemical deposition and pulsed laser ablation [3–6]. Some unique features of V_2O_5 include its orthorhombic layered structure, high electrochromic activity, high stability and ease of thin film formation by numerous deposition techniques. Among the various preparation methods, the electrodeposition method was one of the simplest methods, due to its deposition rate, good uniformity on the substrates and thickness control of the film. The main advantage of this electrodeposition coating is the conformal resist layer, independent of the substrate geometry. Electrodeposition coating is the most suited technique to pattern structures that run in and across cavities or when a smaller line width is required. In this present work, the films were prepared by an electrodeposition technique and were characterized to study the optical and structural properties using XRD, SEM with EDAX, UV-Vis Spectroscopy and FT-IR Spectra.

2. Experimental

In electrodeposition techniques, structurally and compositionally-modulated alloys and compounds can be deposited and the deposition can be carried out at room temperature enabling the formation of the semiconductor junctions without interdiffusion. The V_2O_5 films were prepared by electrodeposition technique having a bath 0.2 M of vanadium pentoxide powder mixed with hydrogen peroxide which was used as the stock solution. The parameters like the concentration of the solution, pH, current and temperature were optimized. The electrodeposition process was carried out with three electrode systems, one is ITO coated plate acting as working electrode, the other the platinum electrode as counter electrode and the third one was the saturated calomel electrode (SCE) as the reference electrode. Two grams of vanadium pentoxide of 99 % purity and 30 % of sulfuric acid were added to avoid the effervescence produced in the solution. Then the stock solution was diluted to get the concentration of 0.1 M. The pH of the solution was maintained as 3.0 and the deposition current was fixed as 1 mA and the temperature maintained at the room temperature. The crystallographic structure of the film was determined from Powder X-ray diffraction patterns obtained by using BRUKER ECO D8 Advance diffractometer with a monochromatic

CuKα radiation ($\lambda = 0.15406$ nm , 40 kV, 20 mA). The surface morphology was studied using SEM (BRUKER ECO D8 ZEISS). The Compositional analysis was done using EDAX spectrometer attached to SEM. The optical transmission studies were done using UV-Vis Spectrophotometer (HP2000). FTIR Spectra were obtained from Perkin-Elmer make model spectrum RXI spectrophotometer.

3. Results and discussion

3.1. XRD Analysis

Figure 1 shows the diffraction pattern of V_2O_5 thin film which was deposited on the ITO substrate. From the analysis, it was found that the V_2O_5 film exhibited uniform thickness [7, 8]. The XRD analysis proves that the V_2O_5 films exhibit polycrystalline nature and the diffraction peaks for (2 2 0), (3 2 0) and (3 0 1) planes were prominent. The other low intensity peaks showed that the as-deposited film has coarsely fine crystallites and nanocrystallites. Sharp diffraction peaks at positions $2\theta = 22.4\ ^\circ$, $27.14\ ^\circ$ and $52.22\ ^\circ$ correspond to the (2 2 0), (3 2 0) and (3 0 1) planes respectively. The XRD pattern suggests that the film is polycrystalline with varying degree of orientation and has FCC structure when compared with the JCPDS (03-0206) value. The smoothness of the XRD pattern confirms the uniformity in the grown film. The average particle size, which was calculated using the Scherrer relation, ranges from 28.21 nm to 30.81 nm.

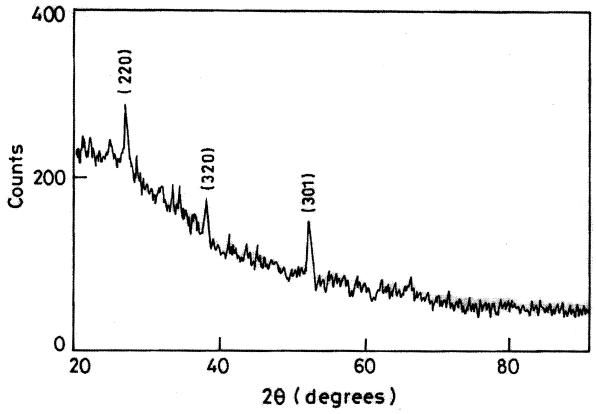

FIG. 1. XRD pattern images of V_2O_5 film on ITO substrate

3.2. Surface morphology studies: SEM with EDAX

The microstructure and morphology analysis of the as-deposited V_2O_5 thin film was carried out. The SEM image in Fig. 2 shows that the film is nearly homogeneous without any pinholes or cracks and covers the substrate well. The particles are spherical in shape. The particle size observed from the SEM images was of the order of 100 – 200 nm [9]. Fig. 3 shows the elemental composition of the as deposited V_2O_5 film. The presence of vanadium and oxygen were confirmed by EDAX analysis and their atomic weight percentages are calculated as 10.45 % and 28.33 % for vanadium and oxygen respectively.

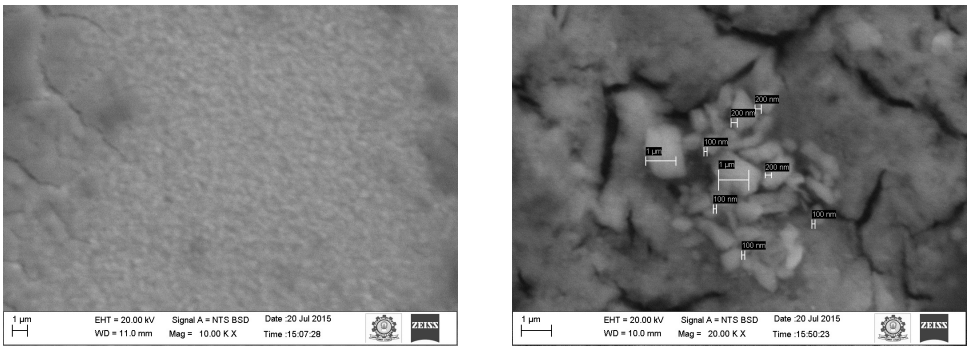

FIG. 2. SEM images of as deposited V_2O_5 film on ITO substrate

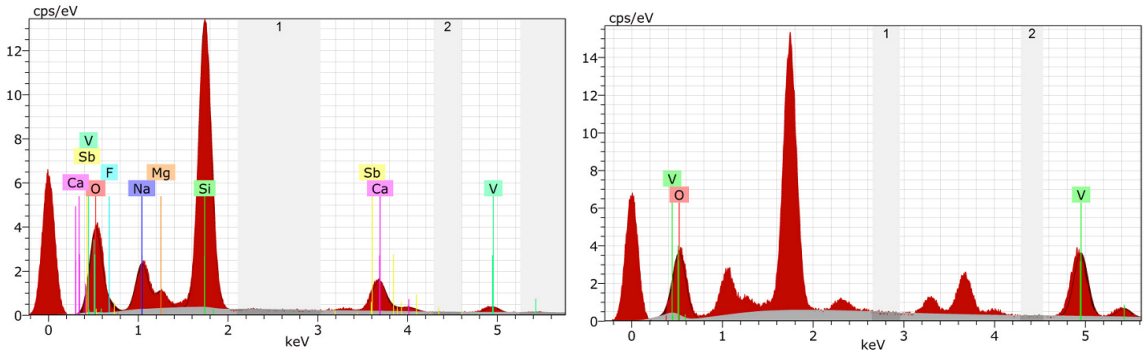

FIG. 3. EDAX spectra of as deposited V_2O_5 film on ITO substrate

3.3. FTIR

The FTIR spectrum of V_2O_5 film is portrayed in Fig. 4. FTIR investigation was performed to study the structural changes and band stretching of vanadium pentoxide. The band at 841 cm^{-1} corresponds to the polycrystalline V_2O_5 also the band at 814 cm^{-1} is assigned to the crystalline V_2O_5. A shoulder type of vanadium band is observed at 767 cm^{-1} and bands located at 530 cm^{-1}, 521 cm^{-1} are assigned to the stretching mode of the oxygen which is shared between 3 vanadium atoms. The band at 431 cm^{-1} is assigned to the bending vibrations of the bound oxygen which is shared by 2 vanadium atoms [10, 11].

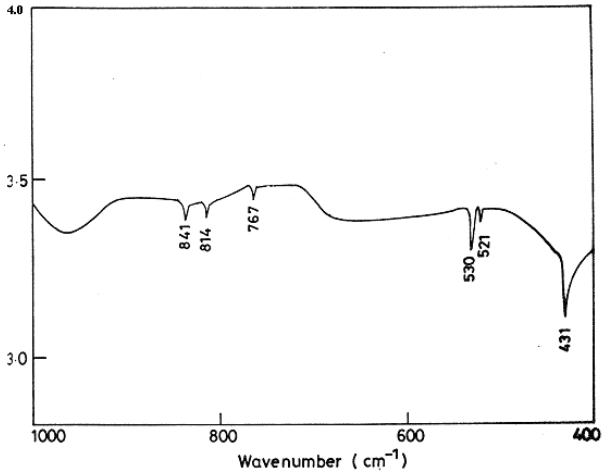

FIG. 4. FTIR Spectra of the V_2O_5 film

3.4. Optical studies

The UV-VIS spectrum measured for V_2O_5 film is shown in Fig. 5(b) and the band gap calculated from Fig. 5(a). The optical parameters are calculated from the transmittance spectrum in the 300 nm to 800 nm wavelength region. The as-deposited film has a steady transmittance of 75 % in the visible region. The oscillations in the curves were due to interference effects that depend on the film thickness and the refractive index. The plot is linear, indicating a direct optical transition and the evaluated energy gap is 2.45 eV, which agrees with the reported values [12, 13] and is similar to the value reported in the pulsed laser deposition technique [13]. Given this data, one can say that a high quality V_2O_5 thin film was obtained using the electrodeposition method.

4. Conclusion

Polycrystalline V_2O_5 thin films were deposited on ITO substrate by electrodeposition method and the films were well adherent, uniform and pinhole-free. The XRD pattern of the V_2O_5 film showed a polycrystalline nature with a preferential (3 0 1) orientation. Morphological studies showed a well-defined structure and elemental composition. The optical band gap of the V_2O_5 thin film was found to be 2.45 eV. The electrochromic studies and coloration efficiency of the vanadium pentoxide thin films are areas for future exploration.

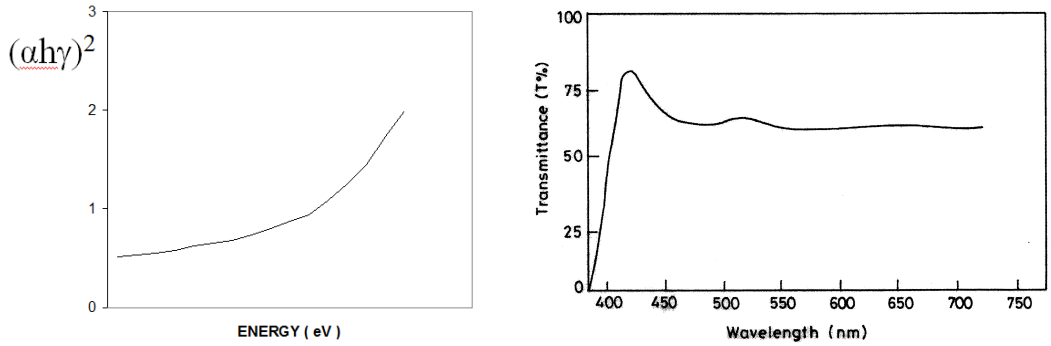

FIG. 5. (a) $(\alpha h\gamma)^2$ versus Photon energy film for V_2O_5 thin film; (b) Transmittance curve for V_2O_5 thin film

References

[1] Julien C. Electrochemical properties of disordered cathode materials. *Ionics*, 1996, **2** (3-4), P. 169–178 .

[2] Ramana C.V., Hussain O.M., Srinivasulu Naidu B., Reddy P. Influence of substrate temperature on the composition and structural properties of electron beam evaporated V_2O_5 thin films. *J. Vaccum*, 1997, **48** (5), P. 431–434.

[3] Bates J.B., Dudney N.J., et al. Fabrication and characterization of amorphous lithium electrolyte thin films and rechargeable thin-film batteries. *J. Power Sources*, 1993, **43**, P. 103–110.

[4] Moshfegh A.Z., Ignatiev A. Formation and characterization of thin film vanadium oxides: Auger electron spectroscopy, X-ray photoelectron spectroscopy, X-ray diffraction, scanning electron microscopy, and optical reflectance studies. *Thin Solid films*, 1991, **198** (1), P. 251–268.

[5] Bouzidi A., Benramdane N., et al. Physical Properties of V_2O_5 sprayed films. *Mater. Sci. Eng. B*, 2002, **95**, P. 141–147.

[6] Julien C., Haro-Poniatowski E., et al. Growth of V_2O_5 thin films by pulsed laser deposition and their applications in lithium microbatteries. *Mater. Sci. Eng. B*, 1999, **65** (3), P. 170–176.

[7] Ramana C.V., Smith R.J., et al. Correlation between Growth Conditions, Microstructure, and Optical Properties in Pulsed-Laser-Deposited V_2O_5 Thin Films. *Chem. Matter*, 2005, **17** (5), P. 1213–1219.

[8] Shiho lwanaga, Darling R.B., Cooden D.H. Stable and erasable patterning of vanadium pentoxide thin films by atomic force microscope nanolithography. *Appl. Physics*, 2005, **86**, P. 133113.

[9] Olivetti E.A., Kim J.H., et al. Sol-Gel syntheis of Vanadium oxide within a block copolymer matrix. *Chem. Matt.*, 2006, **18**, P. 2828–2833.

[10] Culea E., Nicula A.L., Bratu I. An infrared study of $xV_2O_5 \cdot (1?x)B_2O_3$ glasses. *Phys. Status. Solid*, 1984, **83** (1), K15–K18.

[11] Abello L., Husson E., Repelin Y., Lucazeau G. Vibrational spectra and valence force field of crystalline V_2O_5. *Spectrochimica Acta Part A: Molecular Spectroscopy*, 1983, **39** (7), P. 641–651.

[12] Madhuri K.V.,Srinivasa rao K., et al. Optical and electrical properties of $(V_2O_5)_{1-x}$–$(MoO_3)_x$ thin films. *J. Indian Inst. Sci.*, 2001, **81**, P. 653–658.

[13] Ramana C.V., Naidu B.S., Hussain O.M., Pinto R. Low temperature growth of Vanadium pentoxide thin films produced by Pulsed Laser ablation. *J. Phys. D: Appl. Phys.*, 2001, **34**, L35–L38.

NANOSYSTEMS: PHYSICS, CHEMISTRY, MATHEMATICS, 2016, 7 (4), P. 691–694

Optically tuned poly (3-hexylthiophene-2,5-diyl) P3HT/PCBM (modified fullerene) blend for plastic solar cell

Ishwar Naik[1*], Rajashekhar Bhajantri[2], Lohit Naik[2], B. S. Patil[3], Ullas shetti Pragasam[1], Sunil Rathod[4], Jagadeesh Naik[4]

[1]Govt. Arts & Science College, Karwar, India
[2]Dept. of Physics, Karnatak University, Dharwad, India
[3]Govt. First Grade College Poojgeri, Ankola, India
[4]Dept. of Physics, Mangalore University, Mangalore, India
*iknaik@rediffmail.com, rfbhajantri@gmail.com

PACS 73.61.Ph; 73.50.Pz; 81.01.Fb; 81.05.ub; 82.35.Cd; 83.80.Tc

DOI 10.17586/2220-8054-2016-7-4-691-694

Nanotechnology-assisted organic electronics is a wide-spread and promising research field at present in the search for an efficient solar cell. The strong absorption spectra of the donor polymer poly[3-hexylthiophene-2,5-diyl](P3HT) in the visible region and the prominent absorption of the acceptor [6,6]-phenyl C_{61} butyric acid methyl ester(PCBM) in UV region have proved them to be the most popular donor-acceptor pair for preparing photoactive materials. The active blend, having a broad absorption spectrum, is the primary requisite for an efficient solar cell. The present work is focused on optimizing the photoactive blend of (P3HT)) and PCBM for the maximum absorption of the solar energy. P3HT: PCBM blends of weight ratio 3:1, 1:1 & 1:3 were prepared in xylene as the solvent and glass coated samples are prepared by solution cast method. Samples were characterized by JASCO UV Vis NIR V 670 spectrometer. P3HT has strong absorption in the visible region, while PCBM has an effective absorption in the UV region with broad tail of absorption extending up to 800 nm. The spectrum for the blend is a superposition of the spectra of the component moieties. The 1:3 blend of P3HT with PCBM has broad spectral sensitivity for absorption and can be used as the best photoactive blend for construction of a plastic solar cell. The energy difference (band gap) between Highest Occupied Molecular Orbital (HOMO) and the Lowest Un-occupied Molecular Orbital (LUMO) of the samples were determined through Tauc's plot. Calculations from Tauc's plot indicated that pure P3HT sample has an onset wavelength of 640 nm with a band gap of 1.93 eV. The onset wavelengths for 3:1 & 1:1 blends are almost same of about 632 nm with a band gap of 1.96 eV. The optimized blend 1:3 sample has the onset wavelength 653 nm with the least energy gap 1.9 eV.The absorption by the blend can be further enhanced by either dye sensitization or plasmon resonance.

Keywords: P3HT, PCBM, HOMO, LUMO, LSPR.

Received: 5 February 2016

1. Introduction

First generation silicon-based solar cells are are hindered by material cost, installation cost, and fabrication complications. Even the second generation thin film solar cells are also not economical [1]. Plastic solar cells are promising because of their low cost, simple processing and flexibility. Since efficiency is the main drawback of these solar cells, the search for an efficient plastic solar cell has become a global challenge at present in the field of plastic electronics. The physics involved in the energy conversion efficiency of polymer cells is a multistep process, including photon absorption, exciton formation and migration, exciton dissociation, charge transport and charge collection [2]. The bulk heterojunction concept of the donor-acceptor system has provided remarkable progress in the efficiency enhancement in this regard. The exciton diffusion mechanism and the charge collection rate have been significantly increased due to the formation of number of hetero P-N junctions in the blend. The photoactive blend must be properly tuned with respect to the choice of donor-acceptor pair as well as their weight percentage combination to have a broad solar spectral response. Among the conducting polymers, P3HT has the absorption spectrum matching well with the strongest solar spectrum and also has good transport properties. The present work is focused on the preparation of an optimized active blend of the widely used donor polymer Poly[3-hexylthiophene-2,5-dily) (P3HT) and N-type acceptor [6,6]-Phenyl C_{61} butyric acid methyl ester (PCBM), a modified fullerene. The strong absorption spectrum of P3HT in the visible region and the prominent absorption of PCBM in the UV region, along with the broad tail of absorption beyond the visible region are the key factors in selecting them as the donor-acceptor pair. The resulting active blend must show broad spectral absorption extending from the UV to the region beyond the visible for a proper composition between them. Blends of different donor-acceptor weight ratios were prepared in the high boiling point solvent xylene and their glass

coated samples (solution cast method) were characterized by UV-Visible spectra. The blend showing broad spectral sensitivity for absorption is selected as the best photoactive blend.

2. Experimental

The P-type donor polymer P3HT (electronic grade, average mol wt 15000 – 45000, HOMO 5 eV, LUMO 3 eV) and N-type acceptor PCBM (functionalized Fullerene, HOMO 6.1 eV,LUMO 3.7 eV) were purchased from Sigma Aldrich Corporation. The solvent xylene was obtained from Rankem Chemicals. These chemicals are used as received without further purification. The chemical structures of these donor and acceptor molecules are as shown below.

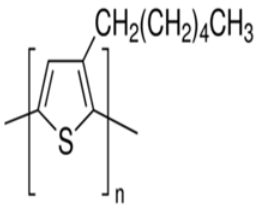

P3HT

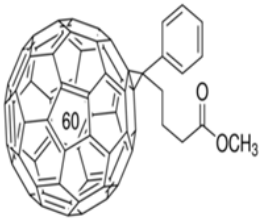

PCBM

10 mg of P3HT and 10 mg of PCBM were dissolved in 100ml of xylene in separate beakers and magnetically stirred for 48 hrs at room temperature until clear solutions were formed. The resulting solutions were of concentrations 0.1 mg/ml each. The solutions were blended with P3HT: PCBM at weight ratios of 3:1, 1:1 & 1:3 keeping the total weight of the film fixed at 4 mg. The mixtures were magnetically stirred for 3 days at room temperature and then transferred to 3 cm diameter petri-plates, dried at room temperature and then at about 50 °C in hot air oven. The film composition is as shown in Table 1.

TABLE 1. Weight proportions of blends

P3HT/Xylene (P type)	PCBM/Xylene (N type)	P:N
4 mg	0 mg	Pure P
3 mg	1 mg	3:1
2 mg	2 mg	1:1
1 mg	3 mg	1:3
0 mg	4 mg	Pure N

3. Result and discussion

One of the major problems in polymer solar cells is insufficient absorption in the solar irradiation spectrum. Even the widely studied phenylene-vinylene polymers have band edges at 550 nm [2]. However, the pure P3HT film has absorption extending from 300 nm to 640 nm. The spectrum has two peaks at 520 nm and 560 nm with one shoulder around 620nm, having onset of absorption (the absorption edge) at about 640 nm, matching well with the strongest solar spectrum (Fig. 1(a)). The first two peaks arise from $\pi - \pi^*$ transition and the shoulder is due to interchain interactions [2]. Pure PCBM shows the strongest absorption in the UV region with a broad tail of absorption extending up to 800 nm (Fig. 1(e)). The strong absorption in the UV region arises from HOMO-LUMO (Highest Occupied Molecular Orbital-Lowest Unoccupied Molecular Orbital) transitions [3] or in other words the strongest absorption is attributed to the formation of higher excited singlet states [4]. The spectra are in good agreement with previously reported results. Spectra for all other blends are the superposition of the component spectra. The effect of PCBM in the blend is to reduce the absorption of P3HT in the visible region followed by increase of absorption in UV region and beyond 650 nm. The modification in the spectrum is because of the interaction between PCBM molecules and P3HT polymer chain. Modified fullerene molecules hinder the interaction among the P3HT chains [5]. Although the 3:1 and 1:1 blends have enough absorption in the visible region as indicated Fig. 1(b) and Fig. 1(c) respectively, the absorption coefficient of 1:3 blend is greater in the UV region and beyond 640 nm as depicted in Fig. 1(d). Relatively, the 1:3 blend has wide spectral sensitivity (Fig. 1(f)) and can be considered as the best photoactive blend among the samples prepared. Pure P3HT sample has onset wavelength of 640 nm with a band gap of 1.93 eV as calculated from Fig. 2(a). Onset wavelengths for 3:1 & 1:1 blends are almost same of about 632 nm with a band gap of 1.96 eV as revealed by Fig. 2(b) and Fig. 2(c). The

calculations from Tauc's plot shows that the onset wavelength of the optimized blend is 653 nm with band gap 1.9 eV in accordance with Fig. 2(d). The absorption by the blend can be further enhanced by doping with metal nano particles, exploiting Localised Surface Plsmon Resonance (LSPR) or by dye sensitization. Nanodoping/dye sensitization of 1:3 P3HT: PCBM blend and construction of solar cell using the same is our work in progress.

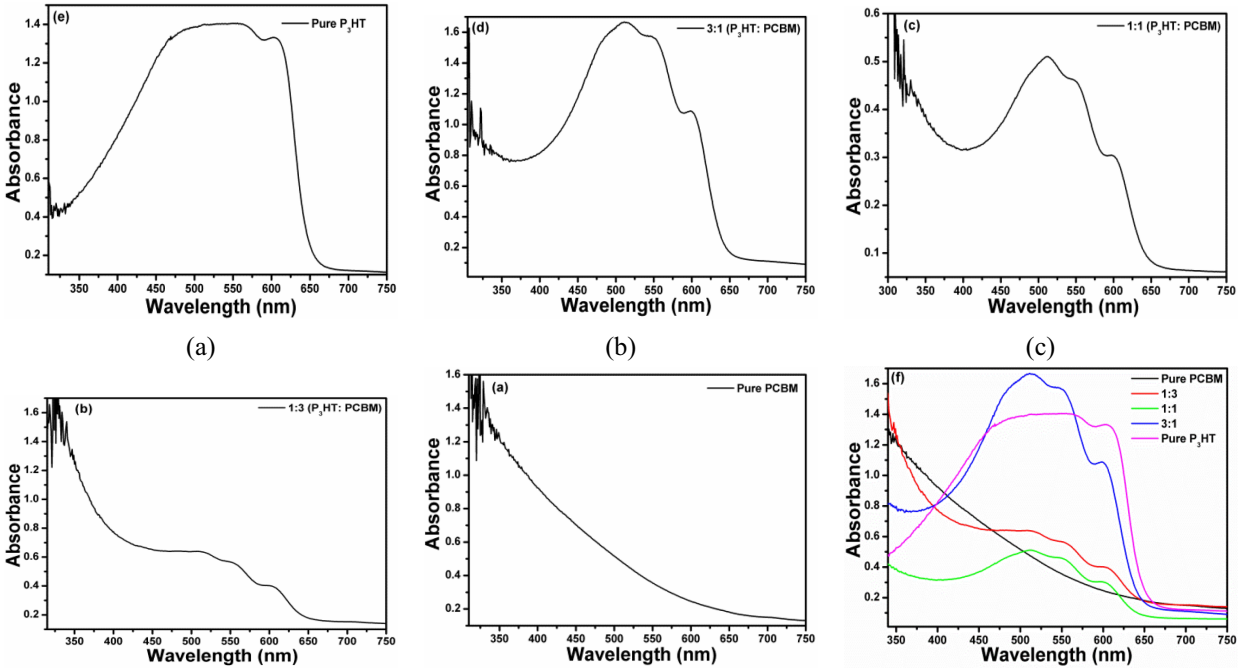

FIG. 1. Spectrum of pure P3HT film (a); 3:1 (b); 1:1 (c); 1:3 (d) P3HT:PCBM; pure PCBM (e) and overlay spectra of all films (f)

4. Conclusion

We have investigated the UV-VISIBLE absorption spectra for 3:1, 1:1, 1:3 blends of P3HT:PCBM mixed p-n junction photoactive material along with their pristine glass coated films. Spectral analysis indicated that increased weight percentage of PCBM in the blend broadened the spectral region of absorption. The 1:3 blend of P3HT:PCBM showed broad spectral absorption and was selected as the best photoactive blend. The optimized blend had the smallest band gap (1.9 eV). By doping the blend with metal oxide nanoparticles or by dye sensitization, the absorption can be further enhanced. Exploiting Plasmon Resonance through nanodoping of the selected blend is an area for future investigation. Additionally, there are plans for dye sensitization of the active blend which are being explored. Finally, we conclude that the 1:3 blend of P3HT:PCBM can be used as a photoactive material for constructing a plastic solar cell and the construction of this solar cell is progressing.

Acknowledgements

Thanks to UGC for sanctioning the Minor research project entitled 'construction and characterization of an organic solar cell (OPV) devised from a self-made low cost spin coating machine'. Order No. 1419-MRP/14-15/KAKA088/UGC-SWRO, dated 04-02-2015.

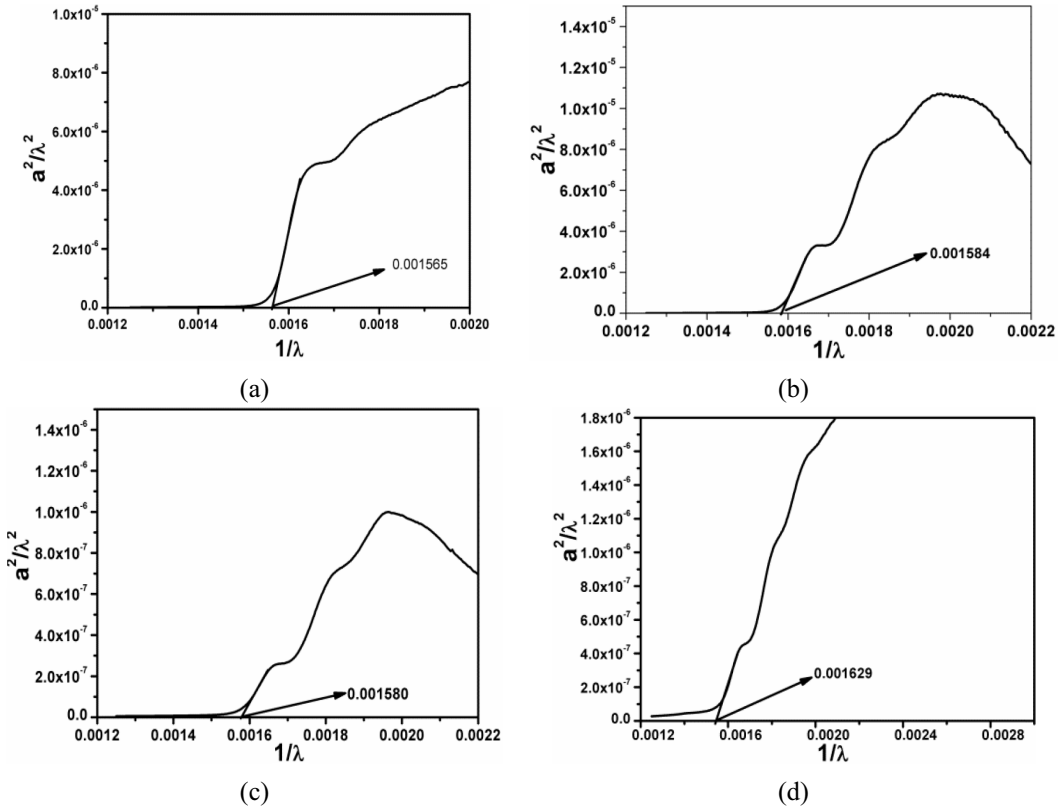

FIG. 2. Tauc's plot for pure P (a); 3:1 P:N (b); 1:1 P:N (c); 1:3 P:N (d)

References

[1] Ritesh Tipnis, Darin Laird, Mathew Mathai. Polymer-based Materials for Printed Electronics: Enabling High Efficiency Solar Power and Lighting. *Material Matters*, 2008, **3** (4), P. 92.

[2] Li G., Vishal Shrotriya, et al. Manipulating regioregular poly (3-hexylthiophene):[6,6]-phenyl-C_{61}-butyric acid methyl ester blends?route towards high efficiency polymer solar cells. *Journal of Materials Chemistry*, 2007, **17**, P. 3126–3140.

[3] Mohamad K.A., Afishah Alias, et al. Mixed P3HT/PCBM Organic Thin-Film Transistors: Relation between Morphology and Electrical Characteristics. *J. Chem. Chem. Eng.*, 2014, **8**, P. 476–481.

[4] Hummelen(Kees) J.C. Improved fullerene materials for plastic photovoltaics. `http://www.rug.nl/msc/research/groups/molecularMaterialsDevices`.

[5] Chirvase D., Parisi J., Hummelen J.C., Dyakonov V. Influence of nanomorphology on the photovoltaic action of polymer-fullerene composites. *Nanotechnology*, 2004, **15**, P. 1317.

NANOSYSTEMS: PHYSICS, CHEMISTRY, MATHEMATICS, 2016, 7 (4), P. 695–698

Visible light degradation of textile effluent using nanostructured TiO_2/Ag/CuO photocatalysts

N. Karthikeyan[1,2], V. Narayanan[3] and A. Stephen[1]

[1]Department of Nuclear Physics, University of Madras, Guindy Campus, Chennai, India
[2]Department of Physics, The Open University of Sri Lanka, Nawala, Nugegoda, Sri Lanka
[3]Department of Inorganic Chemistry, University of Madras, Guindy Campus, Chennai, India
karthikppt@gmail.com, vnnara@yahoo.co.in, stephen_arum@hotmail.com

PACS 62.23.St, 42.70.Qs, 87.85.Rs **DOI 10.17586/2220-8054-2016-7-4-695-698**

TiO_2, Ag and CuO nanomaterials, and nanostructured TiO_2/Ag/CuO photocatalytic materials coupled in different weight percentages were synthesized. The prepared materials were characterized by XRD, SEM, EDX and UV-Vis diffuse reflectance spectroscopy. Photocatalytic degrading capabilities of the pure, as well as the nanostructured TiO_2/Ag/CuO photocatalytic materials were tested on the dye effluent collected from the textile industries. The samples collected during the photocatalytic degradation of textile dye effluent were studied with UV-Vis spectroscopy. The nanostructured TiO_2/Ag/CuO photocatalyst with the composition of 80:10:10 weight percentage exhibited remarkable performance. Coupling of Ag metal nanoparticles and narrow bandgap CuO semiconductor nanomaterial to the wide bandgap TiO_2 semiconductor nanomaterial was found to modify the operative bandgap of the system and generate electron-hole pairs under visible light irradiation. The coupled TiO_2/Ag/CuO system facilitates improved electron transfer to the adsorbed molecules, and thus the system improves the photocatalytic degradation of dyes by enhanced redox mechanism.

Keywords: Coupled TiO_2/Ag/CuO, Nanostructured photocatalysts, bandgap, degradation of textile effluents, advanced oxidation process.

Received: 5 February 2016. Revised: 18 April 2016.

1. Introduction

In 1972, Fujishima and Honda found that TiO_2 could be used as catalytic electrode in a photo-electrolysis cell to decompose water into H_2 and O_2, without applying an external voltage [1]. Further researches established the use of TiO_2 for photo-assisted degradation of organic compounds and reduction of inorganic compounds. Researches on purification of polluted water gained greater importance with ever increasing need to purify the industrial effluents as well as the contaminated water resources by the industrial waste streams which often created serious health and environmental problems. Among the many, textile effluents play significant role in polluting the water resources and the environment. Traditional effluent purification processes often produce end products with carcinogenic compounds, which require further treatment for complete purification. The photocatalytic degradation of textile effluents using nanophotocatalysts through advanced oxidation process is one of the recent scientific explorations that gain importance mainly due to its ability to produce harmless end products [2–4].

Titania is a semiconductor with bandgap energies in the range of 3.2 – 3.4 eV, and hence could produce electron–hole pairs upon UV region photon irradiation. When these photogenerated charge carriers migrate to the surface without recombining, they could interact with the adsorbed water and oxygen molecules to produce radical species. These radicals strike any adsorbed organic dyes and lead to complete or selective degradation. Repeated efforts are being made by the researchers to trigger this degradation process under visible light irradiation, to make the process very economical by using abundantly-available solar light in various photocatalytic applications. Efficient photogeneration of electron – hole pairs, prevention of their recombination and reduction of specific surface area of the particles of the photocatalysts are the key factors in increasing the efficiency of photocatalytic activity. Several researchers have proven that coupling of semiconductors with noble metals and other semiconductor materials at nanoscales plays significant role in modifying the above factors [5–9].

In this exploration, TiO_2, Ag and CuO nanomaterials, and nanostructured TiO_2/Ag/CuO photocatalysts coupled in different weight percentages were synthesized under optimized conditions [10,11] and tested for their degradation efficiency on a model dye and also on an effluent collected from textile industries in Tamil Nadu, India.

2. Experimental methods

Titania was synthesized using the sol-gel method, by dissolving the precursor titanium (IV) isopropoxide in isopropanol under continuous stirring at room temperature, and then by adding citric acid as the chelating agent mixed with deionized water. Ag and CuO were synthesized via thermal decomposition method by heat treatment

of silver acetate and copper acetate, separately in alumina crucibles, by rising the temperature up to 300 °C in steps of 4 °C/min. Then, the respective polycrystalline nanoparticles were synthesized by annealing the as-prepared samples at the optimized temperature of 450 °C for 30 minutes. Details for this protocol were reported elsewhere [12]. Then, the coupled TiO_2/Ag/CuO photocatalysts were synthesized by taking the as prepared samples in three different weight percentages, viz. 80:15:05. 80:10:10 and 80:05:15, grinding them well for 2 hrs, and then annealing at 450 °C for 30 min.

X-ray diffraction studies were carried out on RICH SEIFERT, Germany (model 3000) diffractometer using Cu-$K_{\alpha 1}$ radiation ($\lambda = 1.54056$ Å), 30 kV voltage, and 10 mA current. Surface morphology and elemental composition were carried out using QUANTA 200 FEG high resolution scanning electron microscopy (HR-SEM) and energy-dispersive X-ray spectroscopy (EDX). The optical properties of the samples in UV and Visible ranges were investigated using CARY 5E UV-VIS-NIR spectrophotometer.

3. Results and discussions

3.1. Phase and structure confirmation

Figure 1 shows the powder XRD patterns of the TiO_2, Ag, and CuO, and that of coupled TiO_2/Ag/CuO samples prepared at weight percentages 80:05:15, 80:10:10 and 80:15:05, and annealed at 450 °C. The primary diffraction peaks of the TiO_2 were indexed to anatase phase Titania with tetragonal crystal structure, and the values well matched with the JCPDS card 84-1285. The calculated lattice parameter values are: $a = b = 3.784$ Å and $c = 9.561$ Å.

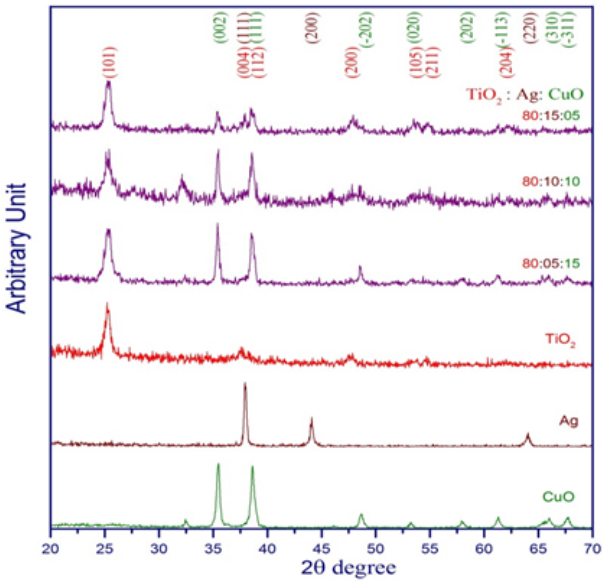

FIG. 1. XRD patterns of all the prepared samples, annealed at 450 °C for 30 min.

The characteristic peaks of the CuO were indexed to monoclinic structure and the values are in good agreement with the reported values in the JCPDS card 89-5896. The determined lattice parameters are: $a = 4.683$ Å, $b = 3.424$ Å and $c = 5.129$ Å.

The diffraction peaks of the prepared sample Ag were indexed to cubic structure and could be matched well with the JCPDS card number 03-0921. The calculated lattice parameters are: $a = b = c = 3.914$ Å.

The crystallite sizes were estimated using the Scherrer's formula, and the estimated average crystallite sizes ranged from 9 to 64 nm. No significant peak shifts were observed in the XRD patterns of the coupled systems.

The HRSEM images, as shown in Fig. 2, of the coupled photocatalysts reveal irregularly-shaped particles, which are agglomeration of the tiny spherically shaped particles. The average particle sizes of the isolated spheres were in the range from 25 to 80 nm. The EDX analysis confirmed the elemental composition in the respective coupled photocatalysts.

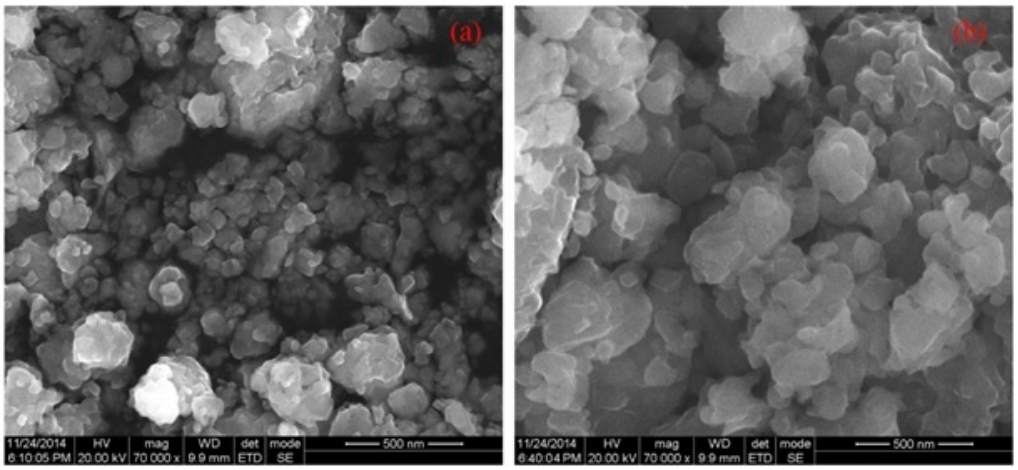

FIG. 2. HRSEM images TiO_2/Ag/CuO at wt%: (a) 80:10:10; (b) 80:15:05

3.2. Optical properties and bandgap energies

UV-Vis Diffuse Reflectance spectrum of the prepared photocatalytic samples TiO_2, TiO_2/Ag/CuO (80:15:05), TiO_2/Ag/CuO (80:10:10) and TiO_2/Ag/CuO (80:05:15) are shown in Fig. 3. The absorption edge of the pure TiO_2 was in the UV region. However, red shifts were observed for the coupled TiO_2/Ag/CuO photocatalysts prepared at three different weight percentages 80:15:05, 80:10:10 and 80:05:15 and their absorption edges have fallen in the visible region.

The estimated optical band gap energies of pure TiO_2 as well as those of the coupled TiO_2/Ag/CuO nanophotocatalysts prepared at three different weight percentages 80:15:05, 80:10:10 and 80:05:15 are shown in Table 1.

TABLE 1. Optical band gap energies of the prepared photocatalysts

Photocatalysts	**Band gap**
TiO_2	3.3 eV
TiO_2/Ag/CuO (80:05:15)	3.0 eV
TiO_2/Ag/CuO (80:10:10)	2.9 eV
TiO_2/Ag/CuO (80:15:05)	3.0 eV

3.3. Photocatalytic degradation test results

All the photocatalysts were tested for their decoloration efficiency on the methylene blue (MB) dye under visible irradiations and the results are shown in Fig. 4. The photocatalyst TiO_2/Ag/CuO synthesized at 80:10:10 wt % showed best efficiency with more than 75 % of decoloration in 120 minutes under visible light irradiation.

Then the best photocatalyst TiO_2/Ag/CuO (80:10:10) was employed in the degradation of the textile effluent and the results are shown in Fig. 5. More than 80 % decoloration of the textile effluent was achieved in 240 minutes under visible light irradiation.

4. Conclusions

TiO_2, Ag and CuO, and coupled TiO_2/Ag/CuO photocatalysts at three different weight percentages 80:05:15, 80:10:10 and 80:15:05 were synthesized. Their structural, morphological and optical properties were analyzed with various characterization techniques. Among the prepared photocatalysts, TiO_2/Ag/CuO (80:10:10) gave the best decoloration (about 79 %) of MB in 2 hours under visible light irradiation. This is in agreement with the results obtained from the optical property studies. The best photocatalyst effectively degraded the textile effluent with an efficiency of about 82 % of decoloration in 4 hours under visible light irradiation. Inclusion of optimal amount of CuO and Ag was found to modify the band gap significantly and make the photocatalyst active under visible light. The CuO acts as sink for photogenerated electrons, prevents recombination and thus enhances the redox reaction and hence the efficiency of the degradations.

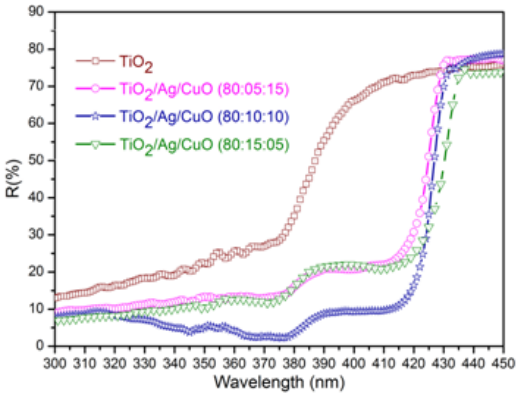

FIG. 3. Diffuse reflectance spectrum of the prepared photocatalysts

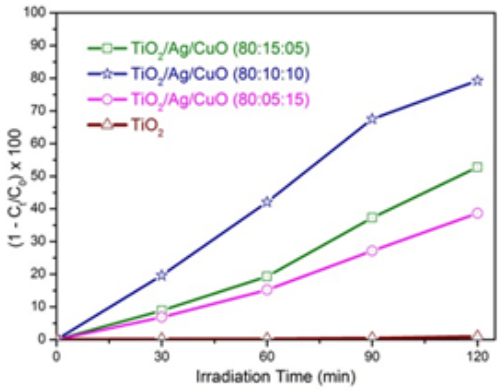

FIG. 4. Degradation profile – Methylene Blue

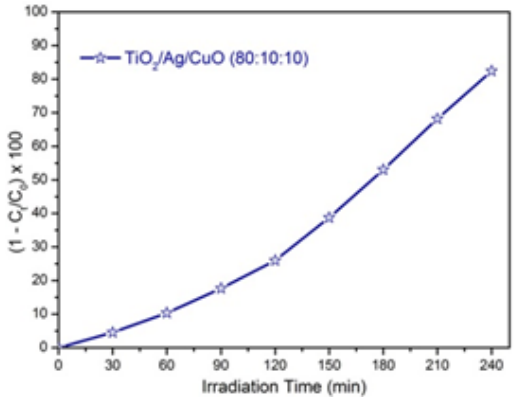

FIG. 5. Degradation profile – Textile Effluent

Acknowledgements

One of the authors, NK, thanks HETC project for the financial support. The authors are thankful to SAIF at IIT Chennai for the HR-TEM and UV-Vis DRS characterization of powder samples.

References

[1] Fujishima A., Honda K. Electrochemical Photolysis of Water at a Semiconductor Electrode. *Nature*, 1972, **238** (5358), P. 37–38.
[2] Hisaindee S., Meetani M.A., Rauf M.A. Application of LC-MS to the analysis of advanced oxidation process (AOP) degradation of dye products and reaction mechanisms. *TrAC Trends in Analytical Chemistry*, 2013, **49**, P. 31–44.
[3] Chequer F.M.D., et al. Analyses of the genotoxic and mutagenic potential of the products formed after the biotransformation of the azo dye Disperse Red 1. *Toxicology in Vitro*, 2011, **25** (8), P. 2054–2063.
[4] Parsons S.A., Williams M. *Advanced Oxidation Processes for Water and Wastewater*. London, UK: IWA Publishing, 2004, 368 p.
[5] Jakob M., Levanon H., Kamat P.V. Charge Distribution between UV-Irradiated TiO_2 and Gold Nanoparticles:? Determination of Shift in the Fermi Level. *Nano Letters*, 2003, **3** (3), P. 353–358.
[6] Wood A., Giersig M., Mulvaney P. Fermi Level Equilibration in Quantum Dot?Metal Nanojunctions. *The Journal of Physical Chemistry B*, 2001, **105** (37), P. 8810–8815.
[7] Anh Tuan V., et al. Synthesis and characterization of TiO_2 photocatalyst doped by transition metal ions (Fe^{3+}, Cr^{3+} and V^{5+}). *Advances in Natural Sciences: Nanoscience and Nanotechnology*, 2010, **1** (1), P. 015009 (4 p).
[8] Rehman S., et al. Strategies of making TiO_2 and ZnO visible light active. *Journal of Hazardous Materials*, 2009, **170** (2–3), P. 560–569.
[9] Qiu R., et al. Photocatalytic activity of polymer-modified ZnO under visible light irradiation. *J. Hazardous Mat.*, 2008, **156** (1–3), P. 80–85.
[10] Saravanan R., et al. Photocatalytic Degradation of Organic Dyes Using ZnO/CeO2 Nanocomposite Material Under Visible Light. *Advanced Materials Research*, 2012, **584** (1), P. 381–385.
[11] Karthikeyan N., Narayanan V., Stephen A. Effect of Annealing on Photocatalytic Degradation of Azo Dye by TiO_2/CuO Binary Nanostructured Materials. 4th Int. Symp. for Research Scholars on Metallurgy, Materials Science and Engineering. *ISRS*, 2012.
[12] Karthikeyan N., Narayanan V., Stephen A. Synthesis and Characterization of Coupled ZnO/Ag/CuO Nanomaterials for Photocatalytic Degradation of Organic Dye under UV irradiation. *Int. J. Inn. Res. Sci. & Eng.*, 2014, **2** (spl), P. 74–79.

NANOSYSTEMS: PHYSICS, CHEMISTRY, MATHEMATICS, 2016, 7 (4), P. 699–702

Temperature influence study on copper selenide films

V. Rajendran[1], S. Arulmozhi Packiaseeli[2], S. Muthumari[3] and R. Vijayalakshmi[3]

[1]Department of Physics, Vivekananda College, Madurai 625234, India
[2]P. G. & Research Department of Physics, Fatima College, Madurai 625018, India
[3]P. G. & Research Department of Physics, Thiagarajar. College, Madurai 625009, India

rajendran.vvc@gmail.com, ramyarv@rediffmail.com

PACS 74.25 Gz, 64.70 ph, 61.05 Cp **DOI 10.17586/2220-8054-2016-7-4-699-702**

Copper selenide was prepared by film is successfully deposited on a Fluorine-doped Tin Oxide (FTO) substrate by a brush plating technique. The film was uniform, had good adherence to the substrate and was annealed at 300 °C and 500 °C. As the annealing temperature increased, the orientation of the crystallites is more randomized than in the as-prepared film. The structural and optical properties of the film were investigated by XRD, SEM, EDAX, UV-Visible and PL. The XRD pattern indicated that this film was crystalline in the structure.

Keywords: Brush plating, copper selenide, optical properties.

Received: 5 February 2016

Revised: 3 May 2016

1. Introduction

Copper selenide (Cu_2Se) thin films have attracted considerable interest over the last year owing their wide range of applications in optoelectronic devices and solar cells. Copper selenide is an interesting metal chalcogenide semiconductor material. A copper selenide thin film has a direct band gap and is transparent over a wide range of the visible spectrum. It is seen that the photoelectronic and other properties of II–VI class of compound thin films are highly optically-sensitive, which in turn, can severely influence device performance [1]. More progress has been achieved in the fabrication of light emitting diodes, dielectric mirrors and other optically sensitive devices.

Selenium-based alloys are not stable under standard operational conditions because their glass transitions are typically close to room temperature. In order to stabilize these glasses it is common to use an additive which acts as a cross-linking agent and increase the dimensionality of structure and stability of the material [2]. The purpose of present study is to explore and report in detail the structural properties and optical properties of copper selenide thin film prepared by brush plating technique.

2. Experimental procedure

The precursor solution was prepared by stirring 1 g of copper(II) sulfate ($CuSO_4$) and 0.05 gm of selenium dioxide (SeO_2) in 5 ml of distilled water until the powder is totally mixed to provide a saturated solution. The Copper Selenide thin films were prepared by Brush Plating technique. The films were grown on Fluorine doped Tin Oxide (FTO) substrate under optimized conditions. These grown films were uniform, blue in color and showed good adherence to the substrate surface. All chemicals were of AR grade.

The as-deposited films were annealed at 300 °C and 500 °C for about 1 hr. The annealed film was utilized for optical- and structural properties studies.

3. Results and discussion

3.1. XRD Analysis

Figures 1(a) and (b) show the X-ray diffraction pattern of the brush plated copper selenide thin film. The XRD pattern obtained correlated well with the standard JCPDS (06-680) data.

Crystallite size (D) was calculated using Debye-Scherrer's formula [3]:

$$D = 0.94\lambda/\beta\cos\theta,$$

where D is the crystallite size, λ is the wavelength of the k_α line, β is the full width at half maxima (FWHM) in radians and θ is the Bragg's angle. The crystallite grain size increased from 2 – 53 nm as the annealing temperature increased [4]. The observed 'd' values 4.5, 2.2, 2.0, 1.5 Å are in good agreement with the standard 'd' values. Peaks corresponding to (1 1 0), (2 2 0), (3 1 0), (4 0 1) were observed [5].

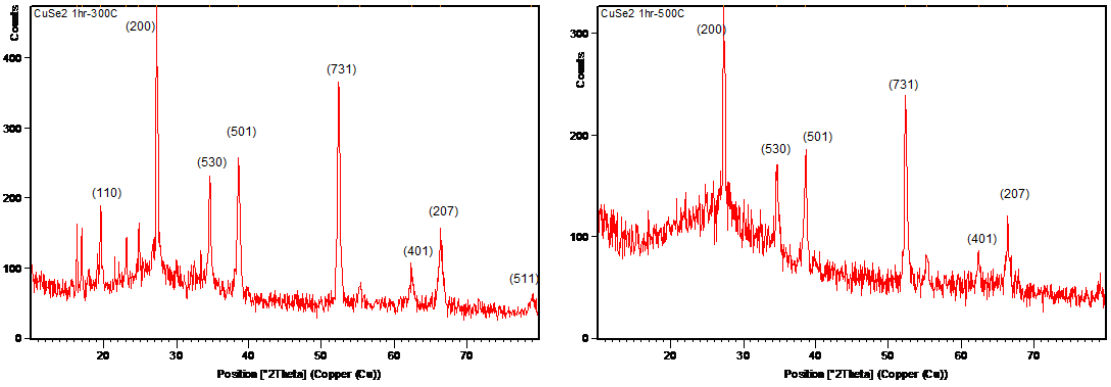

(a) (b)

FIG. 1. XRD pattern of Cu_2Se thin film annealed at 300 °C (a) and 500 °C (b)

3.2. Morphological studies and compositional analysis

Scanning electron microscopy is a convenient tool to study the surface morphology of micro- and nanoscale materials as well as thin films. Fig. 2(a,b) shows the SEM images of CuSe thin films annealed at 300 °C and 500 °C recorded at 20 kV with the magnification 10000 using the instrument JSM-6390. The particle size increased as the annealing temperature increased [6].

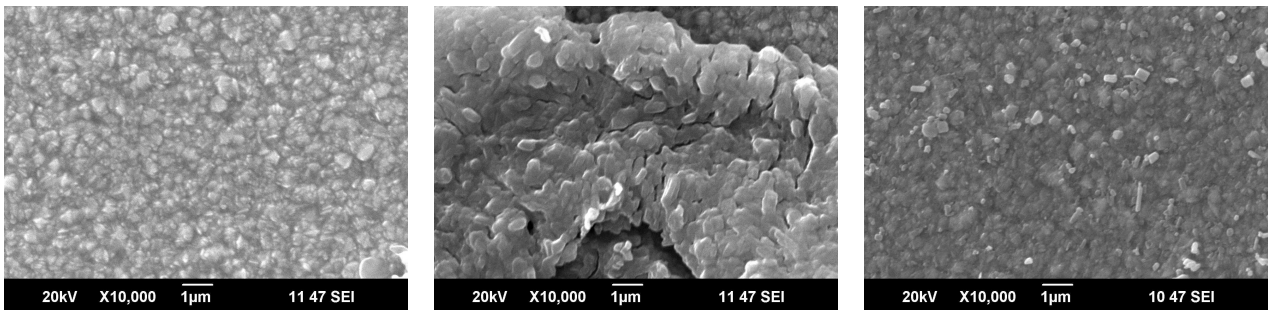

(a) (b) (c)

FIG. 2. SEM image of Cu_2Se as deposited (a); annealed at 300 °C (b) and 500 °C (c)

The EDAX analysis from Fig. 3(a–c) revealed that the presence of copper, selenium, oxygen and other elements like silicon, tin on the FTO substrate. The EDAX spectrum recorded in the binding energy region of 0 – 10 keV showed the presence of copper and selenium in thin films. EDAX analysis of the mass % and atom % of copper selenide films are tabulated in Table 1. EDAX spectrum confirms the presence of copper and selenium in the thin films [7].

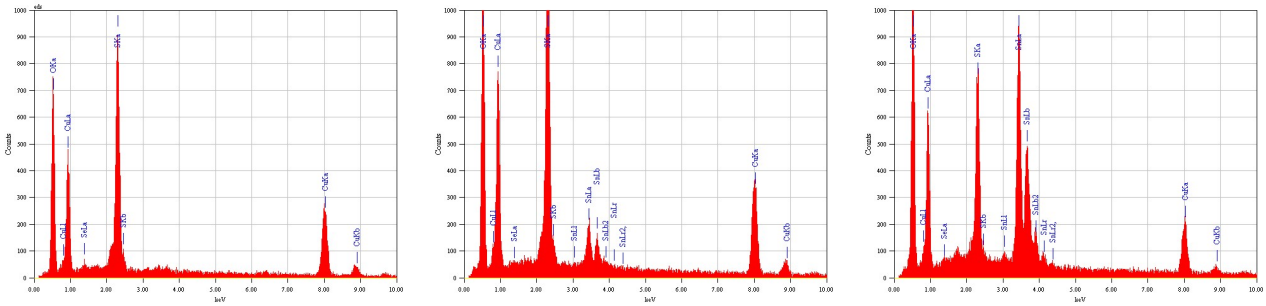

(a) (b) (c)

FIG. 3. EDAX analysis of Cu_2Se as deposited (a); annealed at 300 °C (b) and 500 °C (c)

TABLE 1. Mass and Atom percentage of Cu_2Se annealed at 300 °C and 500 °C

Sample	Mass %		Atom %	
	Copper	Selenium	Copper	Selenium
As-deposited	49.35	1.19	26.23	0.51
Annealed at 300 °C	38.73	0.42	21.78	0.19
Annealed at 500 °C	16.37	0.41	12.89	0.26

3.3. Optical absorption, transmittance and reflectance measurement

The typical optical absorbance, transmittance $T(\%)$ spectra and reflectance spectra of the films prepared using brush plating method are presented in Fig. 4(a–c) respectively for the as-deposited and annealed samples (at 300 °C and 500 °C). Annealing the film at 300 °C and 500 °C resulted in some changes in the optical transmittance and absorbance spectra of the films.

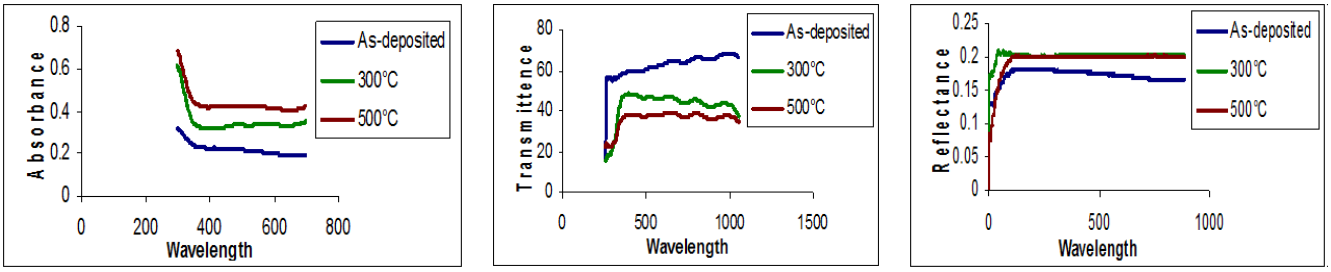

(a) (b) (c)

FIG. 4. Absorption (a), transmittance (b) and reflectance (c) spectra for Cu_2Se

The Egdir values for the samples were as follows: as-deposited – 2.95 eV; 300 °C annealing – 2.86 eV and 500 °C annealing – 2.75 eV. The Egind values were as follows: as-deposited – 2.16 eV; 300 °C annealing – 2.54 eV and 500 °C annealing – 2.38 eV. The indirect band gap values were as follows: re as-deposited – 2.16 eV; 300 °C annealing – 2.54 eV and 500 °C annealing – 2.38 eV. All these optical band gap values are close to those previously obtained for the material used for solar cells, which means that these materials have good utility for this purpose [8].

3.4. Photoluminescence spectrum

The photoluminescence spectra of Cu_2Se thin films are shown in Fig. 5. From the spectra, the photons are excited at a wavelength of 280 nm. As the annealing temperature increases, the intensity of the peak increases. From the spectra, the peaks observed in emission of Cu_2Se thin films are at a wavelength 561 nm [9]. The spectra of the as-deposited Cu_2Se films and the annealed films showed increasing intensity as the annealing temperature increased.

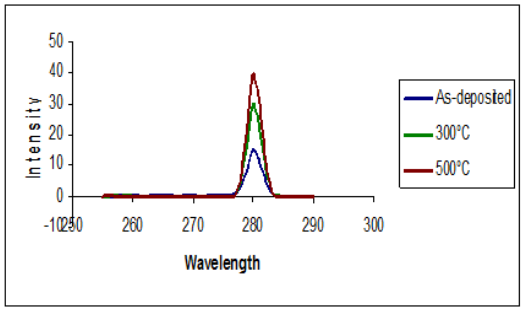

FIG. 5. Excitation Spectra of Cu_2Se

4. Conclusion

Copper Selenide thin films were successfully deposited on FTO substrates by a brush plating technique. The films were uniform and had good aherence to the substrate. The XRD of Copper Selenide films formed a cubic structure. The crystalline size of the films were determined by Scherrer's formula and it increased from 2 – 53 nm as the annealing temperature increased [10]. The energy gap values of the films were determined and compared with the reported one. The emitted and excited wavelength were determined from the photoluminescence spectra. The structural properties, surface morphological studies and chemical composition analysis were investigated and reported.

References

[1] Vipin kumar, Vinod Kumar, Dwivedi D.K. Growth and characterization of zinc telluride thin films for photovoltaic applications. *Physica Scripta*, 2012, **86**, 015604 (4 p.)

[2] Vijayalaksmi R., Chandrasekar L. Bruno, Chandramohan R. Preparation and Characterization of Se-Te-Ag Chalcogenide Thin Film. *Journal of Nanoengineering and Nanomanufacturing*, 2013, **3**, P. 70–72.

[3] Hammad Jamil T.M., Salem K., Harrison R.G. Binding agent affect on the structural and optical properties of ZnO nanoparticles. *Rev. Advanced Material Science*, 2009, **22**, P. 74–80.

[4] Ramesh K., Thanikaikarasan S., Bharathi B. Structural, morphological and optical properties of copper selenide thin films. *International Journal of Chem. Tech. Research*, 2014, **6** (13), P. 5408–5411.

[5] Garcia V.M., Nair P.K., Nair M.T.S. Binding Agent affect on the Structural and Optical Properties of ZnO nanoparticles. *Journal Of Crystal Growth*, 1999, **203**, P. 113–124.

[6] Thi Die Thuy Ung, Quang Liem Nguyen. Structural, Morphological and Optical Properties of Copper Selenide Thin Films. *Adv. Nat. Sci: Nanosci. Nanotechnol.*, 2011, **2**, 045003.

[7] Mehta N., Zulfequar M., Kumar A., Crystallization kinetics of some Se-Te-Ag chalcogenide glasses. *Journal of Optoelectronics and Advanced Materials*, 2004, **6**, P. 441.

[8] Arokiya Mary T., et al. A simple hydrothermal route for synthesizing copper Selenide Nano-Flakes. *Elixir Nanocomposite Materials*, 2012, **50**, P. 10499–10500.

[9] Garcia V.M., Guerrero L., Nair M.T.S., Nair P.K. Effect of thermal processing on optical and electrical properties of copper selenide thin films. *Superficies y Vacio*, 1999, **9**, P. 213–218.

[10] Arulmozhi Packiaseeli S., Rajendran V., Vijayalakshmi R. Structural, optical and morphological study of tungsten selenide thin films. *Nanosystems: Physics, Chemistry, Mathematics*, 2016, **7** (4), P. 703–706.

NANOSYSTEMS: PHYSICS, CHEMISTRY, MATHEMATICS, 2016, 7 (4), P. 703–706

Structural, optical and morphological study of tungsten selenide thin films

S. Arulmozhi Packiaseeli[1], V. Rajendran[2] and R. Vijayalakshmi[3]

[1]P.G. & Research Department of Physics, Fatima College, Madurai, India
[2]Department of Physics, Vivekananda College, Madurai, India
[3]P.G. & Research Department of Physics, Thiagarajar. College, Madurai, India

arulmozhipackiaseeli@gmail.com, ramyarv@rediffmail.com

PACS 68.55-a, 74.25 Gz, 64.70ph, 61.05Cp **DOI 10.17586/2220-8054-2016-7-4-703-706**

Tungsten selenide (WSe_2) film was successfully deposited on FTO substrate by brush plating technique. The film was uniform and well adherent to the substrate and annealed to 300 °C and 500 °C. As the annealing temperature was increased the orientation of the crystallites was more randomized than in the as-prepared film. The structural and optical properties of the film were investigated by XRD, SEM, EDAX, UV-Visible and PL. The XRD pattern indicates that this film was crystallized in the hexagonal structure.

Keywords: WSe thin film, morphology.

Received: 5 February 2016

Revised: 3 May 2016

1. Introduction

Metal Chalcogenide thin films such as tungsten selenide films are promising semiconducting materials suitable for solar cells. Tungsten selenide thin films have band gaps of 2.16 eV $\leq E_g \leq$ 2.65 eV and reasonable overlap with the solar spectrum [1]. Tungsten selenide thin film has direct band gap and is transparent over a wide range of the visible spectrum. It can be seen that the photoelectronic and other properties of class II–VI compound thin films are highly optically sensitive, which in turn can severely influence device performance. More progress has been achieved in the fabrication of light emitting diodes, dielectric mirrors and other optically sensitive devices [2].

2. Experimental procedure

Precursor solution was prepared by magnetically stirring 1 g of tungsten trioxide (WO_3) and 0.05 g of selenium dioxide (SeO_2) with 5 ml of distilled water until the powder was thoroughly mixed to form a homogenous solution. The tungsten selenide thin films were prepared by Brush Plating technique on the FTO (Fluorine doped Tin Oxide) substrate. The as-deposited films were annealed at 300 °C and 500 °C for about 1 hour. The structural optical and morphological properties of the as-deposited and annealed tungsten selenide thin films were studied.

3. Results and discussion

3.1. XRD Analysis

Figure 1(a) shows the XRD pattern of the as-deposited tungsten selenide film on the FTO (Fluorine doped Tin Oxide) substrate. The as-deposited WSe_2 films are amorphous in nature. Fig. 1(b) and 1(c) show the XRD pattern of tungsten selenide films which were annealed at 300 °C and 500 °C respectively. The pattern shows well-defined peaks, suggesting that the films are polycrystalline. Tungsten selenide possesses a hexagonal structure with $a = 3.29$ Å and $b = 12.97$ Å. The XRD pattern obtained correlated well with the standard JCPDS (06-0080) data. Peaks corresponding to (0 0 4), (1 0 2), (1 0 3), (1 0 6), (1 1 0), (1 0 8) were observed. The observed peaks were identified and matched with the reported values [3]. The crystallite grain size in the film was calculated using the Scherer's formula [4]:

$$D = 0.94\lambda/\beta\cos\theta \text{ (nm)},$$

where D is the crystallite size, λ is the wavelength of the k_α line, β is the full width at half maxima (FWHM) in radians and θ is the Bragg's angle. The crystallite grain size increased from 9 – 11 nm as the annealing temperature was increased [5].

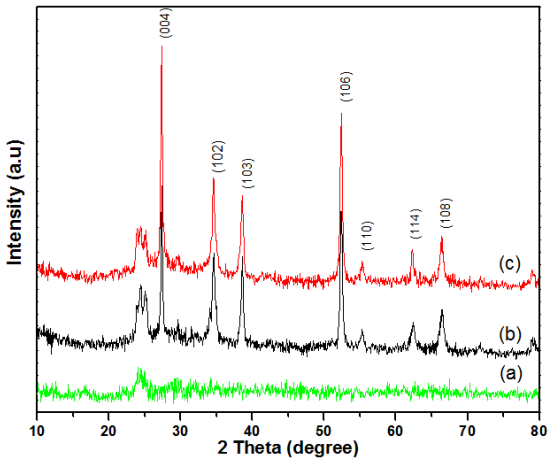

FIG. 1. WSe_2 film as deposited (a); annealed at 300 °C (b) and 500 °C (c)

3.2. Morphological study of tungsten selenide thin films

Figure 2(a-b) shows SEM images of tungsten selenide films. Detailed morphological study of the films was carried out using the JSM-6390 instrument. At 1.500× magnification the film shows a clear picture. When the magnification is increased from 1.500 to 10.000 the flakes type crystals are found. Smooth surface is obtained in the as-deposited film. The particle size was found to increase as the annealing temperature was increased [6].

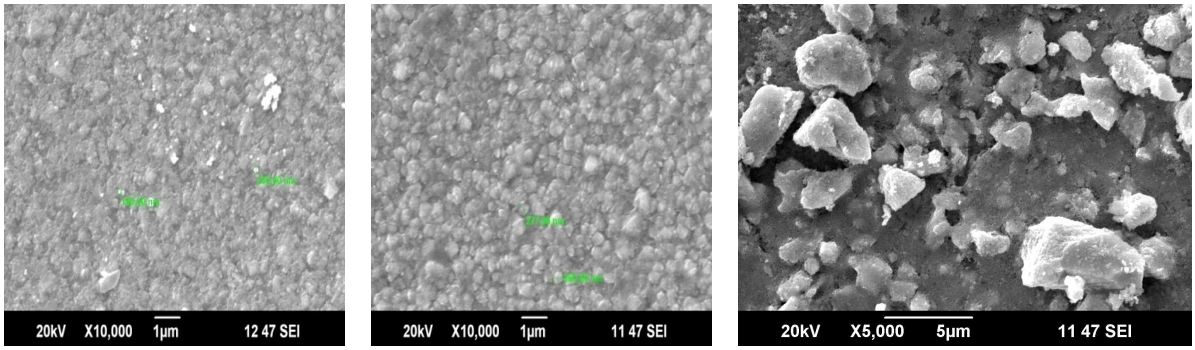

(a) (b) (c)

FIG. 2. As-deposited tungsten Selenide (a); film annealed at 300 °C (b) and 500 °C (c)

3.3. EDAX analysis of tungsten selenide films

The EDAX spectrum was recorded in the binding energy region of 0 – 10 keV Fig. 3(a,b) reveal the presence of tungsten, selenium, oxygen and other elements like silicon, tin on the FTO substrate. EDAX analysis of the elements present, mass % and atom % of tungsten selenide films are also tabulated [7] (Table 1).

TABLE 1. Mass and Atom percentage of WSe_2 annealed at 500 °C and 500 °C

Sample	Mass %		Atom %	
	Tungsten	Selenium	Tungsten	Selenium
As-deposited	2.16	0.47	1.18	0.6
Annealed at 500 °C	42.37	3.82	23.8	4.99

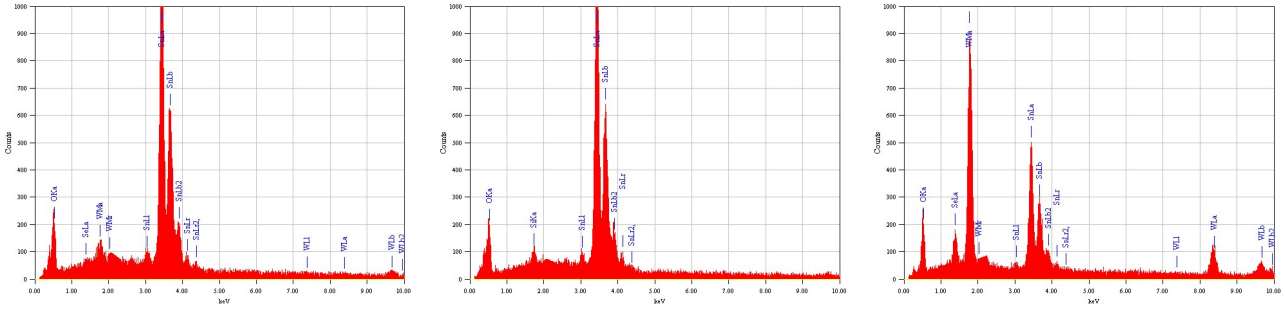

(a) (b) (c)

FIG. 3. WSe_2 as deposited (a); annealed at 300 °C (b) and 500 °C (c)

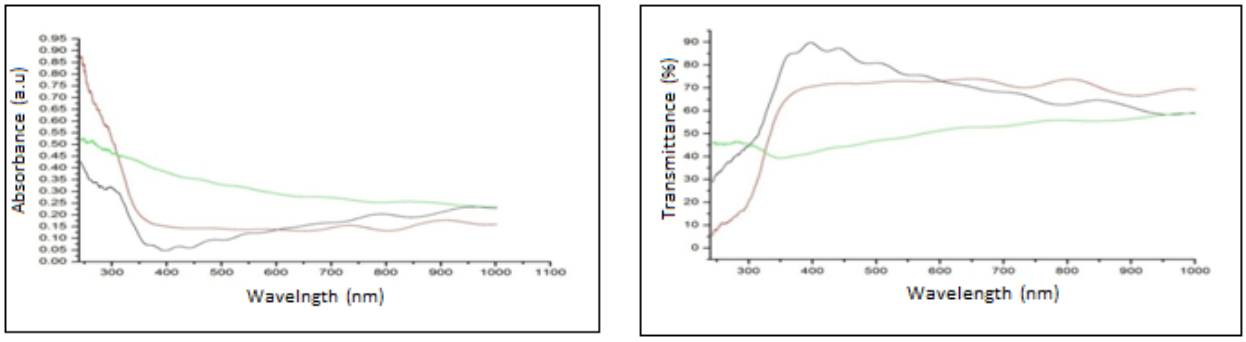

(a) (b)

FIG. 4. Absorption (a) and transmittance (b) spectra for Tungsten Selenide films

3.4. Optical absorption and transmittance measurement

Typical optical absorbance and transmittance T (%) spectra of the films prepared using brush plating method are presented in Fig. 4(a,b) respectively for the as-deposited and annealed samples (at 300 °C and 500 °C). Annealing the film at 300 °C and 500 °C did cause some changes in the optical transmittance and absorbance spectra of the films.

The typical optical absorbance and transmittance spectra of as-deposited and annealed films of tungsten selenide have been recorded and the band gap values for the films were estimated. For this, the transmittance spectra were corrected for the loss due to reflectance. The direct and indirect band gap values were obtained from plots of α_g^2, $\alpha_g^{1/2}$ respectively, against the corresponding photon energy ($h\nu$) values. Table 2 shows band gap energy of Tungsten selenide thin films for as-deposited as well as for the annealed at 300 °C and 500 °C. These optical band gap values are close to that of the already reported materials used in solar cells, which means that these films reveals good optical property necessary for this purpose [8].

TABLE 2. Direct and Indirect band gap of WSe_2

Tungsten Selenide	Direct band gap (eV)	Indirect band gap (eV)
As-deposited film	2.75	2.375
Annealed at 300 °C	2.65	2.20
Annealed at 500 °C	2.48	2.16

3.5. Photoluminescence spectrum

The photoluminescence spectra of the WSe_2 thin films are shown in Fig. 5. From the spectra, the photons are excited at a wavelength of 280 nm. As the annealing temperature increased, the intensity of the peak increased. From the spectra, the peaks observed in the emission spectrum of WSe thin films are at a wavelength of 560 nm.

The spectra of the as-deposited WSe films and the annealed films show an increase in the intensity as the annealing temperature is increased.

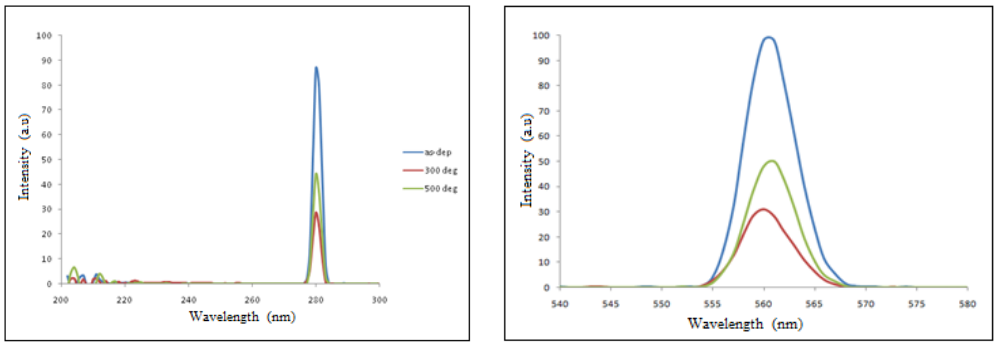

(a) (b)

FIG. 5. Excitation (a) and emission (b) spectra of Tungsten Selenide films

4. Conclusion

Structural and surface morphological studies of tungsten selenide thin films deposited by a brush plating method were carried out with (i) as deposited film, (ii) film annealed at 300 °C and (iii) film annealed at 500 °C. The SEM micrographs reveal changes in the surface morphology from amorphous to polycrystalline at 300 °C and an increase in the size of crystallites when annealed at 500 °C. Also, the EDAX analysis confirmed the presence of tungsten and selenium in the films. Optical characterization has been performed and band gap values were obtained for the films which revealed that the films possessed very good optical properties necessary for the materials used in solar cells [9].

References

[1] Vipin kumar, Vinod Kumar, Dwivedi D.K. Growth and characterization of zinc telluride thin films for photovoltaic applications. *Physica Scripta*, 2012, **86**, P. 015604.

[2] Liu X., Khan B.B., Tikhomirov V.K., Jha A. Semiconducting Chalcogenide Glass III: Applications of Chalcogenide Glasses. *J. Non-Cryst. Solids*, 1999, **294**, P. 256–257.

[3] Salitra G., Hodes G., Klein E., Tenne R. Highly oriented WSe_2 thin films prepared by selenization of evaporated WO_3. *Thin solid films*, 1994, **245**, P. 180–185.

[4] Bari R.H., Ganesan V., Potadar S., Patil L.A. Structural, optical and electrical properties of chemically deposited copper selenide films. *Bull. Mater. Sci.*, 2009, **32**, P. 37–42.

[5] Ramesh K., Thanikaikarasan S., Bharathi B. Structural, Morphological and Optical Properties of Copper Selenide Thin Films. *International Journal of ChemTech Research*, 2014, **6** (13), P. 5408–5411.

[6] Thi Die Thuy Ung, Quang Liem Nguyen. Synthesis and characterization of Fe doped Ti O_2 photocatalyst by the Sol Gel method. *Adv. Nat. Sci: Nanosci. Nanotechnol.*, 2011, **2**, 045003.

[7] Patel P.R., Patel H.S.,et al. Growth, Structural and Electrical Characterization of Tungsten Diselenide crystal. *American Journal of Condensed Matter Physics*, 2013, **3** (1), P. 13–20.

[8] Arokiya Mary T. et al. A simple hydrothermal route for synthesizing copper. *Selenide Nano-Flakes Elixir Nanocomposite Materials*, 2012, **50**, P. 10499–10500.

[9] Rajendran V., Arulmozhi Packiaseeli S., Muthumari S., Vijayalakshmi R. Temperature influence study on the copper selenide films. *Nanosystems: Physics, Chemistry, Mathematics*, 2016, **7** (4), P. 699–702.

NANOSYSTEMS: PHYSICS, CHEMISTRY, MATHEMATICS, 2016, 7 (4), P. 707–710

$ZnO/SnO_2/Zn_2SnO_4$ nanocomposite: preparation and characterization for gas sensing applications

M. Chitra[1], K. Uthayarani[1,*], N. Rajasekaran[2], N. Neelakandeswari[2], E. K. Girija[3], D. Pathinettam Padiyan[4]

[1]Department of Physics, Sri Ramakrishna Engineering College, Coimbatore–641022, Tamilnadu, India

[2]Department of Chemistry, Sri Ramakrishna Engineering College, Coimbatore–641022, Tamilnadu, India

[3]Department of Physics, Periyar University, Salem–636011, Tamilnadu, India

[4]Department of Physics, Manonmaniam Sundaranar University, Abhishekapatti, Tirunelveli–627012, Tamilnadu, India

*uthayaranik@gmail.com

PACS 81.07.-b **DOI 10.17586/2220-8054-2016-7-4-707-710**

Zinc oxide (ZnO) / Tin oxide (SnO_2) / Zinc stannate (Zn_2SnO_4) nanocomposite is prepared via hydrothermal route followed by calcination. The nanocomposite is characterized by X–ray powder diffraction, Fourier Transform Infrared spectroscopy and UV spectroscopy techniques. The nanocomposite's morphology and the elemental composition is recorded using field emission scanning electron microscopy and energy dispersive X–ray spectroscopy analysis. The nanorods dispersed in the matrix of nanoparticles increases the surface active sites for gas adsorption and this material would be explored as a potential candidate for gas sensing applications at room temperature with quick response and recovery in the near future.

Keywords: zinc oxide, tin oxide, zinc stannate, hydrothermal.

Received: 5 February 2016

Revised: 26 April 2016

1. Introduction

A hybrid nanomaterial comprised of zinc oxide (ZnO) and tin oxide (SnO_2) act as multi-component system in which two or more of its combinations result in the enhancement of functional properties. Both ZnO and SnO_2 are well-known wide direct band gap ($E_g = 3.37$ eV and 3.6 eV at 300 K respectively) semiconductors and both serve as potential candidates in the field of gas sensors, solar cells, optoelectronic devices, LED, lithium ion batteries and so on. Recent investigations also state that the addition of a secondary component oxide in the form of the composite inhibits the grain growth of the host material [1] and these coupled oxides with different band gap widths are the effective approaches to enhance the storage capacity, photocatalytic activity, sensing of gases etc., [2] Voluminous reports are available for synthesizing such composites with unique hierarchical morphologies [3]. In this present work, $ZnO/SnO_2/Zn_2SnO_4$ composite is prepared via a hydrothermal route and it is characterized with various state-of-the art techniques and is reported herein.

2. Experimental details

0.1 M aqueous zinc chloride and stannous chloride solution together with glyoxylic acid monohydrate ($C_2H_2O_3 \cdot H_2O$) was prepared. Ammonium hydroxide was added dropwise under constant stirring at room temperature to adjust the pH to 9. The gel was then transferred into a Teflon – lined stainless – steel autoclave and maintained at 160 °C for 3 h. Aerogel was collected, washed with absolute ethanol and deionized water several times and dried in air. The product obtained was calcined at 600 °C for 3 h.

The X-ray powder diffraction (XRD) pattern of the sample was carried out using PANalyticalX'Pert PRO diffractometer with Cu-Kα radiation (λ= 1.54 Å) in 2θ ranging from 20 °–80 °. The crystalline nature of the samples and the identification of different phases were accomplished by comparing the XRD pattern with standard data provided by the International Center for Diffraction data (ICDD). The lattice parameters were calculated by least squares method and the average crystallite size (D) was calculated using the Scherrer formula:

$$D(nm) = \frac{K\lambda}{\beta \cos\theta}, \quad (1)$$

where K is a constant (app 0.9 assuming the particles are spherical), λ is the wavelength of CuKα radiation (1.54056×10^{-10} m), β is full width at half maximum (FWHM) (in radian) and θ is the angle of diffraction (in °). The surface morphology of the sample was examined using ZEISS ultrafield emission scanning electron microscope (FE-SEM). The elemental composition analysis was carried out using an energy dispersive X-ray (EDAX) spectrometer (Oxford EDS INCA PENTA FETX3) attached with FE-SEM. Fourier Transform Infrared (FT-IR) spectra of the samples were recorded in the 4000 – 400 cm^{-1} region using a Perkin Elmer RX1 FT-IR spectrometer by KBr pellet technique. UV-visible spectrum was obtained using JASCO – UV VIS spectrophotometer.

3. Results and discussion

Figure 1 shows the XRD pattern of the as prepared sample. The peaks obtained in the XRD pattern matches both the hexagonal wurtzite structured ZnO(ICDD No:36-1451) and tetragonal structured SnO_2 (ICDD No: 41-1445).

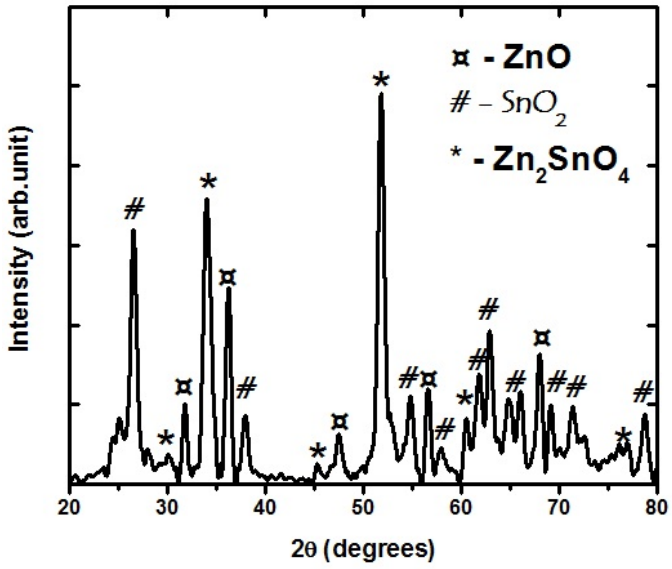

FIG. 1. XRD pattern of ZnO/SnO_2/Zn_2SnO_4 nanocomposite material

In this context, only negligible variation in the lattice parameters occurs for both the phases, which suggests that Zn^{2+} ions might not have been substituted into the SnO_2 lattice due to its larger ionic radius ($Zn^{2+} = 0.79$ Å and $Sn^{4+} = 0.68$ Å). In addition to these two individual oxides, two sharp peaks at (311) and (422) of the secondary phase corresponding to the spinel Zn_2SnO_4 (ICDD No: 24-1470) were observed. This reveals the polycrystalline nature of the composite material and is also supported by the formation of SnO_2 nanoparticles amidst the ZnO nanorods in the FeSEM image. The diffractogram displays a preferential orientation to the ZnO reflection at $2\theta \sim$ 36.195°, SnO_2 reflection at $2\theta \sim$26.476° and Zn_2SnO_4 reflections at $2\theta \sim$ 34.290° and 51.796°. The existence of these three phases for an equimolar (1:1) mixture of Zn/Sn nanocomposite at a higher calcination temperature is supported by the reports of Wang et al [1], Ruvini Dharmadasa et. al. [2]. The crystallite size of the composite material comprising the peaks of ZnO, SnO_2 and Zn_2SnO_4 were calculated using the Scherrer formula is around 30 nm, 29 nm and 21 nm respectively. The observed smaller crystallite size of 27 nm would enhance the sensitivity of the composite material towards gases.

Fe–SEM image of the composite material in Fig. 2(a) depicts both the smaller spherical and larger hexagonal structured nanoparticles clouded amidst the nanorods. The hexagonally-faceted nanorods of length 105 nm and diameter 30 nm correspond to ZnO. The spherical-shaped nanoparticles of grain size around 25 nm correspond to the SnO_2 nanoparticles. The formation of hexagonal shaped nanoparticles of about 20 nm is due to the existence of the secondary phase Zn_2SnO_4 which inhibits the growth of ZnO nanorods. The presence of Zn (26.79%), Sn (28.81%) and O (44.40%) observed from the EDAX analysis (Fig. 2(b)) also supports the equimolar mixture of the precursors. The nanorods in the matrix of the nanoparticles would increase the surface area of the composite material which might provide more surface active sites for the adsorption of gas molecules.

The FT-IR spectrum of the composite material is shown in Fig. 3. The strong absorbance band around 3524 cm^{-1} corresponds to the stretching vibration (H-O-H) and a peak around 1515 cm^{-1} corresponds to the

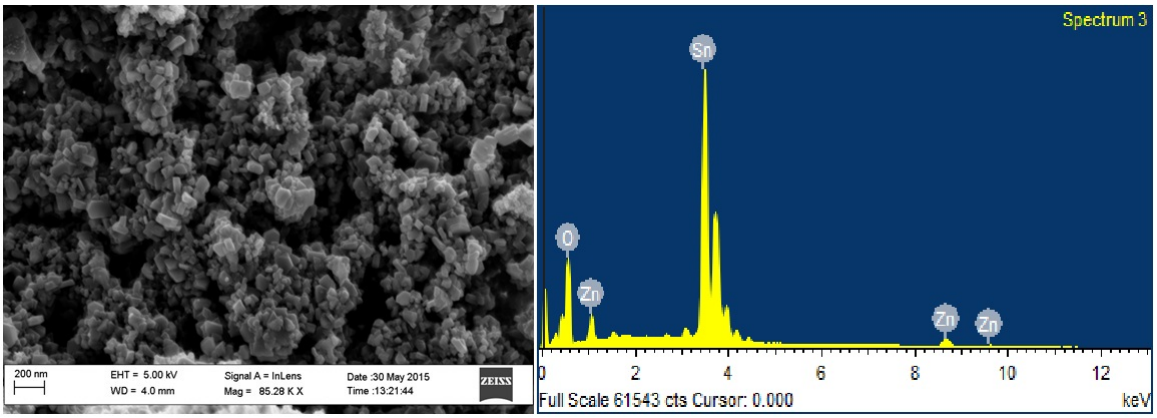

FIG. 2. (a) Fe–SEM image of ZnO/SnO_2/Zn_2SnO_4 nanocomposite material; (b) EDAX spectrum of ZnO/SnO_2/Zn_2SnO_4 nanocomposite material

bending vibrations (O-H) between oxygen and hydrogen atoms of the bound water. The absorption bands at 664.89, 866.81 and 1696.90 cm^{-1} are due to the vibration of M–O or M–O–M groups in ZnO, SnO_2 and Zn_2SnO_4 [4]. The results obtained by FT-IR analysis further confirm the formation of the composite and thus agree with the results obtained in XRD analysis.

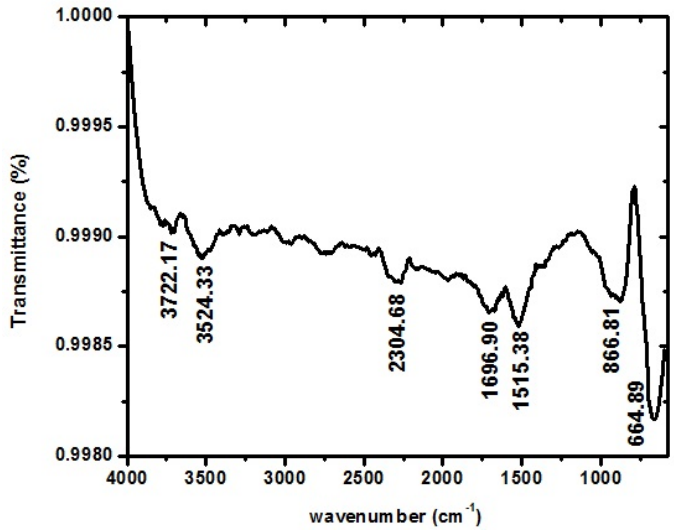

FIG. 3. FT–IR spectrum of ZnO/SnO_2/Zn_2SnO_4 nanocomposite material

Figure 4 shows the UV–Vis absorption spectrum of the composite material measured in the wavelength range of 200–800 nm. The absorption band edges were observed around 223 nm, 226 nm and 376 nm which correspond to the characteristic bands of SnO_2, Zn_2SnO_4 and ZnO respectively. Investigations done on such equimolar mixture of Zn/Sn composites obtain similar kind of absorption edge for the nanoparticles ranging from 40–70 nm. The reported band gap values of ZnO, SnO_2 and Zn_2SnO_4 are 3.37 eV, 3.65 eV and 3.6 eV respectively. The band gap value of the composite material calculated using the Tauc plot (shown in Fig. 5) is 3.7 eV. The smaller band gap value obtained by the composite material is attributed to the synergistic effect of the material.

4. Conclusion

ZnO/SnO_2/Zn_2SnO_4 nanocomposite has been successfully synthesized via a hydrothermal route followed by calcination. The formation of the composite was confirmed by XRD and FT–IR. Fe–SEM image revealed the presence of SnO_2 nanoparticles among the ZnO nanorods. The secondary phase Zn_2SnO_4 in the material inhibited the growth of nanorods, resulting in a larger surface area.

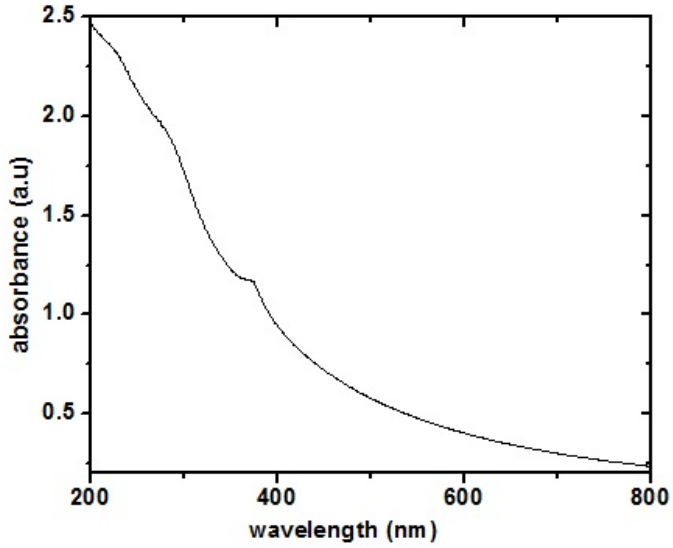

FIG. 4. UV–Vis spectrum of $ZnO/SnO_2/Zn_2SnO_4$ nanocomposite material

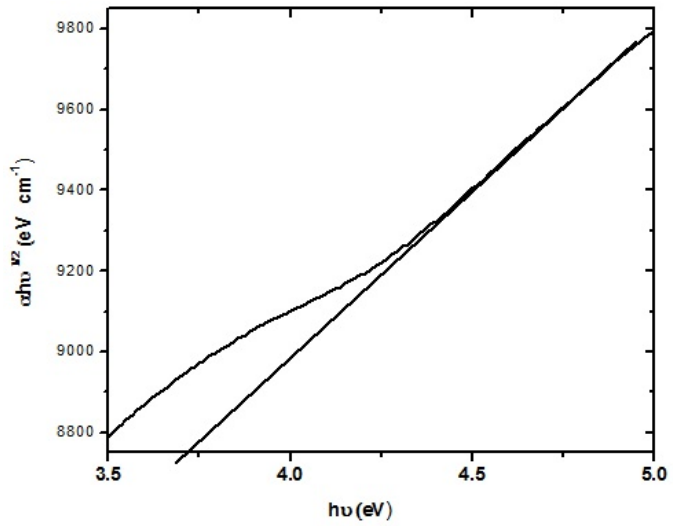

FIG. 5. Tauc plot of $ZnO/SnO_2/Zn_2SnO_4$ nanocomposite material

References

[1] Chen L., Bai S., Zhou G., Li D., Chen A., Chung C.L. Synthesis of ZnO–SnO_2 nanocomposites by microemulsion and sensing properties of NO_2. *Sensors and Actuators B*, 2008, **134**, P. 360–366.

[2] Tiekun J., Junwei Z., Fang F., Zhao D., Weimin W. Zhengyi Fu., Fancheng M. Synthesis, characterization, and photocatalytic activity of Zn-Doped SnO_2/Zn_2SnO_4 coupled nanocomposites. *International Journal of Photoenergy*, 2014, 197824.

[3] Ruvini D., Asif A., Tahir, K.G., Upul W. Single step growth and characterization of zinc Oxide, tin Oxide and composite ($Zn_xSn_{1-x}O_y$) nanoplate and nanocolumn Electrodes. *J. Am. Ceram. Soc.*, 2011, **94**(10), P. 3540–3546.

[4] Guang S., Saisai Z., Yanwei L. Solvothermal synthesis of Zn_2SnO_4 nanocrystals and their photocatalytic properties. *International Journal of Photoenergy*, 2014, 580615.

NANOSYSTEMS: PHYSICS, CHEMISTRY, MATHEMATICS, 2016, 7 (4), P. 711–723

Inhibition of corrosion of mild steel in well water by TiO_2 nanoparticles and an aqueous extract of May flower

P. Nithyadevi[1], R. Joseph Rathish[2], J. Sathiya Bama[1], S. Rajendran[3,*], R. Maria Joany[4], M. Pandiarajan[1], A. Anandan[5]

[1]PG and Research Department of Chemistry, GTN arts College, Dindigul–624005, India

[2]PSNA College of Engineering and Technology, Dinidgul, India

[3]Corrosion Research Centre, Department of Chemistry, RVS Educational Trust's Group of Institutions, Dindigul–624005,India

[4]Sathyabama University, Chennai, India

[5]SKV Higher Sec School, Kandampalayam–637201, India

wmanonithi@gmail.com, *susairajendran@gmail.com

PACS 81.07.-b **DOI 10.17586/2220-8054-2016-7-4-711-723**

Titanium dioxide nanoparticles have been used to control corrosion of mild steel in well water in the absence and presence of an aqueous May flower extract. As the concentration of TiO_2 increases, the inhibition efficiency also increases. 100 ppm of TiO_2 offers 84 % inhibition efficiency. The addition of 10mlof May flower extract enhances the inhibition efficiency to 95 %. Adsorption of TiO_2 on the metal surface follows Langmuir adsorption isotherm. Polarization study reveals that the flower extract-TiO_2 system functions as mixed type of inhibitor, controlling both anodic and cathodic reactions. AC impedance spectra reveal the formation of a protective film on the metal surface. This technology may find application in cooling water systems and concrete technology.

Keywords: corrosion inhibition, nanoparticles, TiO_2, flower extract, *Delonix regia*, adsorption isotherm.

Received: 5 February 2016

Revised: 9 April 2016

1. Introduction

Nanotechnology is an emerging field through which new productions on nano scale can be manufactured. Producing a new generation of textiles which possess antimicrobial properties using nanoparticles has attracted a great deal of attention from both scientists and consumers in recent years [1, 2]. Furthermore, metal nanoparticles show unique properties due to their peculiar electronic configuration, very large surface area and high amount of surface atoms [3]. For instance, metal nanoparticles show a broad absorption band in the visible region of the electromagnetic spectrum [4]. Some amazing properties of metals are used in order to improve the photocatalytic activities of semiconductors, such as TiO_2 and SiO_2, which are among the most efficient ones, resulting in better photocatalytic properties, even under visible rays [5]. Some noble metals, such as Ag [6], Au [7] and Pd [8] have stood the test of time in the field of producing nanocomposites.

Several nanoparticles have been used as corrosion inhibitors. As the particle size decreases, the inhibition efficiency increases because the surface area covered by the nanoparticles on the metal's surface increases. Nano-TiO_2 particles have improved the corrosion resistance of carbon steel [9], Ni-base alloys [10], aluminum surface [11]. A TiO_2 nanoparticle coating has been used to prevent biofilm formation in water and wastewater installations. Copper nanoparticles have improved the corrosion inhibition efficiency of carbon steel. Titanium dioxide (TiO_2) is a very promising metal oxide which has been widely studied as a photocatalyst for organic synthesis [12] and environmental cleaning processes [13]. Recent applications, based on the photocatalysis and photoactivity of TiO_2, include antifouling, antibacterial, deodorizing and self-cleaning functions [14]. In close connection with the developments in academic research, TiO_2 photocatalysis technology has also become more attractive in industrial applications due to its effectiveness, availability, low cost and chemical stability [15].

In this work, TiO_2 nanoparticles were prepared using commercially available titanyl chloride solution and characterization studies by SEM, EDS. The corrosion resistance of mild steel in well water in the presence of titanium dioxide nanoparticles and an aqueous extract of may flower (*Delonix regia)* by weight loss method, polarization study and AC impedance spectra.

2. Experimental methods

2.1. Preparation of TiO_2 nano particles

Stage1: 50 g of titanium tetrachloride of AR grade was chilled in a freezer overnight and placed in a 500 ml flask. To this, 250 ml of deionized ice water was added drop-wise while continuously shaking the flask. The reaction produced an aqueous titanyl chloride.

Stage 2: The titanyl chloride solution was then added dropwise to a solution of 10 ml glycolic acid (Merck, 70 %) in a flask. Deionized water was added dropwise until a total volume of 300 ml was reached, while continuously shaking the flasks.

Stage 3: The precursor solution was then allowed to stand for 15 days at room temperature, until white precipitates formed. The precipitates were filtered using a pressure filtration unit and then washed with water and methanol [16].

2.2. SEM and EDAX spectra

A few drops of the solution containing TiO_2 nanoparticles were dried on a glass plate. The solid mass was used for recording SEM and EDAX. SEM and EDAX were recorded in field Emission Scanning Electron Microscopy (FESEM-SUPRA 5S)-(ARLZEISS, GERMANY).

2.3. Preparation of the specimen

Mild steel specimens (0.026 % S, 0.06 % P, 0.4 % Mn, 0.1 % C, and the rest iron) of the dimensions 1.0 cm $\times$4.0 cm $\times$ 0.2 cm were polished to a mirror finish and degreased with trichloroethylene and used for the weight loss method and surface examination studies.

2.4. Preparation of May flower extract

An aqueous extract of May flower (*Delonix regia*) was prepared by grinding 10 g of flower using sterile mortar and pestle, filtered through three layers of muslin cloth and make up to 100 ml using double distilled water. This aqueous extract was used as corrosion inhibitor. The image of May flower are shown in Fig. 1.

FIG. 1. May flower

2.5. Determination of corrosion rate

The weighed specimens in triplicate were suspended by means of glass hooks in 100 ml of well water containing various concentration of TiO_2 nanoparticles in the presence and absence of may flower extract (FE) for one day. The specimens were taken out, washed in running water, dried, and weighed. From the change in weights of the specimens, corrosion rates were calculated using the following relationship:

$$CR = [(Weight\ loss\ in\ mg)/(Area\ of\ the\ dspecimens\ in\ dm^2 \times Immersion\ periods\ in\ days)]\ mdd. \quad (1)$$

Corrosion inhibition efficiency (IE %) was then calculated using the equation:

$$I.E. = 100[1 - (W_2/W_1)]\%, \quad (2)$$

where, W_1 – corrosion rate in the absence of the inhibitor, and W_2 – corrosion rate in the presence of the inhibitor.

2.6. Potentiodynamic polarization

Polarization studies were carried out in a CHI – Electrochemical workstation with impedance, Model 660A. A three-electrode cell assembly was used. The three electrode assembly is shown in Fig. 2. The working electrode was mild steel. A saturated calomel electrode (SCE) was the reference electrode and platinum was the counter electrode. From the polarization study, corrosion parameters such as corrosion potential (E_{corr}), corrosion current (I_{corr}) and Tafel slopes (anodic = *b*a and cathodic =*b*c) and Linear polarization resistance (*LPR*) were calculated. The scan rate (V/S) was 0.01 and the hold time at (Efcs) was zero and quit time(s) was two.

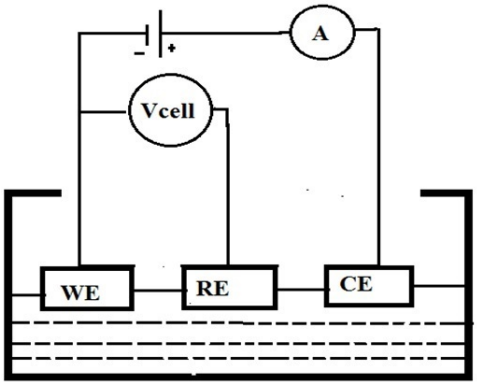

FIG. 2. Circuit diagram of three-electrode cell assembly. WE- working electrode (mild steel), RE-Reference electrode (saturated calomel electrode (SCE)), CE- Counter electrode (platinum)

2.7. AC impedance spectra

AC impedance spectral studies were carried out in a CHI – Electrochemical workstation with impedance, Model 660A. A three-electrode cell assembly was used. The working electrode was mild steel. A saturated calomel electrode (SCE) was the reference electrode and platinum was the counter electrode. The real part (Z') and imaginary part (Z") of the cell impedance were measured in ohms at various frequencies. Values of the charge transfer resistance (R_t) and the double layer capacitance (C_{dl}) were calculated.

3. Results and Discussion

3.1. Characterization of TiO_2 nanoparticles

The TiO_2 nanoparticles have been synthesized. The SEM image of the TiO_2 nanoparticles is shown in Fig. 3. The quantitative results for TiO_2 are shown in Fig. 4.

3.2. Analysis of EDS

EDAX spectrum of TiO_2 nanoparticles is shown in Fig. 5. The data derived from the spectra are given in Table 1. The processing option during recording the spectrum was normalized (all elements were analyzed). The number of iterations was 3. The following standards were used: carbon – $CaCO_3$; oxygen – SiO_2; titanium – Ti. The size of TiO_2 nanoparticles is shown in Fig. 6. The size of TiO_2 nanoparticles was shown to range from 70 – 90 nm.

TABLE 1. Date derived from EDAX

Element	Weight%	Atomic%
O K	9.03	22.90
Ti K	90.97	77.10
Totals	100.00	

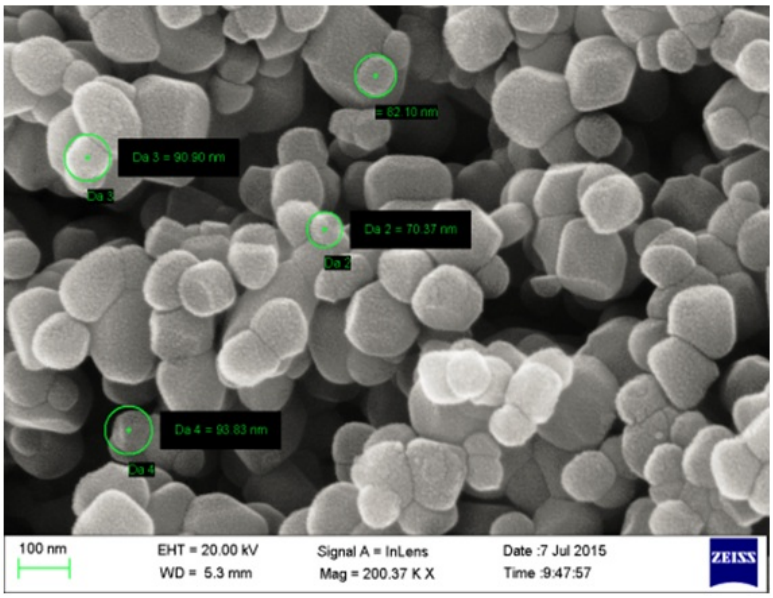

FIG. 3. The SEM image of TiO_2 nanoparticles

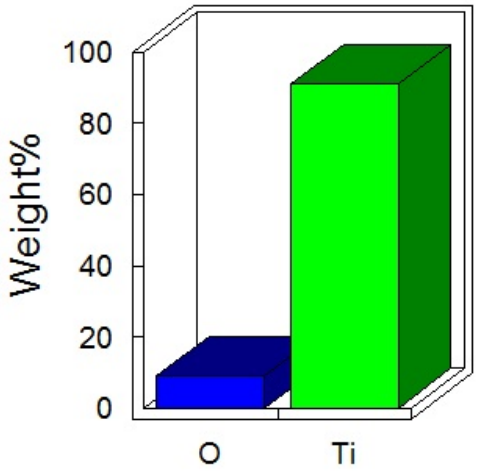

FIG. 4. The quantitative results of TiO_2 nanoparticles

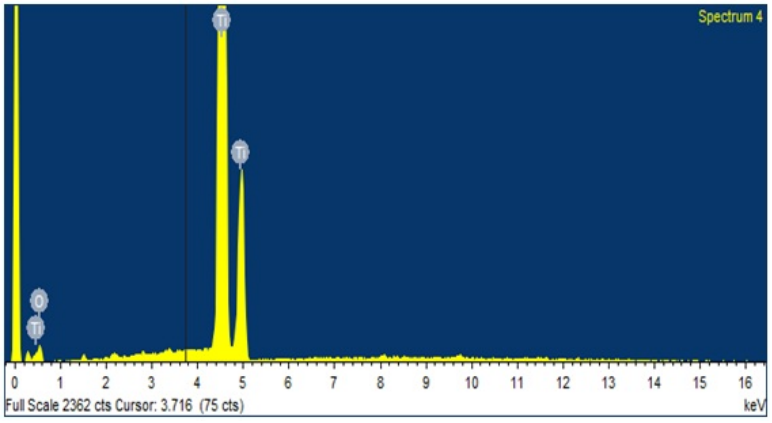

FIG. 5. EDAX spectrum of TiO_2 nanoparticles

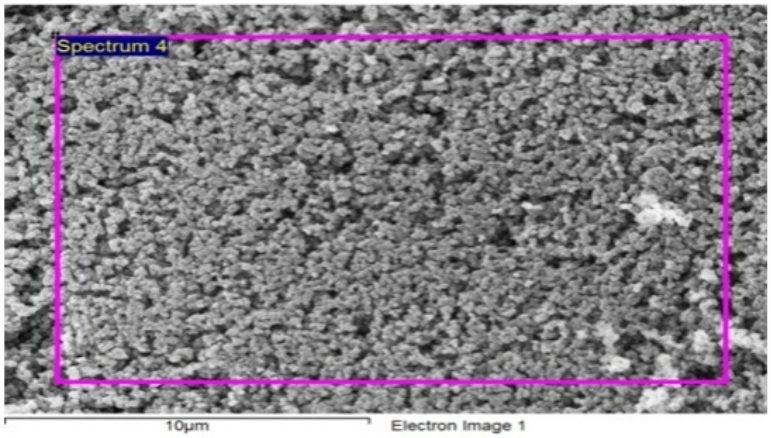

FIG. 6. The size of TiO_2 nanoparticles

4. Weight loss method

4.1. Corrosion inhibition by TiO_2 system

Corrosion rates (CR) of mild steel immersed in well water (WW) in the absence and presence of TiO_2 and the inhibition efficiencies (IE) obtained by weight loss method are given in Table 2. It was observed that when 100 ppm of TiO_2 was added to well water, the corrosion rate decreases to a great extent; and an inhibition efficiency of 80 % was obtained. This is due to the adsorption of TiO_2 nanoparticles on the metal's surface. As the concentration of TiO_2 increases, the corrosion rate decreases and the inhibition efficiency increases (Fig. 7) [17–20].

TABLE 2. Corrosion rates (CR) of mild steel immersed in well water (WW) in the absence and presence of TiO_2 and the inhibition efficiencies (IE) obtained by the weight loss method

TiO_2 Ppm	CR mdd	IE %
0	23.45	-
0	13.93	41
40	11.26	52
60	7.50	68
80	6.80	71
100	4.69	80

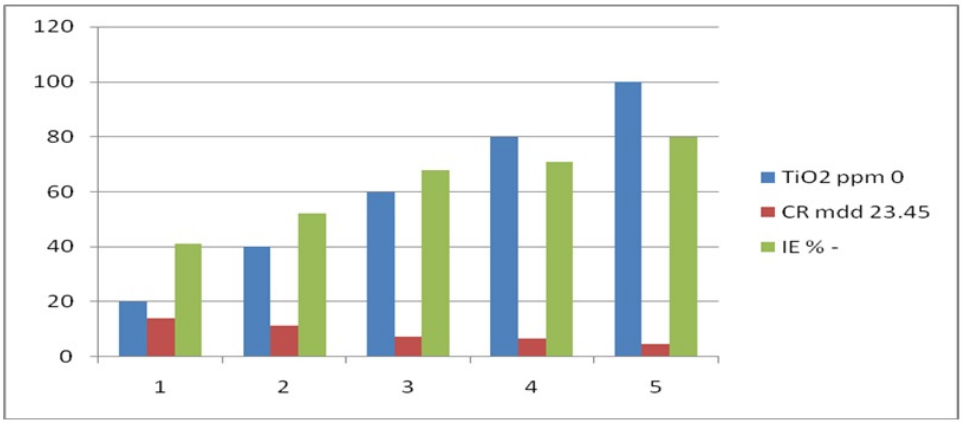

FIG. 7. Correlation between concentration of TiO_2, corrosion rate and inhibition efficiency

4.2. Corrosion inhibition by May flower extract (FE) system

Corrosion rates (CR) of mild steel immersed in well water (WW) in the absence and presence of May flower extract and the inhibition efficiencies (IE) obtained by weight loss method are given in Table 3. It was observed that when 10 ml of flower extract was added to well water, the corrosion rate decreases significantly and an inhibition efficiency of 84 % was obtained. This is due to the adsorption of active principles of May flower extract on the metal surface. As the concentration of flower extract increases, the corrosion rate decreases and the inhibition efficiency increases. (Fig. 8).

TABLE 3. Corrosion rates (CR) of mild steel immersed in well water (WW) in the absence and presence of May flower extract and the inhibition efficiencies (IE) obtained by weight loss method

FE ml	CR mdd	IE %
0	23.45	-
2	12.66	46
4	10.55	55
6	7.97	66
8	6.10	74
10	3.75	84

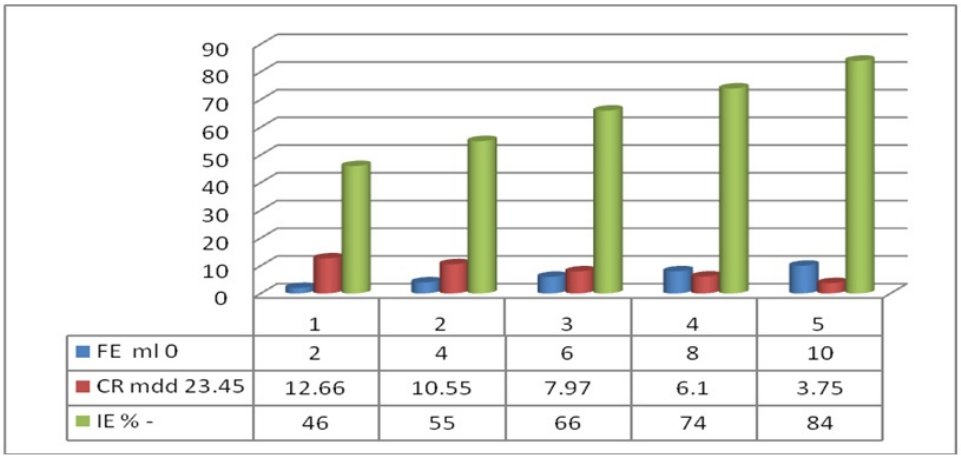

FIG. 8. Correlation between concentration of May flower extract, corrosion rate and Inhibition Efficiency (IE)

4.3. Corrosion inhibition by WW+ TiO_2 100 ppm + 10 ml of May FE System

Corrosion rates (CR) of mild steel immersed in well water (WW) in the absence and presence of TiO_2 and an aqueous extract of May flower extract (FE) and the inhibition efficiencies (IE) obtained by weight loss method are given in Table 4. It was observed that when 100 ppm of TiO_2 was added to well water, the corrosion rate significantly decreased, and an inhibition efficiency of 80 % was obtained. This is due to the adsorption of TiO_2 nanoparticles on the metal surface. When 10 ml of flower extract was added to well water, the corrosion inhibition efficiency was 84 %. When both 100 ppm of TiO_2 and 10 ml May flower extract were added, the IE was 95 %. Hence, one can conclude that the WW+ TiO_2 100 ppm + 10 ml of FE system offers the best inhibition efficiency. TiO_2 is adsorbed on the metal surface and offers corrosion protection by preventing water molecules and aggressive ions from reaching the metal surface. The active principles of FE are adsorbed on the TiO_2 layers. These layers are hydrophobic in nature and prevent water molecules reaching the metal surface (Fig. 9).

5. Adsorption isotherm for TiO_2 system

The adsorption of inhibitor molecules (TiO_2 ppm) obeys Langmuir Adsorption Isotherm (Fig. 10). A graph was made by plotting C vs C/θ, where C is concentration of inhibitor and θ is surface coverage. A linear plot

TABLE 4. Corrosion rates (CR) of mild steel immersed in well water (WW) in the absence and presence of TiO_2 and an aqueous May flower extract (FE) and the inhibition efficiencies (IE) obtained by weight loss method

System	CR mdd	IE %
WW	23.45	-
WW+$TiO_2$100 ppm	4.71	80
WW+10ml of FE	3.77	84
WW+$TiO_2$100 ppm + 10ml of FE	1.18	95

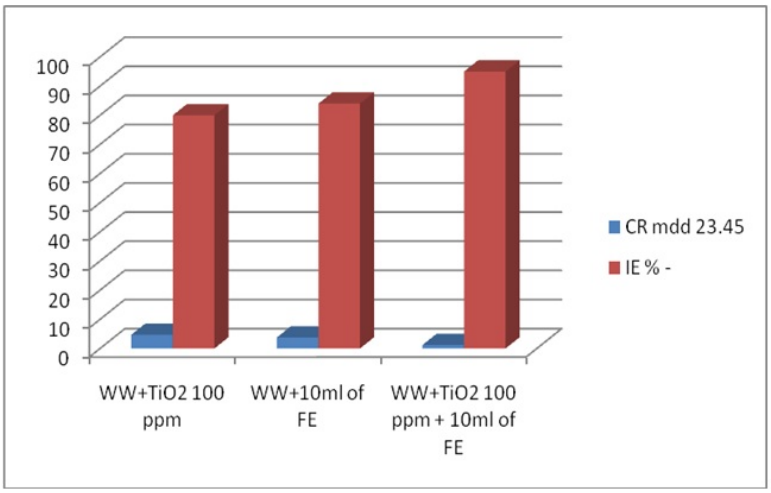

FIG. 9. Correlation between corrosion rates and inhibition efficiencies for various systems

was obtained with R^2 value of 0.980. This indicated that the adsorption of molecules on the metal surface obeyed the Langmuir adsorption isotherm. The slope was 0.940 and intercept was 33.88. The Langmuir constant, K (calculated from the relation Intercept = log K), was found to be 7.59×10^{33}.

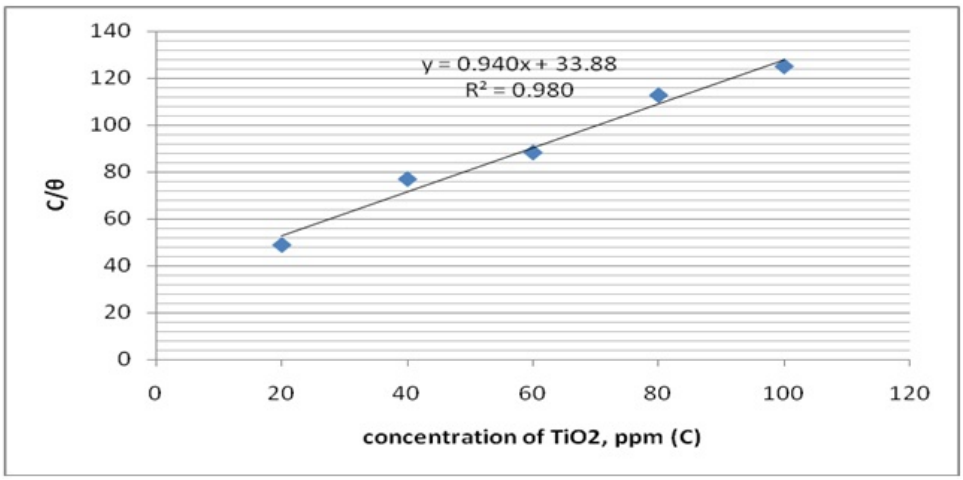

FIG. 10. Langmuir adsorption isotherm for TiO_2 system

Since the Langmuir adsorption isotherm is obeyed, it implies that:

- The adsorption of a single adsorbate onto a series of equivalent sites on the surface of the solid.
- The surface containing the adsorbing sites is perfectly flat plane with no corrugations (assuming an homogeneous surface).

- The adsorbing molecule adsorbs into an immobile state.
- All sites are equivalent.
- Each site can hold at most one molecule of inhibitor (monolayer coverage only).
- There are no interactions between adsorbed molecules on adjacent sites.
- The formation of Langmuir monolayers by adsorption onto a surface dramatically reduces the entropy of the molecular system

5.1. Adsorption isotherm for May flower system

The adsorption of inhibitor molecules (May flower extract in ml) obey Langmuir Adsorption Isotherm (Fig. 11). A graph was made by plotting C vs C/θ, where C is concentration of inhibitor and θ is surface coverage. A linear plot was obtained with R^2 value of 0.970. This indicated that the adsorption of molecules on the metal surface obeyed the Langmuir adsorption isotherm. The slope was 0.933 and the intercept was 3.088. The Langmuir constant, K (calculated from the relation Intercept = log K) was found to be 1225×10^3.

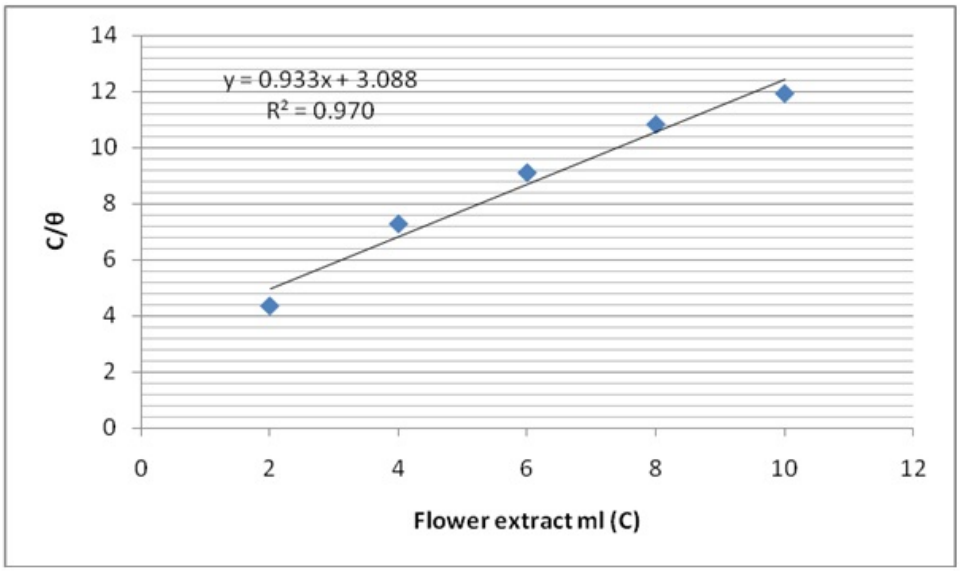

FIG. 11. Langmuir adsorption isotherm for May flower system

6. Potentiodynamic polarization study

Electrochemical analyses, such as Polarization study and AC impedance spectra, have been used to investigate the corrosion resistance of metals [20–25].

In the polarization study, if corrosion resistance increases, linear polarization Resistance (LPR) value increases and corrosion current decreases. In the present study, the corrosion resistance of mild steel immersed in well water in the presence and absence of an aqueous May flower extract and TiO_2 has been investigated by a potentiodynamic polarization study (Fig. 12). The corrosion parameters such as corrosion potential (Ecorr), Tafel slopes (bc = cathodic, ba = anodic), LPR values and corrosion current (Icorr), derived from the TAFEL plots, are given in the Table 5.

When mild steel was immersed in well water (WW), the corrosion potential was -631 mV vs SCE, the LPR value was 7249 ohm cm^2 and the corrosion current was 5.268×10^{-6} A/cm^2.

It is interesting to note that when mild steel was immersed in well water containing 100 ppm of TiO_2, the corrosion resistance of mild steel increased. This was due to the presence of TiO_2 nanoparticles in the medium. The nanoparticles were adsorbed onto the metal surface, forming a protective film. Hence, corrosion resistance increased. This was revealed by the fact that when the mild steel was immersed in WW containing TiO_2, the LPR value increased from 7249 ohm cm^2 to 8350 ohm cm^2. The corrosion current value decreased from 5.268×10^{-6} A/cm^2 to 1.587×10^{-6} A/cm^2.

When mild steel was immersed in WW+10 ml of FE + system, it was inferred that the corrosion resistance of mild steel increased. This was revealed by the fact that, in presence of flower extract, the LPR value was high (30994 ohm cm^2); the corrosion current decreased to 1.045×10^{-6} A/cm^2 and the corrosion potential shifted

TABLE 5. Corrosion parameters of mild steel immersed in well water (WW) in the absence and presence of TiO_2 and an aqueous flower extract (FE), obtained by polarization study

System	E_{corr} mV vs SCE	b_c mV/decade	b_a mV/decade	LPR ohm cm^2	I_{corr} A/cm^2
WW	−631	202	155	7249	5.268×10^{-6}
WW+TiO_2 100 ppm	−663	221	120	8350	1.587×10^{-6}
WW+10 ml of FE	−670	199	119	30994	1.045×10^{-6}
WW+TiO_2 100 ppm + 10 ml of FE	−641	186	165	36770	1.035×10^{-6}

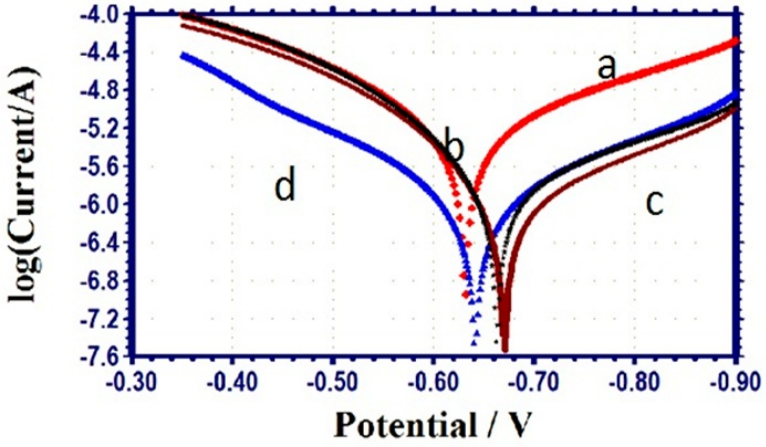

FIG. 12. Polarization curves of mild steel immersed in various test solutions (a) WW, (b) WW+TiO_2 100 ppm, (c) WW+10 ml of FE, (d) WW+TiO_2 100 ppm + 10 ml of FE

to the cathodic side (from −631 to −641 mV vs SCE). This means that the cathodic reaction was controlled predominantly. The active principle present in the flower extract forms a protective film on the metal surface. The transfer of electrons from the metal to the bulk of the system was prevented. Because of the necessity of electrons, the cathodic reaction, which involves the interaction of electrons with oxygen and water, is minimized, thus, the formation of hydroxide ions is reduced.

When mild steel was immersed in theWW+10 ml of FE + TiO_2 100 ppm system, the corrosion resistance of mild steel further appeared to be further increased. This is revealed by the fact that, in presence of flower extract, the LPR value was very high (36770 ohm cm^2); the corrosion current decreased to 1.035×10^{-6} A/cm^2 and the corrosion potential shifted to the cathodic side (from −631 to −670 mV vs SCE). This means that the cathodic reaction was controlled predominantly. The active principle present in the May flower extract forms a protective film on the metal surface. The transfer of electrons from the metal to the bulk of the system was prevented. Because of the need for electrons, the cathodic reaction, which involves the interaction of electrons with oxygen and water, is limited, thus, the formation of hydroxide ions is reduced. However, when compared with the WW+10 ml of FE system, (−670 mV vs SCE), the shift is anodic (−641 mV vs SCE). This shift revealed that in presence of TiO_2, the anodic reaction is also controlled. Moreover, when compared with −631 mV vs SCE, this shift is very small. So it can be considered that the "WW+10 ml of FE + TiO_2 100 ppm system" functions as a mixed inhibitor system, controlling both the anodic and cathodic reactions. **Thus, the polarization study leads one to the conclusion that the corrosion resistance of mild steel in various test solutions decreases in the order:**

WW+$TiO_2$100 ppm+10 ml of FE system>WW+10 ml of FE>WW+$TiO_2$100 ppm>WW

From the data, one can conclude that the WW+$TiO_2$100 ppm + 10ml of FE system offers better inhibition efficiency than other systems.

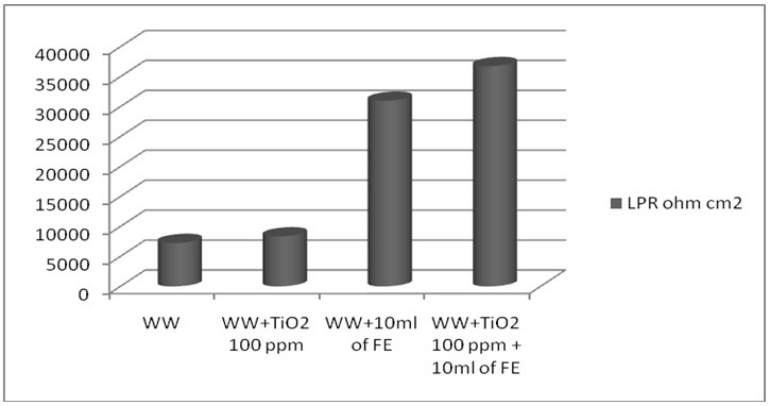

FIG. 13. Comparison of LPR values of various systems

6.1. AC impedance spectra

AC impedance spectra have been used to investigate the corrosion resistance of metals. When corrosion resistance increases, the charge transfer resistance values (R_t) increase, impedance values increase and double layer capacitance values (c_{dl}) decrease [26–30]. AC impedance spectra of mild steel immersed in various test solution are shown in Figs. 14 – 17. Nyquist plots are shown in (Fig. 14), and Bode plots are shown in Fig. 15 – 17. The corrosion parameters are given in Table 6.

TABLE 6. Corrosion parameters of mild steel immersed in well water (WW) in the absence and presence of TiO_2 and an aqueous May flower extract (FE), obtained by AC impedance spectra

System	R_t ohm cm^2	C_{dl} F/cm^2	Impedance Log(z/ohm)
WW	181	2.78×10^{-8}	2.543
WW+$TiO_2$100 ppm	782	0.639×10^{-8}	3.152
WW+10 ml of FE	1021	0.490×10^{-8}	3.251
WW+$TiO_2$100 ppm + 10 ml of FE	1080	0.463×10^{-8}	3.261

It was observed from Table 6 that when the inhibitor (TiO_2 100 ppm) was added to well water, the charge transfer resistance ($R_{t)}$ increased from 181 Ω cm^2 to 782 Ω cm^2. The C_{dl} value decreased from 2.78×10^{-8} F/cm^2 to 0.639×10^{-8} F/cm^2 and the impedance value increased from 2.543 to 3.152. These results lead one to conclude that a protective film was formed on the metal surface. Nanoparticles of TiO_2 have adsorbed on the metal surface forming protective film. The surface becomes hydrophobic, hindering water molecules and aggressive ions from reaching the surface, thus protecting the metal from corrosion.

When the inhibitor (10 ml of may flower extract) was added to well water, the charge transfer resistance (R_t) increased from 181Ω cm^2 to 1021 Ω cm^2, the C_{dl} value decreased from 2.78×10^{-8}F/cm^2 to 0.490×10^{-8} F/cm^2 and the impedance value increased from 2.543 to 3.251. These results would seem to indicate that a protective film was formed on the metal surface. This film is more compact and hydrophobic than the previous case, which is why the R_t value of this system is higher than that of the previous system.

It was observed that the WW+$TiO_2$100 ppm + 10 ml of FE system is more corrosion resistant than the previous system because for this system, the R_t value increases to 1080 Ω cm^2 and the C_{dl} value decreases to 0.463×10^{-8} F/cm^2 and the impedance value increases to 3.261. It seems that the flower extract and TiO_2 particles are adsorbed jointly on the metal surface and thus form a better protective film. Thus, AC impedance spectra lead to the conclusion that corrosion resistance of mild steel in various test solutions decreases in the following order:

WW+TiO_2 100 ppm+10 ml of FE system>WW+10 ml of FE>WW+TiO_2 100 ppm>WW.

The WW+TiO_2 100 ppm + 10 ml of FE system offers better inhibition efficiency than other systems. This view is in agreement with the polarization study results.

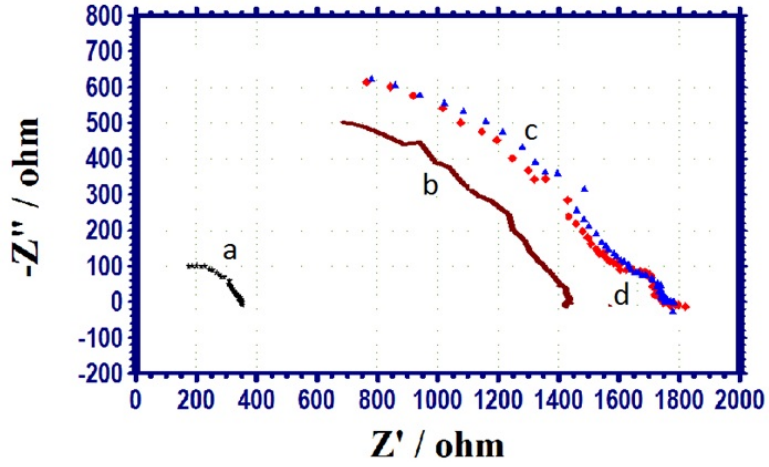

FIG. 14. AC impedance spectra (Nyquist Plots) of mild steel immersed in various test solutions (a) WW, (b) WW+TiO_2 100 ppm, (c) WW+10 ml of FE, (d) WW+TiO_2 100 ppm + 10 ml of FE

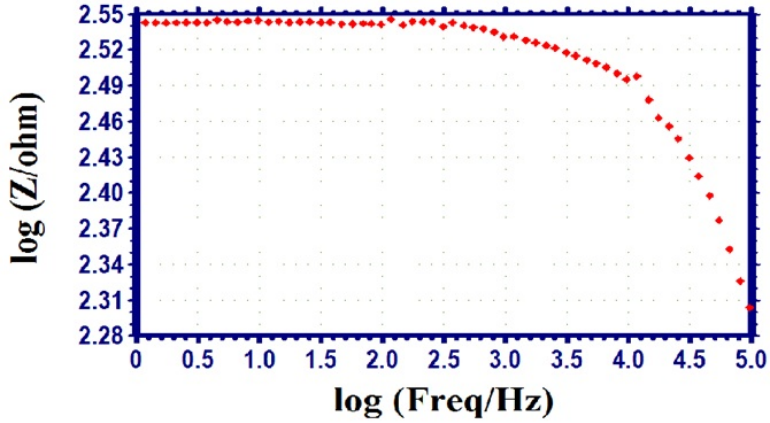

FIG. 15. AC impedance spectrum (Bode Plot- impedance) of mild steel immersed in well water (a) WW

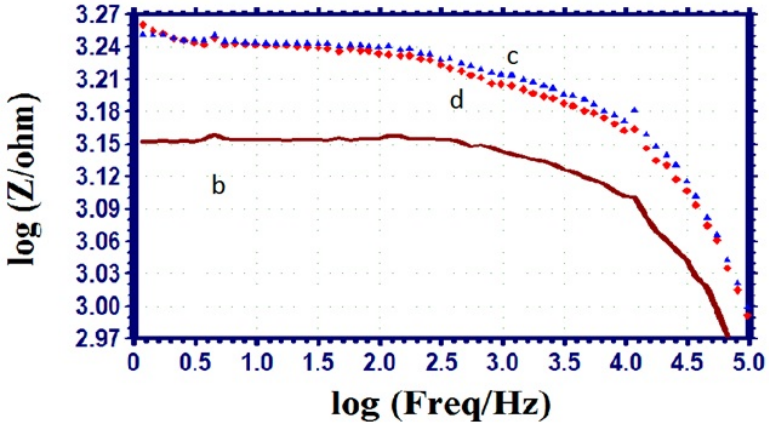

FIG. 16. AC impedance spectra (Bode Plots-impedance) of mild steel immersed in various test-solutions (b) WW+TiO_2 100 ppm, (c) WW+10 ml of FE, (d) WW+TiO_2 100 ppm + 10 ml of FE

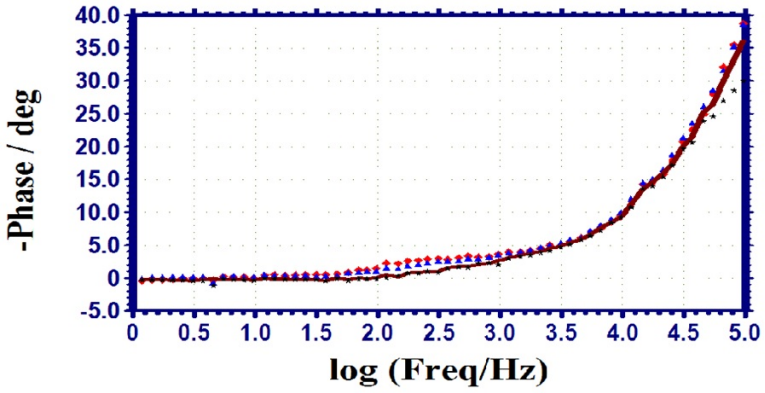

FIG. 17. AC impedance spectra (Bode Plots-phase angle) of mild steel immersed in various test Solutions. black line – WW, grey line – WW+ TiO_2 100 ppm, blue line – WW+ 10 ml of FE, red line – WW+TiO_2 100 ppm + 10 ml of FE

7. Conclusion

The present study leads to the following conclusions:

- Titanium dioxide nanoparticles, along with an aqueous may flower extract has been synthesized successfully.
- The formulation consisting of 100 ppm of TiO_2 nanoparticles and 10 ml may flower extract afforded a 95 % IE for mild steel immersed in well water.
- Polarization study reveals that 100 ppm of TiO_2 nanoparticles and 10 ml may flower extract functions as mixed inhibitor system, controlling both anodic and cathodic reactions.
- AC impedance spectra reveal that the formation of protective film on the metal's surface.

Acknowledgement

The authors are thankful to their respective management and Defence Research and Development Organisation, New Delhi.

References

[1] Lee H.J., Yeo S.Y., Jeong S.H. Antribacterial effect of nanosized silver colloidal solution on textile fabrics. *J. Master. Sci*, 2003, **38**, P. 219–2204.
[2] Alimohammadi F. *Stabilization of silver nanoparticles and antibacterial characterization on the cotton surface against washing*. M.Sc Thesis, Islamic Azad University Tehran South Brach, 2009.
[3] Aiken J.D., Finke R.G. A review of modern transition-metal nanoclusters: their synthesis, characterization, and applications in catalysis. *J. Mol. Catal, A:Chem*, 1999, **145**, P. 1–44.
[4] Liu R., Chen H., Hu S. Synthesis and characterization of nanometals with coreshell structure. *China Particuol*, 2004, **2**(4), P. 160–163.
[5] Sung-Suh H.M., Choi J.R., Hah H.J., Koo S.M., Bae Y.C. Comparison of Ag deposition effects on the photo catalytic activity of nanoparticle TiO_2, under visible and UV light irradiation. *J. Photochem. Photobiol. A*., 2004, **163**, P. 37–44.
[6] Valentine Rupa A., Manikandan D., Divaker D., Sivakumar T. Effect of deposition of Ag on TiO_2 nanoparticles on the photodegradation of Reactive Yellow-17. *J. Hazard, Mater.*, 2007, **147**, P. 906–913.
[7] Uddin M.J., Cesano F., Scarano D., Bonino F., Agostini G., Spoto G., Bordiga S., Zecchina A. Cotton textile fibers coated by Au/TiO_2 films: Synthesis characterization and self-cleaning properties. *J. Photochem. Photobiol. A.*, 2008, **199**, P. 64–72.
[8] Sclafant A., Herrmann J.M. Influence of metallic silver and of platinum-silver bimetallic deposits on the photocatalytic activity of titania (anatase and rutile) inorganic and aqueous media. *J. Photochem. Photobiol. A.*, 1998, **113**, P. 181–188.
[9] Deyab M.A., Keera S.T. Effect of nano-TiO_2 particles size on the corrosion resistance of alkyl coating. *Chemistry and Physics*, 2014, **146**(3), P. 406–411.
[10] Kim K.M., Lee E.H., Hur D.H. Corrosion behavior on Ni-base alloys applied with Nano-TiO_2 in high temperature caustic water. *Current Nanoscience*, 2014, **10**(1), P. 89–93.
[11] Liu T., Qiang L. Research on inhibition marine microbial adherence of a novel nano-TiO_2 coating on aluminium. *Advanced Materials Research*, 2012, **557-559**, P. 1687–1690.
[12] Sakata T., Kawai T., Hashimoto K. Catalytic Properties of Ruthenium Oxide on n-Type Semi-conductors under Illumination. *J. Phys. Chem.*, 1984, **88**, P. 2344–2350.
[13] Fu X.Z., Zeltner W.A., Anderson M.A. Photocatalytic Generation of H_2 from Seawater. *Appl. Catal.,* 1995, **B6**, P. 209–220.
[14] Sopyan I., Watanabe M., Murasawa S., Hashimoto K., Fujishima A. A film-type photocatalyst incorporating highly active TiO_2 powder and fluororesin binder: photocatalytic activity and long-term stability. *J. Electroanal. Chem.*, 1996, **415**, P. 183–186.

[15] Zhang X., Fujishima A., Alexei M.J., Emeline V. Murakami T. Double-Layered TiO_2-SiO_2. Nanostructured Films with Self-Cleaning and Antireflective Properties. *J.Phys Chem*, 2006, **B110**, P. 25142–25148.
[16] Zhou et al. Titanium dioxide nanoparticles and nanoparticle suspensions and methods of making the same. US Patent 7326399 B2, 2008.
[17] Hansoon C.M. Volume Relationship for C-S-H Formation Based on General Concepts. *Cem. Concr. Res*, 1984, **14**, P. 574.
[18] Nakayama N., Obuchi A. Inhibitory effects of 5-aminouracil on cathodic reactions of steels in saturated $Ca(OH)_2$ solution. *Corros. Sci.*, 2003, **45**, P. 2075–2092.
[19] Manivannan M., Rajendran S. Investcation of inhibitive action of urea-Zn^{2+} system in the corrosion control of carbon steel in sea water. *International of Engineering science and Technology*, 2011, **3**, P. 19–23.
[20] Johnsirani V., Sathiyabama J., Rajendran S, Shanthi T., Muthumegala T.S., Krishnaveni A. Inhibitive action of malachite green-Zn^{2+} system. *Bulgarian Chemical Communication*, 2012, **44**, P. 41–51.
[21] Epshiba R., Peter Pascal Regis A., Rajendran S. Inhibition Of Corrosion Of Carbon Steel In A Well Water By Sodium Molybdate – Zn^{2+} System. *Int. J. Nano. Corr. Sci. Engg.*, 2014, **1**(1), P. 1–11.
[22] Kavitha N., Manjula P. Corrosion Inhibition of Water Hyacinth Leaves, Zn^{2+} and TSC on Mild Steel in neutral aqueous medium. *Int. J. Nano. Corr. Sci. Engg.*, 2014, **1**(1), P. 31–38.
[23] Nagalakshmi R., Nagarajan L., Joseph Rathish R., Santhana Prabha S., Vijaya N., Jeyasundari J., Rajendran S. Corrosion Resistance of SS316l In Artificial Urine In Presence Of D-Glucose. *Int. J. Nano. Corr. Sci. Engg.*, 2014, **1**(1), P. 39–49.
[24] Angelin Thangakani J., Rajendran S., Sathiabama J., M.Joany R. Joseph Rathis R., Santhana Prabha S. Inhibition of Corrosion of Carbon Steel In Aqueous Solution Containing Low Chloride Ion By Glycine – Zn^{2+} System. *Int. J. Nano. Corr. Sci. Engg.*, 2014, **1**(1), P. 50-62.
[25] Nithya A., Shanthy P., Vijaya NJoseph Rathish. R., Santhana Prabha S., Joany R.M., Rajendran S. Inhibition of Corrosion of Aluminium By An Aqueous Extract of Beetroot (Betanin), *Int. J. Nano Corr. Sci. Engg.*, 2015, **2**(1), P. 1–11.
[26] Gowrani T., Manjula P., Nirmala Baby C. Manonmani, Sudha K.N., Vennila R. Thermodynamical Analysis of MBTA on The Corrosion Inhibition of Brass In 3 % NaCl Medium. *Int. J. Nano. Corr. Sci. Engg.*, 2015, **2**(1), P. 12–21.
[27] Namita K., Johar K., Bhrara R., Epshiba R., Singh G. Effect Of Polyethoxyethylene N, N, N‘ 1, 3 Diamino Propane on The Corrosion of Mild Steel In Acidic Solutions. *Int. J. Nano Corr. Sci. Engg.*, 2015, **2**(1), P. 22–31.
[28] Christy Catherine Mary A., Rajendran S., Hameed Al-Hashem, Joseph Rathish R., Umasankareswari T., Jeyasundari J. Corrosion Resistance Of Mild Steel In Simulated Produced Water In Presence Of Sodium Potassium Tartrate. *Int. J. Nano Corr. Sci. Engg.*, 2015, **2**(1), P. 42–50.
[29] Sangeetha M.,Rajendran S., Sathiyabama J., Umasankareswari T., Krishnaveni A., Joany R.M., *Int. J. Nano. Corr. Sci. Engg*, 2015, **2**(3), P. 14–21.
[30] Nithya Devi P., Sathiyabama J., Rajendran S. Joseph Rathish R., Santhana Prabha S. Influence of citric acid-Zn^{2+} System on Inhibition of Corrosion of Mild Steel in Simulated Concrete Pore Solution. *Int. J. Nano Corr. Sci. Engg.*, 2015, **2**(3), P. 1–13.

NANOSYSTEMS: PHYSICS, CHEMISTRY, MATHEMATICS, 2016, 7 (4), P. 724–727

Cashew nut shells as source of chemicals for preparation of chalcogenide nanoparticles

E. B. Mubofu[1,*], S. Mlowe[1,2], N. Revaprasadu[2]

[1]Chemistry Department, University of Dar es Salaam, P.O. Box 35061, Dar es Salaam, Tanzania

[2]Chemistry Department, University of Zululand, Private Bag X1001, KwaDlangezwa, 3886, South Africa

[*]ebmubofu@gmail.com, ebmubofu@udsm.ac.tz, sixb2809@gmail.com, RevaprasaduN@unizulu.ac.za

PACS 81.07.-b **DOI 10.17586/2220-8054-2016-7-4-724-727**

Cashew nut shell wastes produced in cashew nut processing factories cause environmental problems. Currently, these wastes are being converted to a variety of bio-based chemicals and functional materials. Cashew nut shells (CNS) produce cashew nut shell liquid (CNSL), a dark reddish brown viscous liquid (*ca*. 30 – 35 wt. %) which is extracted from the soft honeycomb of the CNS. CNSL offers multitude interesting possibilities for the synthesis of speciality chemicals, high value products and polymers due to their functionalities. Our recent research have demonstrated that CNSL constituents can be transformed into diverse functional chemicals. This contribution will report on how cashew nut shells (an agro waste from cashew nut processing factories) have been employed to produce anacardic acid capped chalcogenide nanoparticles.

Keywords: anacardic acid, cashew nut shell liquid, chalcogenide, nanoparticles.

Received: 5 February 2016

Revised: 7 May 2016

1. Introduction

Metal chalcogenides quantum dots (QDs) or semiconducting nanocrystals are interesting due to their highly refined chemistry, availability, and super tunable optical and electronic properties suitable for variety of applications in different fields, such as photovoltaics, light-emitting devices, environmental sciences and nanomedicine [1–7]. Recently, increasing concern about the environment has led researchers to focus on 'green chemistry', i.e. the utilization of nontoxic chemicals, environmentally benign solvents and renewable materials. The aforementioned are some of the key issues that merit important consideration in a green synthesis strategy. In order to reduce the environmental and health effects associated with nanoparticle synthesis, greener synthetic routes are being investigated [8, 9]. Green chemistry aims at addressing ways to reduce environmental and health impacts of chemical production [10]. In the field of nanotechnology, green synthesis involves three key issues; "utilization of non-toxic chemicals, environmentally benign solvents, and renewable materials" [11].

Recently, researchers have begun using green renewable chemicals for the generation of inorganic nanostructures and materials. These chemicals have shown the capability to control architectures of materials at nanoscale level. Castor oil and ricinoleic acid [12], olive oil and oleic acid [13–16] and anacardic acid [17, 18] are some of the green chemicals that have been used as capping agents to fabricate nanoparticles. In the present communication, we extend our earlier work using cashew nut shell liquid extracts for the synthesis of metal chalcogenides (Cadmium and lead sulfide, selenide and telluride) nanoparticles via a solution-based technique. Synthetic methods based on naturally occurring resources not only provide an alternative, friendly means of obtaining these metal chalcogenides nanoparticles, but also have a well-defined size and morphology. The use of cashew nut shell liquid and its isolate, anacardic acid (Fig. 1), in nanoparticle synthesis is associated with their chemical structures, easy availability, non-toxicity, low cost, non-food competition, high boiling point and high viscosity.

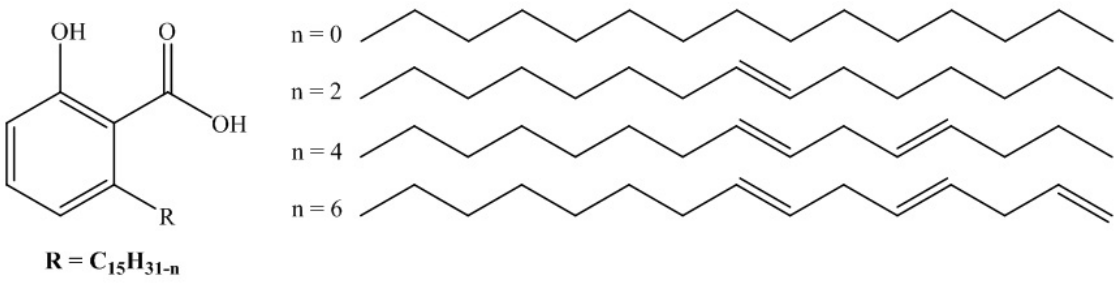

FIG. 1. Structure of Anacardic acids [19]

2. Experimental procedure

The chemical reduction and thermolysis route has been employed in this work. The cashew nut shell liquid and its isolate, anacardic acid, were extracted using a procedure reported by Paramashivappa *et al.* [20] with slight modifications reported by Lucio *et al.* [21]. Other chemicals, characterizations and procedures are similar to our earlier publications [17, 18]. The reaction scheme is shown in Fig. 2. The as-synthesized particles were characterized by TEM and HRTEM techniques.

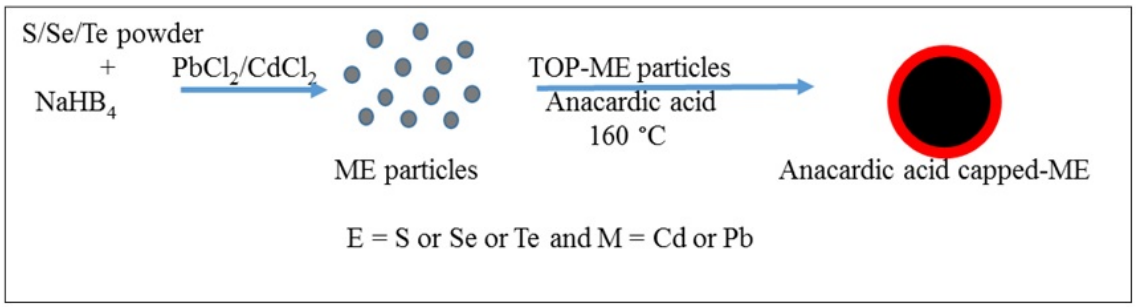

FIG. 2. Reaction scheme for the synthesis of anacardic acid-capped ME nanoparticles

2.1. Results and discussion

The morphology of the metal chalcogenide nanoparticles was studied by transmission electron microscopy (TEM). A typical TEM micrograph of the cadmium chalcogenide nanoparticles is given in Fig. 3. Fig. 3(a) shows anisotropic shaped anacardic acid-capped CdS nanoparticles, synthesized at 160 °C with average width of 11.8±2.4 nm and length 32.6±4.2 nm. CdSe (Fig. 3b) displayed uniform rod-shaped nanocrystals with a narrow size distribution on the TEM grid. A similar trend was observed for CdTe nanoparticles, showing rod shaped particles with an average width of 16.3±3.0 nm and length 48.4±4.5 nm (Fig. 3(c)). There is almost an equal inter-particle distance of approximately 3 nm for the CdSe and CdTe particles as observed from the TEM images.

The TEM image of the as-synthesised anacardic acid capped PbS (Fig. 4(a)) consists of small undefined spherical like particles with an average size of 9.8±1.8 nm. PbSe nanocrystals revealed the formation of small triangle-shaped particles with an average size of 12.6±3.1 nm (Fig. 4(b)). The presence of interspersed particles supports the fact that the formation of nanocrystals may be due to the influence of anacardic acid. While for PbTe nanoparticles (Fig. 4(c)), rod shaped and some cubic shaped particles, typical for PbTe [22] were formed. Rods of width 11.9 nm and length 37.8 nm and cubes of 20.9 nm were estimated.

3. Conclusion

Cadmium and lead chalcogenide (ME where M = cadmium or lead and E = S, Se or Te) nanoparticles have been successfully synthesized using anacardic acid as a coordinating solvent. The TEM studies reveal a mosaic-like pattern for all samples. Furthermore, monodispersed spherical to cubic shaped PbE nanoparticles were obtained. The results reveal that anacardic acid could be an effective and potential capping agent in the synthesis of metal chalcogenide nanoparticles. The method utilized an inexpensive and non-toxic naturallyoccurring acid as a capping agent which proved to be a good choice for high quality, monodispersed nanoparticles.

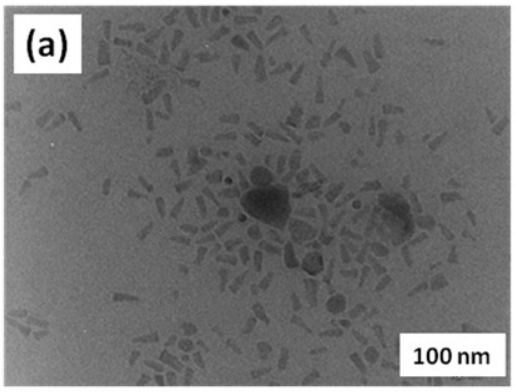

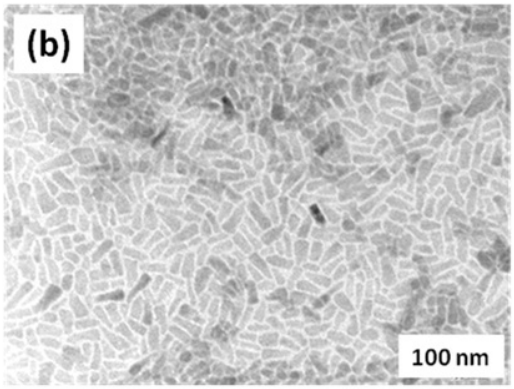

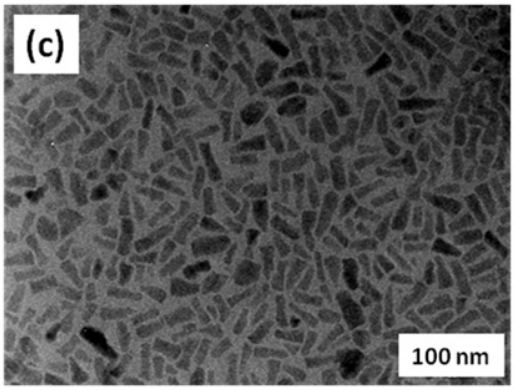

CdE (E=S,Se,Te)	Width /size (nm)	Length (nm)
CdS	11.8	32.6
CdSe	15.2	43.2
CdTe	16.3	48.4

(d)

FIG. 3. TEM images of anacardic acid capped CdS (a), CdSe (b) and CdTe (c), and table showing their sizes (d) synthesized at 160 °C

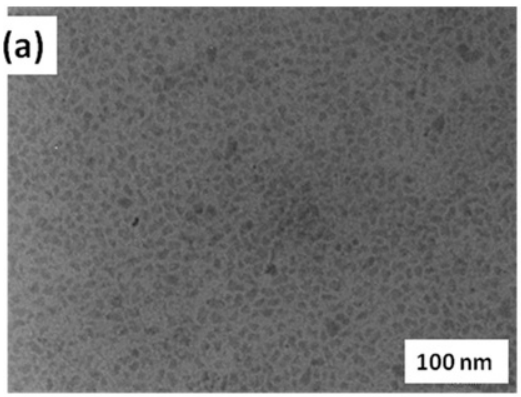

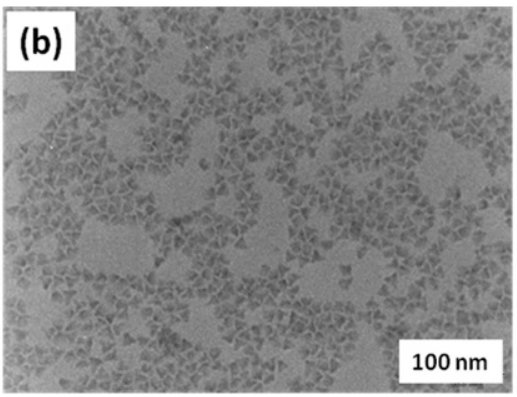

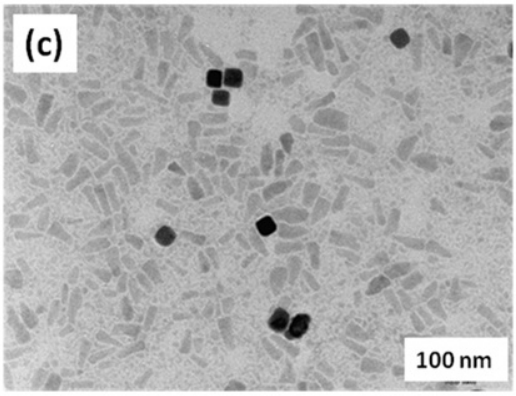

PbE (E=S,Se,Te)	Width/size (nm)	Length (nm)
PbS	9.8	
PbSe	12.6	
PbTe (rods/cubes)	11.9/20.9	37.8

(d)

FIG. 4. TEM images of anacardic acid capped PbS (a), PbSe (b) and PbTe (c), and table showing their sizes (d) synthesized at 160 °C

References

[1] Fan F-J., Wu L., Yu S-H. Energetic I–III–VI_2 and I_2–II–IV–VI_4 nanocrystals: synthesis, photovoltaic and thermoelectric applications. *Energy Environ. Sci.*, 2014, **7**, P. 190–208.

[2] Lewis D.J., Kevin P., Bakr O., Muryn C.A., Malik M.A. and O'Brien P. Routes to tin chalcogenide materials as thin films or nanoparticles: a potentially important class of semiconductor for sustainable solar energy conversion. *Inorg. Chem. Front.*, 2014, **1**, P. 577–598.

[3] Min Y., Moon G.D., Kim C-E., Lee J-H., Yang H., Soon A., Jeong U. Solution-based synthesis of anisotropic metal chalcogenide nanocrystals and their applications. *J. Mater. Chem. C*, 2014, **2**, P. 6222–6248.

[4] Santra P.K., Kamat P.V. Tandem-Layered Quantum Dot Solar Cells: Tuning the Photovoltaic Response with Luminescent Ternary Cadmium Chalcogenides. *J. Am. Chem. Soc.*, 2013, **135**(2), P. 877–885.

[5] Pan Z., Mora-Seró I., Shen Q., Zhang H., Li Y., Zhao K., Wang J., Zhong X., Bisquert J. High-Efficiency "Green" Quantum Dot Solar Cells. *J. Am. Chem. Soc.*, 2014, **136**(25), P. 9203–9210.

[6] Kaewsaneha C., Tangboriboonrat P., Polpanich D., Eissa M., Elaissari A. Janus Colloidal Particles: Preparation, Properties, and Biomedical Applications. *ACS Appl. Mater. Interfaces*, 2013, **5**(6), P. 1857–1869.

[7] Akhtar J., Malik M.A., O'Brien P., Wijayantha K.G.U., Dharmadasa R., Hardman S.J.O., Graham D.M., Spencer B.F., Stubbs S.K., Flavell W.R., Binks D.J., Sirotti F., El Kazzi M., Silly M. A greener route to photoelectrochemically active PbS nanoparticles. *J. Mater. Chem.*, 2010, **20**, P. 2336–2344.

[8] Da Silva E.C., Da Silva M.G., Meneghetti S.M., Machado G., Alencar M.A., Hickmann J.M., Meneghetti M.R. Synthesis of Colloids Based on Gold Nanoparticles Dispersed in Castor Oil. *J Nanopart Res.*, 2008, **10**, P. 201–208.

[9] Devendran P., Alagesan T., Ravindran T.R., Pandian K. Synthesis of Spherical CdS Quantum Dots Using Cadmium Diethyldithiocarbamate as Single Source Precursor in Olive Oil Medium. *Current Nanoscience.*, 2014, **10**, P. 302–307.

[10] Paul A., Warner T., John C. *Green Chemistry: Theory and Practice*. Oxford [England], New York: Oxford University Press, 1998.

[11] Raveendran P., Fu J., Wallen S.L. Completely "Green" Synthesis and Stabilization of Metal Nanoparticles. *J. Am. Chem. Soc.*, 2003, **125**, P. 13940–13941.

[12] Kyobe J.W., Mubofu E.B., Makame Y.M.M., Mlowe S., Revaprasadu N. CdSe quantum dots capped with naturally occurring biobased oils. *New J. Chem.*, 2015, DOI: 10.1039/C5NJ01460C.

[13] Nyamen L.D., Revaprasadu N., Ndifon P.T. Low temperature synthesis of PbS and CdS nanoparticles in olive oil. *Mater. Sci. Semicond. Process.*, **27**, P. 191–196, 2014.

[14] Devendran P., Alagesan T., Ravindran T.R., Pandian K. Synthesis of spherical CdS quantum dots using cadmium diethyldithiocarbamate as single source precursor in olive oil medium. *Curr. Nanosci.*, 2014, **10**, P. 302.

[15] Sapra S., Rogach A.L., Feldmann J. Phosphine-free synthesis of monodisperse CdSe nanocrystals in olive oil. *J. Mater. Chem.*, 2006, **16**, P. 3391–3395.

[16] Chen J., Song J.L., Sun X.W., Deng W.Q., Jiang C.Y., Lei W., Huang J.H., Liu R.S. An oleic acid-capped CdSe quantum-dot sensitized solar cell. *Appl. Phys. Lett.*, 2009, **94**, P. 153115. doi: 10.1063/1.3117221.

[17] Mlowe S., Pullabhotla V.S.R., Mubofu E.B., Ngassapa F.N., Revaprasadu N. Low temperature synthesis of anacardic acid capped cadmium chalcogenide nanoparticles. *Int. Nano. Lett.*, 2014, **4**, P. 106.

[18] Mlowe S., Pullabhotla V.S.R., Mubofu E.B., Ngassapa F.N., Nejo A.A., O'Brien P., Revaprasadu N. Lead chalcogenides stabilized by anacardic acid. *Mater. Sci. Semicond. Process.*, 2013, **16**, P. 263–268.

[19] Tyman J.H.P. Long-chain phenols. V. Gas chromatographic analysis of cashew nut-shell liquid. (Anacardium occidentale). *J. Chromatog*, 1975, **111**, P. 285–292.

[20] Paramashivappa R., Kumar P.P., Vithayathil P.J., Rao A.S. Novel method for isolation of major phenolic constituents from cashew (Anacardium occidentale L) Nut Shell Liquid. *J. Agric. Food Chem.*, 2001, **49**, P. 2548–2551.

[21] Lucio P.L.L., Santos C.O., Romeiro L.A.S., Costa A.M., Ferreira J.R.O., Cavalcanti B.C., Moraes O.M., Costa-Lotufo L.V., Pessoa C., Santos M.L. Synthesis and cytotoxicity screening of substituted isobenzofuranones designed from Anacardic acids. *Eur. J. Med. Chem.*, 2010, **45**, P. 3480–3489.

[22] Mokari T., Zhang M., Yang P. Shape, size, and assembly control of PbTe nanocrystals. *J. Am. Chem. Soc.*, 2007, **129**, P. 9864–9865.

NANOSYSTEMS: PHYSICS, CHEMISTRY, MATHEMATICS, 2016, 7 (4), P. 728–731

Investigation on the preparation and properties of nanostructured cerium oxide

G. Jayakumar, A. Albert Irudayaraj*, A. Dhayal Raj, M. Anusuya

PG & Research Department of Physics, Sacred Heart College, Tirupattur, Vellore District, Tamil Nadu, India

*gjayaphysics@gmail.com

PACS 61.46.-w **DOI 10.17586/2220-8054-2016-7-4-728-731**

Cerium oxide (CeO_2) nanoparticles were successfully synthesized by the hydrothermal method with different reaction times. The synthesized CeO_2 nanoparticles were characterized by Powder X-Ray diffraction (XRD), Scanning Electron Microscopy (SEM), UV-Vis spectroscopy and FTIR spectroscopy. The effects of the reaction time on the structure and morphology of the prepared samples were investigated using XRD and SEM. The XRD studies reveal that the ceria nanoparticles have face-centered cubic structure. The SEM images reveal that the prepared Ceria nanoparticles are an aggregated form of spherical nanoparticles and the particle size decreases with increasing reaction time. FTIR analysis confirms the presence of CeO_2 in the prepared samples. UV-Vis spectral studies show that the UV cut off wavelength decreases and the optical band gap increases with increased reaction time. Photoluminescence (PL) studies indicate that the PL emission of both the samples occurs at 683 nm, however, the emission intensity increases with longer reaction times.

Keywords: ceria nanoparticles, hydrothermal method, photoluminescence.

Received: 8 February 2016

Revised: 10 May 2016

1. Introduction

Cerium oxide (CeO_2) is a refractory material possessing cubic fluorite crystal structure [1, 2]. It is one of the most reactive rare earth metal oxides due to its oxygen storage capacity (OSC), oxygen deficiency, and electronic conductivity. It has promising applications in fuel cells, oxygen sensors and mechanical polishing. It also has utility as an ultraviolet blocking agent, luminescent material and photocatalyst. Ceria nanoparticles can be prepared by methods such as hydrothermal [3], reverse micelles, micro-emulsion [4], homogeneous precipitation [5] etc. The main objective of this research paper is studying the effect of reaction time on the structural and optical properties of nanostructured cerium oxide prepared by the hydrothermal method.

2. Experimental

2.1. Synthesis

All the reagents used in the synthesis process were of analytical grade purity and used without any further purification. In the synthesis process, 0.274 g of ammonium ceric nitrate ($(NH_4)_2Ce(NO_3)_6$) was dissolved in 5 ml distilled water and 0.499 g of Sodium hydroxide (NaOH) was dissolved in 25 ml distilled water. These two solutions were mixed and the mixture was stirred for 30 min. To the resultant precursor solution obtained, 0.1808 g of urea ($CO(NH_2)_2$) dissolved in 10 ml of distilled water, was added. The solution was transferred to a Teflon-lined autoclave which was maintained at 200°C for 24 hours. The autoclave was allowed to cool down naturally and to reach the room temperature. The final product was collected from the autoclave and washed several times with distilled water and ethanol. The product was dried at 80°C for 6 hours. The dried sample was calcined at 400°C for 2 hrs.

$$CO(NH_2)_2 + 3H_2O \rightarrow 2NH_4^+ + 2OH^- + CO_2 \uparrow$$

$$NH_4^+ + OH^- \leftrightarrow NH_3 \cdot H_2O \leftrightarrow H_2O + NH_3 \uparrow$$

$$(NH_4)_2Ce(NO_3)_6 + 4NaOH \xrightarrow{200^\circ C} Ce(OH)_4 + 4NaNO_3 + 2NH_3 \uparrow + 2NO_3 + H_2 \uparrow$$

$$Ce(OH)_4 \cdot xH_2O \xrightarrow{80^\circ C} Ce(OH)_4 + xH_2O \uparrow$$

$$Ce(OH)_4 \xrightarrow{400^\circ C} CeO_2 + 2H_2O \uparrow$$

2.2. Characterizations

The XRD measurements were carried out using Rigaku X-ray diffractometer with CuKα (λ = 1.54187 Å) radiation in the range of 10 – 80 ° at room temperature. The surface morphology of the particles was studied by scanning electron microscope.The optical transmittances of the samples were studied by Varian Cary 50 UV-Visible spectrophotometer in the range 200 – 800 nm. The FTIR spectra were recorded in the range of 400 – 4000 cm^{-1} by PERKIN ELMER SPECTRUM II FTIR spectrometer. The photoluminescence spectra were obtained by PERKIN ELEMER LS45 fluorescence spectrophotometer using excitation wavelength of 343 nm.

3. Results and discussions

3.1. XRD analysis

The powder XRD patterns of CeO_2 nanoparticles prepared with different reaction times are shown in Fig. 1. The peaks are indexed using JCPDS card #34-0394. Both 12 hour and 24 hour CeO_2 samples have Face Centered Cubic structure with lattice parameters $a = b = c = 5.411$ Å and $\alpha = \beta = \gamma = 90$ °. The diffraction peaks found at 28.27, 33.09, 47.34, 53.36, 69.26 and 76.75 ° showed a broadening effect, which suggests the formation of nanosized CeO_2. The absence of impurities indicates that pure CeO_2 is synthesized by the hydrothermal method. The average crystallite sizes (D) of the CeO_2 nanoparticles prepared with different reaction times, were calculated using the Debye-Scherrer equation:

$$D = \frac{K\lambda}{\beta \cos\theta},$$

where λ is the wavelength of the CuKα radiation, D is the crystallite size, K is a constant and its value is taken as 0.9, θ is the diffraction angle and β is the full-width half maximum (FWHM). The average crystallite size decreased slightly from 3.9 nm to 3.6 nm as the reaction time increased from 12 to 24 hours. The decrease of crystallite size with increasing reaction time was also confirmed from SEM images.

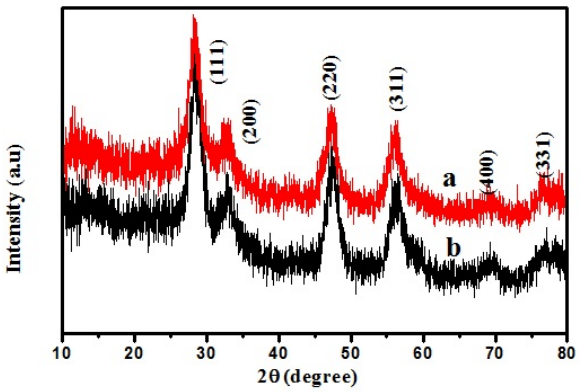

FIG. 1. XRD spectra of the CeO_2 nanoparticles prepared at (a) 24 hours and (b) 12 hours

3.2. FTIR spectra

The FTIR spectra of CeO_2 nanoparticles prepared by hydrothermal method with different reaction times are shown in Fig. 2. The band below 700 cm^{-1} is due to the Ce–O stretching vibrations [6–8].

3.3. UV-Visible spectra

The optical properties of synthesized CeO_2 were examined by UV-Visible spectrophotometer and the results are depicted in Fig. 3. The UV cutoff wavelength of the 12 hour sample was 349 nm, while the UV cutoff wavelength of the 24 hour sample was 343 nm. Additionally, the UV-Visible spectra showed no other peak related with impurities and structural defects, which confirmed that the synthesized nanoparticles are pure CeO_2. The band gap energy of 12 hour sample was 3.54 eV, whereas the band gap energy for the 24 hour sample was found to be 3.67 eV. As the reaction time increased, the band gap energy increased while the crystallite size decreased.

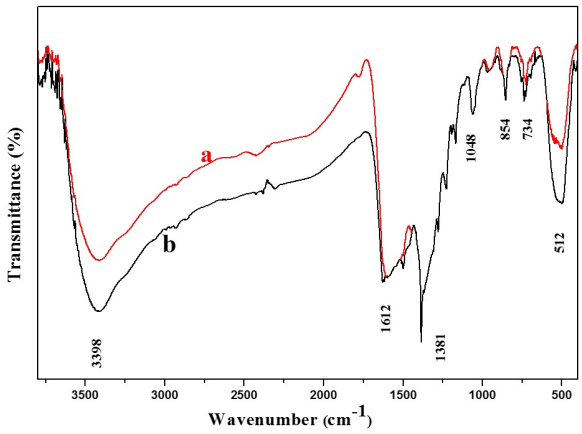

FIG. 2. FTIR spectra of the CeO_2 nanoparticles prepared at (a) 24 hours and (b) 12 hours

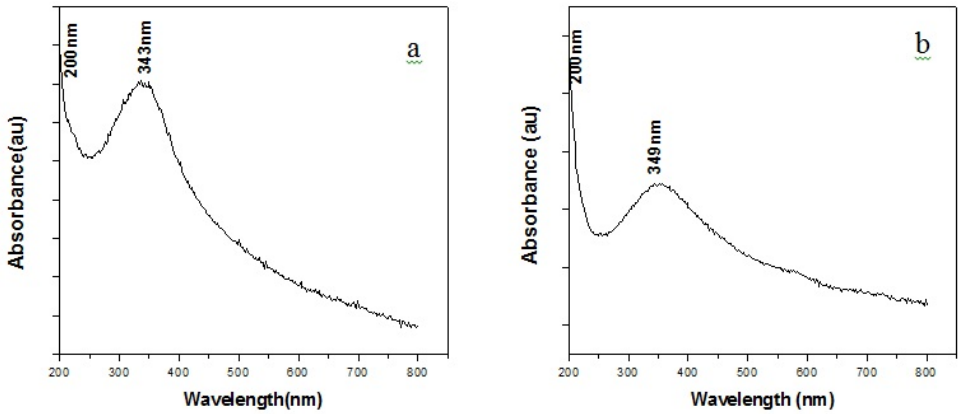

FIG. 3. UV-Vis spectra of the CeO_2 nanoparticles prepared at (a) 24 hours and (b) 12 hours

3.4. Scanning electron microscopy

The SEM images of the CeO_2 nanoparticles prepared by hydrothermal method with different reaction times are shown in Fig. 4. The CeO_2 nanoparticles prepared with 12 hours reaction time had sphere-like structure with an average particle size of 78 nm. The CeO_2 nanoparticles prepared with 24 hours reaction time also had sphere-like structure with an average particle size of 63 nm. Hence, it may be said that the change in the reaction time does not lead to any change in the shape of the CeO_2 nanoparticles, however, the change in the reaction time definitely had an effect on the particle size. The particle size decreased with additional reaction time.

3.5. Photoluminescence studies

The PL spectra of the CeO_2 nanoparticles prepared with different reaction time are shown in Fig. 5. The samples were excited by 343 nm wavelength, and the emission wavelength of these samples was obtained at approximately 683 nm. This emission peak corresponds to red-light. The emission intensity increased from 110.8 a.u to 132.6 a.u with longer reaction times.

4. Conclusions

CeO_2 nanoparticles were successfully synthesized by hydrothermal method and were analyzed by XRD, FTIR, SEM, UV-Visible spectroscopy and photoluminescence measurements. The studies indicate that the reaction time has an effect on the particle size and hence on the optical properties of CeO_2 nanoparticles. The CeO_2 nanoparticles prepared at 24 hours exhibited smaller particle size. The XRD studies revealed that they have face centered cubic structure and have the average grain size of 3.6 nm. From the SEM studies, the average particle size of CeO_2 nanoparticles prepared at 24 hours was found to be 63 nm. The UV-visible spectroscopic studies and PL studies

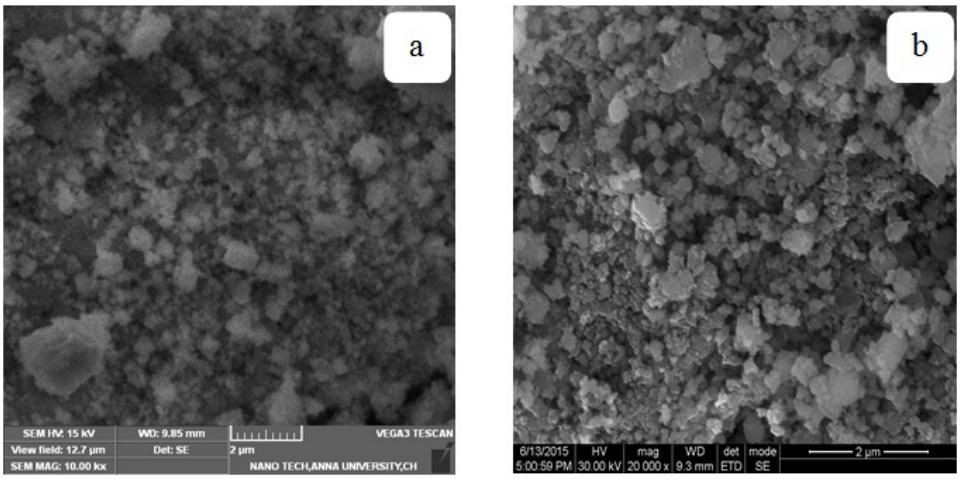

FIG. 4. SEM images of the CeO_2 nanoparticles prepared at (a) 24 hours and (b) 12 hours

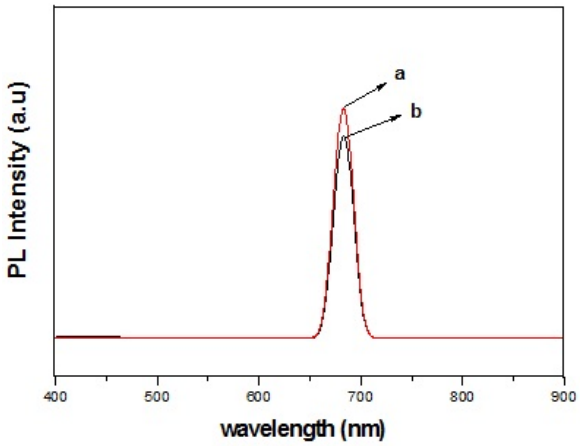

FIG. 5. PL spectra of CeO_2 nanoparticles prepared at (a) 24 hours and (b) 12 hours

reveal that the CeO_2 nanoparticles prepared at 24 hours have a lower UV cut off wavelength, wider optical transmission range and higher PL emission intensity; i.e. it has better optical properties.

References

[1] Kang H.S., Kang Y.C., Koo H.Y., Ju S.H., Kim D.Y., Hong S.K., Sohn J.R., Jung K.Y., Park S.B. Nano-sized ceria particles prepared by spray pyrolysis using polymeric precursor solution. *Journal of Materials Science and Engineering B*, 2006, **127**, P. 99–104.

[2] Jayakumar G., Albert Irudayaraj A., Dhayal Raj A., Magimai Antoni Raj D., Daniel Lawrence D. Comparative studies on Cerium Phosphate and Cerium Oxide Nanoparticles. *Journal of Chem. Tech Research*, 2015, **7**(3), P. 1385–1391.

[3] Masui T., Fujiwara K., Machida K., Adachi G. Characterization of cerium (IV) oxide ultrafine particles prepared by reversed micelles. *Journal of Chem. Mater.*, 1997, **9**, P. 2197–2204.

[4] Chen H., Chang H. Homogeneous precipitation of cerium dioxide nanoparticles in alcohol/water mixed solvents. *Colloids and Surfaces A: Physicochem. Eng. Aspects*, 2004, **242**, P. 61–69.

[5] Khan S.B., Faisal, Mohammed Rahman M., Jamal A. Exploration of CeO_2 nanoparticles as a chemi-sensor and photo-catalyst for environmental applications. *Science of the total Environment*, 2011, **409**, P. 2987–2992.

[6] Wang G., Mu Q., Chen T., Wang Y. Synthesis, characterization and photoluminescence of CeO_2 nanoparticles by a facile method at room temperature. *Journal of Alloys and Compounds*, 2010, **493**, P. 202–207.

[7] Bo Liu, Bingbing Liu, Li, Zepeng Li Q, Ran Liu, Xu Zou, Wei Wu, Wen Cui, Zhao dong Liu, Dongmei Li, Bo Zou, Tian Cui, Guangtian Zou. Solvothermal synthesis of monodisperse self-assembly CeO_2 nanospheres and their enhanced blue-shifting in ultraviolet absorption. *Journal of Alloys and Compounds*, 2010, **503**, P. 519–524

[8] Kumar E., Selvarajan P., Muthuraj D. Synthesis and characterization of CeO_2 nanocrystals by solvothermal route. *Journal of Materials Research*, 2013, **16**, P. 269–276.

NANOSYSTEMS: PHYSICS, CHEMISTRY, MATHEMATICS, 2016, 7 (4), P. 732–739

Polyaniline-Titanium dioxide composite as humidity sensor at room temperature

S. Kotresh[1], Y. T. Ravikiran[1,*], H. G. Raj Prakash[2], S. C. Vijaya Kumari[3]

[1]Department of PG Studies and Research in Physics, Government Science College, Chitradurga 577501, India

[2]Department of Physics, JNN College of Engineering, Shivamogga 577204, India

[3]Department of Physics, SJM College of Arts, Science and Commerce, Chitradurga 577501, India

*ytrcta@gmail.com

PACS 81.07.Pr **DOI 10.17586/2220-8054-2016-7-4-732-739**

In the present work, Polyaniline (PANI) and Polyaniline-Titanium dioxide (PANI-TiO_2) composite have been synthesized separately by chemical polymerization of aniline without/with TiO_2. Characteristic absorption bands of PANI and TiO_2 in the composite were confirmed by FT-IR studies, indicating the interaction of PANI with TiO_2. Comparative study of XRD patterns of PANI and the composite confirmed superficial deposition of PANI on TiO_2 and the average size of the composite particle was found to be 25 nm. The aggregated granular porous morphology of the composite was confirmed by its SEM image. The composite's sensing response to humidity at room temperature was tested and was found to be 84.21 % in the range 25 % – 95 % RH. The response and recovery time of the composite at 95 % RH were measured to be 60s and 100s respectively and its sensing stability over a period of one month was also confirmed.

Keywords: polyaniline composites, humidity sensor, sensitivity, stability.

Received: 9 February 2016

Revised: 26 April 2016

1. Introduction

In recent years, nanocomposites have evolved as the most sought after materials in various fields such as sensors, super capacitors, catalysis, light emitting diodes and fuel cells because they offer flexibility in terms of tuning their electrical and mechanical properties for best synergetic effects [1–5]. Thus, reliable fabrication of devices using these materials by cost effective methods is a major concern of many researchers. One such method is the incorporation of metal/metal oxides into the conducting polymers via a chemical or electrochemical route [6–12].

With the advancement of moisture-sensitive technologies and the increasing awareness for quality of life issues, humidity sensing has gained in importance in various areas like medicine, agriculture and electronic industries [13]. With the rapid advances in technology, increasing efficiency, reducing cost, reliability and miniaturization for fabrication of sensors are the major concerns in any research. In recent years, conducting polymer based sensors have become more favorable over metal oxide based sensors in terms of increased sensitivity, simple processing and their room temperature operation [14]. Among all conducting polymers, PANI is the most preferred because of its unique characteristics, such as tunable electrical and chemical properties, easy processing and low costs [15]. Recently, PANI based metal oxide composites have been found to be more advantageous in terms of enhanced humidity sensitivity and such composites have been studied by many researchers. Electrospun PANI composite nanofibers have shown good sensitivity to humidity with a good recovery and response time as reported by Q. Lin *et al.* [16]. M.T.S. Chani *et al.* Studied the humidity sensitivity of an orange dye PANI composite film by impedance measurements and have showed a uniform change in impedance for humidity values ranging from 30 – 90 % RH [17]. Room temperature humidity sensing of PANI-PVA composite has been studied by Y. Li and others, and they showed that the sensitivity of the composite increases with increased impedance from 10 – 90 % RH and has both quick response and recovery times [18]. K. C. Sajjan et al. have reported better humidity sensing response for a PANI-Cr_2O_3 composite over the range 20 – 95 % RH [19]. S.C. Nagaraju et al. have reported good humidity sensing response for PANI-Pr_2O_3 composites in the range 10 – 90 % RH [20]. In this work, we have attempted to fabricate a low cost humidity sensing device made of PANI-TiO_2 composite which can be easily prepared and operable at room temperature. We preferred TiO_2 with PANI for the composite because it is a white n-type transition metal oxide semiconductor with a wide band gap (3.0 – 3.2 eV) and has a large dielectric constant ($\sim$100) [21,22]. This compound's compatible physical properties were considered favorable for use in fiber optics, photovoltaics, gas sensors, biocompatible materials, electrolytic capacitors and dye sensitized solar cells [21].

In this work, PANI and PANI-TiO_2 composite were synthesized by a cost effective, simple in situ chemical polymerization method and were structurally characterized using FTIR, XRD and SEM techniques. Based on these studies, humidity sensitivity of the composite's film prepared by spin coating technique was tested and analyzed. Its stability, recovery and response time have also been studied. Both processability and sensing studies were carried out at room temperature.

2. Experimental

2.1. Materials

Aniline ($C_6H_5NH_2$) (99.5 %), ammonium persulfate [$(NH_4)_2S_2O_8$] (98 %), hydrochloric acid (HCl) (34.5%) and titanium dioxide (TiO_2) (99.5 %), all of analytical grade reagents were purchased from s.d. Fine Chemicals, Mumbai, India. Aniline monomer was doubly distilled before use.

2.2. Preparation of PANI-TiO_2 composite

The method of preparation of pure PANI and the PANI-TiO_2 composite at room temperature is as follows; firstly, a solution of 6.7 ml of aniline monomer in 60 ml 1M HCl was prepared. It was added to 180 ml of deionized water in which 0.67 g of TiO_2 powder was previously dispersed. Then adsorption of aniline on TiO_2 was facilitated by sonication of the above mixture. Then 7.5 g of $(NH_4)_2S_2O_8$ in 60 ml deionized water was added dropwise into the above mixture with continuous stirring for 30 min and then allowed to polymerize for 8 – 10 hrs. The reaction product was collected by centrifugation and washed successively with deionized water and acetone until a clear precipitate was obtained which was dried in vacuum until it turned dark green.

2.3. Characterization of the samples

The FTIR spectra of pristine PANI, PANI-TiO_2 composite and TiO_2 were recorded using Nicolet 750 FT-IR spectrometer in KBr medium at room temperature. The X-ray diffraction pattern of each sample was obtained by employing Siemens D-5000 powder X-Ray diffractometer with Cu$K\alpha$ source radiation of wavelength 1.54×10^{-10} m. SEM images of PANI and the composite samples were recorded using a Hitachi S-520 scanning electron microscope.

2.4. Humidity sensing measurements

The experimental set up used for humidity sensing measurements has been described previously in our literature [23]. A film of the composite was prepared by dissolving the composite powder in m-cresol and then coating it on a glass plate using spin coating unit (Make: Delta Scientific Pvt. Ltd, India, Model: Delta Spin I). Then, interdigitated silver electrodes were printed on it and it was then placed in a specially designed glass chamber well equipped for maintaining required relative humidity. The chamber was tightly closed at the top with a cork. One end of these electrodes were connected to the film by passing through the cork while the other ends were connected to a digital LCR meter (Make: Hioki, Japan, Model: 3532-50) which recorded the impedance changes before and after exposing the sample to humidity at a selected frequency of 100 Hz. The relative humidity in the chamber was varied using saturated salt solutions and monitored using humidity meter (Mextech-DT-615).

3. Results and discussion

3.1. Fourier transform infrared spectroscopy

FT-IR analysis was used to examine the composite structure after polymerization. The FT-IR spectra of TiO_2, PANI and PANI-TiO_2 composite are shown in Fig. 1.

The FT-IR spectrum of pure TiO_2(Fig. 1(c)) shows strong absorption bands at 648 cm^{-1} and 419 cm^{-1} which are the characteristic vibrations of TiO_2. These are respectively assigned to the Ti-O-Ti stretching vibration and for Ti-O and Ti-O-Ti combined stretching vibrations and all these results agreed with the published literature [24].

In the FT-IR spectrum of pristine PANI (Fig. 1(b)), the absorption bands at 3419 cm^{-1}, 1600 cm^{-1}, 1498 cm^{-1}, 1299 cm^{-1}, 1147 cm^{-1} and 880 cm^{-1} are attributed to the PANI chain. These are respectively assigned to O-H stretching of absorbed water, the C=C stretching of quinoid ring, the C=C stretching of benzenoid ring, the C-N stretching of imine and secondary amine of PANI backbone, the C-H stretching in-plane bending vibration and the 1,4 coupling of aromatic ring and all these have agreed well with the pattern published in the literature [25,26].

The FT-IR spectrum of the composite sample (Fig. 1(a)), exhibited characteristic absorption bands at 3425 cm^{-1}, 1630 cm^{-1}, 1497 cm^{-1}, 1299 cm^{-1}, 1136 cm^{-1}, 896 cm^{-1}, 611 cm^{-1} and 419 cm^{-1}, which are associated with the characteristic vibrations of both PANI and TiO_2 but with a small shift are due to the interaction of oxygen ions of TiO_2 and nitrogen atoms of PANI macromolecules present in the composite [27].

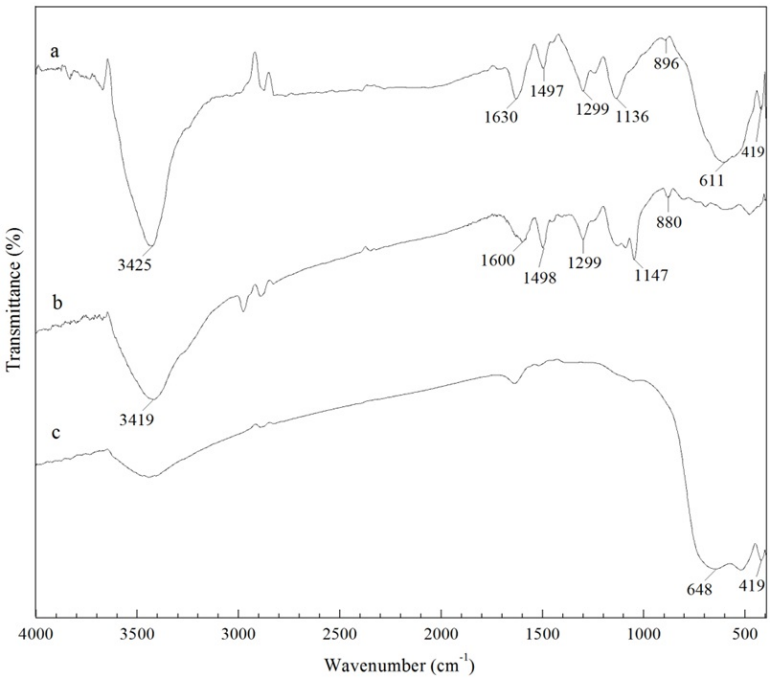

FIG. 1. Fourier transform infrared spectra of (a) PANI-TiO_2 composite (b) Pristine PANI and (c) TiO_2

3.2. X-ray diffraction

The XRD patterns of PANI, PANI-TiO_2 composite and that of TiO_2 with assigned *hkl* values are shown in Fig. 2. The XRD pattern of pristine PANI (Fig. 2(a)), reveals some degree of crystallinity with the appearance of broad peaks corresponding to (100) and (110) planes [JCPDS No. 53-1718] in the region 2θ = 15 – 25 ° similar to those reported in our earlier literature [**?**, 28] The XRD pattern of TiO_2 (Fig. 2(c)) clearly shows peaks corresponding to the planes (110) (101) (200) (111) (210) (211) (220) (002) (310) and (112) in the range 2θ = 20 – 70 ° and the peaks when compared with JCPDS No. 870710 were confirmed to be of rutile TiO_2. The same pattern for TiO_2 has also been confirmed in previous literatures [29, 30].

Comparison of XRD patterns of PANI, TiO_2 and the PANI-TiO_2 composite (Fig. 2(b)) indicates predominance of TiO_2 in the composite, the rutile phase (110) of TiO_2 has remained while the broad weak peaks of PANI have disappeared. All these suggest that there is interaction between PANI and TiO_2 and that TiO_2 has restricted the growth of PANI chains hampering its crystalline behavior. So it can be concluded that PANI has just deposited on TiO_2 and has no effect on the crystalline behavior of TiO_2. Similar study has been reported in earlier literature [30].

Applying the Scherrer formula [31] using Eq. (1) to the most prominent sharp peak at 28 °, we obtained the size of the crystallite t to be 25 nm:

$$t = \frac{k\lambda}{b\cos\theta}, \tag{1}$$

where b is the breadth in radians, θ is the Bragg angle and λ is the wavelength of radiation. The coefficient k normally takes a value close to 0.9.

3.3. Scanning electron microscopy

The morphology of TiO_2, PANI and PANI-TiO_2 composite are shown in Fig. 3. The morphology of pristine PANI shown in Fig. 3(a) is an agglomerated granular structure with uniform surface. The morphology of the composite (Fig. 3(b)) shows predominance of TiO_2 particles, their surface being covered by PANI, which agrees very well with the results obtained by XRD studies.

The Scanning electron micrograph of TiO_2 shown in Fig. 3(c) reveals aggregated granular morphology and agrees well with the SEM images in previously reported studies [32].

The average grain size D_{Avr} of the composite material calculated using Mendelson's formula [33] given by Eq. (2) is 25 nm:

$$D_{Avr} = \frac{1.56 \times C_L}{M' N_i}, \tag{2}$$

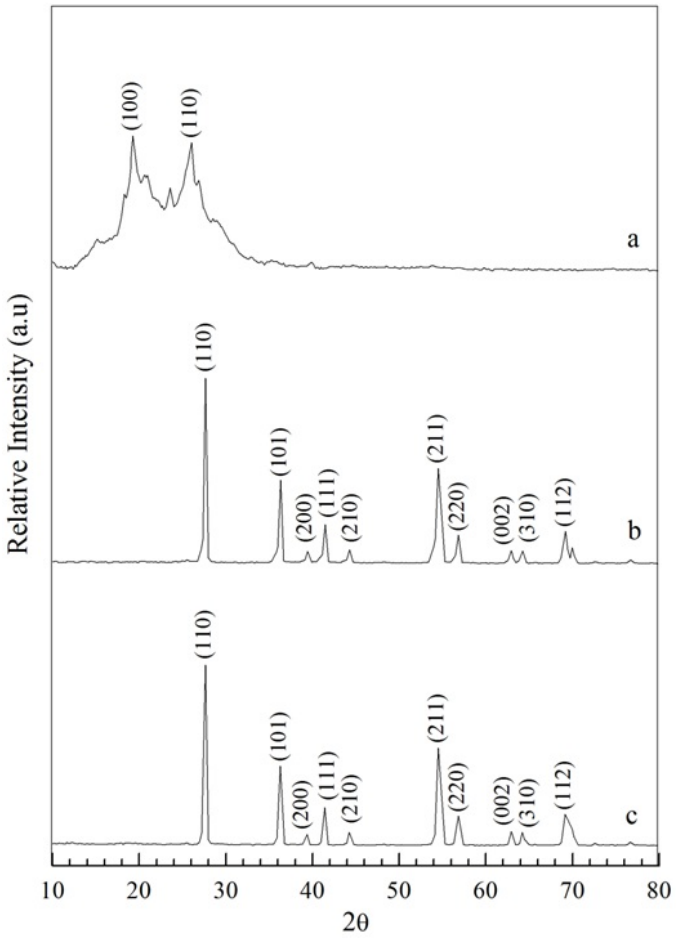

FIG. 2. X-ray diffraction spectra of (a) Pristine PANI (b) PANI-TiO_2 composite and (c) TiO_2

where C_L is the total length of the test line used, N_i is the number of intercepts and M' is the magnification of the photograph.

3.4. Humidity sensing response studies

The sensing response of the composite for various % RH are measured at 100 Hz using fractional base line manipulation method [34] using Eq. (3):

$$S_H = \frac{Z_0 - Z_{RH}}{Z_0} \times 100 \tag{3}$$

where Z_0 is the impedance of the sample before exposure to moisture (dry air with 25 % RH) and Z_{RH} is the impedance at various % RH.

The sensing response characteristic curve of the composite thus obtained by the above method is shown in Fig. 4. It can be seen that the composite is sensitive and its response is linear in the 25 – 95 % RH range with a maximum sensing response of 84.21 %. This linear response of the composite in this range with increasing humidity may be attributed to the following probabilities: (i) At low RH mobility of TiO_2 ions in the composite is restricted due to curling up of polymer chains. As humidity increases, polymer chain uncurls and becomes aligned by absorbing water molecules paving way for faster hopping of charge carriers, resulting in increased sensing response of the composite [21,35]. (ii) Porosity of the polymers as revealed by SEM studies may facilitate absorption of water molecules as RH increases causing a decrease in the impedance of the composite [13].

Efficiency of the composite as a sensing device was studied by measuring its response and recovery times [36]. Humidity sensing response and recovery characteristic curve of the composite at 100 Hz is shown in Fig. 5. For the purposes of our study, two chambers, one with 25 % RH and another with 95 % RH were maintained separately. The response time of 60 s was recorded when the sample was moved from 25 % RH to 95 % RH and a recovery

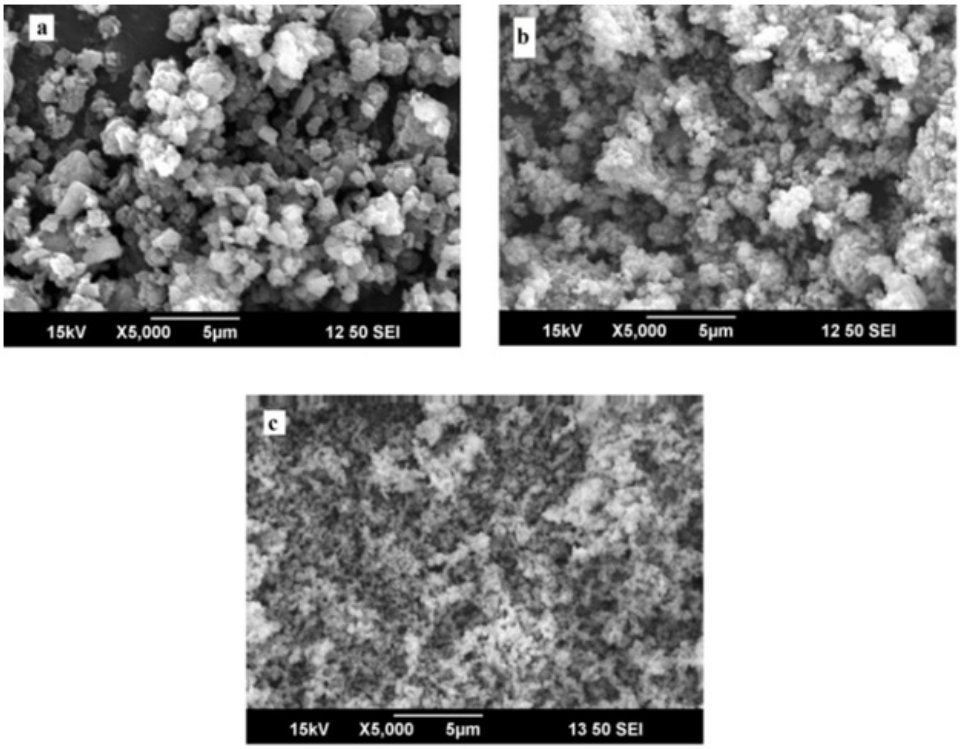

FIG. 3. Scanning electron micrographs of (a) Pristine PANI (b) PANI-TiO_2 composite and (c) TiO_2

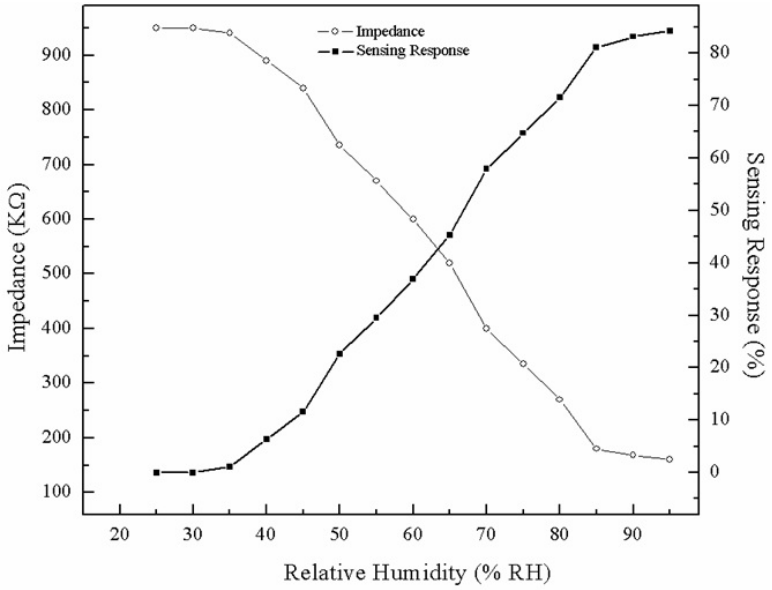

FIG. 4. Variation of sensing response and Impedance with relative humidity at 100 Hz

time of 100 s was recorded when the sample was moved from 95 % RH to 25 % RH, switching time being 1s in both the cases, establishing that the composite can become a good humidity sensing device.

To examine the practical viability of the composite for use as a sensor, variation of sensing response at 55 % RH and at 95 % RH at a frequency of 100 Hz after every one week for one month was studied [37]. The results presented in the graph shown in Fig. 6 suggest stable sensing ability both during adsorption and desorption with a negligible degradation of 3 % in sensing response. This finding suggests that the composite, apart from being a good sensor, is also stable and so it can be practically feasible to utilize it in a sensor device.

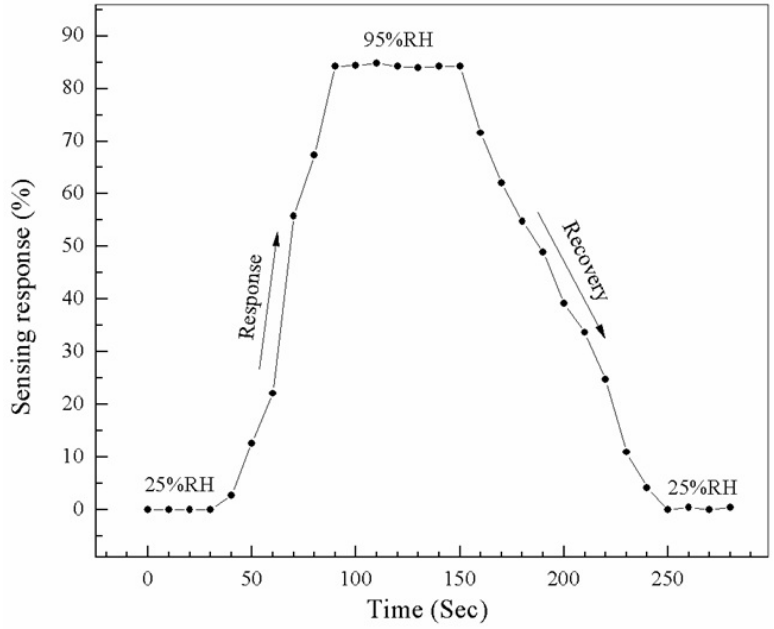

FIG. 5. Response and recovery characteristic curves of PANI-TiO_2 composite at 100 Hz

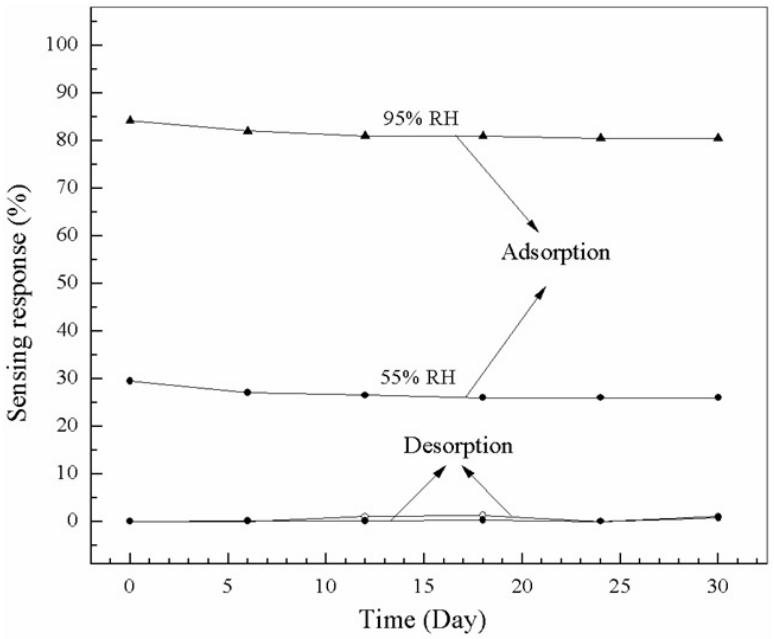

FIG. 6. Stability of PANI-TiO_2 composite at 100 Hz

4. Conclusions

The PANI-TiO_2 composite synthesized by simple chemical polymerization method showed a room temperature sensing response of 84.21 % in the range 25 % – 95 % RH. The sensing response of the composite film prepared by cost effective spin coating method was measured using LCR meter at a selected frequency of 100 Hz. The efficiency of the composite as a sensor was also confirmed with a recorded response time of 60s and a recovery time of 100s. The composite has shown stable sensing ability over a period of one month. All these results show that the composite has the potential to become an efficient humidity sensing device operable at room temperature besides being easily prepared and cost effective.

Acknowledgement

The author is thankful to the University Grants Commission, New Delhi, for their financial support provided under major research project (41-917/2012 (SR) dated: 23/07/2012), to carry out this work. The Author wishes to acknowledge SAIF, Cochin, for providing facility for characterization of the samples. The author is also thankful to Commissioner, Department of Collegiate Education, Government of Karnataka and Principal Prof. C.M. Vivekananda, Government Science College, Chitradurga for their encouragement and support to carry out this research work.

References

[1] Tang W., Peng L., Yuan C., Wang J., Mo S., Zhao C., Yu Y., Min Y., Epstein A.J. Facile synthesis of 3D reduced grapheme oxide and its Polyaniline nanocomposites for super capacitor application. *Synth. Met.*, 2015, **202**, P. 140–146.

[2] Bahloul A., Nessark B., Briot E., Groult H., Mauger A., Zaghib K., Julien C.M. Polypyrrole-covered MnO_2 as electrode material for supercapacitor. *J. Power Sources.*, 2013, **240**, P. 267–272.

[3] Rajesh., Ahuja T., Kumar D. Recent progress in the development of nano-structured conducting polymers/nanocomposites for sensor applications. *Sens. Actuators B.*, 2009, **136**, P. 275–286.

[4] Memjoglu F., Bayrakceken A., Tuba Oznuluer T., Metin A.K. Synthesis and characterization of polypyrrole/carbon nanocomposite as a catalyst support for fuel cell applications. *Int. J. Hydrogen Energy.*, 2012, **37**, P. 16673–16679.

[5] Shin S., Kim S., Kim Y. H., Kim S. Enhanced performance of organic light-emitting diodes by using hybrid anodes composed of polyaniline and conducting polymer. *Curr. Appl. Phys.*, 2013, **13**, P. S144–S147.

[6] Ali Y., Vijay K., Sonkawade R.G., Shirsat M.D., Dhaliwal A.S. Two-step electrochemical synthesis of Au nanoparticles decorated Polyaniline nanofiber. *Vacuum*, 2013, **93**, P. 79–83.

[7] Ali Y., Kashma S., Kumar V., Sonkawade R.G., Dhaliwal A.S. Polypyrrole microspheroidals decorated with Ag nanostructure: Synthesis and their characterization. *Appl. Surf. Sci.*, 2013, **280**, P. 950–956.

[8] Ali Y., Vijay K., Sonkawade R.G., Dhaliwal A.S. Effect of swift heavy ion beam irradiation on Au–Polyaniline nanocomposite films. *Vacuum*, 2013, **90**, P. 59–64.

[9] Kadam S.B., Datta K., Ghosh P., Kadam A.B., Khirade P.W., Kumar V., Sonkawade R.G., Gambhire A.B., Lande M.K., Shirsat M.D. Improvement of ammonia sensing properties of poly(pyrrole)–poly (n-methylpyrrole) nanocomposite by ion irradiation. *Appl. Phys.*, A 2013, **100**, P. 1083–1088.

[10] Ghoreishi K.B.,Yarmo M.A., Nordin N.M., Samsudin M.W. Enhanced catalyst activity of WO_3 using polypyrrole as support for acidic esterification of Glycerol with Acetic Acid. *J. Chem.*, 2013, article ID 264832, P. 1–10.

[11] Lee S.B., Lee S.M., Lee S., Chung D.W. Preparation and characterization of conducting polymer nanocomposite with partially reduced grapheme oxide. *Synth. Met.*, 2015, **201**, P. 61–66.

[12] Kanwal F., Siddiqi S.A., Batool A., Imran M., Mushtaq W., Jamil T. Synthesis of polypyrrole–ferric oxide (Ppy–Fe_2O_3) nanocomposites and study of their structural and conducting properties. *Synth. Met.*, 2011, **161**, P. 335–339.

[13] Ramaprasad A.T., Rao V. Chitin-polyaniline blend as humidity sensor. *Sens. Actuat. B*, 2010, **148**, P. 117–125.

[14] Zeng F.W., Liu X., Diamond D., Lau K.T. Humidity sensors based on Polyaniline nanofibres. *Sens. Actuat. B*, 2010, **143**, P. 530–534.

[15] MaDiarmid A.G. Semiconducting and metallic polymers: The fourth generation of polymeric materials. *Synth. Met.*, 2002, **125**, P. 11–22.

[16] Lin Q., Li Y., Yang M. Highly sensitive and ultrafast response surface acoustic wave humidity sensor based on electrospunpolyaniline/poly (vinyl butyral) nanofibres. *Anal. Chim. Acta.*, 2012, **748**, P. 73–80.

[17] Chani M.T.S., Karimov K.S., Khalid F.A., Abbas S.Z., Bhatty M.B. Orange dye polyaniline composite based impedance humidity sensors. *Chin. Phys.*, 2012, **22**, P. 010701.

[18] Li Y., Deng C., Yang M. Novel surface acoustic wave-impedance humidity sensor based on composite of polyaniline and poly (vinyl alcohol) with a capacity of detecting low humidity. *Sens. Actuators, B*, 2012, **143**, P. 7–12.

[19] Sajjan K.C., Roy A.S., Parveen A., Khasim S. Analysis of DC and AC properties of a humidity sensor based on polyaniline-chromium oxide composites. *J Mater Sci: Mater Electron.*, 2014, **25**, P. 1237–1243.

[20] Nagaraju S.C., Aashis S. Roy., Prasanna Kumar J.B., Anilkumar K.R., Ramagopal G. Humidity sensing properties of surface modified Polyaniline metal oxide composites. *J. Eng.*, 2014, 8 pages.

[21] Vlazan P., Ursu D.H., Moisesc C.I., Miron I., Sfirloaga P., Rusu E. Structural and electrical properties of TiO_2/ZnO core-shell nanoparticles synthesized by hydrothermal method. *Mater. Charact.*, 2015, **101**, P. 153–158.

[22] Marinel S., Choi D.H., Heuguet R., Agarval D., Lanagan M. Broadband dielectric characterization of TiO_2 ceramics sintered through microwave and conventional processes. *Ceram. Int.*, 2013, **39**, P. 299–306.

[23] Kotresh S., Ravikiran Y.T., Vijayakumari S.C., Raj Prakash H.G., Thomas S. Polyaniline niobiumpentoxide composite as humidity sensor at room temperature. *Adv. Mater. Lett.*, 2015, **6**, P. 641–645.

[24] Ba-Abbad M.M., Kadhum A.A.H., Abu B.M., Takriff M.S., Sopian K. Synthesis and catalytic activity of TiO_2 nanoparticles for photo-chemical oxidation of concentrated chlorophenols under direct solar radiation. *Int. J. Electrochem. Sci.*, 2012, **7**, P. 4871–4888.

[25] Quillard S., Louarn G., Lefrant S., MacDiarmid A.G. Vibrational analysis of polyaniline: A comparative study of leucoemeraldine, emeraldine, and pernigraniline bases. *Phys. Rev. B: Condens. Matter.*, 1994, **50**, P. 12496–12508.

[26] Wang P.C., Dan Y., Liu L.H. Effect of thermal treatment on conductometric response of hydrogen gas sensors integrated with HCl-doped Polyaniline nanofibers. *Mater. Chem. Phys.*, 2014, **144**, P. 155–161.

[27] Nasirian S., Moghaddam H.M. Hydrogen gas sensing based on polyaniline/anatase titania nanocomposite. *Int. J. Hydrogen Energ.*, 2014, **89**, P. 630–642.

[28] Ravikiran Y.T., Kotresh S., Vijayakumari S.C., Thomas S. Liquid petroleum gas sensing performance of polyaniline carboxymethyl cellulose composite at room temperature. *Curr. Appl. Phys.*, 2014, **14**, P. 960–964.

[29] Nasirin S., Moghaddam H.M. Effect of different titania phases on the hydrogen gas sensing features of polyaniline/TiO_2 nanocomposite. *Polymer*, 2014, **55**, P. 1866–1874.
[30] Li X., Chen W., Bian C., He J., Xu N., Xue G. Surface modification of TiO_2 nanoparticles by polyaniline. *Appl. Surf. Sci.*, 2003, **217**, P. 16–22.
[31] Patterson A.L. The scherror formula for x-ray particle size determination. *Phys. Rev. B*, 1939, **56**, P. 978–982.
[32] Marija B.R., Milica V.M., Dejan S.M., Edin H.S., Gordana N.C.M., Maja M.R., Zoran V.S. Influence of TiO_2 nanoparticles on formation mechanism of PANI/TiO_2 nanocomposite coating on PET fabric and its structural and electrical properties. *Surf. Coat. Technol.*, 2015, **278**, P. 38–47.
[33] Mendelson M.I. Average grain size in polycrystalline ceramics. *J. Am. Ceram. Soc.*, 1969, **52**, P. 443–446.
[34] Sen T., Shimpi N.G., Mishra S., Sharma R. Polyaniline/γ-Fe_2O_3 nanocomposite for room temperature LPG sensing. *Sens. Actuat. B*, 2014, **190**, P. 120–126.
[35] Lin W.D., Chang H.M., Wu R.J. Applied novel sensing material graphene/Polypyrrole for humidity sensor. *Sens. Actuat. B*, 2013, **181**, P. 326–331.
[36] Qi Q., Zhang T., Wang S., Zheng X. Humidity sensing properties of KCl-doped ZnO nanofibers with super-rapid response and recovery. *Sens. Actuat. B*, 2009, **137**, P. 649–655.
[37] Zhang Y., Zheng X., Zhang T., Gong L., Dai S., Chen Y. Humidity sensing properties of the sensor based on $Bi_{0.5}K_{0.5}TiO_3$ powder. *Sens. Actuat. B*, 2010, **147**, P. 180–184.

NANOSYSTEMS: PHYSICS, CHEMISTRY, MATHEMATICS, 2016, 7 (4), P. 740–746

Zinc oxide-palladium material an efficient solar-light driven photocatalyst for degradation of congo red

Karuppannan Rokesh[1], Kulandaivel Jeganathan[2], Kandasamy Jothivenkatachalam[1,*]

[1]Department of Chemistry, Anna University – BIT Campus, Tiruchirappalli–620024, Tamil Nadu, India

[2]Centre for Nanoscience and Nanotechnology, School of Physics, Bharathidasan University, Tiruchirappalli–620024, Tamil Nadu, India

*jothivenkat@yahoo.com

PACS 81.07.-b **DOI 10.17586/2220-8054-2016-7-4-740-746**

Zinc oxide - palladium nanocomposite material $(ZnO\text{-}Pd)_{NCM}$ was prepared and then characterized by UV-Vis spectroscopy, photoluminescence spectroscopy, X-ray diffraction analysis, energy dispersive X-ray analysis and field emission-scanning electron microscopy. The photocatalytic performance of $(ZnO\text{-}Pd)_{NCM}$ was investigated by degradation of Congo red under solar light irradiation. Zinc oxide modified with palladium metal could greatly enhance its photocatalytic activity and effectively degraded by Congo red dye.

Keywords: zinc oxide, palladium, nanocomposite, photocatalyst, congo red, degradation.

Received: 11 February 2016

Revised: 23 April 2016

1. Introduction

Dyes from textile industries strongly pollute water resources and produce serious environmental problems. Photocatalysis is an efficient technique to remove the dyes in waste water [1]. Nanostructured semiconductors and their composite materials have been preferred as catalyst (photocatalyst) for the photocatalysis process [2, 3]. Zinc oxide (ZnO) is a wide band gap (3.37 eV) semiconductor material; it is used as one of the efficient photocatalyst and photoelectrocatalyst [4–6]. This compound can be prepared by several techniques with collection of different morphologies and sizes. The nanostructured ZnO and ZnO–metal nanocomposite materials have been found huge attention in the field of photocatalysis [7–9], because of their high surface-volume ratio, stability and surface charge (SPR effect of metal nanoparticles). The metal support with ZnO to increase the photoexcited electrons-hole charge separation, transfer process and decreases the electron-hole recombination rate. Moreover, metal increases the adsorption of pollutant on catalyst surfaces afterwards improved its photocatalytic oxidation and reduction process [10, 11]. Once the ZnO-Pd nanocomposite material was prepared, it was characterized and its photocatalyic activity was investigated by degradation of Congo red dye under solar light.

2. Materials and methods

2.1. Materials

The materials such as zinc acetate dihydrate, palladium acetate, hydrazine hydrate and were obtained from Merck, and sodium borohydride, congo red were purchased from S. D. Chemicals, Mumbai.

2.2. Preparation of ZnO-Pd nanocomposite material

ZnO nanomaterial was prepared by simple microwave assisted technique. A 100 ml mixture of 0.05 M aq. zinc acetate and 0.2 M aq. Hydrazine hydrate was stirred for 30 min then subjected to microwave irradiation 15 min. The obtained white precipitate was washed, centrifuged and calcined at 200 °C for 2 hrs. Then, the prepared ZnO and palladium acetate precursor was added to an aqueous solution with 100:2.5 weight percentage and stirred for few hrs. Then, freshly prepared sodium borohydride solution was added to afford ZnO-Pd nanocomposite material.

2.3. Characterization

The prepared ZnO and $(ZnO\text{-}Pd)_{NCM}$ materials absorbance spectra were recorded using a Shimadzu UV-2550 UV-Vis spectrometer. Photoluminescence was recorded using JASCO-FP-6500 spectrofluorometer. The crystalline nature of prepared materials was studied by XRD pattern using a Bruker Advance with Cu Kα radiation. The morphology and elemental composition of the samples were recorded by Carl Zeiss FE-SEM and Bruker EDX instruments.

2.4. Photocatalytic study

The photocatalytic experiment was carried out by photodegradation of Congo red (CR) under solar light irradiation. A 20 mg of prepared ZnO and ZnO-Pd composites material was suspended into 50 ml of Congo red (CR) 25 ppm aq. solution. Then the dye solution was exposed to solar light irradiation in open air condition, time between 11 am to 2 pm with continuous aeration. Subsequently, at a given time interval 3 ml aliquots were collected and centrifuged. The degradation process was monitored and confirmed by UV-Vis absorbance spectroscopy by measuring its absorption.

3. Results and discussion

3.1. Optical property

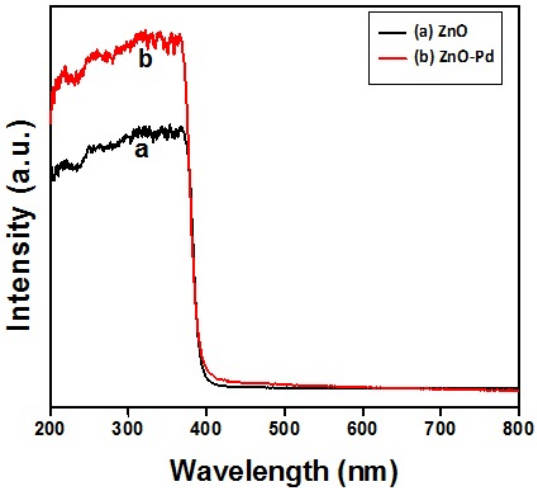

FIG. 1. UV-Diffuse reflectance spectra of (a) ZnO (b) $(ZnO\text{-}Pd)_{NCM}$

The UV-DRS measurement reveals that the band energy and optical properties of semiconductors materials. UV-DRS spectra of the ZnO and $(ZnO\text{-}Pd)_{NCM}$ samples were measured at room temperature and are shown in Fig. 1. The prepared ZnO and $(ZnO\text{-}Pd)_{NCM}$ showed strong absorption below 400 nm in near-UV spectral region, confirming the wide band of ZnO semiconductor material. The $(ZnO\text{-}Pd)_{NCM}$ does not show any absorption in the visible region due the particle size and amount of Pd in the composite is much less. Moreover, the $(ZnO\text{-}Pd)_{NCM}$ have existed higher absorbance intensity than bare ZnO in UV region, which indicates that the Pd improves the quantum efficiency of the ZnO material [12].

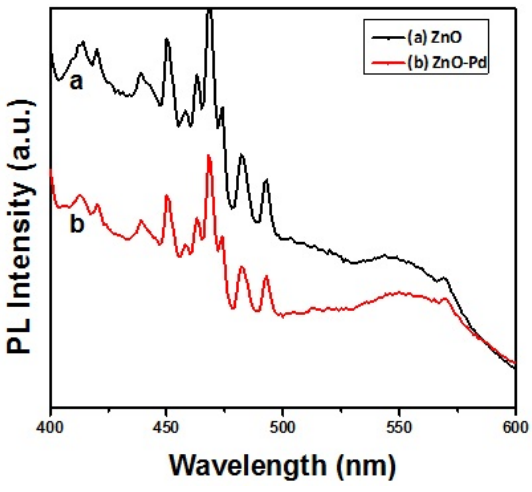

FIG. 2. Photoluminescence spectra (a) ZnO (b) $(ZnO\text{-}Pd)_{NCM}$

The PL spectra showed wide band emission at visible region (Fig. 2). This extended emission is due to the recombination of photogenerated electron-hole and oxygen vacancy sites in the materials. The ZnO and (ZnO-Pd)$_{NCM}$ where observed weak emission at 468 nm due to band edge free excitons. The blue and green emission peaks were observed around 520–580 nm for the prepared samples due to presence of oxygen vacancies in the material's surface [13]. The emission intensity of ZnO decreased with the addition of palladium metal because of the Pd trapped excited electrons from the zinc oxide.

3.2. Crystalline properties

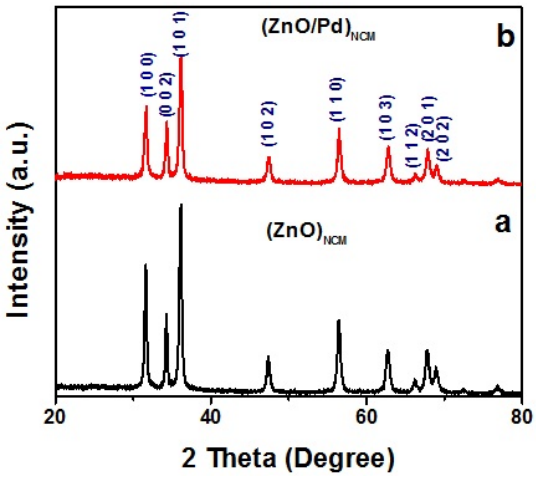

FIG. 3. XRD pattern of (a) ZnO and (b) (ZnO-Pd)$_{NCM}$

The XRD pattern of ZnO and (ZnO-Pd)$_{NCM}$ composite material is shown in Fig. 3. All the diffraction peaks in XRD are confirmed that the prepared ZnO in hexagonal wurtzite structure (JCPDS No. 36-1451). The diffraction peaks of palladium was not observed in (ZnO-Pd)$_{NCM}$ due to the very minimum percentage of Pd present in the composite [13, 14]. The absence of any other peak in XRD is confirmed that the prepared materials are highly pure.

3.3. Morphology and elemental analysis

The morphology and elemental composition of synthesized materials were studied by FE-SEM and EDX analysis is shown in Fig. 4. The synthesized ZnO and ZnO-Pd composite material displays flower buds-like morphology with average size about 1 to 2 μm (Fig. 4(a,c)). The spherical like Pd nanoparticles are deposited on ZnO surface can be confirmed by FE-SEM image. The ZnO buds have exhibited rough surface which formed by the agglomeration of small nanoparticles. EDX analysis provided the elemental composition of the materials is shown in Fig. 4(b,d). In Fig. 4(d) the spectrum confirms that the Zn, O and Pd elements are present in the composite material, as evidence for formation of (ZnO-Pd)$_{NCM}$. The absence of any other elemental peaks in EDX spectrum confirmed that the as-synthesized materials were very pure.

3.4. Photocatalytic study

The photocatalytic experiment was carried out by photodegradation of Congo red (CR) under solar light irradiation. The effect of different parameters such as catalyst loading, solution pH and dye concentration on photodegradation efficiency were evaluated using ZnO and (ZnO-Pd)$_{NCM}$ [15, 16].

The experiment was carried out by 25 ppm (mg/l) of CR in aqueous solution in the presence of 20 mg/50 ml of ZnO and (ZnO-Pd)$_{NCM}$ photocatalysts. The percentage of degradation was significantly increased for the zinc oxide - palladium nanocomposite and nearly attained maximum degradation efficiency of 100 % in 3 hrs under solar irradiation. The result displays that the photocatalytic activities of (ZnO-Pd)$_{NCM}$ are higher than that of ZnO, shown in Fig. 5. Because the palladium metal acts as electron sink, it therefore enhanced the electron-hole charge separation and reduced the charge recombination process. This process promotes the hydroxide radical and superoxide radical generation [12, 13, 16]. These generated active radicals are the effective degradation agents for the CR dye molecules.

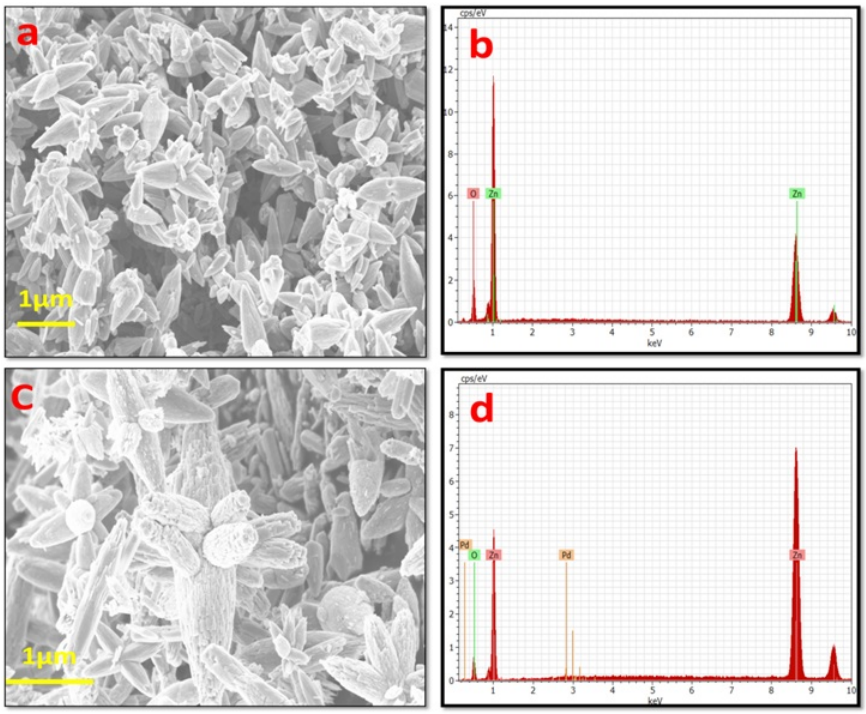

FIG. 4. FE-SEM and EDX spectrum of ZnO (a,b) and $(ZnO\text{-}Pd)_{NCM}$ (c,d)

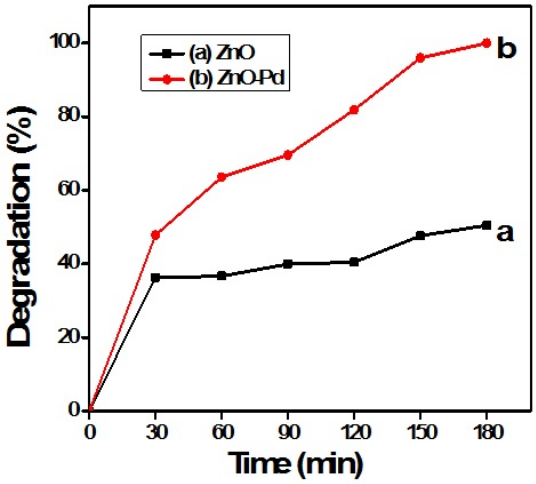

FIG. 5. The photocatalytic degradation of congo red (25 ppm) using (a) ZnO and $(ZnO\text{-}Pd)_{NCM}$ using 20 mg/50 ml

3.4.1. Effect of the catalyst loading. This experiment was carried out using different amounts of $(ZnO\text{-}Pd)_{NCM}$ (5 to 40 mg/50 ml) catalyst and dye concentration 25 ppm. In Fig. 6, the results showed that the photodegradation efficiency was increased with increasing amounts of catalyst and the maximum efficiency was observed at 20–40 mg of catalyst loading In this case, 20 mg/50 ml catalyst amount was found to have the highest photodegradation efficiency with lower catalyst loading and it's also consider as the optimum amount of catalyst. In general, the amount of catalyst is proportional to the generation of number of active radical such as OH and $O2^-$ which rapidly degrade the adsorbed dye molecules. A catalyst at higher loading increases the total active sites of the catalyst but dye molecules is constant at fixed concentration. Hence, the optimum amount of catalyst is enough for the efficient degradation of CR at above optimum concentration [17, 18].

3.4.2. Influence of pH. The influence of initial dye pH value on the degradation efficiency of CR was investigated is shown in Fig. 7. The pH of dye solution was adjusted using dilute sulfuric acid or dilute sodium hydroxide.

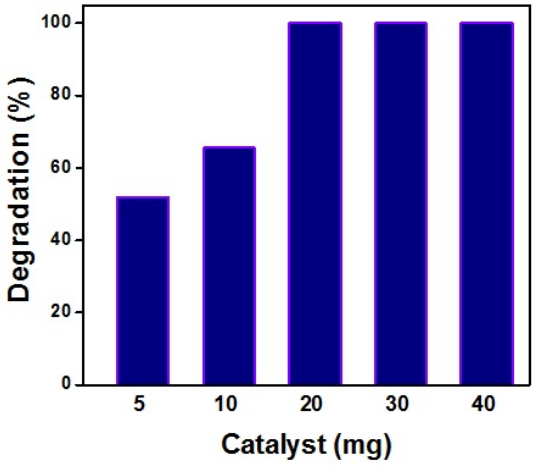

FIG. 6. Photocatalytic degradation of of congo red (25 ppm) using $(ZnO\text{-}Pd)_{NCM}$ with different amount of catalyst

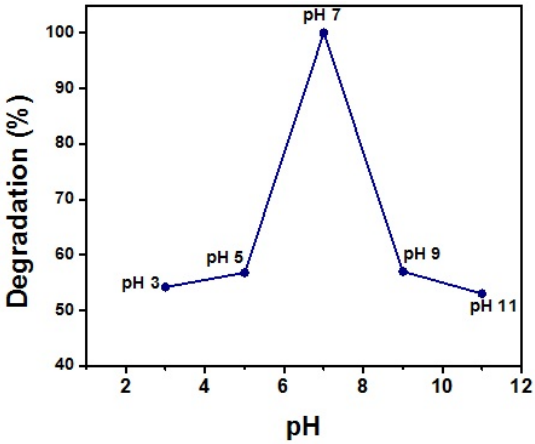

FIG. 7. Effect of dye solution pH on the photocatalytic degradation of congo red (25 ppm) using $(ZnO\text{-}Pd)_{NCM}$ 20 mg/50 ml

The result showed that the higher degradation efficiency was observed at neutral pH (pH 7). On the other hand, the degradation efficiency decreased at both acidic and basic pH. From that result the photocatalytic degradation of CR is favorable at neutral pH in presence of $(ZnO\text{-}Pd)_{NCM}$ [17–19].

3.4.3. Effect of the initial dye concentration. The effect of initial concentration of CR dye on photodegradation activity was studied by varying the CR dye concentration from to 10 to 40 ppm (Fig. 8). The degradation efficiency of Congo red was high with increased dye concentration up to 25 ppm, however, after that, the degradation efficiency was decreased. This may be due to competition of adsorption between dye molecules and catalyst surface. At higher dye concentrations, the number of dye molecules is high, but the available active sites on the catalyst surface are constant, hence the fixed catalyst amount occupies a fixed number of active sites. Hence, it is possible to have a constant amount of dye molecule adsorption and degradation and it is not enough to degrade a large number of dye molecules (higher concentration) [16–19].

3.4.4. Photocatalytic mechanism. Photocatalytic mechanism of ZnO-Pd nanocomposite for degradation of Congo red is shown in Fig. 9. When sunlight is exposed to the ZnO-Pd nanocomposite, it undergoes photoexcitation followed by electron movement to the conduction band (CB) and the holes are generated in the valence band (VB) of ZnO. The photoinduced holes are captured by surrounding water molecules, producing hydroxyl radicals (OH). Then, the photoinduced electrons can be trapped by oxygen molecules on the catalyst surface and formed superoxide radicals ($O2^{-}$). Afterward, the generated free radicals effectively degraded the CR dye molecules in aqueous solution. Moreover, the electron-hole can be recombining together during the light irradiation and this process is effectively prevented by palladium metal on zinc oxide's surface. At the time, the metal nanoparticle

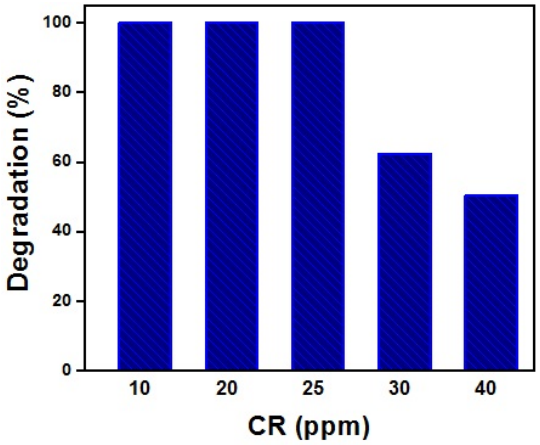

FIG. 8. Effect of initial congo red concentration on the photocatalytic degradation of congo red using $(ZnO\text{-}Pd)_{NCM}$ 20 mg/50 ml

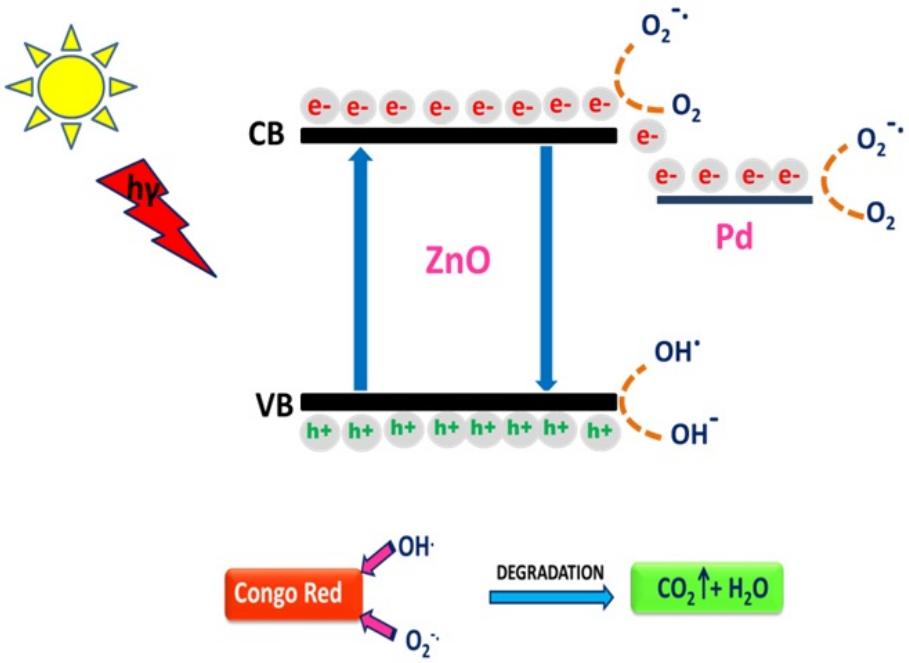

FIG. 9. Photocatalytic mechanism for ZnO-Pd nanocomposite-catalyzed degradation of Congo red

traps the surface electron from conduction band of ZnO and transfers it to oxygen molecules adsorbed on the catalyst surface [12, 13, 20].

4. Conclusion

ZnO and ZnO-Pd nanocomposite materials have been successfully synthesized and characterized by UV-DRS, PL, XRD, EDX and FE-SEM. The UV-DRS displayed the optical properties and PL spectra explained the photochemical charge separation and transfer properties of the materials. The XRD pattern confirmed crystalline nature and EDX analysis confirmed the elemental composition of the materials. The FE-SEM showed the surface morphology of ZnO and ZnO-Pd nanocomposite materials. The photocatalytic activity of $(ZnO\text{-}Pd)_{NCM}$ was investigated by the decomposition of Congo red under solar light irradiation. The zinc oxide-palladium nanocomposite material exhibited efficient photocatalytic activity due to synergic effect of palladium and promote the photocatalytic degradation of Congo red.

References

[1] Paola A.D., Lopez E.G., Marci G., Palmisano L. A survey of photocatalytic materials for environmental remediation. *J. Hazard. Mater.*, 2012, **3-29**, P. 211–212.

[2] Hu X., Li G., Yu J.C. Design, fabrication, and modification of nanostructured semiconductor materials for environmental and energy application. *Langmuir*, 2010, **26**(5), P. 3031–3039.

[3] Tong H., Ouyang S., Bi Y., Umezawa N., Oshikiri M., Ye J. Nano-photocatalytic materials: possibilities and challenges. *Adv. Mater.*, 2012, **24**, P. 229–251.

[4] Ahmad M., Zhu J. ZnO based advanced functional nanostructures: synthesis, properties and applications. *J. Mater. Chem.*, 2011, **21**, P. 599–614.

[5] Nithya A., Jothivenkatachalam K. Chitosan assisted synthesis of ZnO nanoparticles: an efficient solar light driven photocatalyst and evaluation of antibacterial activity. *J. Mater. Sci.–Mater. Electron.*, 2015, **26**(12), P. 10207–10216.

[6] Rokesh K., Pandikumar A., Chandra Mohan S., Jothivenkatachalam K. Aminosilicate sol-gel supported zinc oxide-silver nanocomposite material for photoelectrocatalytic oxidation of methanol. *J. Alloys Compd.*, 201; DOI: 10.1016/j.jallcom.2016.04.089.

[7] Ansari S.A., Khan M.M., Ansari M.O., Lee J., Cho M.H. Biogenic synthesis, photocatalytic, and photoelectrochemical performance of Ag-ZnO nanocomposite. *J. Phys. Chem. C*, 2013, **117**(51), P. 27023–27030.

[8] Li P., Wei Z., Wu T., Peng Q., Li Y. Au-ZnO hybrid nanopyramids and their photocatalytic properties. *J. Am. Chem. Soc.*, 2011, **133**, P. 5660–5663.

[9] Zong Y., Li Z., Wang X., Ma J., Men Y. Synthesis and high photocatalytic activity of Eu-doped ZnO nanoparticles. *Ceram. Int.*, 2014, **40**, P. 10375–10382.

[10] Xie W., Li Y., Sun W., Huang J., Xie H., Zhao X. Surface modification of ZnO with Ag improves its photocatalytic efficiency and photostability. *J. Photochem. Photobiol. A*, 2010, **216**, P. 149–155.

[11] Georgekutty R., Seery M.K., Pillai S.C. A highly efficient Ag-ZnO photocatalyst: synthesis, properties, and mechanism. *J. Phys. Chem. C*, 2008, **112**, P. 13563–13570.

[12] Chang Y., Xu J., Zhang Y., Ma S., Xin L., Zhu L., Xu C. Optical properties and photocatalytic performances of Pd modified ZnO samples. *J. Phys. Chem. C*, 2009, **113**, P. 18761–18767.

[13] Zhang Y., Wang Q., Xu J., Ma S. Synthesis of Pd/ZnO nanocomposites with high photocatalytic performance by a solvothermal method. *Appl. Surf. Sci*., 2012, **258**(24), P. 10104–10109.

[14] Zeng Y., Lou Z., Wang L., Zou B., Zhang T., Zheng W., Zou G. Enhanced ammonia sensing performances of Pd-sensitized flowerlike ZnO nanostructure. *Sens. Actuators, B,* 2011, **156**, P. 395–400.

[15] Zhong J.B., Li J.Z., He X.Y., Zeng J., Lu Y., Hu W., Lin K. Improved photocatalytic performance of Pd-doped ZnO. *Curr. Appl. Phys.*, 2012, **12**, P. 998–1001.

[16] Erdemoglu S., Aksu S.K., Sayılkan F., Izgi B., Asilturk M., Sayılkan H., Frimmel F., Guçer S. Photocatalytic degradation of congo red by hydrothermally synthesized nanocrystalline TiO_2 and identification of degradation products by LC-MS. *J. Hazard. Mater.*, 2008, **155**, P. 469–476.

[17] Jothivenkatachalam K., Prabhu S., Chandra Mohan S., Jeganathan K. Solar, visible and UV light photocatalytic activity of $CoWO_4$ for the decolourization of methyl orange. *Desalin. Water Treat.*, 2014, P. 1–12, DOI: 10.1080/19443994.2014.906324.

[18] Jothivenkatachalam K., Prabhu S., Nithya A., Jeganathan K. Facile synthesis of WO_3 with reduced particle size on zeolite-Y and enhanced photocatalytic activity. *RSC Adv.*, 2014, **4**, P. 21221–21229.

[19] Subash B., Krishnakumar B., Swaminathan M., Shanthi M. Highly active Zr co-doped Ag-ZnO photocatalyst for the mineralization of acid black 1 under UV-A light illumination. *Mater. Chem. Phys.*, 2013, **141**, P. 114–120.

[20] Khalil A., Gondal M.A., Dastageer M.A. Augmented photocatalytic activity of palladium incorporated ZnO nanoparticles in the disinfection of Escherichia coli microorganism from water. *Appl. Catal. A*, 2011, **402**, P. 162–167.

NANOSYSTEMS: PHYSICS, CHEMISTRY, MATHEMATICS, 2016, 7 (4), P. 747–751

Electrochemical synthesis of p-type copper oxides

C. V. Niveditha, M. J. JabeenFatima, S. Sindhu*

Department of Nanoscience and Technology, University of Calicut, Kerala–673635, India

*sindhu.swaminath@gmail.com

PACS 82.45. Aa, 81.07.-b, 87.80Kc, 82.45Yz **DOI 10.17586/2220-8054-2016-7-4-747-751**

Copper oxide is a narrow band gap, low cost, nontoxic, photoactive metal oxide and can be considered as the best candidate for photo-electrochemical applications. Thin films of p-type copper oxide are prepared by cyclic voltammetric technique. The electrochemical method is a cost effective low temperature technique for the preparation of functional thin films. Tools like, GIXRD, Raman Spectroscopy, UV-Vis Spectroscopy, PL, SEM and EIS analysis are done to study the structure, phase, optical, morphological and electrochemical behavior of the copper oxide thin film. The effect of deposition conditions on the electrical and optical properties of the thin films are analyzed in detail.

Keywords: cyclic voltammetry, electrochemical impedance analysis.

Received: 14 February 2016

Revised: 26 April 2016

1. Introduction

Copper oxide is a low cost, non-toxic, narrow band gap metal oxide [1]. Oxides of copper crystallize mainly in two forms, cuprous oxide (Cu_2O) and cupric oxide (CuO) [1, 2]. Cuprous oxide is a direct bandgap [1] and cupric oxide is an indirect band gap [1] metal oxide. These metal oxides exhibit interesting properties suitable for catalytic [3], electrochromic [4], electrochemical [4], photoelectrochemical [5] and photovoltaic applications [4]. Due to the narrow band gap (Cu_2O – 1.9–2.2 eV and for CuO is 1.2–1.7 eV) it has high potential in photovoltaic and photoelectrochemical applications. Commonly, copper oxide films have been synthesized by the high temperature thermal oxidation of copper metal [6] that limits the control over the interfacial features like surface area, particle size, and grain boundaries etc, which affect the optical and electrochemical properties. Hence, the present study focus on electrodeposition method [7] which is an attractive method for thin film synthesis under low temperature conditions. The efficiency of electronic and charge transfer mechanism between the nanoparticles or the nanoparticles and the adjacent layer depends highly on the shape and size of the particles participating in the process. This highlights the significance of deposition of size and shape controlled nanostructures by electrochemical deposition.

2. Experimental method

Electrodeposition of copper oxide is done using three electrode system, where cleaned FTO is used as the working electrode, platinum wire as counter electrode and Ag/AgCl as reference electrode. The Cu_2O is deposited on the FTO substrate under neutral pH the potential is swept between 0 V to -0.8 V from the solution containing 5 mM $CuSO_4$ and 50 mM KNO_3 and repeat the cycles three times to get a yellow colored film. The CuO is deposited from solution containing 5 mM $CuSO_4$ and 50 mM KNO_3 under acidic (2.5 mM H_2SO_4) pH the potential is swept between 0 V to -0.8 V and repeat the cycles three times to obtain a black colored film. Fig. 1 shows the photographs of the obtained yellow and black films of copper oxides.

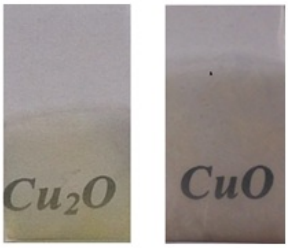

FIG. 1. Photographs of Cu_2O and CuO films

3. Result and discussion

3.1. Cyclic voltammetry

Figure 2 depicts the cyclic voltammogram for the electrodeposition of both Cu_2O and CuO. Cu_2O formed under neutral pH. In Fig. 2(a), the peak at -0.21 V shows the film formation and there are two peaks at Fig. 2(b) shows the conversion of Cu^{2+} ion from Cu^{+}ion i.e, the formation of CuO. The Cu^{2+} ion accepts an electron from the electrode and becomes a Cu^{+} ion to attain a stable electronic configuration. The positive nature of the metal ion helps, forming weak Van der Waals interactions with the non-bonded electrons of oxygen atom of the water and the adsorbed Cu-H_2O complex on FTO substrate is neutralized by releasing H^{+} ion, which resulted in the deposition of Cu_2O. An increase in cathodic current is found near a cathodic potential of -0.21 V, indicating the deposition of Cu_2O film. When the cycle is repeated, the deposition current diminishes with an increase in film coverage on the substrate, since Cu_2O is less conducting than FTO. But at acidic pH, the H^{+} ion from H_3O^{+} ion complex reduced by accepting electron from Cu^{+} ion, leads to the formation of Cu^{2+} ion which is the then converted into CuO.

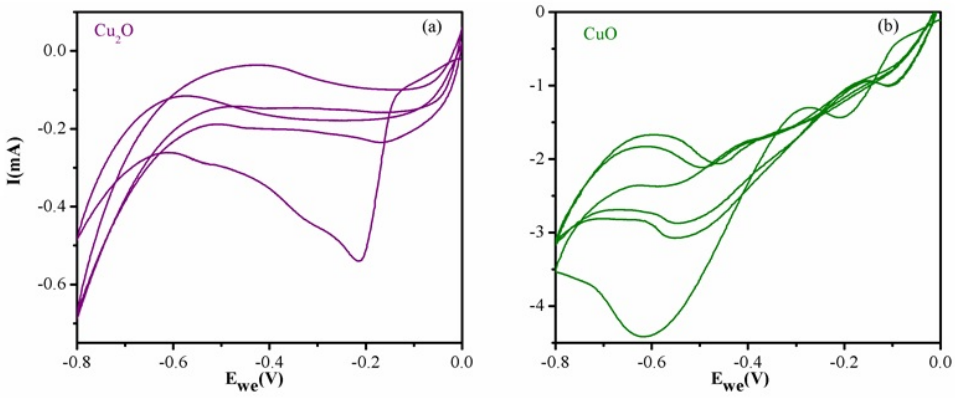

FIG. 2. Cyclic voltammogram of electrodeposition of (a) Cu_2O and (b) CuO

3.2. Structural analysis

The crystallinity of the deposited films was analyzed using a grazing angle X-ray diffraction (GIXRD). Fig. 3 depicts the XRD spectra of the deposited films and is compared with standard JCPDS files 78-2076, 80-1917, which correspond to cubic and monoclinic crystal structures respectively for cuprous and cupric oxide of space groups Pn3m and C1c1. In cubic Cu_2O, the copper atoms are at fcc sub lattices and oxygen atoms are at bcc sub lattices [8]. In the case of monoclinic CuO, the copper atom is coordinated by four oxygen atoms in an approximately square planar configuration and the oxygen is coordinated to four copper atoms at the corners of a distorted tetrahedron [9].

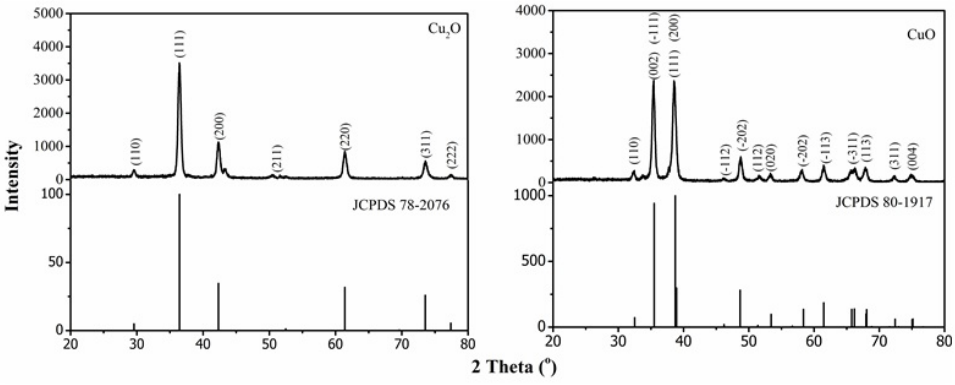

FIG. 3. XRD spectra of Cu_2O and CuO films compared with standard JCPDS

3.3. Morphology

The morphology of the film obtained from SEM analysis. Fig. 4 depicts the average size of Cu_2O is 75 nm and that of CuO is 93 nm. The morphology of Cu_2O is square in shape, while that of CuO is spherical shape.

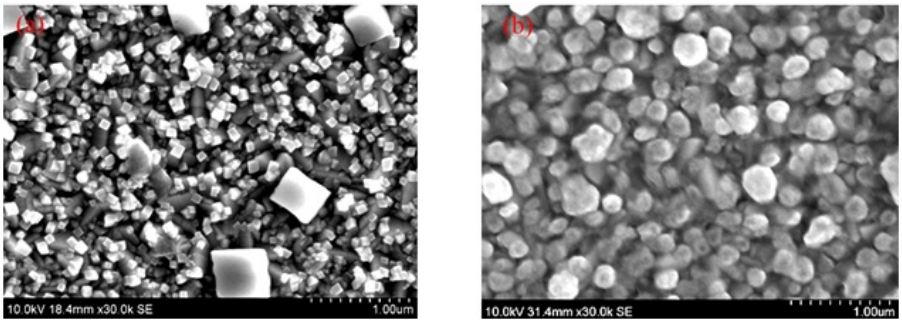

FIG. 4. SEM image of Cu_2O and CuO films

3.4. Optical properties

Optical properties of the films were analyzed by using UV-Visible spectroscopy. The absorption spectra and Tauc plots for Cu_2O and CuO are shown in Fig. 5. The band gap is estimated from the Tauc plot and the obtained values are 2.43 eV and 1.73 eV respectively for Cu_2O and CuO. The PL spectra give idea about the defect state. Fig. 6 depicts three peaks in the PL spectra corresponding to band edge emission, oxygen ion vacancy and copper ion vacancy [10]. The band edge emission is slightly red shifted (562 nm) in the case of cupric oxide than cuprous oxide (527 nm). All the defect emissions are also red shifted. The p-type nature of the films is due to the presence of copper ion vacancies.

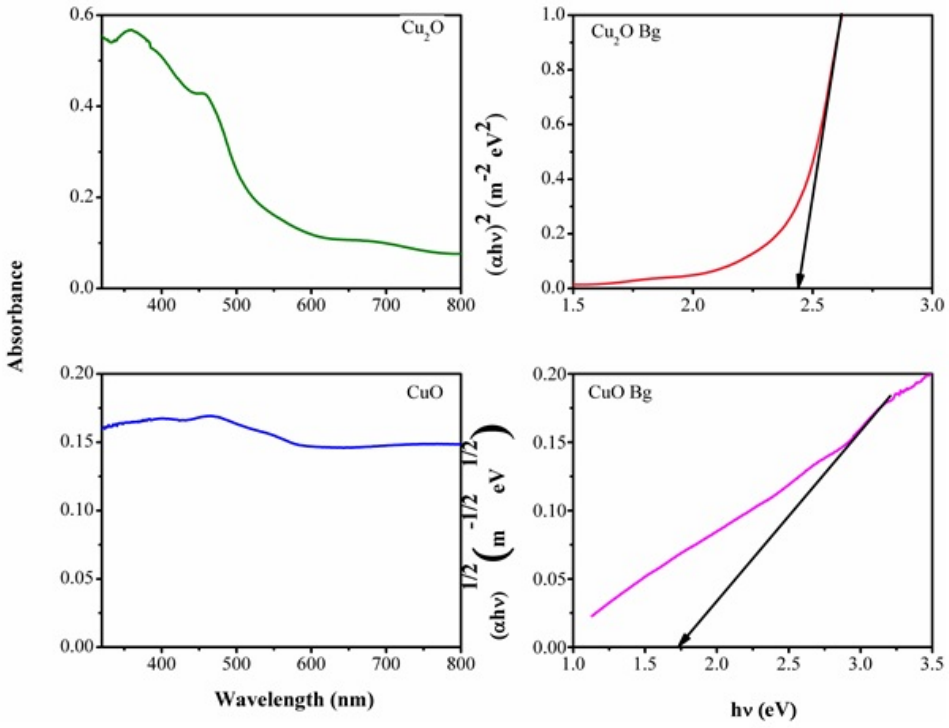

FIG. 5. UV-Visible spectra and Tauc plot of Cu_2O and CuO films

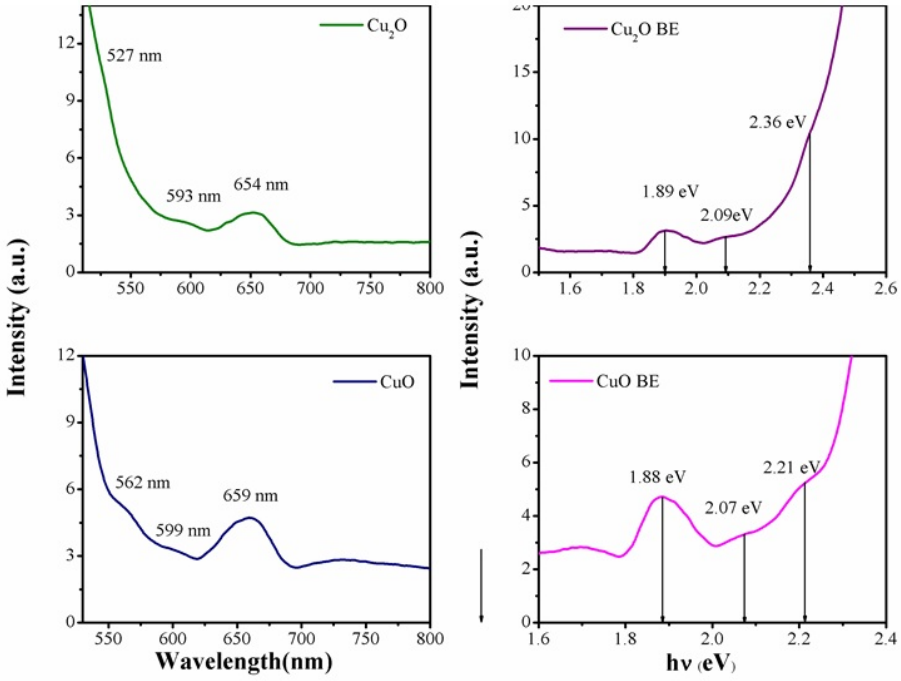

FIG. 6. PL spectra of Cu_2O and CuO films

3.5. Electrical properties

The electronic properties of the films are studied using hall measurement system. From this measurement both Cu_2O and CuO are p-type semiconductors with conductivity of 4.71×10^2 Scm^{-1} and 4.12×10^3 Scm^{-1} respectively. Fig. 7. depicts the Nyquist plots obtained from electrochemical impedance (EIS) analysis of copper oxides, which measure the interfacial resistance between the electrode and electrolyte in the dark and light condition. This analysis confirms the photo activity of copper oxide. Cu_2O is more photoactive than CuO.

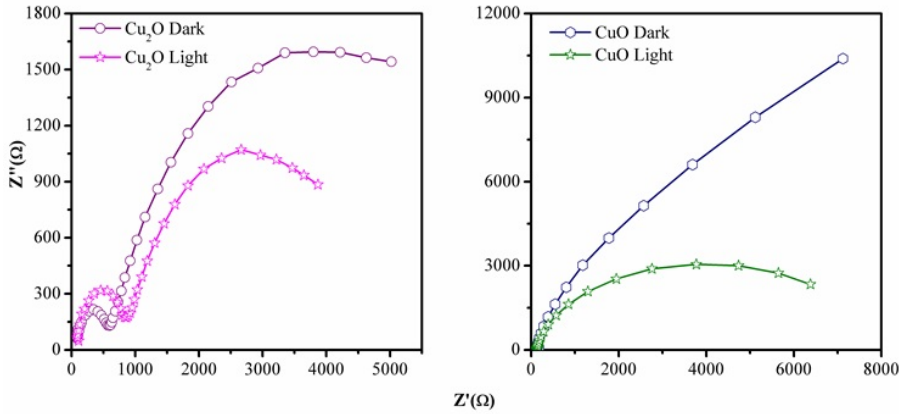

FIG. 7. Nyquist plots of electrodeposited Cu_2O and CuO films

The efficiency of the cell was obtained from chronoamperometric analysis in 0.1 M Na_2SO_4 electrolyte by using three electrode system where deposited film was a working electrode, Pt wire was a working electrode and Ag/AgCl was the reference electrode. The efficiency is calculated from equation 1, where η is the efficiency of the cell, I is the steady current density obtained from I-t curves (shown in Fig. 8), V is the applied potential -0.2 V and J_{Light} is the irradiance intensity of 100 mW/cm^2. The efficiencies obtained for Cu_2O and CuO were 0.5 % and 0.2 % respectively.

$$\eta = \frac{I(1.23 - V)}{J_{Light} \cdot 100}. \tag{1}$$

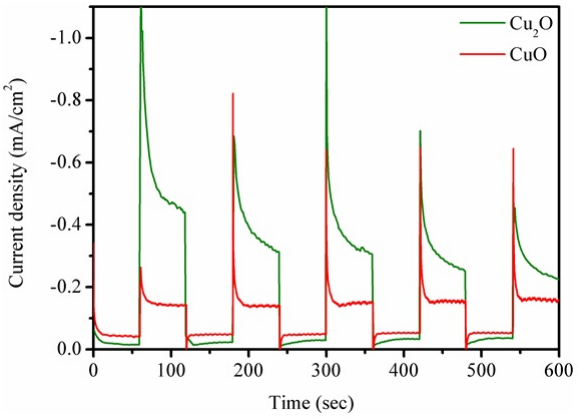

FIG. 8. Chronoamperometric spectra of electrodeposited Cu_2O and CuO films

4. Conclusion

Cyclic voltammetric deposition techniques were utilized to synthesize p-type copper oxides at potentials ranging from 0 V to −0.8 V at a scan rate of 20 mV/s. Cu_2O is formed under neutral pH and CuO is formed at lower pH values. The band gaps of both copper oxides are narrow ie; 2.43 eV and 1.73 eV for Cu_2O and CuO respectively. The p-type nature is confirmed from Hall measurement system. Both are p-type copper oxides. The electrochemical impedance analysis shows that the cuprous oxide thin films are more photoactive than cupric oxide, which was confirmed through chronoamperometric analysis. The efficiencies of Cu_2O and CuO were 0.5 % and 0.2 % respectively.

Acknowledgement

Authors Niveditha C.V. and Jabeen Fatima acknowledge CSIR for financial assistant in the form of Senior Research Fellowship. Sindhu S acknowledges Kerala State Council for Science Technology and Environment (KSCSTE), Govt. of Kerala, and Council of Scientific and Industrial Research (CSIR), Govt. of India for financial assistance. Support obtained from Satyabhama University, Chennai and NIT Calicut for GIXRD and SEM analysis are greatly acknowledged.

References

[1] Kari E.R.B., Kyoung-Shin C. Electrochemical synthesis and characterization of transparent nanocrystalline Cu_2O films and their conversion to CuO films. *ChemComm*, 2006, P. 3311–3313.
[2] Samarasekara P. Characterization of low cost p-Cu_2O/n-CuO junction, *GESJ.: Physics*, 2010, **2**(4), ISSN-1512-1461.
[3] Yongqian W., et al. Controllable fabrication nanostructured copper compound on Cu substrate by one-step route. *RSC.Adv.*, 2015, P. 1–17.
[4] Ahmad S.Z., et al. Nanostructured copper oxide semiconductor: a perspective on materials, synthesis method and applications. *J. Mater. Chem. C.*, 2014, **2**, P. 5247.
[5] Chia-Yu L., et al. Cu_2O/NiO_x nanocomposite as an inexpensive photocathode in photoelectrochemical water splitting. *Chem. Sci.*, 2012.
[6] Kasim U.I., et al. Effect of oxidation temperature on the properties of copper oxide thin films prepared from thermally oxidised evaporated copper thin films. *IOSR-JAP*, 2013, **3**, P. 61–66.
[7] Rachel O., Usha R., Sajeeviraja. Characteristics of electron beam evaporated and electrodeposited Cu_2O thin films-comparative study. *Int. J. Electrochem. Sci.*, 2012, **7**, P. 8288–8298.
[8] Reimann K., Syassen K. Raman Scattering and Photoluminescence in Cu_2O under Hydrostatic Pressure. *Phys. Rev. B*, 1989, **39**, P. 11113–11119.
[9] Ahmad S.Z., Rozina A.R., Anthony J.M., Anthony P.O., Kourosh K. Nanostructured Copper Oxide Semiconductors: A Perspective on Materials, Synthesis Methods and Application. *J. Mater. Chem. C*, 2014, **2**, P. 5247–5270.
[10] Jiji K., Soosen S.M., Anoop C., George K.C. Optical Properties of CuO Nanoparticles. *AIP Conf. Proc.*, 2011, **1391**, P. 576–578.

NANOSYSTEMS: PHYSICS, CHEMISTRY, MATHEMATICS, 2016, 7 (4), P. 752–754

Application of gel electrolyte in dye sensitized solar cells

P. Nijisha, N. M. Bhabhina, S. Sindhu*

Department of Nanoscience and Technology, University of Calicut, Kerala–673635, India

nijisha31@gmail.com, bhabhinanm@gmail.com, *sindhu.swaminath@gmail.com

PACS 88.40.fh, 88.40.H, 88.40.hj, 88.40.J **DOI 10.17586/2220-8054-2016-7-4-752-754**

The volatility of liquid electrolytes has been a major problem for their application in dye-sensitized solar cells (DSSC). In this study, liquid electrolyte was replaced by polymer based gel electrolyte. Polyvinyl alcohol is chosen as the polymeric matrix to gelate the liquid electrolyte with iodide-triiodide redox couple and suitable organic solvent. The amorphous nature and the physical cross linking formed between polymer-polymer and polymer-solvent is analyzed from XRD and FT-IR. Cell was fabricated and characterization was done. I-V and EIS measurements of the cell was taken. Easy fabrication and its advantages over liquid electrolyte makes gel electrolyte a promising alternative for liquid electrolyte.

Keywords: dye sensitized solar cells, quasi solid state dye sensitized solar cells, gel electrolyte.

Received: 14 February 2016. Revised: 26 April 2016.

1. Introduction

DSSC have received great attention owing to their low production costs and high efficiencies [1, 2]. The certified record efficiency of DSSC is 12–13 %. A DSSC consists of a photo anode, a semiconductor film coated on a transparent conducting oxide layer, which is dye sensitized, a counter electrode, usually FTO coated with a catalytic material and electrolyte which includes a redox couple usually I^- /I_3^- system and a suitable solvent. In DSSC, the electrolyte is the medium for charge transportation between the two electrodes and acts as a source for dye regeneration [3]. The long term stability of the device strongly depends on the electrolyte component [4]. The highest efficiency reported in DSSC was by employing liquid electrolyte. But there are some practical impediments when using this liquid electrolyte like leakage while sealing and volatilization of the solvent, desorption and photo-degradation of the attached dye, corrosion of the counter electrode etc., which prevent DSSC's from further application and commercialization [4, 5]. So, as an alternative to liquid electrolyte, solid state electrolytes and quasi solid state electrolytes (gel electrolytes) were introduced. Though solid state electrolytes seem to be an ideal material for DSSC, the efficiency was not up to expectations [6]. This might be due to poor interfacial contact and poor charge carrier mobility. When coming to gel electrolyte, all the problems related to liquid and solid state electrolyte can be resolved. It remains as quasi solid at room temperature and as a highly viscous liquid at high temperatures. Thus, a gel electrolyte possesses both the cohesive property of solid as well as diffusive transport property of liquid [7]. In the present work a polymer-based gel electrolyte is synthesized and its behavior in the performance of dye sensitized solar cell is studied by using two different photoanode materials – TiO_2 and ZnO.

2. Experimental

2.1. Materials

Fluorine doped tin oxide (FTO-7Ω/Sq.), N719 ($Ru(dcbpy)_2(NCS)_2$) -95%), Hexachloroplatinic acid (H_2PtCl_6), Potassium iodide (KI) (bio ultra, 99.5 %), Polyvinyl alcohol (PVA, 99 % hydrolyzed) were purchased from Sigma-Aldrich. Dimethyl sulfoxide (DMSO) and Iodine (I_2) is supplied by MERCK.

2.2. Gel electrolyte synthesis

Polyvinyl alcohol is used as the polymeric matrix. Gel electrolyte is prepared by adding adequate amount of polymer, KI and I_2 to dimethyl sulfoxide. The resulting mixture is heated to 2 hrs and stirred continuously to obtain the gel.

2.3. Assembling of quasi solid state dye sensitized solar cell

The nanocrystalline TiO_2 photo anode was fabricated by doctor blading TiO_2 paste on FTO substrate. The film was air dried and sintered at 450°C for 30 mins. The sintered sample was then cooled to room temperature and was dipped in the dye solution for 24 hrs. The dye loaded sample was then air dried and sealed. The counter electrode was made by electrodepositing Pt on FTO surface. The two electrodes were then kept face to face with gel electrolyte in between to obtain a sandwich structure and is then clamped tightly.

3. Results and discussion

3.1. Gel characterization

Figure 1 shows the FT-IR of pure PVA and PVA based gel electrolyte. The presence of broad band at 3416 shows the inter-molecular hydrogen bonding. In PVA-G, the intensity of the band was found to increase, and this is because of extensive hydrogen bonding between the polymeric chains due to its complete expansion. The band at 2914 cm^{-1} shows the –CH- stretching vibration. The band at 1654 cm^{-1} is for terminal vinyl group. Bands at 1783 cm^{-1} and 1806 cm^{-1} correspond to the ester group present. The 1315 cm^{-1} and 1434 cm^{-1} bands correspond to S-O stretching, while those at 1024 cm^{-1}, 1083 cm^{-1}, 1186 cm^{-1} show the C-O vibration of PVA.

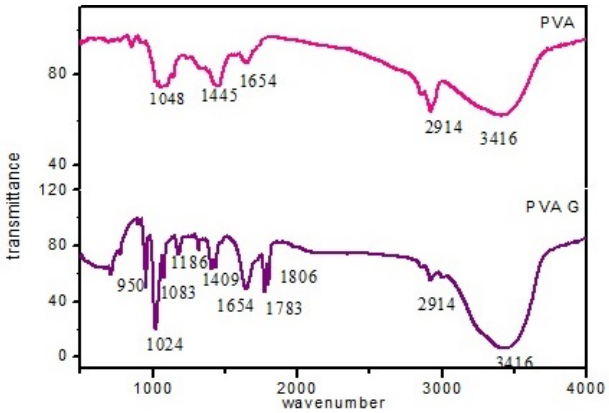

FIG. 1. FT-IR spectra of pure PVA and PVA gel electrolyte

The XRD spectra of gel electrolyte, pure PVA, KI, and I $_2$ are shown in figure 2. Diffraction peak at 2θ – 40.76 is ascribed to pure PVA. Diffraction peak at 2θ – 21.67, 30.80, 54.98 and 24.62, 25.07, 29.04 is for pure KI and I_2 respectively, shows the crystalline nature of the ionic salt. An amorphous peak is observed for polymer gel electrolyte, which shows the complete dissolution of the ionic salt and also increased liquid electrolyte uptake by the matrix.

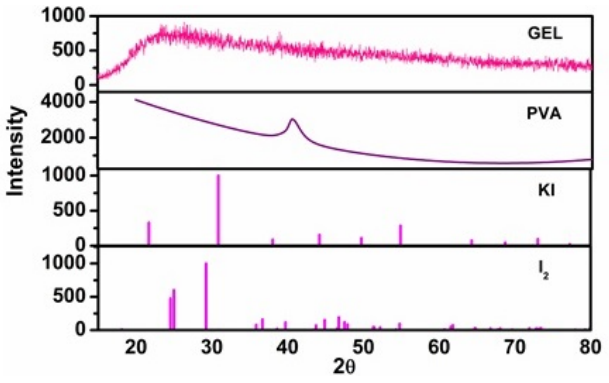

FIG. 2. XRD of pure I_2, KI, PVA and polymer gel electrolyte

3.2. Cell characterization

The current-voltage characteristics and Nyquist plot of the DSSCs based on polymer gel electrolyte were performed with two different photoanode semiconductor materials-TiO_2 and ZnO. The table below summarizes the best values of their photovoltaic parameters.

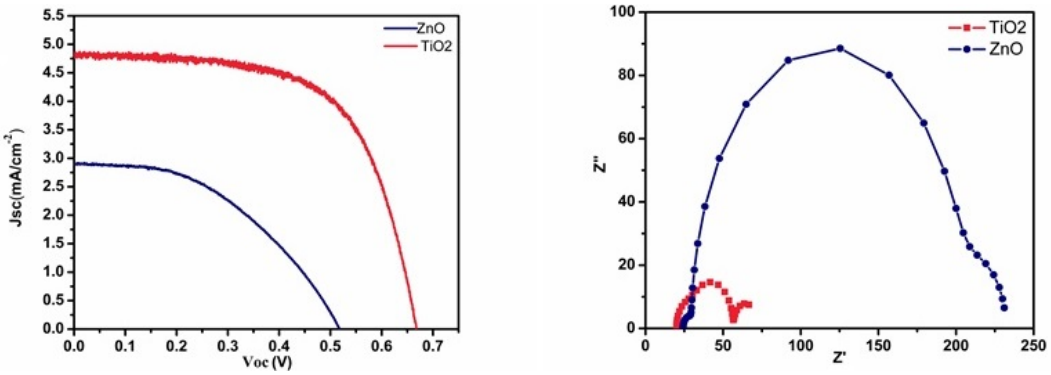

FIG. 3. (a) Jsc-Voc curve, (b) nyquist plot of the cell

TABLE 1. Photovoltaic parameters of TiO_2 and ZnO based DSCs with gel electrolyte

Photoanode material	Jsc(mA/cm^2)	Voc(V)	FF(%)	Eff(%)
TiO_2	1.21	0.67	63.6	2.05
ZnO	0.723	0.517	45.8	0.684

The obtained efficiencies are 2.05 and 0.68 % respectively for TiO_2 and ZnO based DSSC with PVA gel electrolyte. Here, the pure PVA based gel electrolyte of KI/I_2 in DMSO/EC mixture without ionic liquid and any additives or fillers is used. An enhancement in the efficiency is anticipated with ionic liquid and other additives in the gel electrolyte and more studies in this direction are ongoing to enhance the efficiency. The efficiency values are low compared to perovskite-based DSSC. Perovskites give better efficiency and absorption coefficient as a sensitizer along with conventional electrolytes. However, focus of current work is on the synthesis of gel electrolyte, a better substitute for liquid electrolytes, and its application in electrochemical cells.

The charge transfer or transport behavior of the cell was measured by utilizing electrochemical impedance spectroscopy. The three semicircle from left to right gives the electrochemical behavior at the Pt counter electrode,TiO_2/dye/electrolyte interface and Warburg diffusion. The resistance offered at each interface when using ZnO as photoanode is very high when compared to the cell fabricated with TiO_2 as the photoanode. This confirms the lower performance of the ZnO-based quasi solid state dye sensitized solar cell.

4. Conclusion

PVA based polymer gel electrolyte was synthesized. DSSC were fabricated with two different photoanode materials to study the performance of the cell. Photovoltaic studies show that the gel works well with TiO_2-based solar cell, displaying an overall efficiency of 2.05 %.

References

[1] O'Regan B., Gratzel M. A low-cost, high-efficiency solar cell based on dye-sensitized colloidal TiO_2 films. *Nature*, 1991, **353**, P. 737–740.
[2] Yuh-Lang Lee., Yu-Jen Shen., Yu Min Yang. A hybrid PVDF-HFP/nanoparticle gel electrolyte for dye-sensitized solar cell application. *Nanotechnology*, 2008, **19**, P. 455201.
[3] Nogueira A.F., Longo C., De Paoli M.A. Polymers in dye sensitized solar cells: overview and perspectives. *Coordination Chemistry Reviews*, 2004, **248**, P. 1455–1468.
[4] Jo-Lin Lan, Tzu-Chien Wei, et al. Effects of iodine content in the electrolyte on the charge transfer and power conversion efficiency of dye sensitized solar cells under low light intensities. *The J. Phys. Chem. C*, 2012, **116**, P. 25727–25733.
[5] Kun Seok Lee, Yongseok Jun, Jong Hyeok Park. Controlled Dissolution Of Polystyrene nanobeads: Transition from Liquid Electrolyte to Gel Electrolyte. *Nano Lett.*, 2012, **12**, P. 2233–2237.
[6] Chih-Hung Tsai, Chun-Yang Lu, et al. Efficient gel-state dye-sensitized solar cells adopting polymer gel electrolyte based on poly(methyl methacrylate). *Organic electronics*, 2013, **14**, P. 3131–3137.
[7] Wataru Kubo, Kei Murakoshi, et al. Quasi-solid-state dye-sensitized TiO_2 solar cells:Effective charge transport in mesoporous space filled with gel electrolytes containing iodide and iodine. *J.Phys.Chem. B*, 2001, **105**, P. 12809–12815.

NANOSYSTEMS: PHYSICS, CHEMISTRY, MATHEMATICS, 2016, 7 (4), P. 755–758

An investigative study on application of carbon nanotubes for strain sensing

M. R. Khodke[1], Satishchandra V. Joshi[2]

[1]Mechanical Engineering Department, Vishwakarma Institute of Technology Pune–411037, Maharashtra, India

[2]Principal, Padmabhushan Vasantraodada Patil Institute of Technology, Budhgaon–416304, Sangli, Maharashtra, India

moreshwar.khodke@vit.edu, joshisv17@gmail.com

PACS 61.48.De; 07.10.Pz; 73.50.Dn **DOI 10.17586/2220-8054-2016-7-4-755-758**

Traditional strain sensors, such as metal foil gauges, can measure the strains only on the structural surface in designated directions and locations. Hence, there is a need to develop new types of strain sensors which can function on both the micro-and macro-scale, either on the surface or embedded in the structure, and able to behave as multifunctional materials. Owing to its outstanding electrical and mechanical properties carbon nanotubes (CNTs) can be used as strain sensing material. A film (Bucky paper/CNT network) made from multiwalled carbon nanotubes by use of solvent/surfactant and vacuum filtration method is used as strain sensor.

The paper discusses the experimental work involving preparation of CNT film sensor specimen, its application on aluminum and brass strips along with conventional foil gauge and subjecting the metal strips to axial loading to measure gauge factor. It was found that CNT film strain sensor shows linear relationship between change in resistance and strain. Furthermore, the gauge factor increases as the film aspect ratio increases, and for the same aspect ratio, a higher gauge factor was observed for brass than aluminum.

Keywords: carbon nanotube, strain sensor, bucky paper, sensitivity, gauge factor.

Received: 22 March 2016

1. Introduction

Mechanical strain sensors are widely used for structural health monitoring and vibration control. Traditional strain sensors such as strain gauges are sensitive, stable, of low cost and easy to use. However, strain gauges can only measure the strains on the structural surface in designated directions and locations; also strain sensing is usually the only function they can offer. Carbon nanotubes (CNTs) possess excellent physical and chemical properties [1] and strain sensor made of carbon nanotube material can alleviate this difficulty and can behave as multifunctional material.

Comprehensive reviews on sensors based on carbon nanotubes and their composites are presented by Christofer Hierold et al. [2] and Chunyu Li et al. [3]. A study by Dharap et al. [4] showed that pure SWCNT films ('bulky paper') can serve as strain sensors if they are bonded to the structural surface as conventional strain sensors.

Strain sensitivity is one of the most important parameters to consider and is expressed as the gauge factor (GF), a dimensionless number describing the change in resistance as a ratio of applied strain, and is given by [5]:

$$GF = \frac{\text{Relative change in resistance}}{\text{Applied strain}} = \frac{\left(\Delta R/R\right)}{\varepsilon}. \tag{1}$$

The effect of aspect ratio on sensitivity of CNT film sensor is not reported in the literature. The investigation of this relationship is the objective of this study.

2. Carbon nanotube film

Many applications of CNT film are reported in the literature [6]. Some of them are in field emission, energy storage and conversion, electronics, humidity and temperature sensor, gas sensors, bio sensor etc. The methods for preparation of CNT film are chemical vapor deposition growth, electrophoretic deposition, drop drying from solvent etc. Vacuum filtration method as outlined in [7] is used in this study.

2.1. Preparation of CNT Film

Multiwalled carbon nanotubes (MWCNTs) having an average inner and outer diameters 4–13 nm, and length of 1–4 μm was procured from D & D Advanced Materials, Pune, India. 25 mg of MWCNT, as procured, was mixed in 100 ml of Dimethylformamide (DMF) solvent. DMF-MWCNT solution was then ultrasonicated in a bath sonicator (DC-80H, MRC, 80 W) for 3 hours and by an ultrasonic tip (Vibra-Cell VCX130, Sonics, USA) for 20 min in an alternating sequence. CNT suspension was then filtered by using vacuum filtration method. The film is peeled off from filter paper and dried in oven at 60 to 80 °C for 12 hours. The film after drying is cut in required aspect ratios and used as strain sensor.

3. Experimental setup

The setup consists of Universal Testing Machine (UTM) for tensile loading (1–10 kN) of specimens and Agilent 34410A digital multimeter for measuring the resistance change. The CNT film strain sensors and conventional metal foil strain gauge are bonded on opposite side of on aluminum or brass strip by epoxy adhesive. The terminals for the electrical resistance measurements were taken from film through silver paste.

Four sensors of different aspect ratio as mentioned in Table 1, were used on Aan aluminum strip of size 300 mm×30 mm×3 mm and on a Brass strip of size 300 mm×50 mm×6 mm.

TABLE 1. Specifications of CNT Film and metal foil strain sensors

Sensor Type	CNT Film Size	Aspect Ratio	Used on	Initial Resistance, R_0, Ohm
Sensor 1	30 mm × 10 mm	3:1	Aluminium Strip	19.0365
Sensor 2	20 mm × 10 mm	2:1	Aluminium Strip	11.2752
Sensor 3	10 mm × 10 mm	1:1	Aluminium Strip	5.0815
Sensor 4	30 mm × 10 mm	3:1	Brass Strip	42.1362
Metal Foil 1			Aluminium Strip	349.565
Metal Foil 2			Brass Strip	350.005

4. Results and discussion

The relative change in resistance with respect to applied strain for three CNT film sensors, Sensor 1 to 3 and conventional metal foil gauge applied on aluminum strip is shown in Fig. 1.

The relative change in resistance with respect to applied strain for sensor 4 and one conventional metal foil gauge applied on brass strip is shown in Fig. 2.

Gauge factor is slope of straight line fitted in the graphs shown in Fig. 1 and Fig. 2. The gauge factors were determined for all these six sensors using equation (1) i.e. slope of straight lines fitted are listed in Table 2.

TABLE 2. Gauge factors for CNT sensors of different aspect ratio

Sensor Type	Film Size	Aspect Ratio	Used on	Initial Resistance, R_0, Ohm	Gauge Factor observed
Sensor 1	30 mm × 10 mm	3:1	Aluminium	19.0365	1.05
Sensor 2	20 mm × 10 mm	2:1	Aluminium	11.2752	0.59
Sensor 3	10 mm × 10 mm	1:1	Aluminium	5.0815	0.38
Sensor 4	30 mm × 10 mm	3:1	Brass	42.1362	1.38
Metal Foil 1			Aluminium	349.565	2.10
Metal Foil 2			Brass	350.005	1.99

Gauge factor for metal foil strain gauge as supplied by the manufacturer is 2.0, which validates the observations shown in Table 2.

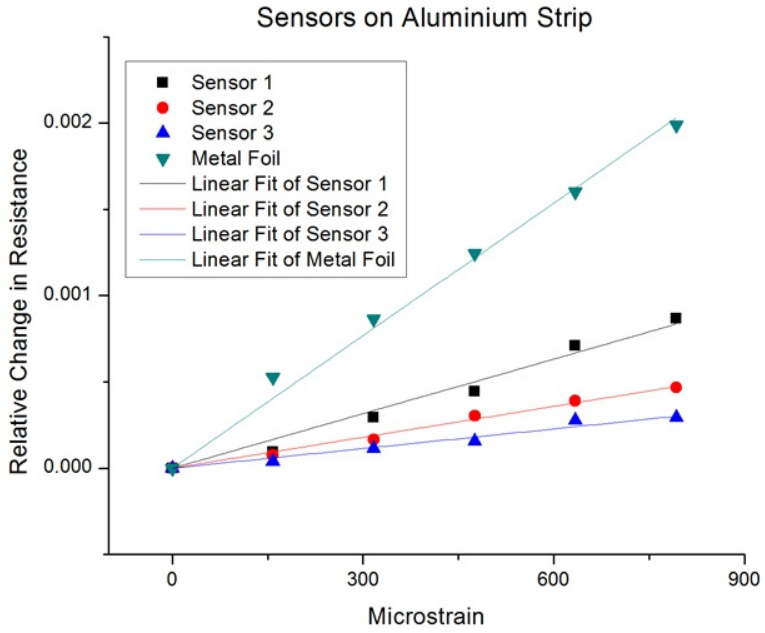

FIG. 1. Relative resistance change vs applied strain for sensors on Aluminium strip

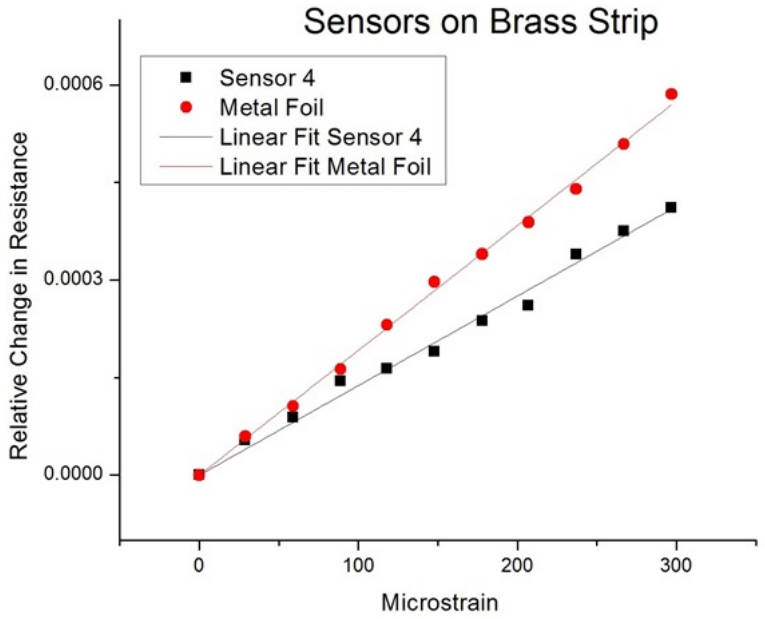

FIG. 2. Relative resistance change vs applied strain for sensors on Brass strip

5. Conclusion and future scope

CNT film sensors show nearly linear response to applied strain similar to conventional metal foil gauges. Sensitivity of CNT film sensor is affected by aspect ratio. Higher aspect ratios were shown to result in better sensitivity. Additionally, a higher gauge factor noted for CNT sensor mounted brass strip than that mounted on an aluminum one, suggesting its better suitability for brass material.

5.1. Future scope

The following two points can be suggested as future scope of study:

(1) Magnitude of resistance change for a CNT film is proportional to its initial resistance which in turn depends on its thickness. Hence, resistance change and sensitivity of sensor can be increased by reducing film thickness i.e. by lowering CNT content in film.

(2) Alternatively, initial resistance of CNT film can also be increased by manufacturing composite film of CNT with polymers, e.g., Poly Dimethyl Siloxane (PDMS).

Acknowledgement

Authors gratefully acknowledge the Research Grant No. 13ENG001061 received from the Board of College and University Development (BCUD), Savitribai Phule Pune University, Pune, India, for the research work.

References

[1] Dresselhaus M.S., Dresselhaus G., Charlier J.C., Hernandez E., Electronic, thermal and mechanical properties of carbon nanotubes. *Philos. Trans. R. Soc. A Math. Phys. Eng. Sci.*, 2004, **362**(1823), P. 2065–2098.

[2] Hierold C., Jungen A., Stampfer C., Helbling T. Nano electromechanical sensors based on carbon nanotubes. *Sensors Actuators A Phys.*, 2007, **136**(1), P. 51–61.

[3] Li C., Thostenson E.T., Chou T.-W. Sensors and actuators based on carbon nanotubes and their composites: A review. *Compos. Sci. Technol.*, 2008, **68**(6), P. 1227–1249.

[4] Dharap P., Li Z., Nagarajaiah S., Barrera E.V. Nanotube film based on single-wall carbon nanotubes for strain sensing. *Nanotechnology*, 2004, **15**(3), P. 379–382.

[5] Stephan B., Graham E., Michael K., Neil W. *MEMS Mechanical Sensors*. Artech House, Boston, 2004, 86 p.

[6] Zhu H., Wei B. Assembly and applications of carbon nanotube thin films. *J. Mater. Sci. & Technol.*, 2008, **24**(4), P. 447–456.

[7] Rein M.D., Breuer O., Wagner H.D. Sensors and sensitivity: Carbon nanotube buckypaper films as strain sensing devices. *Compos. Sci. Technol.*, 2011, **71**(3), P. 373–381.

NANOSYSTEMS: PHYSICS, CHEMISTRY, MATHEMATICS, 2016, 7 (4), P. 759–764

Synthesis and characterization of neomycin functionalized chitosan stabilized silver nanoparticles and study its antimicrobial activity

R. K. Preethika[1], R. Ramya[2], M. Ganesan[1], S. Nagaraj[3], K. Pandian[2,*]

[1]Department of Chemistry, Thiagarajar College, Madurai–625009, India

[2]Department of Inorganic Chemistry, University of Madras, Guindy Campus, Chennai–600025, India

[3]CASBotany, University of Madras, Guindy Campus, Chennai–600025, India

[*]jeevapandian@yahoo.co.uk

PACS 82.65.+r **DOI 10.17586/2220-8054-2016-7-4-759-764**

A simple green method was developed for the synthesis of silver nanoparticles in the presence of a neomycin-functionalized chitosan as stabilizing agent using a fresh lemon juice as green reducing agent. The stabilizing agent was synthesized based on the Schiff base formation reaction between the chitosan dialdehyde and neomycin antibiotic in 0.05 mM at pH 7.0. The combined form of neomycin antibiotic with chitosan can be used as stabilizing agent for silver nanoparticles (AgNPs) synthesized by a biogenic method using lemon juice as a green reducing agent. The neomycin functionalized chitosan stabilized AgNPs were characterized by various analytical techniques, including UV-Visible spectra studies, FTIR, XRD and SEM. The antimicrobial activity of these composite was tested against human pathogenic Gram-positive and Gram-negative bacteria. The synergetic effect of the neomycin functionalized chitosan protected silver nanoparticles was tested against various drug resistant microorganisms. These chitosan derivatives can be used in combination with an anti-bacterial agent to treat and inhibit a resistant bacterial infection or the growth of resistant bacterial infection.

Keywords: silver nanoparticles, lemom juice, neomycin, chitosan, antimicrobial activity.

Received: 3 April 2016

Revised: 5 July 2016

1. Introduction

Due to its biocompatibility, biodegradability and non-toxicity, chitosan has increasingly been used in the biomedical and pharmaceutical fields [1–4]. Chemical modifications have been used to prepare chitosan derivatives with enhanced biological and physicochemical properties. Recently, aldehyde-functionalized chitosans have received considerable interest. The preparation of chitosan derivatives containing aldehyde groups have been achieved by reaction with periodates. The latter selectively cleaves the 2, 3 C-C bond and converts chitosan into a dialdehyde derivative [5, 6]. Aldehyde-functionalized chitosans have also been prepared by reaction with nitrous acid (HNO_2) [7–10]. In this method, chitosan undergoes deaminative cleavage of the 1, 4-glycosidic bonds, producing 2, 5-anhydro-D-mannose as the reducing end, which contain an aldehyde group. Hydrogen peroxide was also used to synthesis chitosan containing 2, 5-anhydro-D-mannose recently [11]. The periodate oxidation of chitosan was performed which yielded a dialdehyde chitosan (DAC) that can be used for the construction of biosensor and drug delivery applications [12]. Similarly, chitin and chitosan can be easily processed into hydrogels for various types of biomedical applications such as drug and gene delivery, wound healing and tissue engineering [13–15]. Drug loaded chitosan hydrogels have been generated using diffusion, entrapment and tethering techniques [16]. Chitosan membrane and its derivative have shown a prolonged antibacterial activity and decreased potential toxicity of silver [17, 18].

Recently, a facile and green method was reported in the literature to synthesize stable Ag nanoparticles (AgNPs) with a narrow size distribution. It is well established that chitosan (DAC) and its derivatives were widely used as both a reducing as well as stabilizing agent for the synthesis of metal nanoparticles. In the present study, we investigated the antibacterial activity of both neomycin-functionalized chitosan as well as the combined form of Neo-chit stabilized silver nanoparticles because of the synergetic microbial activity. Here, lemon juice was used to prepare narrow size silver nanoparticles, as previously reported in the literature.

2. Materials and methods

2.1. Materials

Analytical grades chitosan and sodium periodate were purchased from Sigma-Aldrich. The other reagents and solvents were analytical grade. All materials were used without further purification.

2.2. Preparation procedures

2.2.1. Oxidation of chitosan. About 1g chitosan (5.34 mM) was dispersed in 50 ml HCl (10^{-3} M) (pH ranging from 4–5) with magnetic stirring. Then, 1 ml aqueous sodium periodate 0.534 mM was added, the reaction mixture was allowed to stir at 4 °C in the dark for 30 minutes. After completion of the reaction, to eliminate the unreacted periodate, 1 ml of ethylene glycol was added. The oxidized chitosan was washed by distilled water and the sample was frozen and lyophilized for 4 h.

2.2.2. Synthesis of neomycin functionalized chitosan (Neo-Chit). 10 ml of chitosan dialdehyde mixed with 0.05 mM of neomycin sulfate and then the reaction mixture was stirred for 2 h. The powder form of the sample was isolated by by lyophilization after freezing with liquid nitrogen.

2.2.3. Synthesis of silver nanoparticles. 1 ml of freshly prepared lemon juice was diluted with 3 ml of distilled water and then the pH of the solution was adjusted to 11. Then, 2 ml 1 M aq. $AgNO_3$ was added dropwise to the above vigorously-stirred lemon juice solution. The polyphenol group present in the lemon juice reduced the silver ions to silver metal nanoparticles in th aq. medium. The appearance of reddish brown color solution indicated the formation of silver nanoparticles. Then, th silver nanoparticles were isolated via centrifugation.

2.2.4. Neomycin functionalized chitosan stabilized silver nanoparticles. To prepare Neo-Chit stabilized AgNPs, 0.1 g neomycin-functionalized chitosan was mixed with 1 ml of silver nanoparticle solution and then allowed to stir for 30 min. The Neo-Chit @ AgNPs was isolated by centrifugation followed by drying under nitrogen atmosphere in the dark. The powdered samples were collected and stored in dark until further use Fig. 1.

2.2.5. Instrumentation. UV-Visible spectral studies were carried out by using a Shimadzu UV-Visible Spectrophotometer, Japan (Model UV-1800). The characterization of functional groups on the surface of AgNPs performed by FT-IR (perkin-Elmer, Germony) the spectra were scanned over 500 to 4000 cm^{-1}.

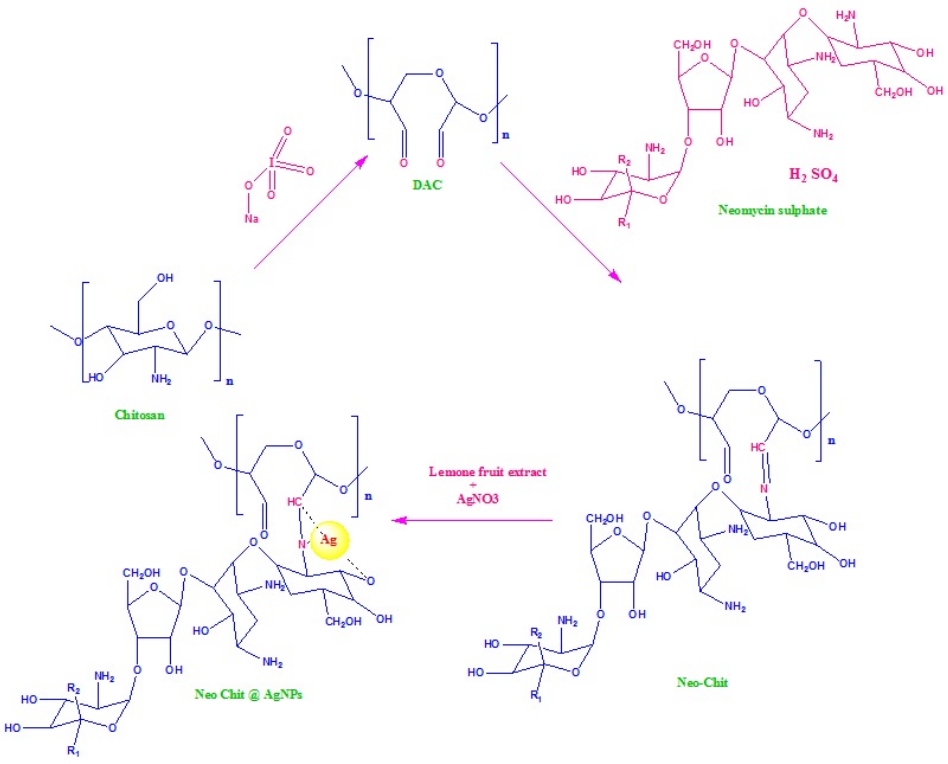

FIG. 1. Schematic representation of the synthetic route of Neomycin functionalized chitosan stabilized silver nanoparticles

3. Result and discussion

3.1. UV-Vis spectroscopy

The UV-Visible spectrum of silver nanoparticles and Neo-chit protected AgNP are shown in Fig. 2. The Plasmon absorption peak was observed at 408 nm which indicated the formation of silver nanoparticles. From the UV-Visible spectral studies, it is clearly seen that the particle size of the silver nanoparticles ranged from 5–20 nm. The peak shape of AgNPs is narrow and sharp, providing evidence for the uniform size distribution of the silver nanoparticles in lemon juice solution. The appearance a sharp Plasmon band is due to the formation of silver nanoparticles having a narrow size range. A slight shift in Plasmon band position is due to the surface modification of silver nanoparticles using neomycin-functionalized chitosan as stabilizing agent. The decrease in Plasmon band position is due to the surface modification of the neomycin functionalized AgNP. The broadening of the peak position was also observed which is due to the partial aggregated particles of the silver nanoparticles.

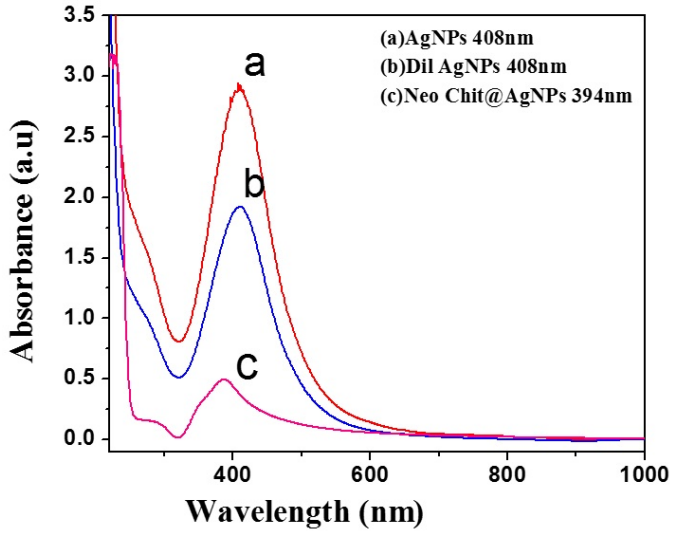

FIG. 2. (a) UV-Visible spectrum of AgNPs obtained from lemon juice reduction method; (b Dilute AgNPs and (c) Neo-chit @ AgNPs

3.2. FT-IR-spectrum of neomycin functionalized chitosan modified AgNPs

The FT-IR spectrum was recorded for both neomycin-functionalized chitosan and neomycin-functionalized chitosan protected silver nanoparticles. The major bands at 2926, 2851, 1746, 881, 774 cm^{-1} are assigned for the characteristic bands for aldehyde group that resulted from periodate mediated oxidation was observed at Fig. 3(b). The bands at 1077 and 1020 cm^{-1} are typical for neomycin-functionalized chitosan modified AgNPs was observed at Fig. 3(c), Table 1.

TABLE 1. FT-IR bands related to chitosan/modified chitosans and their respective assignments

FT-IR band(cm^{-1})	Assignment	FT-IR band(cm^{-1})	Assignment
3356, 2926	N-H,C-H	1071, 1020	C-O-C
3425	O-H	2352, 1323	N-N,NO_2
2851	C-H	2075	O-H
1746	C=O	1077	C-O
1626	C-C	881,774	C-H, NO_3
1406	C=O		

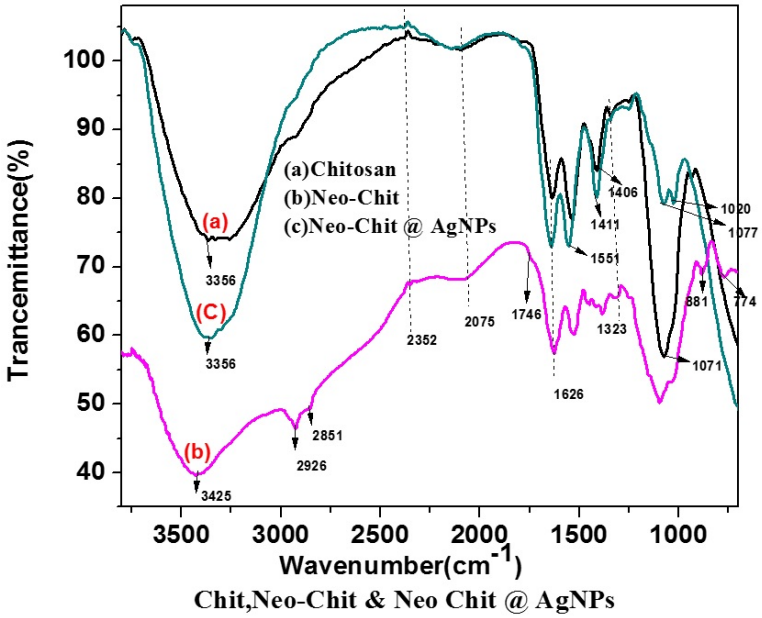

FIG. 3. FT-IR spectrum of chitosan and neomycin functionalized chitosan

3.3. Scanning Electron Microscopic studies

Conventional high vacuum scanning electron microscopy (SEM) images were also taken to envision the structure of oxidized chitosan and Chitosan dialdehyde with neomycine@AgNPs. Fig. 4 shows that there is no change for the stretched out and fibrous network of chitosan, but on the surface of oxidized chitosan one can see a slight degradation of some foliage. The EDX pattern of chitosan dialdehyde with neomycin @ AgNPs is shown in Fig. 5. This pattern shows peaks for the elements **Ag** and **C** are the major components. From these studies, we conclude that the the chitosan dialdehyde-functionalized neomycin stabilizes the AgNPs.

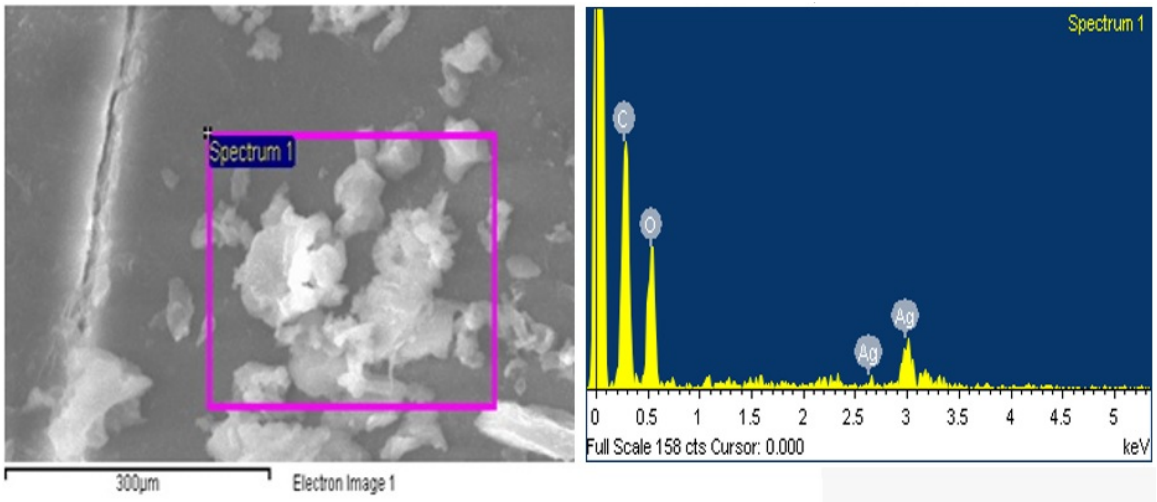

FIG. 4. SEM – EDAX of Chitosan dialdehyde with neomycin @ AgNPs

3.4. Antibacterial activity of Neo-Chit @ AgNP

It is well established that silver nanoparticles with various capping agents have shown excellent antimicrobial activity [18, 19]. In the present study, we demonstrate the antimicrobial activity of silver nanoparticles, neomycin-functionalized chitosan modified AgNPs against various Gram negative and Gram positive bacteria. The disc diffusion method was used for the quantification of inactivation of microbial growth. From the experimental

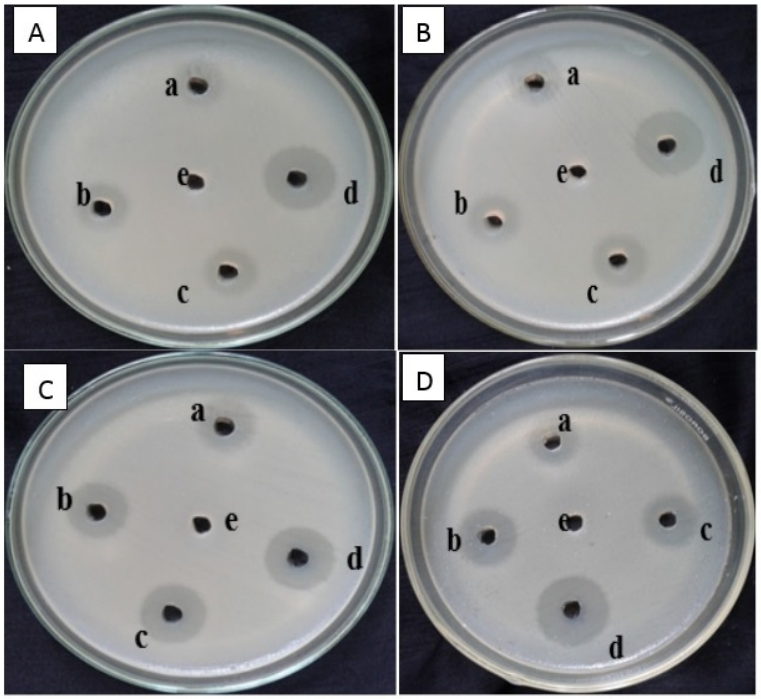

FIG. 5. Antibacterial activity of the Neo-chit and Neo-chit@AgNPs against A, C – Staphylococcus aureus and B, D – Salmonella typhi

studies it is inferred that Neo-chit@AgNPs have shown an enhanced antimicrobial activity than the Neo-chit as well as bare AgNP (Table 2).

TABLE 2. Antimicrobial activity of the Neo-chit and Neo-chit @ AgNPs against Gram positive and Gram negative bacteria

	Gram positive bacteria					**Gram negative bacteria**				
Sample (μg/ml)	***Staphylococcus aureus***					***Salmonella typhi***				
	a	**b**	**c**	**d**	**e**	**a**	**b**	**c**	**d**	**e**
Neo-chit	2.5	3	3.5	8	–	–	–	–	11	–
Neo-chit@AgNPs	3	6	8	14	–	4	6	9	24	–

4. Conclusion

We have synthesized neomycin antibiotic drug-functionalized chitosan by a Schiff base reaction using chitosan dialdehyde. The neomycin-functionalized chitosan was isolated in pure form by dialysis followed by freeze drying method. From the FT-IR result it is confirmed that neomycin aminoglucoside antibiotic drug molecules effective functionalized on chitosan backbone. The neomycin-functionalized chitosan was used further to stabilize the green synthesized silver nanoparticles using lemon juice as reducing agent. The antibacterial activity of the Neo-chit and Neo-chit@AgNP were tested. An enhanced antimicrobial activity was noted in the case of neo-chit-stabilized silver nanoparticles system than the neo-chit system and silver nanoparticles. The combined form of silver nanoparticles and Neo-Chit showed can be used to eradicate the microbial drug resistance organisms.

References

[1] Enxian Lu, Scott Franzblan, Carmen Popesu. Preparation of aminoglycoside-loaded chitosan nanoparticles using dextran sulphate as a counter ion. *J. Micro encapsulation: Micro and Nano carriers*, 2009, **26**(4), P. 346–354.

[2] Jayakumar R., Deepthy Menon, Manzoor K., Tamura H. Biomedical application of chitin and chitosan based nanomaterials. *Carbohydrate polymers*, 2010, **82**(2), P. 227–232.

[3] Chen J., Liu Q., Zhang X., Zhang Q. Prevaporation and characterization of chitosan membranes cross linked by 3-aminopropyltriethoxysilane. *J. Member. Sci*, 2007, **292**, P. 125–132.

[4] Ravi Kumar M.N.V. A review of chitin and chitosan applications. *Reactive and Functional Polymers*, 2000, **46**, P. 1–27.

[5] Vold I.M., Christensen B.E. Periodate oxidation of chitosans with different chemicalCompositions. *Carbohydr Res*, 2005, **340**, P. 679–684.

[6] Xin Liu, Yunhui. Preparation process and Antimicrobial Properties of cross-linking chitosan on to periodate-oxidised bamboo pulp fabric. *J. of Fibers and polymers*, 2014, **15**, P. 1887–1894.

[7] Jolanta kumirska, Mirko X., Weinhold, Jorg Thoming, Piotr Stepnowski. Biomedical Activity of Chitin/Chitosan Based Materials- Influence of properties Apart from Molecular Weight and Degree of N-Acetylation. *J. Polymer*, 2011, **3**, P. 1875–1901.

[8] Hilde K. Holme, Lene Davidsen, Are Kristiansena. Kinetics and mechanism of depolymerization of alginate and chitosan in aqueous solution. *Carbohydrate polymers*, 2007, **73**, P. 656–664.

[9] Tommeraas K., Varum K.M., Christensen B.E., Smidsrod O. Preparation and characterisation of oligosaccharides produced by nitrous acid depolymerisation of chitosans. *Carbohydr. Res*, 2001, **333**, P. 137–144.

[10] Lin C.W., Lin J.C. Characterization and blood coagulation evaluation of the water soluble chitooligosaccharides prepared by a facile fractionation method. *Biomacromolecules*, 2003, **4**, P. 1691–1697.

[11] Tian F., Liu Y., Hu K., Zhao B. Study of the depolymerization behavior of chitosan by hydrogen peroxide. *Carbohydr. Polym.*, 2004, **57**, P. 31–37.

[12] Yan Feng, Limin Yang, Feng Li. A novel sensing platform based on periodate-oxidized chitosan. *Anal. Methods*, (2010), **2**, P. 2011–2016.

[13] Jayakumar R., Divya Rani V.V., Shalumon K.T., Sudheesh Kumar P.T. Nair S.V., Furuike T., et al. Bioactive and osteoblast cell attachement studies of novel α-and β-chitinmembranes for tissue engineering applications. *Int. J. Biol Macromol*, 2009, **45**, P. 260–4.

[14] Jayakumar R., Prabaharan M., Reis R.L., Mano J.F. Graft copolymerized chitosan – present status and applications. *Carbohydr. Polym.*, 2005, **62**, P. 142–58.

[15] Prabaharan M., Mano J.F. Chitosan-based particles as controlled drug delivery systems. *Drug Deliv*, 2005, **12**, P. 41–57.

[16] Lin C.C., Anseth K.S. PEG hydrogels for the controlled release of biomolecules in regenerative medicine. *Pharm. Res*, 2009, **26**, P. 631–43.

[17] Mi F.L., Wu Y.B., Shyu S.S., Chao A.C., Lai J.Y., Su C.C. Asymmetric chitosan membranes prepared by dry/wet phase separation: a new type of wound dressing for controlled antibacterial release. *J. Membr Sci*, 2003, **212**, P. 237–54.

[18] Sharma V.K., Yangard R.A. Green Synthesis and their antimicrobial activities. *J. Colloid Interface. Sci*, 2009, **9**, P. 83–96.

[19] Kora A.J., Rastogi L. Enhancement of antibacterial activity of capped silver nanoparticles in combination with antibiotics, on model Gram-negative and Gram-positive bacteria. *Bioinorg. Chem. Appl*, 2013, P. 1–7.

NANOSYSTEMS: PHYSICS, CHEMISTRY, MATHEMATICS, 2016, 7 (4), P. 765–767

Surfactant assisted synthesis of nanocrystalline n-Bi_2Se_3 thin films at room temperature via arrested precipitation technique

N. D. Desai, S. M. Patil, K. V. Khot, R. M. Mane, P. N. Bhosale*

Materials Research Laboratory, Department of Chemistry, Shivaji University, Kolhapur–416004, India

*p_n_bhosale@rediffmail.com

PACS 81.07.-b **DOI 10.17586/2220-8054-2016-7-4-765-767**

In the present investigation, we have successfully synthesized nanocrystalline bismuth selenide (Bi_2Se_3) thin films using an arrested precipitation technique at room temperature. The optostructural, morphological, compositional and photoeletrochemical properties were studied for Bi_2Se_3 thin films prepared via surfactant-assisted synthesis. The optical study reveals the presence of direct allowed transition with band gap energy ranging from 1.40–1.80 eV. The X-ray diffraction (XRD) pattern confirms rhombohedral crystal structure. Scanning electron microscopy study shows the morphological transition from an interconnected mesh to nanosphere-like morphology and finally, lamellar sphere. Atomic force microscopy (AFM) study carried out to determine surface roughness and surface topography of thin films. Energy dispersive spectroscopy (EDS) analysis reveals the presence and ratio of elemental bismuth and selenium. Finally, the photoelectrochemical (PEC) performance of all the as-synthesized thin films were carried out using iodide-polyiodide redox couple.

Keywords: Bi_2Se_3, APT, surfactant.

Received: 16 April 2016

Revised: 22 April 2016

1. Introduction

Currently, there is significant research interest in the development of semiconducting materials for solar cell applications. Bi_2Se_3 is V-VI group binary chalcogenide which has been a material of interest for many years [1, 2]. The novel optostructural and morphological properties of Bi_2Se_3 are useful in numerous fields, such as thermoelectric devices, photosensitive devices, photovoltaic cells, Hall Effect magnetometer, refrigeration, high frequency power sensors, topographic insulator, etc [3–7].

Several methods have been developed to obtain nanostructured Bi_2Se_3 such as SILAR, MOCVD, CBD, Sputtering, Microwave assisted synthesis, etc. Among all these metods, APT is a simple, attractive and cost effective method. Hence, we have selected an APT method for deposition of Bi_2Se_3 thin films. There are very few reports available on the PEC performance of Bi_2Se_3 thin films. Hence, in the present article, we are reporting on the PEC performance for Bi_2Se_3 thin films prepared by a surfactant-assisted APT protocol.

2. Experimental

Nanocrystalline Bi_2Se_3 thin films have been synthesized via an arrested precipitation technique (APT) at room temperature. 0.05 M bismuth triethanolamine complex (Bi-TEA) and 0.25 M sodium selenosulphite (Na_2SeSO_3) were used as precursor solution for Bi and Se respectively. TEA was used as a complexing agent. In a typical synthesis, both precursor solutions were added in a 2:3 ratio. The pH was adjusted to 10. The pre-cleaned glass substrate was placed vertically in the reaction bath. The total volume of reaction bath was made 40 mL by addition of double distilled water (D/W). The reaction bath is maintained at room temperature without disturbing for 8 hrs. When the terminal growth stops, thin films were taken out and washed 2–3 times with D/W. Thin films were dried at room temperature and used for further characterization.

3. Optical study

The thicknesses of Bi_2Se_3 were measured using a surface profilometer. The thickness was found in the range of 630 nm to 910 nm.

The UV-Visible spectrum of as-deposited Bi_2Se_3 thin film was recorded for wavelengths ranging from 500–1100 nm, as shown in Fig. 1(a). In order to determine the band gap of Bi_2Se_3 thin films, the classical absorption equation is used:

$$\alpha h\nu = A(h\nu - E_g)^n. \quad (1)$$

The optical band gap was found to be 1.7 eV with directly-allowed transition, as shown in Fig. 1(b)

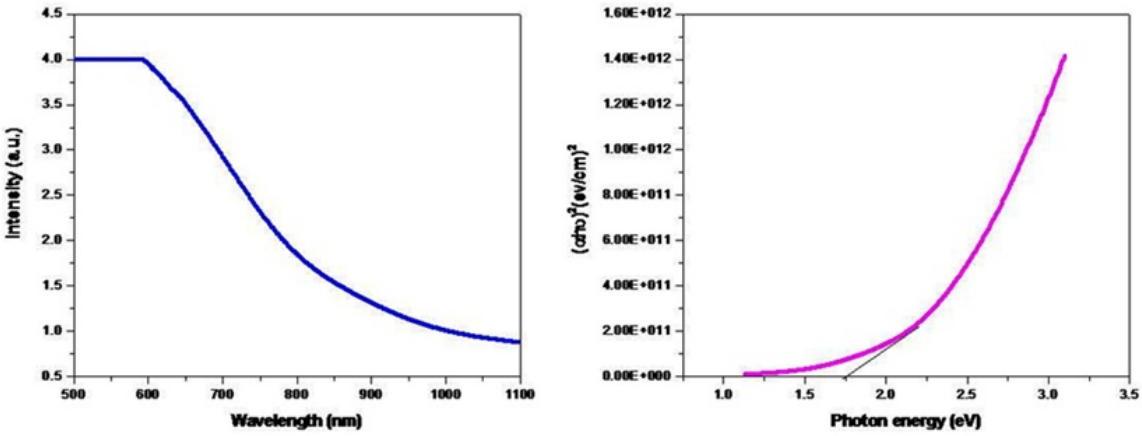

FIG. 1. (a) Optical absorption spectrum of Bi_2Se_3 thin films (b) Plot of $(\alpha h\nu)^2$ vs. $h\nu$

4. Structural study

The phase determination of as-deposited Bi_2Se_3 thin film was done using XRD. All peaks in the XRD pattern are well matched with rhombohedral crystal structure (JCPDS 33-021). The most intense peak is observed at 29.33° for (015) plane. The crystallite size is calculated by the Debye-Sheerer equation.

$$D = 0.9\lambda/\beta\cos\theta. \tag{2}$$

The crystallite size is found to be 47.89 nm.

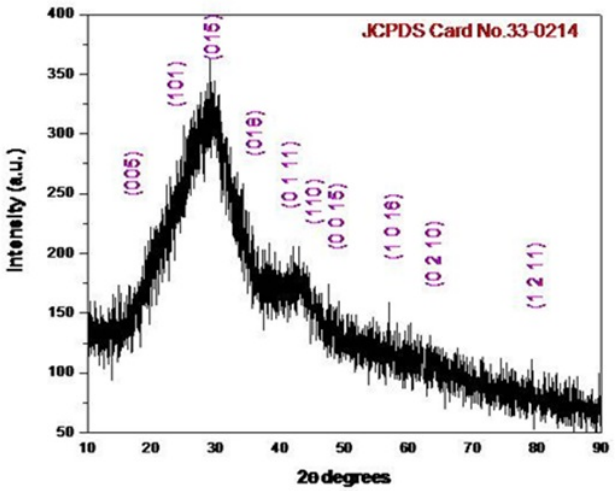

FIG. 2. XRD Patterns of Bi_2Se_3 thin films

5. Morphological and compositional study

The SEM image indicates a uniform, well-adherent and pinhole-free deposition for the Bi_2Se_3 thin film. The SEM micrograph shows an interconnected mesh-like structure.

In order to determine the chemical composition of Bi_2Se_3 thin films, EDS analysis was also carried out. The presence of Bi^{3+} and Se^{2-} was confirmed from EDS. The expected and observed atomic percentages of Bi and Se are in good agreement with standard data. The excess percentage of bismuth is most likely due to an antisite defect. Antisite defects means that excess Bi enters the lattice by replacing Se. The higher percentage of Bi may also attributed to the more metallic character of Bi and its high reactivity towards Se. The small difference in the electronegativity between Bi and Se is also responsible for antisite defect.

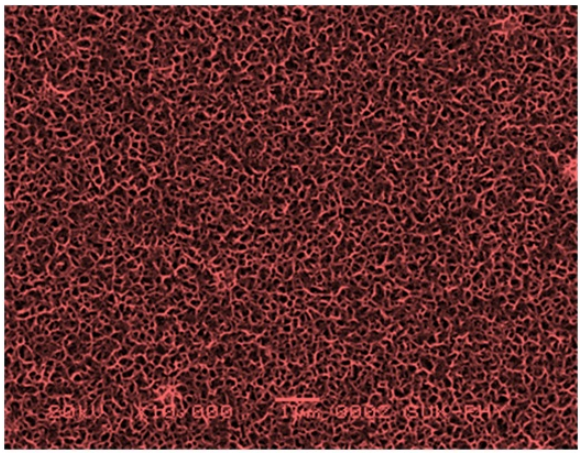

FIG. 3. SEM images of Bi_2Se_3

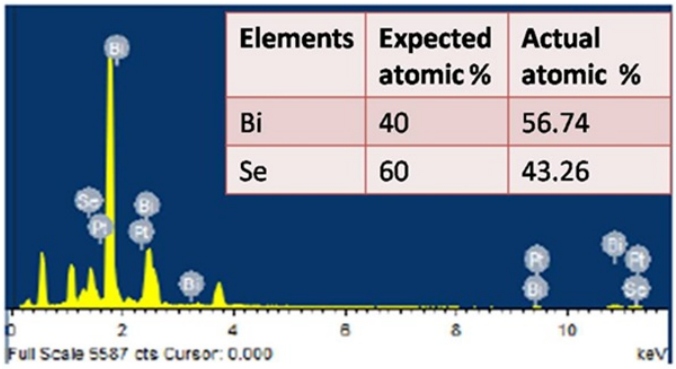

FIG. 4. EDS pattern of Bi_2Se_3 thin films

6. Conclusion

Bi_2Se_3 thin films were synthesized via simple and low cost APT. The optostructural and morphological properties were studied to a film prepared using a surfactant-assisted protocol. The XRD pattern confirmed rhombohedral crystal structure. The SEM pattern revealed an inetrconnected mesh-like structure. The EDS pattern determined the stoichiometric ratio for Bi and Se in the thin film formation.

All these results showed that Bi_2Se_3 thin films may be useful for solar cell application.

References

[1] Osterloh F.E. Inorganic nanostructures for photoelectrochemical and photocatalytic water splitting. *Chem. Soc. Rev.*, 2013, **42**, P. 2294–2320.

[2] Yang J., Li Y., Liu F., Jiang L., Ye J., Liu Y. The electrochemical self assembly of hierarchical dendritic Bi_2Se_3 nanostructures. *Cryst. Eng. Comm.*, 2014, **16**, P. 2823–2834.

[3] Jagminas A., Valiunas I., Vernese G.P., Juskenas R., Rutavicius A. Alumina template assisted growth of bismuth selenide nanowire arrays. *J. Cryst. Growth*, 2008, **310**, P. 428–433.

[4] Xiao F., Hangarter C., Yoo B., Rheem Y., Lee K., Myung N.V. Recent progress in electrodeposition of thermoelectric thin films and nanostructures. *Electrochim. Acta*, 2008, **53**, P. 8103–8117.

[5] Xiao C., Li Z., Li K., Huang P., Xie Y. Decoupling Interrelated Parameters for Designing High Performance Thermoelectric Materials. *Acc. Chem. Res.*, 2014, **47**, P. 1287–1295.

[6] Ko J., Kim J., Choi S., Lim Y., Seo W., Lee K. Nanograined thermoelectric $Bi_2Te_{2.7}Se_{0.3}$ with ultralow phonon transport prepared from chemically exfoliated nanoplatelets. *J. Mater. Chem.*, 2013, **1**, P. 12791–12796.

[7] Borisova S., Krumrain J., Luysberg M., Mussler G., Gruitzmacher D. Mode of Growth of Ultrathin Topological Insulator Bi_2Te_3 Films on Si (111) Substrates. *Cryst. Growth Des.* 2012, **12**, P. 6098–6103.

NANOSYSTEMS: PHYSICS, CHEMISTRY, MATHEMATICS, 2016, 7 (4), P. 768–773

Antibacterial and catalytic properties of silver nanoparticles loaded zeolite: green method for synthesis of silver nanoparticles using lemon juice as reducing agent

J. Selvamuthumari[1], S. Meenakshi[2], M. Ganesan[1], S. Nagaraj[3], K. Pandian[2,*]

[1]Department of Chemistry, Thiagarajar College, Madurai–625009, India

[2]Department of Inorganic Chemistry, University of Madras, Guindy Campus, Chennai–600025, India

[3]CAS Botany, University of Madras, Guindy Campus, Chennai–600025, India

*jeevapandian@yahoo.co.uk

PACS 82.65.+r **DOI 10.17586/2220-8054-2016-7-4-768-773**

Zeolite Y is a cage-like alumina silicate which is widely used as solid support to immobilize metal and metal sulfide nanoclusters. We have attempted to synthesis silver nanoparticle-loaded zeolite Y by an ion exchange method followed by a biogenic reduction method using lemon juice as a reducing agent. The antimicrobial activity of the silver ion, silver nanoparticles and silver chloride-modified zeolite was investigated against various Gram negative and Gram positive microorganisms. The silver nanoparticle-loaded zeolite was further functionalized with amoxicillin antibiotic which exhibited a strong antimicrobial action to kill drug resistant microorganisms. The catalytic behavior of silver nanoparticles was investigated to reduce 4-Nitrophenol in presence of $NaBH_4$. The catalytic reaction is found to be pseudo-first order, resulting in a rate constant that was comparable with previously-reported results.

Keywords: zeolite-Y, silver nanoparticles, amoxicillin, catalytic reduction of 4-aminophenol, antibacterial studies.

Received: 3 May 2016

Revised: 25 June 2016

1. Introduction

Zeolites are an important group of crystalline aluminosilicates currently available for various fields of applications. These minerals are widely used as sorbents, ion exchangers, catalysts and biosensors [1–4]. The catalytic nature, reactivity and other properties of zeolite can be greatly improved by cation exchange methods [5]. These materials are negatively charged with a high density of active acid sites, high thermal stability, high size selectivity and unique porous properties, which impart their ability act as catalysts for various industrial catalytic studies at elevated temperature with wider pH ranges. Because of void space and swelling behavior which can be used in petrochemical cracking, ion-exchange, gas and solvent separation, and removal of pollutants [6]. Metal ion, charged species, redox and photoactive molecules can be immobilized within the pores of zeolite system and these composites can be used in sensors and catalytic applications [7–10].

Silver (Ag) is a metallic element that has been widely used in various excellent fields [11]. Silver ions (Ag^+) and silver nanoparticles are effective in inhibiting bacterial growth and may damage the DNA of both Gram-positive and Gram-negative bacteria [12–15]. Silver modified zeolite has been used in various fields such as catalyst, biosensors, water purification, antifungal and antimicrobial activity [16, 17].

The aim of this study is to prepare AgNPs/Zeo-Y nanocomposites using lemon juice as reducing agent by green synthesis method and study of its applications in the catalytic reduction of 4-Nitrophenol and the antibacterial activity of the system.

2. Experimental Section

2.1. Chemicals

Zeolite-Y and silver nitrate were purchased from Sigma Aldrich, USA. 4-Nitrophenol and liquid ammonia (30% v/v) were received from Fisher Scientific Pvt. Ltd., India. Sodium borohydrate, sodium chloride and amoxicillin were received from Merck, India. Hydrochloric acid and sulphuric acid were purchased from SRL Pvt. Ltd., India. All reagents and chemicals were used received from commercial source with an analytical grade and without further purification.

2.2. Preparation of AgNPs/Zeo-Y

To prepare AgNPs/Zeo-Y nanocomposite, 0.1 M $AgNO_3$ was dissolved in 20 mL of distilled water and then 1 % solution of NH_4OH was added dropwise to the aq. solution of $AgNO_3$ [18]. The color of the solution changed from greenish gray to colorless. 1 g of natural zeolite-Y was added to above mixture and stirred overnight. The product was collected and washed with distilled water and then dried at 100 °C for 2 h. Finally, the AgNPs/Zeo-Y nanocomposite was collected for further studies.

2.3. Synthesis of AgCl/ Zeo-Y

The Ag^+ ion loaded Zeo-Y was placed in a sealed 100 ml round bottom flask and then purged with HCl gas which was generated from NaCl in presence of conc.H_2SO_4 continuously to obtain AgCl immobilized Zeo-Y for a period of 2 h.

2.4. Preparation of AgNPs/Zeo-Y using lemon juice as reducing agent

To 3 mL of DD water was added a fresh 1 mL of lemon juice and the pH of the medium was adjusted to 11 followed by 0.01 M of silver nitrate solution was added. Finally, the yellowish green colored solution was changed to reddish brown color which indicated the formation of silver nanoparticle immobilized zeolites.

2.5. Preparation of Amoxicillin modified AgNPs/Zeo-Y

A known amount of AgNPs/Zeo-Y was dispersed an aqueous solution of 0.01M amoxicillin and then allowed stand for 1 h to obtain amoxicillin protected AgNPs/Zeo-Y. The final product was obtained by centrifugation.

2.6. Instrumentation

UV-Visible spectral studies were carried out using Shimadzu UV-Visible Spectrophotometer, Japan (Model UV-1800). The XRD patterns with diffraction intensity versus 2 θ were recorded in a JSO Debye Flex 2002 Seifert diffractometer using Cu Kα radiation (λ=1.5406 Å) from 10 to 80° at a scanning speed of 1° min^{-1}. X-ray tube voltage and current were set at 40 kV and 40 mA, respectively. Morphological and structural investigations were carried out using field emission scanning electron microscopy (FE-SEM, SU6600, Hitachi, Japan).

2.7. Antibacterial test

To evaluate the antibacterial properties of AgNPs/Zeo-Y and amoxicillin modified AgNPs/Zeo-Y, *Bacillus subtilis* and *Salmonella typhi* were selected as Gram-negative and Gram-positive bacteria, respectively. One has the ability to measure the effectiveness of an antibacterial agent by determining a zone of inhibition. A standard inoculum of the test organism with 1×10^7 colony forming units (CFU)/mL was swabbed onto the surface of a LB agar plate, AgNPs/Zeo-Y and Amoxicillin/AgNPs/Zeo-Y antibacterial agents were placed on the surface of agar. The plates were incubated overnight at 37°C, and the clear zones around the antibacterial agents were then measured. The above experiments were repeated thrice and the average values were taken.

3. Results and discussion

3.1. Characterization of AgNPs loaded Zeolite Y

The UV-Visible spectra of a) AgNPs/Zeo-Y, b) lemon juice, c) amoxicillin and d) AgNPs/Zeo-Y with amoxicillin are shown in Fig. 1. The silver nanoparticles loaded zeolite Y nanocomposite shows a silver nanoparticle peak at 420 nm due to surface plasmon resonance (SPR). The lemon juice not showing any peak and the amoxicillin peak was obtained at 270 nm. After the incorporation of amoxicillin drug into the silver nanoparticles loaded zeolite Y nanocomposite two major peaks were observed one at 360 nm and another one at 250 nm. Thus, these results confirm that amoxicillin drug was effectively attached to the silver nanoparticles loaded zeolite Y nanocomposite through ionic interaction.

The X-ray diffraction pattern of a) zeolite-Y and b) AgNps/Zeo-Y nanocomposite are shown in Fig. 2. As shown in Zeo-Y, the peaks at 31.04, 32.74, 33.24, 34.34, 35.94, 36.64, 37.76, 40.24, 41.74, 41.92, 52.80, 54.48, 56.54, 57.58, 58.74, 65.22, 66.54, 69.34, 71.10, 72.92, 75.96, and 77.82° are assigned for the presence of zeolite (JCPDS: 01-072-2344) [19]. In AgNPs/Zeo-Y, the characteristics peaks are due to the presence of silver chloride are attributed at 27.6, 32.05, 46.05, 54.6, 57.3, 67.4, 74.5 and 76.6° with plane of 111, 200, 220, 311, 222, 400, 311 and 420 reflections owing to the AgCl phase. These results confirm that the silver nanoparticles loaded within zeolite Y matrix.

The structural and morphology were confirms by FE-SEM images. The mesoporous material of zeolite has octahedral shaped particles with various sizes around 1 μm (Fig. 3(a)) [20]. From AgNPs loaded zeolite Y, the

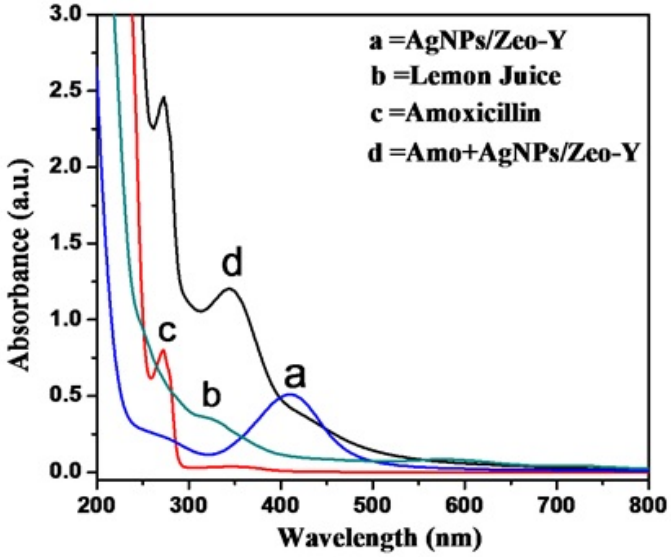

FIG. 1. UV-Visible spectrum of a) AgNPs/Zeo-Y, b) lemon, c) amoxicillin and d) AgNPs/Zeo-Y with amoxicillin

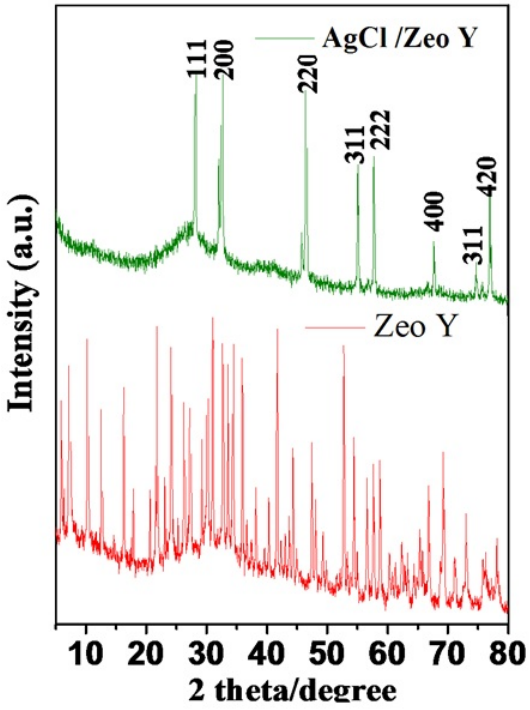

FIG. 2. XRD analysis a) zeolite Y and b) AgNPs loaded Zeo-Y

silver nanoparticles loaded on surface of mesoporous zeolite and also regular shaped silver nanoparticles and the size of the silver nanoparticles are roughly 0.1 μm as shown in Fig. 3(b). Therefore, the present method can be exploited for the effective loading of silver nanoparticles on zeolite surface.

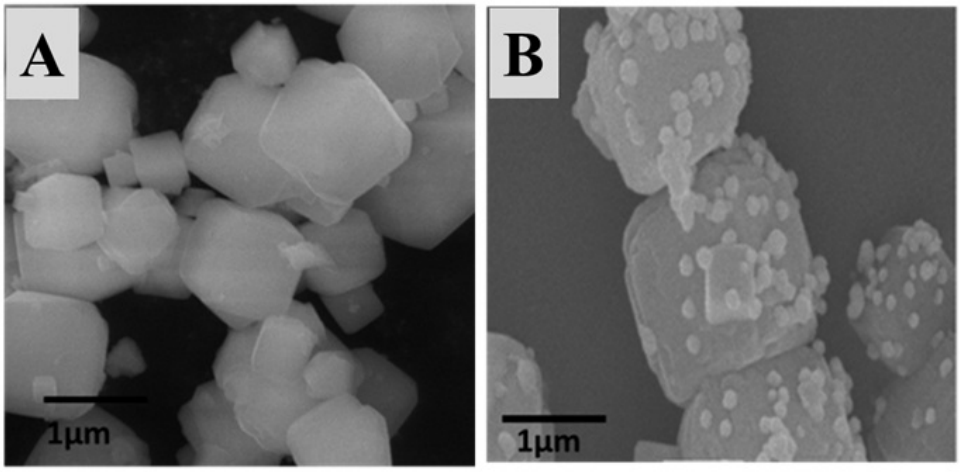

FIG. 3. FE-SEM images for Zeolite-Y (A) and AgNPs/Zeo-Y (B)

3.2. Catalytic activity of Zeolite Y loaded AgNPs

The catalytic activity of AgNPs/Zeo-Y was tested against the catalytic reduction of 4-Nitrophenol (4-NP) in the presence of $NaBH_4$. Upon the addition of $NaBH_4$ (Fig. 4(a)), the absorption peak of 4-Nitrophenol undergoes an immediate red-shift from 317 nm to 400 nm indicating the formation of 4-Nitrophenolate ions, evidenced by the visible color changes from light yellow to yellow green in color. After the addition of AgNPs/Zeo-Y using lemon juice nanocomposite, the absorption peak at 400 nm gradually decreased in intensity along with increase in absorption of a new peak at 300 nm, indicating the formation of 4-Aminophenol (4-AP). Under these reaction conditions, the reduction was completed within 10 and 5 mins for the addition catalytic amount 5 mg and 10 mg respectively (Fig. 4(b) and Fig. 4(c)).

The rate of reaction forb the reduction of 4-NP in presence of the AgNPs/Zeo-Y nanocomposite is due to decrease in absorbance values at 400 nm. Therefore, the rate constant of the reaction can be calculated using the following formula:

$$\ln C/C_0 = -kt, \tag{1}$$

where k is the constant, t is the reaction time; C and C_0 are the concentration of 4-NP at time t and 0, respectively. The concentration or borohydride used in the entire study was 0.1 M, which is large excess when compared to the concentration of 4-NP, thus the reduction reaction is considered to be pseudo first order so that the rate of the reaction depends primarily on the concentration of 4-NP. The rate of the reaction (k) obtained from the slope of the straight line was found to be 0.083 min^{-1} and 0.32 min^{-1} for 5 and 10 mg of catalyst used for the catalytic studies (Fig. 4(d)). The rate of the reaction increases with increasing of the catalyst concentration which is due to the increase of the catalytic activities.

3.3. Antibacterial activity

It is well established that silver nanoparticles modified substrates have shown an enhanced antimicrobial activity [12, 13]. In the present study, we studied the antimicrobial activity of silver nanoparticles, AgNPs/Zeo-Y and amoxicillin incorporated AgNPs/Zeo-Y against various Gram negative and Gram positive bacteria. Obviously, amoxicillin modified AgNPs/Zeo-Y showed a good antimicrobial activity against *Bacillus subtilis* and *Salmonella typhi.* The antimicrobial activity of AgNPs/Zeo-Y and Amoxicillin/AgNPs/Zeo-Y against various Gram positive and Gram negative bacteria as shown in Table 1.

4. Conclusion

In summary, the biogenic method was established to synthesize silver nanoparticle-loaded zeolite Y through an ion exchange approach followed green chemical reduction using lemon juice. This method is a fast and easy way to synthesize the AgNPs/Zeo-Y in large scale. The activity of AgNPs/Zeo-Y was studied, displaying excellent

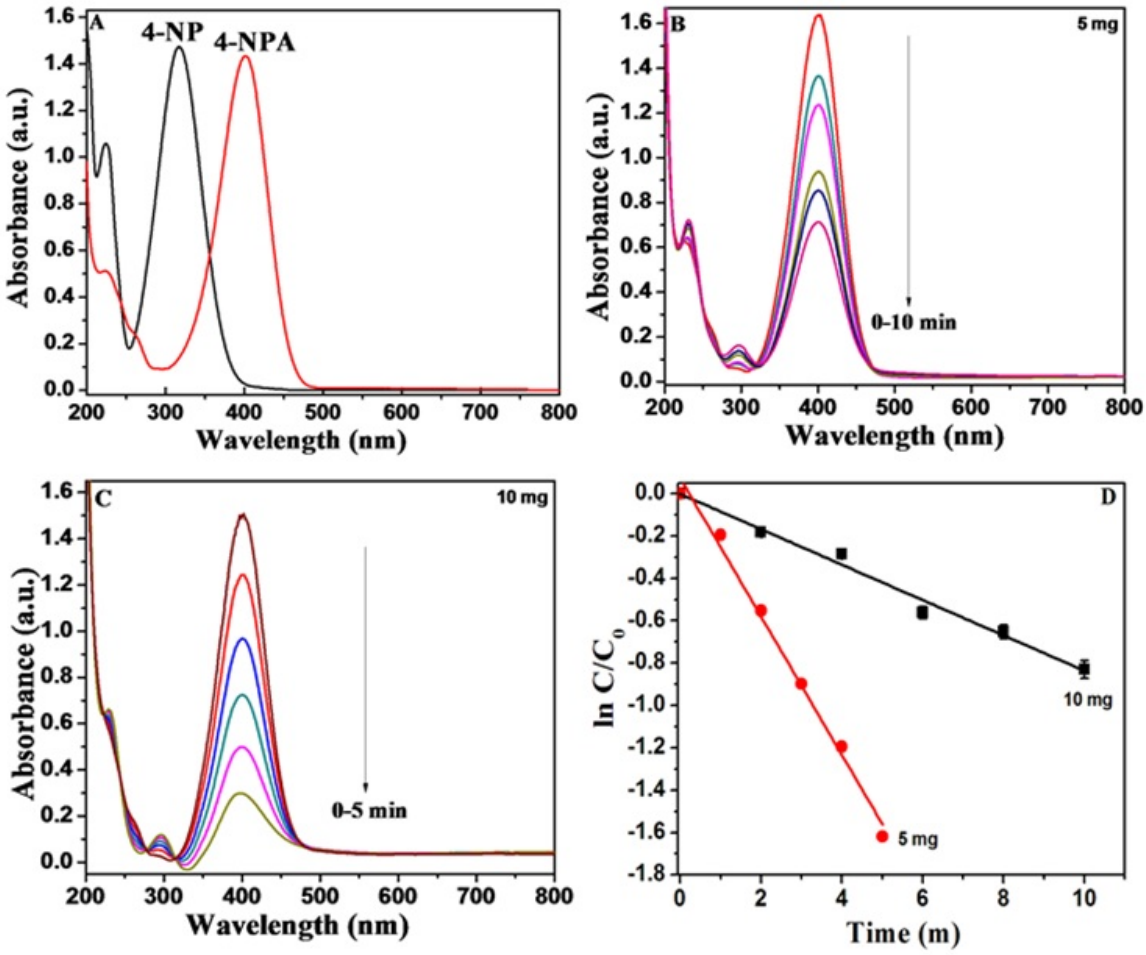

FIG. 4. UV-Visible spectra capturing the conversion of 4-NP to 4-AP upon reaction with $NaBH_4$(A), in presence of 5 mg and 10 mg of AgNPs/Zeo-Y (B), (C) and kinetic plot. Error bars designates the standard deviation for five independent measurements (D)

TABLE 1. Antibacterial activity of AgNPs/Zeo-Y and Amoxicillin/AgNPs/Zeo-Y against *Bacillus subtilis* and *Salmonella typhi*

Sample (mg/mL)	Gram Positive Bacteria					Gram Negative Bacteria				
	Bacillus subtilis					*Salmonella typhi*				
	a	b	c	d	e	a	b	c	d	e
AgNPs/Zeo-Y	2.2	6.5	7.3	16.4	-	3.3	6.5	8.4	20.5	-
Amoxicillin AgNPs/Zeo-Y	-	3.1	3.5	7.5	-	-	-	-	9.4	-

a = (25 μg/ml), b = (50 μg/ml), c = (75 μg/ml), d = (25 μg/ml (Standard) chloramphenicol), e = 50 μg/ml 0.1 % DMSO

catalytic activity for the conversion of 4-NP to 4-AP. The amoxicillin-protected AgNPs/Zeo-Y system can be exhibited an enhanced antimicrobial activity as compared to AgNPs/Zeo-Y.

Acknowledgement

The authors (Dr. K. P. and S. M.) is grateful the UGC-CPEPA for providing partial financial assistance to carry out a part of this work.

References

[1] Bandura L., Franus M., Jozefaciuk G., Franus W. Synthetic zeolites from fly ash as effective mineral sorbents for land-based petroleum spills cleanup. *Fuel*, 2015, **147**, P. 100–107.
[2] Rees L.V.C., Zuyi T. Rare-earth ion exchange in zeolite Y. *Zeolites*, 1986, **6**, P. 201–205.
[3] Yu J., Xiao F., Corma A. Preface to special issue on zeolite materials and catalysis. *Chinese Journals of Catalysis*, 2015, **36**, P. 787–788.
[4] Serban S., Murr N.E. Synergetic effect for NADH oxidation of ferrocene and zeolite in modified carbon paste electrodes: New approach for dehydrogenase based biosensors. *Biosensors and Bioelectronics*, 2004, **20**, P. 161–166.
[5] Onyango M.S., Kojima Y., Aoyi O., Bernardo E.C., Matsuda H. Adsorption equilibrium modeling and solution chemistry dependence of fluoride removal from water by trivalent-cation-exchanged zeolite F-9. *Journal of Colloid and Interface Science*, 2004, **279**, P. 341–350.
[6] Banerjee R., Furukawa H., Britt D., Knobler C., Keeffe M.O., Yaghi O.M. Control of pore size and functionality I isoreticular zeolitic imidazolate frameworks and their carbon dioxide selective capture properties. *J. Am. Chem. Soc.*, 2009, **131**, P. 3875–3877.
[7] Zhang Y., Yu X., Wang X., Shan W., Yang P., Tang Y. Zeolite nanoparticles with immobilized metal ions:isolation and MALDI-TOF-MS/MS identification of phosphopeptides. *Chem. Commun.*, 2004, **25**, P. 2882–2883.
[8] Mitsuo Y. Immobilization of toxic heavy metals using hydrotalcite minerals: possible applications for decontamination of polluted land and water. *Journal of Ecotechnology Research*, 2002, **8**, P. 248–249.
[9] Kharlamov V.V., Minachev K.M., Gulyaeva L.P., Slyunadev P.I. The investigation of redox properties of palladium-zeolite catalysts. *Russian Chemical Bulletin*, 1995, **44**, P. 621–623.
[10] Peter A., Cozmuta L.M., Cozmuta A.M., Nicula C. Photocatalytic efficiency of zeolite-based TiO_2 composites for reduction of Cu (II): Kinetic models. *Int. J. Appl. Ceram. Technol.*, 2014, **11**, P. 568–581.
[11] Guzman M., Dille J., Godet S. Synthesis and antibacterial activity of silver nanoparticles against gram-positive and gram-negative bacteria. *Nanomedicine: Nanotechnology, Biology and Medicine*, 2012, **8**, P. 37–45.
[12] Castanon G.A.M., Martinez N.N., Gutierrez F.M., Mendoza J.R., Ruiz F. Synthesis and antibacterial activity of silver nanoparticals with different sizes. *J. Nanopart Res*, 2008, **10**, P. 1343–1348.
[13] Rai M., Yadav A., Gade A. Silver nanoparticals as a new generation of antimicrobials. *Biotechn. Adv.*, 2009, **27**, P. 76–83.
[14] Xie W.R.L.X.B., Shi Q.S., Zeng H.Y., Yang Y.S.O., Chen Y.B. Antibacterial activity and mechanism of silver nanoparticles on Escherichia coli. *Appl. Microbial Biotechol*, 2010, **85**, P. 1115–1122.
[15] Baker C., Pradhan A., Pakstis L., Darrin J. Pochan, Shah S. Ismat. Synthesis and antibacterial properties of silver nanoparticles. *J. Nanosci. Nanotech.*, 2005, **5**, P. 244–249.
[16] Garza M.R., Olguin M.T., Sosa I.G., Alcantara D., Fuentes G.R. Silver supported on natural Mexican zeolite as an antibacterial material. *Microporous and Mesoporous Materials*, 2000, **39**, P. 431–444.
[17] Kaur B., Srivastava R., Satpati B. Silver nanoparticle decorated polyaniline zeolite nanocompoite material based non-enzymatic electrochemical sensor for nanomolar detection of lindane. *RSC Adv.*, 2015, **5**, P. 57657–57665.
[18] Meenakshi S., Devi S., PAndian K., Devendiran R., Selvaraj M. Sunlight assisted synthesis of silver nanoparticles in zeolite matrix and study of its application on electrochemical detection of dopamine and uric acid in urine samples. *Mat. Sci. Eng. C*, 2016, **69**, P. 85–94.
[19] Shameli K., Ahmad M.B., Zargar M., Yunus W.M.Z.W., Ibrahim N.A. Fabrication of silver nanparticles doped in the zeolite framework and antibacterial activity. *Int. J. Nanomed.*, 2011, **6**, P. 331–341.
[20] Reddy V.R., Currao A., Calzaferri G., Zeolite A., Zeolite L. Monolayers modified with AgCl as photocatalyst for water oxidation to O_2. *J. Mater. Chem.*, 2007, **17**, P. 3606–3609.

NANOSYSTEMS: PHYSICS, CHEMISTRY, MATHEMATICS, 2016, 7 (4), P. 774–779

In-situ functionalization of aniline oligomer onto layered graphene sheet and study of its application on electrochemical detection of ascorbic acidin food samples

S. Devasena[1], S. Meenakshi[2], R. Sayeekannan[1], K. Pandian[2,*]

[1]Department of Chemistry, Thiagarajar College, Madurai–625009, India

[2]Department of Inorganic Chemistry, University of Madras, Guindy, Chennai–600025, India

*jeevapandian@yahoo.co.uk

PACS 82.47.Rs **DOI 10.17586/2220-8054-2016-7-4-774-779**

Aniline oligomers are considered as one of the electron transfer mediators for the electrochemical oxidation of ascorbic acid. The electrochemical oxidation of ascorbic acid was investigated using aniline oligomer-functionalized polymer modified electrode. In the present investigation, we demonstrated a novel methodology for the in-situ modification of aniline oligomer onto the layered graphene sheet by using diazonium salt form as precursor molecule. An enhanced electrocatalytic current was obtained for the oxidation of ascorbic acid using aniline pentamer-functionalized reduced graphene oxide (AP-rGO). Detailed studies have been carried out to study the surface modified rGO by FTIR spectroscopy. A linear relationship between peak current against the concentration of ascorbic acid was observed within the ranges from 1 μM to 10 μM. The detection limit was measured at signal/noise (S/N) of 3. The present method can be utilized for the electrochemical detection of ascorbic acid present in food products like fruit juices.

Keywords: graphene oxide, pentamer, voltammetric method, ascorbic acid, food samples.

Received: 3 May 2016

Revised: 25 June 2016

1. Introduction

Ascorbic acid is one of most important biological compounds involved in various human metabolisms. It is used to ameliorate a number of illnesses, such as the scurvy, common cold, cancer and AIDS [1]. Moreover it is present in fresh fruits, vegetables and also available in pharmaceutical products and foodstuffs as an oxidant as well as stabilizer. Thus, the development of inexpensive and easy methods for the determination of ascorbic acid is particularly important in the pharmaceutical and food industries. There are several reported methods for the detection of ascorbic acid in foodstuffs, such as chromatography [2], spectrophotometry [3], capillary electrophoresis [4] and most recently, electrochemical methods [5–7].

The amperometric determination of ascorbic acid is based on its electrochemical oxidation, which occurs at high potential at carbon or metal electrodes, however, fouling by oxidation products leads to poor reproducibility [8]. Numerous attempts to decrease the high working electrode potential and improve reproducibility have been made by modifying the electrode surface with various active mediators for the electrochemical oxidation of ascorbic acid. Attempts have been made to develop a chemically-modified electrode with various redox mediators like 7,7,8,8-tetracyanoquinodimethane, osmium 2,2-bipyridyl poly-4-vinyl pyridine chloride complex, lanthanum 2,6-dichlorophenolindophenol, manganese dioxide and a cobalt (II) phthalocyanine and Prussian blue was also used to oxidize ascorbic acid [9, 10]. The electrocatalytic oxidation of ascorbic acid on conducting polymer modified electrodes, in particular on polyaniline, has also been studied. Recently, aniline oligomer-functionalized polymers have been used for the electrochemical oxidation of ascorbic acid has been developed that has both a low applied operating potential and a low detection limit.

In the present investigation, we demonstrated the preparation of an aniline oligomer-modified graphene oxide based on chemical reductive binding of diazonium salt form of aniline oligomer in presence of graphene oxide. The electrocatalytic behavior of an aniline oligomer-functionalized graphene oxide-modified glassy carbon electrode was tested against the electrochemical oxidation of ascorbic acid in phosphate buffer solution. The greater sensitivity and low detection limits were achieved by the differential pulse voltammetry method. Thus, the present method can be considered as an efficient one for electrochemical detection of ascorbic acid in food products.

2. Experimental Section

2.1. Chemicals

Graphite powder, Ascorbic acid and N, N-diphenylamine were received from Sigma Aldrich, USA. Ammonium hydroxide and sodium nitrite were purchased from Fisher Scientific Pvt. Ltd. India. DMF, HCl, H_2SO_4 and ethanol were received from SRL Pvt. Ltd. India. Ethanol and $KMnO_4$ were procured from Merck, India. All reagents and chemicals were used an analytical grade and without further purification.

2.2. Preparation of pentamer

2.28 g amino capped aniline trimer and 3.04 g N, N-diphenylamine were dissolved with 80 mL of DMF. 20 mL of water and 10 mL of 36 % of HCl were then added to the above solution with vigorous stirring at 4 hrs for room temperature. The HCl-doped aniline pentamer was obtained by filtration and then washed by a mixture of DMF/water. The product was doped in 100 mL of 1 ML^{-1} ammonium hydroxide for 30 m to produce aniline pentamer in emeraldine state. The emeraldine aniline pentamer was reduced by phenylhydrazine and was precipitated in a H_2O/ethanol mixture. The leucomeraldine aniline pentamer was collected by filtration and washed thoroughly with H_2O/ethanol mixture. The product was finally dried in vaccum oven.

2.3. Preparation of graphene oxide

20 g of graphite powder stirred with 500 mL of conc. H_2SO_4 in 1L beaker for 30 min. Then, 60 g of $KMnO_4$ was gradually added to this solution (added 20 g/30 minutes). The solution was then stirred for an additional 5 to 8 h and then added one l L water (900 mL) to the above mixture. Then, the reaction was terminated by addition of 50 mL H_2O_2 solution. Repeated centrifugation was done by using 5 % HCl aqueous solution followed by washed with deionized water until the pH of the solution reaches neutral. Then 160 mL of water was added resulting in the formation of precipitate. A uniform suspension of grapheme oxide (GO) nanoparticles was obtained after sonication [11].

2.4. Preparation of AP-rGO

The modification of GO was accomplished by dispersing GO (10 mg) in DI water (5 mL) to which aniline pentamer (10 mg) in 2 mL water was added. After complete dispersion of the reagent 0.011 g sodium nitrite in 1 ml of conc. HCl was added drop wise. The mixture was stirred for 4 h and then filtered, washed successively with deionized water followed by methanol. Finally, the powdered form of the product was isolated and then dried under nitrogen atmosphere in overnight.

2.5. Instrumentation

FTIR spectrum was recorded in the range of 400 to 4000 cm^{-1} FTIR spectrum was collected against the background spectrum of KBr. The cyclic voltammetric experiment was carried out using CHI 660A electrochemical instrument, USA and Gamry model 330, USA. A conventional three electrode system comprising of glassy carbon electrode (GCE) of 3 mm of geometrical surface area was purchased from BAS. Pvt. Ltd., USA. The Ag/AgCl and platinum wire were used as a reference electrode and counter electrode, respectively. The working electrode was polished using Bioanalytical system (BAS, USA) polishing kit.

3. Results and discussion

3.1. Characterization of AP-rGO

The FTIR spectrum of pentamer and AP-rGO are shown in Fig. 1. The absorption of aniline pentamer showed main bands at 1590 cm^{-1} and 1485 cm^{-1} assigned to the absorption of benzene ring and the quinoid ring. The 1273 cm^{-1} band was attributed to C-N stretching in the proximity of quinoid rings as shown in Fig. 1 [12]. After modification of AP-rGO, the benzenoid and quinoid peaks are bounded in the surface of graphene oxide. So these results confirm that the pentamer modified on graphene oxide surface.

The electrochemical behavior of AP-rGO was studied and the resulting cyclic voltammetry responses are shown in Fig. 2. As seen from Fig. 2(A), the typical cyclic voltammogram of AP-rGO in presence of 0.1 M H_2SO_4. With increase of scan rate the electrocatalytic oxidation peak current also increased gradually in the range from 5–100 mV/s. A linear relationship exists between peak current (I_p) versus scan rate (ν) and a linear regression equation of y = 0.406 – 5.685 with correlation coefficient (R^2) of 0.9959 as shown in Fig. 2(B), which illustrates a reversible electron transfer process with adsorption controlled one.

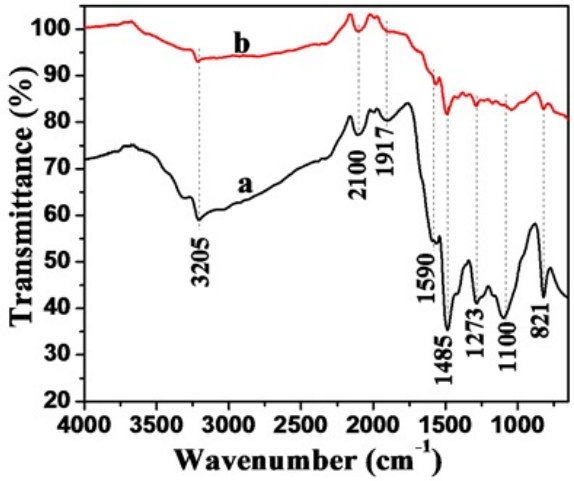

FIG. 1. FTIR spectrum of a) pentamer and b) AP-rGO

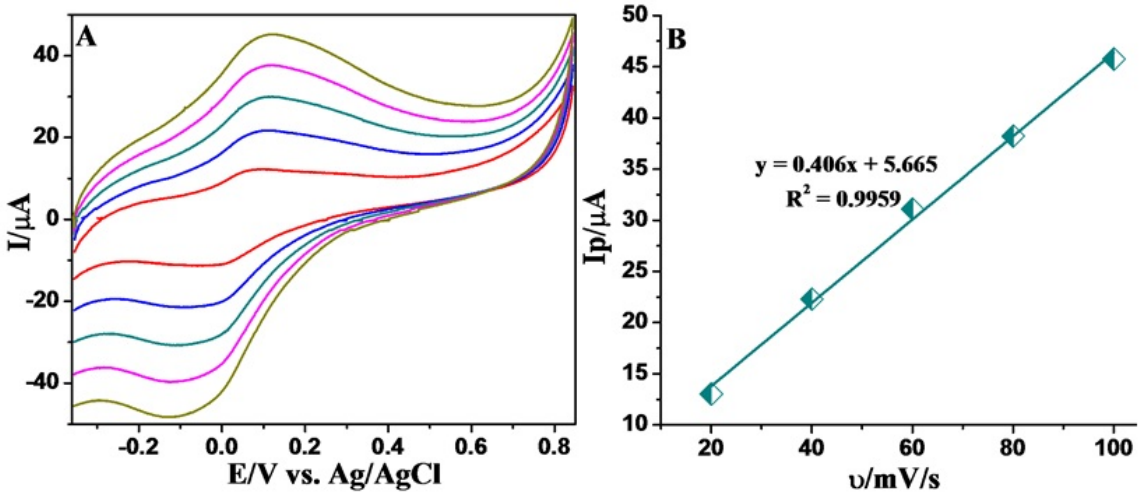

FIG. 2. A) CV of AP-rGO modified GCE at different scan rates (5-100 mV/s) in presence of 0.1 M H_2SO_4. B) Linear plot of Ip vs. υ

3.2. Electrochemical oxidation of ascorbic acid

The electrochemical behaviors of a) bare, b) bare-with ascorbic acid and c) AP-rGO modified GCE in presence of AA are shown in Fig. 3.(A) poor anodic current response was observed for the AA oxidation on bare GCE where as a well define oxidation peak was observed at +0.05 V (vs. Ag/AgCl) in the case of AP-rGO modified GCE.

The electrochemical behavior of AP-rGO/GCE at different concentrations of ascorbic acid (1×10^{-4} – 7×10^{-4} M) were investigated in 0.1 M pH 7.0 PBS by cyclic voltammetry (CV). As can be seen in Fig. 4(A), the AP-rGO/GCE after addition of AA to the buffer solution, an irreversible oxidation peak was observed at a scan rate of 50 mV/s with a anodic oxidation peak potential of +0.05 V (vs. Ag/AgCl). In Fig. 4(B) shows a linear regression equation of $y = 0.092x - 0.14$ with correlation coefficient is 0.9994.

The influence of peak potential scan rate against the electrochemical oxidation of ascorbic acid was investigated using AP-rGO/GCE in presence of 1mM of ascorbic acid at 0.1 M PBS (pH 7) with various scan rates as shown in Fig. 4(C). From AP-rGO modified GCE, the oxidation peak current of AA was increased by increasing the scan rates (10–120 mV/s) and linearity was observed by plotting the peak current values versus the square of scan rates with correlation coefficient of 0.9920 (Fig. 4(D)), suggesting that the electrochemical oxidation of AA is diffusion controlled electron transfer process.

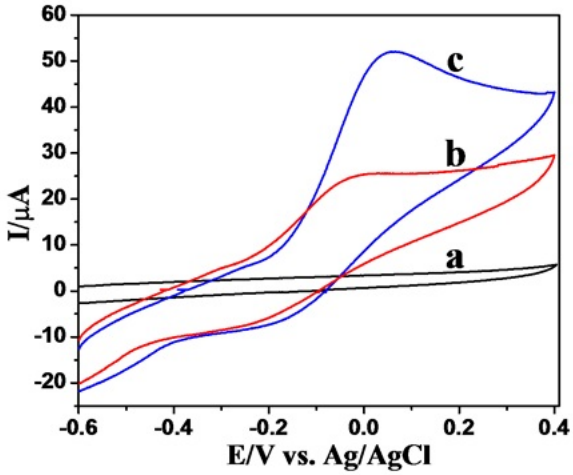

FIG. 3. Electrocatalytic behavior of a) bare, b) bare-with AA (1 mM) and c) AP-rGO/GCE with 1 mM of AA in 0.1 M PBS (pH 7) at scan rate 50 mV/s

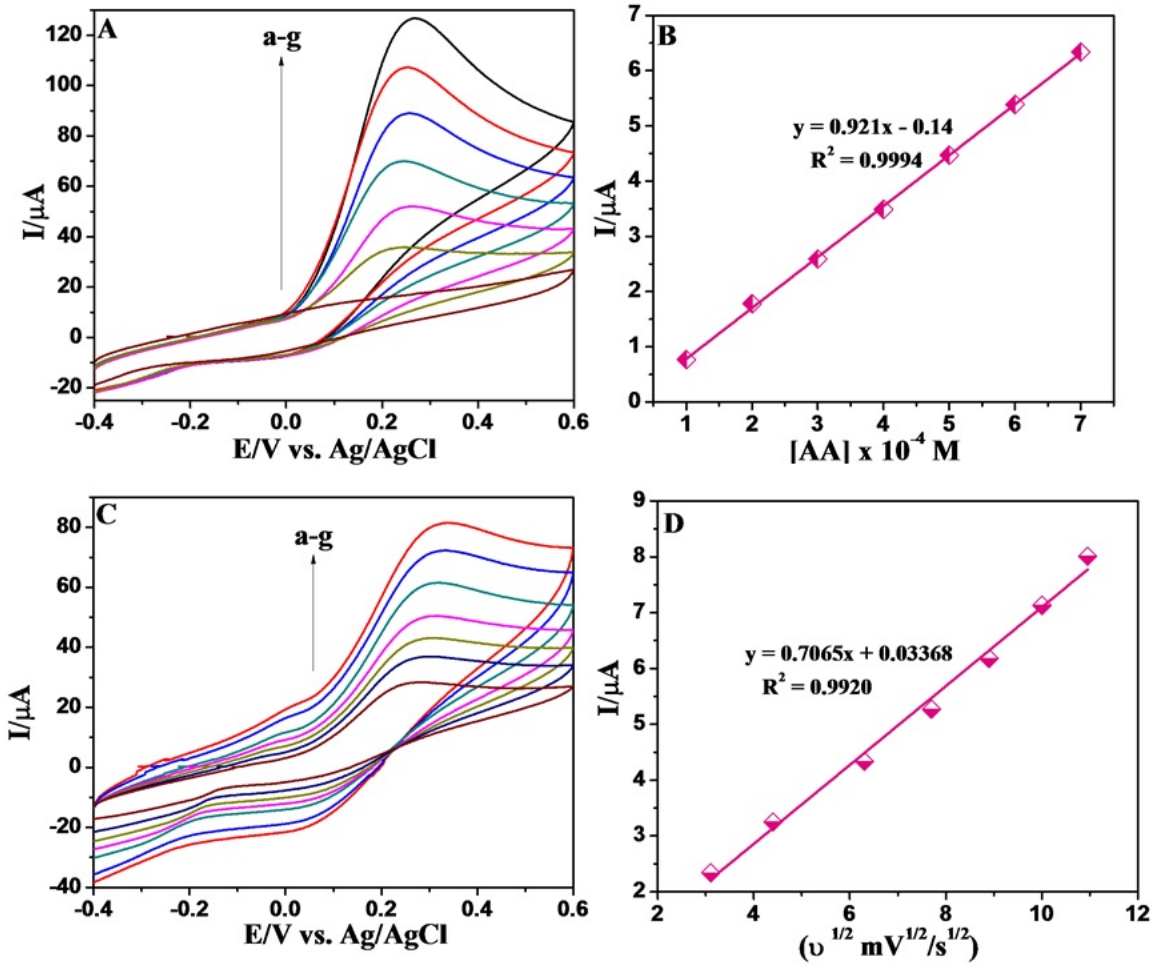

FIG. 4. A) AP-rGO/GCE in presence of AA in 0.1 M PBS (pH 7) at scan rate 50 mV/s and B) Linear plot of conc. vs. peak current. C) AP-rGO/GCE in presence of AA at different scan rates in 0.1 M PBS (pH 7) and D) Linear plot of Ip vs. $\upsilon^{1/2}$

3.3. Differential pulse voltammetry method

For the quantitative detection of ascorbic acid (AA) present in the pharmaceutical formulations and fruits samples at low concentration levels, the differential pulse voltammetry method was demonstrated using AP-rGO modified GCE under optimized experimental conditions. Fig. 5(A) shows differential pulse voltammogram for the electrocatalytic oxidation of AA using AP-rGO/GCE in PBS (pH 7) containing various concentrations of AA. The result shows the electrocatalytic peak current of AA oxidation at the AP-rGO/GCE was linearly dependent on the AA concentration and its ranges from 0.3 μM to 3 μM. As seen from Fig. 5(B), the calibration plot shows electrocatalytic peak current (I_p) versus AA concentrations with linear regression equation of $y = 0.494x - 0.212$ with correlation coefficient of 0.9923 and the detection limit (3σ/slope, σ is a standard deviation) is found to be 20 nM. These results strongly suggest that the oxidation of AA can be good selective and sensitive at aniline AP -rGO/GCE.

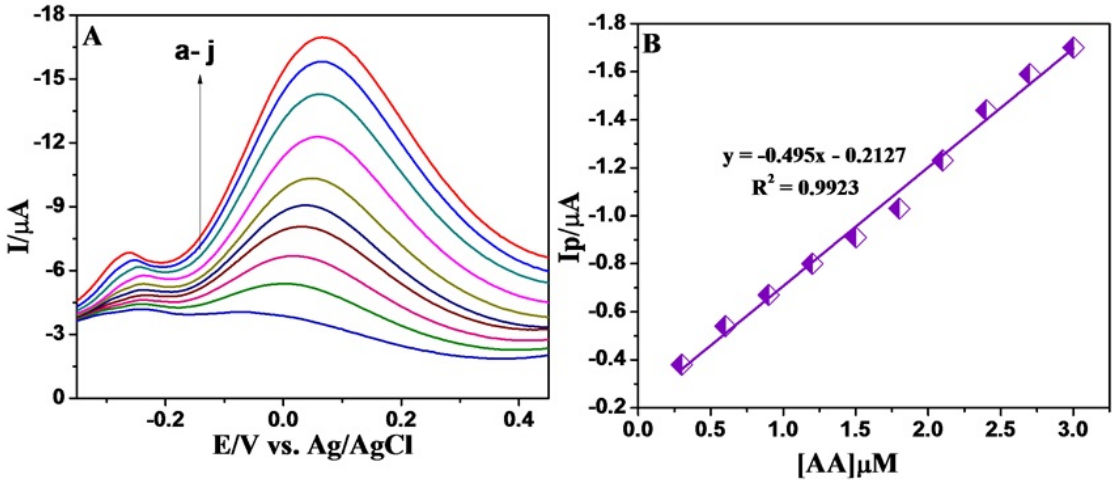

FIG. 5. A) DPV of AP-rGO/GCE in presence of AA at various concentrations (0.3–3.0 μM) in 0.1 M PBS (pH 7). B) Linear plot of concentration vs. peak current

3.4. Food sample analysis

In order to estimate the amount of AA present, fruit juice food samples were analyzed. Based on the repeated differential pulse voltammetric responses ($n = 5$) of the diluted analyte, samples were spiked with specified concentration of AA, measurements were made for determination of AA concentration in food samples. The results are listed in Table 1. The AP-rGO/GCE possessed reasonable selectivity and produced satisfactory recovery result with an average recovery of 100.3 % and the RSD was less than 5.3 %. The measured data of AA concentration was in good agreement with the results found in the titration measurements, suggesting the good accuracy and reliability.

TABLE 1. Determination of AA in fruit samples

Samples	Added (10^{-6} g/ml^{-1})	Found (10^{-6} g/ml^{-1})	Recovery (%)
Apple	0.50	1.024	99.3
Pineapple	0.70	1.208	100.6
Orange	1.50	2.133	101

4. Conclusion

A single step method was adapted to modified graphene sheet with aniline pentamer as electron transfer mediator. The surface modification of graphene was confirmed from FTIR and cyclic voltammetry studies. A simple differential pulse voltammetry method was developed to determine low concentration ranges of ascorbic acid using aniline pentamer grafted graphene sheet. Enhanced detection limits was achieved using this method. The present method can be utilized for the electrochemical detection of ascorbic acid in pharmaceutical and fruit samples.

Acknowledgement

The authors (Dr. K. P and S. M.) are grateful to DST purse programme to upgrade the Gamry 330 electrochemical system (DPV software).

References

[1] DeNobili M.D., Perez C.D., Navarro D.A., Stortz C.A., Rojas A.M. Hydrolytic stability of L-(+)-ascorbic acid in low methoxyl pectin films with potential antioxidant activity at food interfaces. *Food Bioprocess Technol.*, 2011, **6**, P. 186–197.

[2] Jens L. Determination of ascorbic acid and dehydroascorbic acid in biological samples by high performance liquid chromatography using subtraction methods: Reliable reduction with tris (2-carboxyethyl) phosphine hydrochloride. *Anal. Biochem.*, 2000, **282**, P. 89–93.

[3] Yu Y.H., Donat P.H. UV-B-induced formation of reactive oxygen species and oxidative damage of the cyanobacterium *Anabaena sp.*: protective effects of ascorbic acid and N-acetyl-L-cysteine. *J. Photochem. Photobio. B: Biology*, 2002, **66**, P. 115–124.

[4] Wu T., Guan Y., Ye J. Determination of flavonoids and ascorbic acid in grapefruit peel and juice by capillary electrophoresis with electrochemical detection. *Food Chem.*, 2007, **100**, P. 1573–1579.

[5] Ping J., Wang Y., Wu J., Ying Y., Ji F. Determination of ascorbic acid levels in food samples by using an ionic liquid carbon nanotube composite electrode. *Food Chem.*, 2012, **135**, P. 362–367.

[6] Francis F.J. *Wiley encyclopedia of food science and technology*, 2-nd ed., Vol 4. Wiley, New York, 1999.

[7] Habibi B., Pournaghi-Azar M.H. Simultaneous determination of ascorbic acid, dopamine and uric acid by use of a MWCNT modified carbon-ceramic electrode and differential pulse voltammetry. *Electrochimica Acta*, 2012, **55**, P. 5492–5498.

[8] Roy P.R., Saha M.S., Okajima T., Ohsaka T. Electrooxidation and amperometric detection of ascorbic acid at GC electrode modified by electropolymerization of N, N-Dimethylaniline. *Electroanalysis*, 2004, **16**, P. 289–297.

[9] Florou A.B., Prodromidis M.I., Stella M.T.K., Miltiades I. Fabrication and voltammetric study of lanthanum 2,6-dichlorophenolindophenol chemically modified screen printed eletrodes: Application for the determination of ascorbic acid. *Anal. Chimica Acta*, 2000, **423**, P. 107–114.

[10] Zuo X., Zhang H., Li N. An electrochemical biosensor for determination of ascorbic acid by cobalt (II) phthalocyanine- multiwalled carbon nanotubes modified glassy carbon electrode. *Sensors Actuat.*, 2012, **161**, P. 1074–1079.

[11] Hummers W.S., Offemn R.E. Preparation of graphitic oxide. *J. Am. Chem. Soc.*, 1958, **80**, P. 1339.

[12] Huang L., Hu J., Lang L., Wang X., Zhang P., Jing X., Wang X., Chen X., Lelkes P.I., MacDiarmid A.G., Wei Y. Synthesis and characterization of electroactive and biodegradable ABA block copolymer of polylactide and aniline pentamer. *Biomaterials*, 2007, **28**, P. 1741–1751.

NANOSYSTEMS:

PHYSICS, CHEMISTRY, MATHEMATICS

Журнал зарегистрирован
Федеральной службой по надзору в сфере связи, информационных технологий и массовых коммуникаций
(свидетельство ПИ № ФС 77 - 49048 от 22.03.2012 г.)
ISSN 2220-8054

Учредитель: федеральное государственное автономное образовательное учреждение высшего образования
«Санкт-Петербургский национальный исследовательский университет информационных технологий, механики и оптики»

Издатель: федеральное государственное автономное образовательное учреждение высшего образования
«Санкт-Петербургский национальный исследовательский университет информационных технологий, механики и оптики»

Отпечатано в Учреждении «Университетские телекоммуникации»
Адрес: 197101, Санкт-Петербург, Кронверкский пр., 49

Подписка на журнал НФХМ
На первое полугодие 2017 года подписка осуществляется через
ОАО Агентство «Роспечать»
Подписной индекс 57385 в каталоге «Издания органов научно-технической информации»